SURFACE FUNCTIONALIZED NOBLE METAL NANOPARTICLES AND THEIR ENCAPSULATION IN POROUS SILICA: A SYNTHESIS, CHARACTERIZATION AND CATALYTIC STUDY

A THESIS SUBMITTED TO THE

UNIVERSITY OF PUNE

FOR THE DEGREE OF

DOCTOR OF PHILOSOPHY

IN

CHEMISTRY

BY

ANUPAM SAMANTA

Dr. R. NANDINI DEVI

(RESEARCH GUIDE)

CATALYSIS AND INORGANIC CHEMISTRY DIVISION

NATIONAL CHEMICAL LABORATORY

PUNE 411008

INDIA

MARCH 2014

DECLARATION BY RESEARCH GUIDE

Certified that the work incorporated in the thesis entitled: **"Surface Functionalized Noble Metal Nanoparticles and Their Encapsulation in Porous Silica: A Synthesis, Characterization and Catalytic Study",** submitted by Mr. Anupam Samanta, for the Degree of ***Doctor of Philosophy,*** was carried out by the candidate under my supervision at Catalysis and Inorganic Chemistry Division, National Chemical Laboratory, Pune-411008, India. Such material as has been obtained from other sources has been duly acknowledged in the thesis.

Dr. R. Nandini Devi

(Research Supervisor)

DECLARATION BY RESEARCH SCHOLAR

I hereby declare that the thesis entitled **"Surface Functionalized Noble Metal Nanoparticles and Their Encapsulation in Porous Silica: A Synthesis, Characterization and Catalytic Study",** submitted for the ***Degree of Doctor of Philosophy*** to the University of Pune, has been carried out by me at Catalysis and inorganic Chemistry Division, National Chemical Laboratory, Pune-411008, India, under the supervision of Dr. R. Nandini Devi. The work is original and has not been submitted in part or full by me for any other degree or diploma to this or any other University.

Anupam Samanta

.....DEDICATED

TO MY PARENTS

Acknowledgement

It gives me immense pleasure to express my deep sense of gratitude to my supervisor and mentor ***Dr. R. Nandini Devi*** *for her excellent guidance, continuous encouragement, and generous support in achieving this entire endeavour. Wholeheartedly, I am very much grateful to her for motivating me in the field of Nanocatalysis. Without her encouragement and constant guidance, I could not have finished my doctoral degree. I do sincerely acknowledge the freedom rendered by her in the laboratory for the independent thinking, planning and execution of research. Working with her was really a great pleasure and fetched me a lot of learning experience.*

My heartfelt thanks to Dr. Sayam Sen Gupta, D. B. L. V. Prasad, Dr. Chithra Manikandan and Dr. Suresh Bhat for useful discussions. It gives me great pleasure to thank Dr. Asmita Prabhune and Dr. Basab B. Dhar for fruitful collaboration work.

I sincerely acknowledge the help provided by Dr. Paresh L Dhepe, Dr. Anil Kinage, Dr. T. Raja, Dr. C. V. V. Satyanarayna, Dr. C. S. Gopinath, Dr. C. P. Vinod, Dr. T. G. Ajith Kumar. Dr. Rajmohanan, Dr. S. K. Asha, Dr. Rahul Banerjee, Dr. V. Panchagnula, Dr. H. V. Thulasiram, I am also thankful to Anuj and Panderaj for TEM and Ketan for SEM.

It gives me great pleasure to thank my labmates Dr. Kala Raj, Rajesh, Jijil, Leena, Soumiya, Sourik, Sandhya Lekha, Sharanya, Shibin, Sumona, Monojit, Manoj, Dr. Atul , Dr. Ramakanta for their kind help and support, invaluable discussions which we shared and maintaining a lively environment in the laboratory during every walk of life in the laboratory to achieve this goal and also thank to trainee students worked with me, Prakriti and Rajith. Especially I want to thank Rajesh for helping me a lot to study CO oxidation reaction.

I am thankful to my colleagues Ruchira, Vilas, Ajeet, Kaushl, Venugopal, Kanak, Suman, Sharath and Vysakh for their invaluable help.

I would like to to express my appreciation to my friends Debasis Pati, Anal, Debasis Dey, Sumantra, Chandan, Sujitda, Pradipda, Binoy, Partho, Sumanta, Prithvi, Tamos, Krisanu, Shyam, Joyashish, Vaibav, Yogesh for spending wonderful time with them.

I also spent some good time with the juniors Arpan, Mrinmoy, Saikat, Subhadeep Saha, Sankho, Subhadeep Das, Anjan, Achinta, Susanta, Pravat, Arya, Arijit, Chandan, Soumen, Anup, Prasenjit, Sagar, Sandip, Tanushree and Richa.

It gives me great pleasure to thank my parents and family members, for their love and unconditional support. I would like to address a special word of thanks to my brother Goutam for encouraging me to do science. I must acknowledge my wife and best friend Deepa without whose love, encouragement and editing assistance, I would not have finished this thesis.

Finally, my thanks are due to Council of Scientific and Industrial Research, Government of India, for awarding the research fellowship, and to Dr. S. Sivaram, former Director and Dr. Sourav Pal, Director, National Chemical Laboratory, to carry out my research work and extending all possible infrastructural facilities, and to allow me to submit this work in the form of a thesis for the award of Ph.D. degree.

…….……..***Anupam***

ABSTRACT

Ultra-small noble metal nanoclusters < 2 nm in diameter have attracted much attention in the past decade due to their unique physicochemical properties, such as intrinsic photo-luminescence and selective catalytic properties. Due to the ultra-small size, these nanoclusters induce quantum confinement effect and do not show surface plasmon resonance band. As a result nanoclusters behave like single molecules and show HOMO-LUMO electronic transitions. Therefore these nanoclusters posses intense fluorescence emission property which makes them promising candidates for biolabelling and bioimaging applications, provided they are water dispersible. Ultra fine size and biocompatibility as a consequence of appropriate functionalization, also make them more applicable compared to quantum dots. Therefore, there is a growing interest for the development of a facile method for the fabrication of stable biocompatible ultra fine noble metal nanoclusters which can be used for biomedical applications.

Catalysis by noble metal nanoparticles like Au, Ag, Pd and Pt becomes highly interesting also because of their unusual reactivity and selectivity. Supported noble metal catalysts are widely used for industrial applications. Though supported metal nanocatalysts are highly active for various types of reactions, one of the major problems associated with it is deactivation of the catalyst under reaction condition or during storage. It is proposed that agglomeration of metal nanoparticles on the support is one of the major reasons for this deactivation. Coalescence of smaller particles leading to bigger particles is one of the mechanisms of agglomeration and this decreases the surface area and alters surface properties of the nanoparticles consequently affecting catalytic activity detrimentally. This can be addressed by encapsulating metal nanoparticles in porous silica shell to get both activity and stability. So there is a good opportunity to work on the area of noble metal nanoclusters and their silica encapsulation study for various applications.

In the present work, a novel alkylammonium thiol ligand capable of synthesizing water dispersible noble metal nanoclusters and nanoparticles has been designed. Nanoclusters are used for bioimaging application and further utilized as precursors for the synthesis of porous silica encapsulated metal nanoparticles.

Chapter 1 presents a general introduction to the role of noble metal nanoclusters and nanoparticles in versatile applications including catalysis and bioimaging. It gives details about current status of synthesis procedure of noble metal nanoparticles and their application in catalysis and bioimaging. It has described how particle size of metal nanoparticles plays an important role for exhibiting photo physical property like fluorescence and also for catalytic activity. This chapter also describes agglomeration problem in nanocatalysis. Silica encapsulation is one of the solutions to minimize agglomeration. Various examples of silica encapsulated and porous silica encapsulated metal nanoparticles have been described in this chapter.

Chapter 2 describes the synthesis of *N*,*N*,*N*-Tripropyl(11-mercaptoundecyl)ammonium chloride ligand. This ligand has been used for synthesis of ultra-small Au nanoclusters and nanoparticles. Ultra-small Au clusters show good fluorescence intensity at NIR region. This photo physical property has been used for the detection of *E.coli* bacteria cell. Thiolate protected ultra-small Au clusters are further utilized as precursors for the preparation of porous silica encapsulated Au nanoparticle catalysts. The catalyst is found to be a peroxidase mimic nanomaterial following Michaelis-Menten kinetics for enzyme catalyzed reactions. This porous silica encapsulated materials have been used for the detection of very low concentration of glucose and H_2O_2.

Chapter 3 describes that highly stable and water dispersible Pd nanoparticles ranging from nanoclutsers to nanoparticles are prepared by using a *N*,*N*,*N*-Tripropyl(11-mercaptoundecyl)ammonium chloride ligand. Highly sinter resistant silica encapsulated Pd nanocatalyst has been synthesized by utilizing ultra-small Pd clusters as precursors for silica encapsulation. Silica encapsulated Pd nanocatalyst shows good catalytic activity for hydrogenation reaction.

Chapter 4 describes a very simple strategy employed for the synthesis of fully alloyed AuPd nanoparticles encapsulated in porous silica shell. For bimetallic system, a mixture of Au and Pd nanoclusters are used as precursors instead of single nanocluster precursors for silica encapsulation as in case of simple Au or Pd. These alloyed AuPd nanocatalysts are also found to be highly sinter resistant even at high temperature like 750 °C and also highly active for CO oxidation reaction at light-off temperatures.

Chapter 5 describes preliminary study on the synthesis of Ag and Pt nanoclusters and nanoparticles and their silica encapsulation. Thiol ligand, *N*,*N*,*N*-Tripropyl(11-mercaptoundecyl)ammonium chloride is capable of synthesizing a range of nanoparticle from ultra-small clusters to bigger nanoparticles. However, Pt nanostructures could be synthesized only at high thiol concentrations and failed to give any fruitful results with lower concentrations. Ag and Pt nanoclusters are further utilized for silica encapsulation.

Chapter 6 summarizes the observations and gives overall conclusion of the work done. As a whole this thesis describes a novel method for the synthesis of noble metal nanoclusters and their utilization for the fabrication of sinter resistant silica encapsulated nanocatalysts. Particle size can be controlled and reactivity also be retained by utilizing this method.

TABLE OF CONTENTS

List of Figures

List of Schemes

List of Tables

List of Abbreviations

AHL	Acyl homoserine lactone
APTMS	(3-aminopropyl)-trimethoxysilane
BET	Braunauer-Emmett-Teller
BJH	Barrett-Joyner-Halenda
DFT	Density Functional Theory
FID	Flame Ionization Detector
FTIR	Fourier Transform Infrared
GC	Gas Cromatography
GHSV	Gas hour space velocity
GOD	Glucose Oxidase
EDAX	Energy Dispersive X-Ray Analysis
HK	Horvath-Kawazoe method
HRTEM	High Resolution Transmission Electron Microscopy
HRP	horseradish peroxidase
ICP-AES	Inductively Coupled Plasma-Atomic Emission Spectrometry

MCM	Mobil’s Crystalline Material
NMR	Nuclear Magnetic Resonance
NC	Nanocluster
NP	Nanoparticle
P123	Pluronic P123 Triblock Co-polymer
PVP	Poly(vinylpyrrolidone)
SBA	Santa Barbara Amorphous
SEM	Scanning Electron Microscopy
SPR	Surface Plasmon Resonance
TEOS	Tetraethyl orthosilicate
TEM	Transmission Electron Microscopy
TMB	3,3,5,5-tetramethylbenzidine
TTAB	Tetradecyltrimethylammonium bromide
UV-Vis	Ultraviolet-Visible
XRD	X-Ray Diffraction

.

CHAPTER 1

INTRODUCTION AND LITERATURE SURVEY

1.1. INTRODUCTION

Metal nanoparticles have fascinated scientists over a century and are now heavily utilized for several applications [1-6]. Among these, versatile applications in catalysis, sensing and biomedical engineering [7-14], have led to an increased attention on noble metal nanoparticles. However, from the last two decades, research is more focused on the synthesis of stable noble metal nanoclusters because of their unique applications in various fields like catalysis, biolabelling and bioimaging [15-21]. Nanoclusters are nanoparticles smaller than 2 nm, which is comparable to Fermi wavelength of electrons (the de Broglie wavelength of the electrons at the Fermi level is ~ 0.5 nm for Ag and Au). Due to the ultra-small size, these nanoclusters induce quantum confinement effect and do not show surface plasmon resonance band normally exhibited by Ag and Au nanoparticles of size > 2 nm. As a result, nanoclusters behave like single molecules and show HOMO-LUMO electronic transitions [16,21,22]. Therefore these nanoclusters possess intense fluorescence emission property which makes them promising candidates for biolabelling and bioimaging applications, provided they are water dispersible. Ultra fine size and biocompatibility as a consequence of appropriate functionalization, also make them more applicable compared to quantum dots [23]. Therefore, there is a growing interest for the development of facile methods for the fabrication of stable biocompatible ultra fine noble metal nanoclusters which can be used for catalysis and biomedical applications.

1.2. SYNTHESIS OF NOBLE METAL NANOPARTICLES

Various methods including ligand stabilization are available for the synthesis of noble metal nanoparticles [24-30]. Thiol stabilized nanoparticles are well known because of their extraordinary stability and monodispersity [31-36]. After the pioneering work of Brust et al [31] on the synthesis of alkyl thiol stabilized Au nanoparticles, a large amount of work has been performed on these materials. The basic reactions of the Brust method of synthesis include,

i) Phase transfer of a gold salt (reaction is not balanced)

$HAuCl_4$ (aq) + TOABr (tol) → $[AuCl_{4-x}Br_x]$TOA (tol) + HCl (Br) (aq) (1)

ii) Reduction of Au(III) to Au(I)

$[AuCl_{4-x}Br_x]$TOA (tol) + HSR → Au:SR (complexes) (2)

iii) Reduction of Au(I) to Au(0):

Au:SR (tol) + $NaBH_4$ (aq) → $Au_n(SR)_m$ (3)

where, n and m represent the number of gold atoms and thiolate ligands, respectively.

This method of synthesis is attractive because the nanoparticles are highly stable and can be isolated and stored in powder form for a long time and are re-dispersible in solvent [31]; this is in contrast with conventional gold colloids stabilized by electrostatic interaction.

Later many groups including those of Brust, Whetten and Murray have carried out extensive work on developing this method to synthesize stable, monodisperse thiolate protected Au nanoparticles of size 3-5 nm using a variety of thiols, including long-chain alkylthiols (Cn-SH) [37,38], arenethiols [39] and water soluble thiols [40]. Hussain et al have made an excellent protocol to synthesize Au nanoparticles in much smaller size regime (< 5 nm) using polymeric thio-ether as stabilizing agents [41]. Yao et al have synthesized uniform Au nanocrystals (3.3, 4.3, 5.6 nm) with mercaptosuccinic acid as stabilizer [42]. Wang et al have designed polymeric thiol ligands for the preparation of highly monodisperse Au nanoparticles with diameter below 5 nm by using a single step method [43]. Cargnello et al have prepared small and mostly monodisperse thiol-protected Pd nanoparticles with size ~2 nm by using 11-mercaptoundecanoic acid (MUA), 9-mercapto-1-nonanol (MN) and 1-dodecanethiol (DT) as capping agents [44]. There are many other synthetic protocols available for the preparation of nanoparticles in the size range of *ca.* 2-5 nm. Though Brust method is extensively employed for the preparation of thiol protected noble

metal nanoparticles, one of the major disadvantages is the polydispersity of the synthesized nanoparticles.

Various post-synthetic treatments, including size-selective precipitation by adding a non-solvent [45], chromatographic separation [46-49], thermal treatment [50-53] and other methods are performed for getting relatively monodisperse nanoparticles from the polydisperse products. For example, Lin et al have performed thermal ripening method for the preparation of very uniform nanoparticles (~5 nm) starting with highly polydisperse Au nanoparticles stabilized by surfactant didodecyldimethylammonium bromide (DDAB) [54,55]. Alvarez et al have performed extensive work on fractionation of as-synthesized polydisperse Au nanoparticles by choosing appropriate solvent, such as ethanol to get selective precipitation of thiolate protected Au nanoparticles with narrow size distribution [56].

With such a robust research history in the field of nanoparticles, nowadays attention is steered more towards synthesising ultra-small noble metal nanoclusters, especially gold nanoclusters because of their unique quantum confinement effect. Whetten, Murray and others have made modifications to the original Brust protocol by increasing thiol to gold ratio and also using excess amount of reducing agent to make ultra-small Au nanoclustes [57]. Even though a reduction in size of the resultant nanoparticles could be achieved by these modifications, polydispersity still plagued these systems. Since nanoclusters' quantum confinement properties are very sensitive to the number of atoms in the core, several attempts have been made to synthesize monodisperse nanoclusters [58,59]. Murray and co-workers have done lot of work on the synthesis and isolation of molecule-like clusters [60,61]. Tsukuda et al have reported a high resolution PAGE separation on $Au_n(SG_m)$ to get monodisperse nanoclusters and also conducted an impressive study of ESI mass spectrometry analysis of all the isolated species [62]. Recently Jin and co-workers have performed excellent work on the synthesis and electronic property study of ultra-small Au nanoclusters [63-67]. They have focused on the synthetic process of Au nanoclusters formation by thiol ligands by two reduction steps (eqns 1 &2). Formation of Au(I)SR intermediates (eqn 1) is very important for controlling cluster size and monodispersity. Since the formation of Au(I)SR aggregates occurs after the reduction of Au(III) into

Au(I) by excess thiol, temperature of the reaction medium is an important factor to control the formation of Au(I)SR aggregates. By performing the reduction of Au(III) to Au(I) at 0 °C and also by optimizing the stirring speed Au(I)SR aggregate formation can be controlled [Scheme 1.1]. By doing this controlled process, Zhu et al are able to obtain $Au_{25}(SR)_{18}$ clusters in high yield and more importantly in high purity [68].

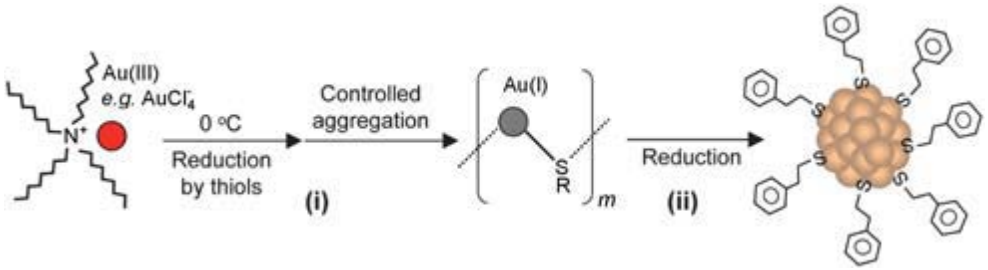

Scheme 1.1. High-yield synthesis of gold thiolate clusters via kinetic control. [Source: Ref. 68]

Compared to Au, only a very few reports exist on other noble metal clusters, for example; Rao et al have prepared silver nanoclusters having the composition $Ag_9(H_2MSA)_7$ (H_2MSA = mercaptosuccinic acid) using a solid-state route [69]. Yuan et al have synthesized thiol protected highly fluorescent Ag and Pt nanoclusters by electrostatically induced reversible phase transfer method [70].

1.3. OPTICAL PROPERTIES OF NOBLE METAL NANOPARTICLES

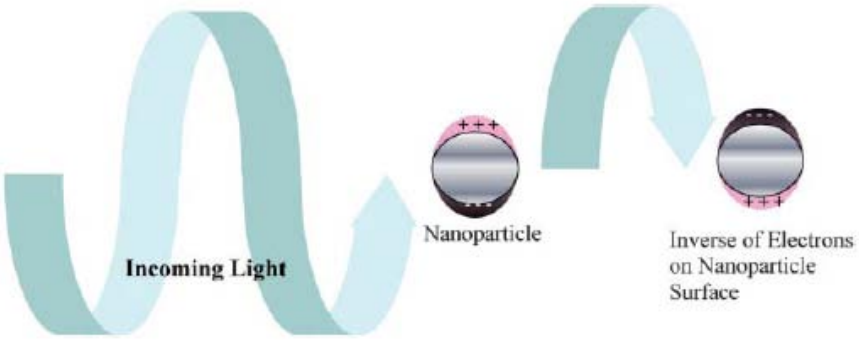

Fig. 1.1. Origin of surface plasmon resonance due to coherent interaction of the electron in the conduction band with light. [Source: Ref. 71].

Some of the noble metal nanoparticles like those of Au and Ag display brilliant colours, which are tunable and strongly depend on their size, shape and the surrounding medium [71]. Recent studies have shown that the colour is due to the collective oscillation of free d electrons in the metal which move freely through the material, known as surface plasmon oscillation [Fig. 1.1]

Light in resonance with the surface plasmon oscillation makes the free electrons on the metal nanoparticle surface to oscillate. As the wave front of the light progresses through the metal surface, the electron density is polarized and oscillates in resonance with the light's frequency resulting in a standing oscillation. The oscillation frequency of Au and Ag nanoparticles is usually in the visible region, generating strong surface plasmon resonance absorption [72]. Size and shape changes in the nanoparticles affect the oscillation frequency of the electrons and generate different cross-sections for the optical properties including absorption and scattering. Gold nanospheres show surface plasmon resonance band at ~ 520 nm but this absorption band is shifted to longer wavelength with increasing diameter of the nanosphere [73]. Gold nanorods show two surface plasmon resonances, one due to the transverse oscillation of the electrons around 520 nm and the other due to the longitudinal plasmon resonance at longer wavelength [73,74].

Optical property of noble metal nanoclusters (e.g., Au, Ag) of size below 2 nm is quite different from that of bigger nanoparticles. These nanoclusters do not exhibit characteristic surface plasmon resonance band but show distinct electronic transition bands in case of monodisperse nanoclusters and an exponential decay curve in case of polydisperse ones [75]. Because of ultra-small size, these nanoclusters induce distinct quantum confinement effect resulting in discrete electronic levels which manifest as molecule-like properties such as photolumininescence, intrinsic magnetism etc [76-78]. Theoretically, the critical size for electronic energy quantization in nanoclusters is calculated to be ~ 1.7 nm for Au and Ag [16,21]. Zhu et. al have performed extensive work to describe electronic structure and optical properties of Au_nSR_m. They have shown three distinct absorption bands characteristic of $Au_{25}(SR)_{18}$ clusters [67]. They have considered $Au_{25}(SH)_{18}^{-1}$ as model compound for doing computational study to find out the molecular orbitals.

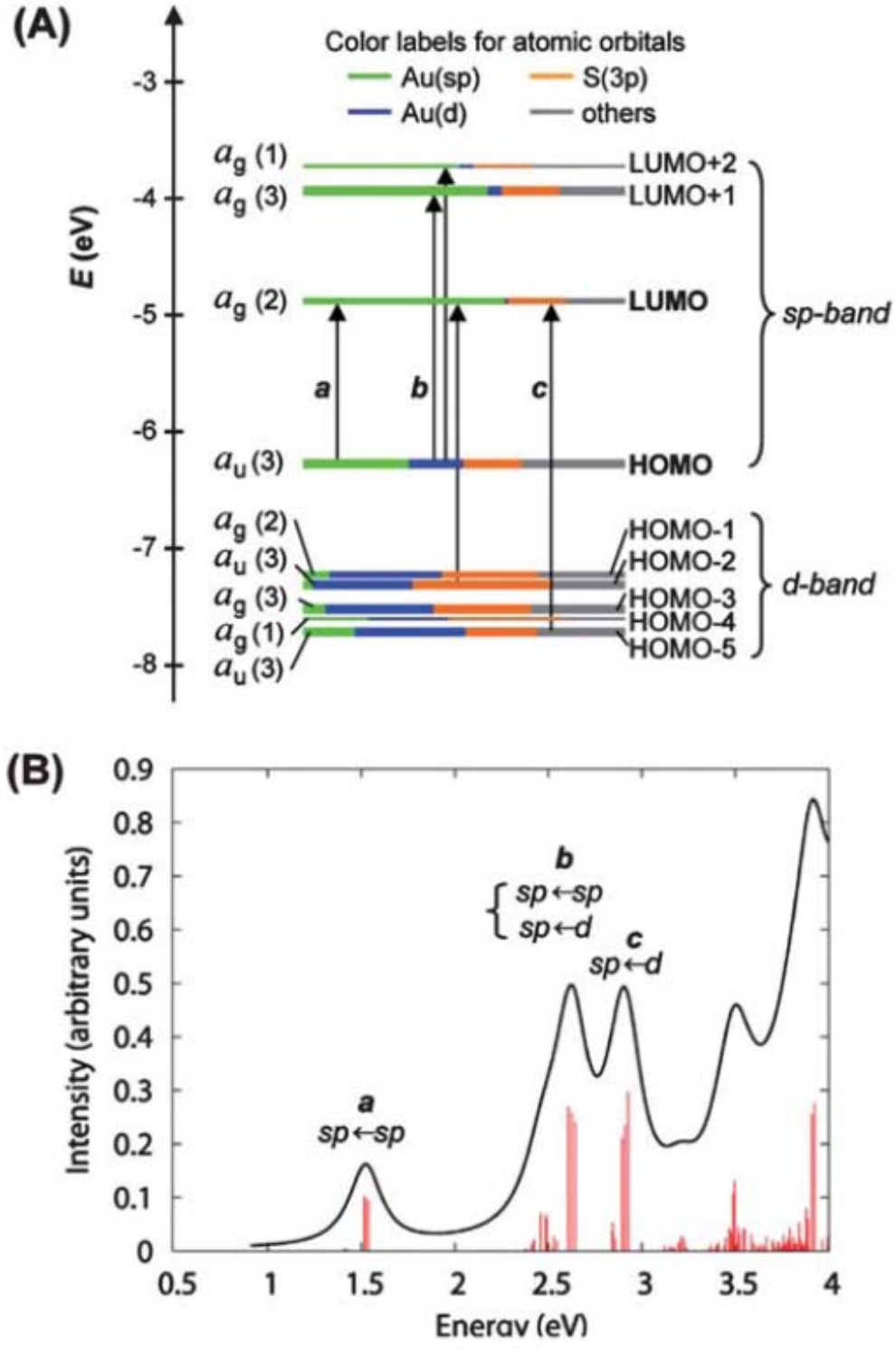

Fig. 1.2. (A) Kohn–Sham orbital energy level diagram for a model compound $Au_{25}(SH)_{18}^{-1}$ and (B) the theoretical absorption spectrum of $Au_{25}(SH)_{18}^{-1}$. [Source Ref. 67]

The calculated Kohn–Sham molecular orbitals (MOs), energies, and atomic orbital (AO) contributions are shown in Fig. 1.2A. In the electronic structure of $Au_{25}(SH)_{18}^{-1}$, the HOMO and the lowest three LUMOs are mainly composed of 6s (or 6sp) atomic orbitals (labelled in green) of gold, thus, these orbitals constitute the sp band keeping the solid-state terminology. The HOMO level is nearly triply degenerate while the LUMO is doubly degenerate. The HOMO-1 through HOMO-5 levels are mainly constructed from the $5d^{10}$ atomic orbitals (labelled in blue) of gold and hence constitute the d-bands. Both sets of HOMO and LUMO orbitals have a significant degree of the S(3p) (labelled in yellow) character, indicating that the ligand influences the electronic structure of the cluster. Further, Zhu et al have done a precise correlation between Au_{25} cluster structure and optical absorption properties from its crystal structure [67]. The theoretical spectrum of $Au_{25}(SH)_{18}^{-1}$ agrees quite well with experiment, especially in the spectral shape (compare Fig. 1.2B and Fig. 1.3).

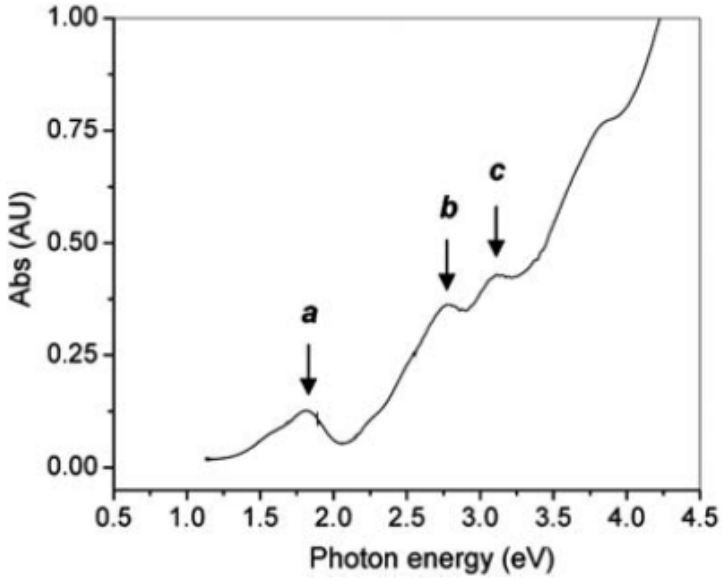

Fig. 1.3. UV-vis spectrum of Au_{25} clusters. [Source Ref. 67]

This cluster serves as a good example to illustrate the quantum size effect on the optical properties of gold clusters. Unlike Au nanoparticles in which surface plamsons (collective excitation of conduction electrons) dominate the optical properties, ultra-small clusters manifest one-electron transitions. Such discrete energy levels give rise to bright fluorescence in these materials which is exploited recently in biolabelling and bioimaging.

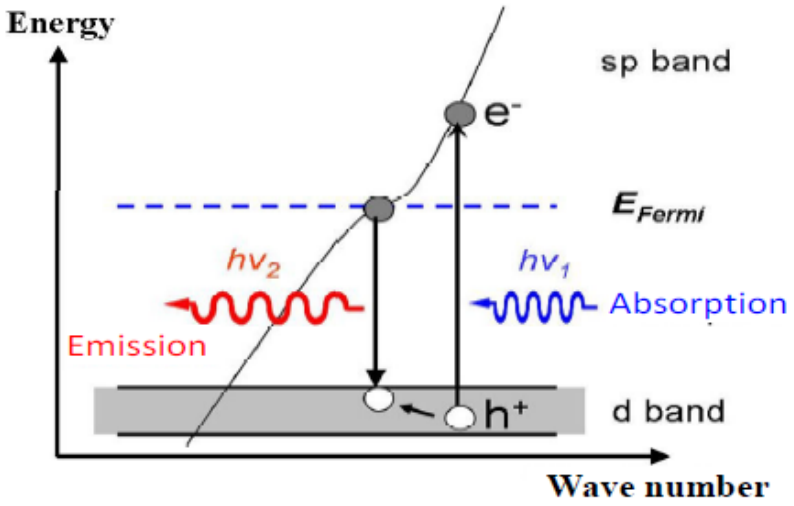

Fig. 1.4. A simple energy diagram of photoluminescence in gold nanoclusters involving d-band excitation. [Source: Ref 21]

Apell et al have described the probable reason for the fluorescence property exhibited by noble metal nanoclusters [21] as recombination involving d-band excitation, as described in Fig. 1.4. Absorption of a photon promotes an electron from the narrow d band to the empty sp band above the Fermi level. After some carrier relaxation, radiative recombination responsible for the emission then occurs between an electron (probably one near or below the Fermi level) and the excited hole, resulting in the visible-near-IR emission.

The emission wavelength of these metallic clusters can be tuned by changing the capping agents. Au nanoclusters, emitting fluorescence at different wavelengths [Fig. 1.5] have been synthesized by using various capping agents [21]. Size dependent fluorescence property is also observed in case of Au nanoclusers; with increasing cluster size, emission wavelength is shifted to longer wavelengths [79-84].

Nanoclusters, especially with red emission are highly advantageous in biomedical application, because red emission can improve the signal-to-noise ratio owing to its maximal penetration in tissue, minimal auto-fluorescence and negligible tissue scattering [85]. Therefore, there is a growing interest for the development of a facile method for the fabrication of monodispersed and red fluorescent nanoclusters for bioimaging applications. Wu et al have reported for the first time, tumor cell

fluorescence imaging *in vivo* by ultra-small near-infrared emitting gold nanoclusters [86].

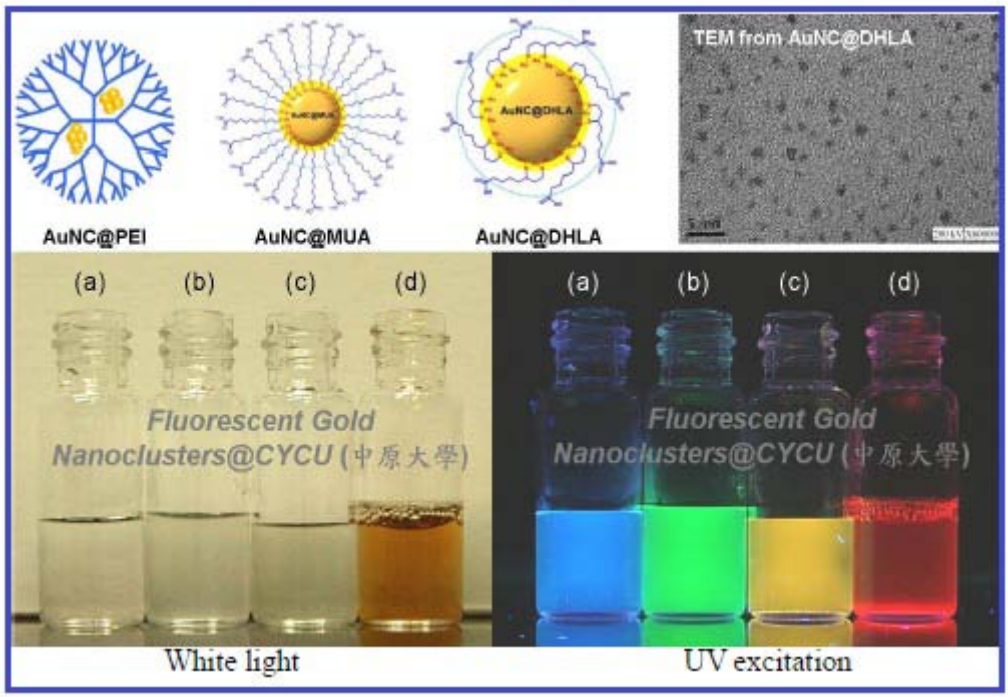

Fig. 1.5. Four distinguishable emission colours of fluorescent gold nanoclusters excited with a UV lamp. Upper left illustrates the possible structures of AuNC@PEI, AuNC@MUA and AuNC@DHLA. Upper right is TEM image of AuNC@DHLA. Lower figures: From left to right (blue to red) which is made in PEI (a), MUA (b,c) or DHLA (d) respectively, the emission maximum are located at 450, 500,550, and 650 nm. [Source: Ref. 21]

Bian et al have prepared red fluorescent Au nanoclusters by one-step method and utilized for cancer cell imaging [ref]. Guevel et al have synthesized bovine serum albumin (BSA) protein stabilized NIR-emitting fluorescent Au nanoclusters for lung tumor cell imaging [85]. Wang et al have developed a turn-on near-infrared (NIR) fluorescent probe by using Transferrin (Tf)-functionalized gold nanoclusters (Tf-AuNCs)/graphene oxide (GO) nanocomposite (Tf-AuNCs/GO) for cancer cell imaging [87]. Fluorescence property of Ag and Pt nanoclusters also has been employed for several applications, albeit to a smaller extent compared to Au nanoclusters, as example; Adhikari et al have synthesized water soluble fluorescent

Ag nanoclusters for Hg (II) sensing [88], Tanaka et al have utilized mercaptoacetic acid (MAA) stabilized Pt nanoclusters and utilized for bioimaging application [89].

1.4. NOBLE METAL NANOPARTICLES IN CATALYSIS

Another important utilization of noble metal nanoparticles like Au, Ag, Pd and Pt occurs in heterogeneous catalysis in various industrially and socially significant processes like petroleum refining, catalytic converters etc. [90-98]. Catalytic activity of noble metal nanoparticles is understood to be due to their peculiar interactions with adsorbed molecules and the energetics involved in such adsorption processes. Not only reactivity but selectivity also is pivotal in defining a catalytic process in current scenario whereby researchers across board are trying to develop green processes. These factors are highly dependent on the surface structure and hence can be easily tuned just by changing the shape or size of the nanomaterials [99-104]. In the early stages, attempts were made to use colloid metal nanoparticles directly in catalysis. Advantageously, surface of these nanoparticles could be functionalized with lipophilic or hydrophilic groups to make them dispersible for performing catalysis in organic and aqueous medium respectively [105-108]. On the other hand colloid nanoparticles are usually stabilized by capping agents like polymers or surfactants to prevent their agglomeration but better capping agents also block the active sites of the metal surface and reduce the catalytic activity [109]. Recently catalysis by noble metal nanoclusters has also become highly interesting because of their extraordinary reactivity. Research groups of Tsukuda and Jin have performed excellent work on catalysis by using noble metal nanoclusters [110, 111]. Tsunoyama et al have performed size specific catalytic activity of polymer stabilized gold nanoclusters for aerobic alcohol oxidation in water [112]. Zhu et al have performed selective hydrogenation of α,β-unsaturated ketone and aldehydes by using Au nanoclusters [111]. Turner et al have synthesized 55-atom Au clusters and supported them on inert materials and used these materials for selective oxidation of styrene by using dioxygen only [113].

Thermal and chemical stability of active metal nanoparticles are very important factors in catalysis. At high temperatures, typically above 300 °C, the organic capping layers are decomposed and metal nanoparticles can deform and aggregate. As a result, the size, shape and composition of nanoparticles during or after

high-temperature reactions could be different from those of pristine nanoparticles which may adversely affect the activity. Many industrially important catalytic processes, including automotive emission abatement processes [114], CO oxidation [115-118], partial oxidation [119] and cracking of hydrocarbons [120] and combustion reactions [121] are carried out at temperatures above 300 °C. In this scenario, catalysts which are stable at high reaction temperatures are in high demand.

Hence researchers have moved towards the synthesis of stable oxide supported nanocatalysts, in which such aggregation and subsequent deactivation could be minimised, instead of poorly stable colloidal nanoparticles. Conventional heterogeneous catalyst preparation methods often involve the deposition of an inorganic salt precursor onto a solid support via incipient wetness impregnation or coprecipitation techniques, followed by rigorous drying, calcination and reduction steps [122]. Such supported noble metal catalysts are widely used for industrial applications. Haruta and co-workers have developed novel ultra-fine Au catalysts supported on reducible transition metal oxides by coprecipitation method and performed low temperature CO oxidation study [123, 124]. After Haruta's pioneering work on low temperature CO oxidation, researchers are motivated to do extensive work on the activity study of gold based catalysts. Current automotive catalysts are based on Pt group of metals which have failed to solve the ''cold start-up'' problem in which much of the CO produced by incomplete combustion is not oxidized for operation temperature below 200 °C [125]. Gold based catalysts can oxidize CO at much lower temperature (even at room temperature or below) and because of this, gold can play a vital role in the future of efficient automotive catalysts [126]. Many catalysts based on solid oxide supported Au nanoparticles are developed for low temperature CO oxidation reaction. Scheuth and co-workers have synthesized highly active Au nanocatalysts supported on iron oxide, magnesium oxide and magnesium hydroxide for low temperature CO oxidation [127]. Many other groups have developed Au based catalysts for this oxidation reaction; Lee et al have prepared γ-Al_2O_3 supported Au catalysts by wet impregnation method [128], Lee et al have synthesized a series of Au/CoOx-TiO_2 with various Co/Ti ratios by deposition-precipitation (DP) method [129], Bulushev et al have prepared highly dispersed Au nanoparticles on activated carbon fibers [130], Lie et al have synthesized highly active

TiO_2-supported Au catalyst (denoted as $Au/Ti(OH)_4$), which was prepared by supporting a Au–phosphine complex on as-precipitated wet titanium hydroxide followed by calcination at 673 K [131]. An extensive number of noble metal catalysts are synthesized by many researchers for the preferential oxidation of carbon monoxide in presence of hydrogen. They are gold-based catalysts like Au/MnOx, $Au/\gamma\text{-}Al_2O_3$, $Au/\alpha\text{-}Fe_2O_3$, Au/TiO_2, Au/CeO_2 [132] and platinum based catalysts Pt/Al_2O_3 [133], Ce promoted Pt/γ-Al2O3 [134]. Apart from CO oxidation, many other oxidation reactions involving supported Au catalysts and O_2 are developed, such as the direct epoxidation of alkene [135, 136], and liquid-phase aerobic oxidations of several substrates like alcohols [137,138], aldehydes [139], and hydrocarbons [140]. Supported Pt nanoparticles are widely employed in various processes including petroleum refining, the oxidation of CO and hydrocarbons in automotive catalytic converters, the oxidation of NH_3 in nitric acid synthesis, hydrosilylation of alkenes and aryl alkynes, hydrogenation of benzene and cyclohexene, and direct decomposition and oxidation of alcohols [141-150]. Many groups have studied extensively on selective hydrogenation of α,β-unsaturated aldehydes to yield unsaturated alcohols using Pt based catalysts since they are industrially valuable products and intermediates for synthesis of fine chemicals [151,152]. Fukuoka and co-workers have performed novel work on preferential oxidation of CO catalysed by Pt nanoparticles supported on mesoporous silica [153, 154]. Chen et al have done selective hydrogenation of acetophenone on Pt/SiO_2 catalyst [155]. An et al have shown enhanced CO oxidation rates at the interface of mesoporous oxides and Pt nanopraticles [156]. Goodman and co-workers have carried out extensive study on the catalytic oxidation of CO by noble metal nanoparticles from ultrahigh vacuum to elevated pressures [143]. Park et al have investigated the role of organic capping layer of Pt nanoparticles in catalytic activity of CO oxidation [157]. Supported Pd nanocatalysts are widely used for hydrogenation and C-C coupling reactions. Palladium (Pd) is the most selective noble metal catalyst also for alkyne semihydrogenation with respect to over all alkene formation [158]. The classic Lindlar catalyst, consisting of metallic Pd on calcium carbonate support modified with lead (II) acetate, is a well known commercially available catalyst for such reactions [159]. Silvestre-Albero et al have studied hydrogenation of 1,3-butadiene on $Pd\text{-}Al_2O_3$ catalysts for a wide range of particle sizes, from 2 to 8 nm [160]. Lim et al have

prepared Pd nanoparticle catalysts having 2-4 nm particle size using silica gel and porous polymer beads as solid supports and utilized these catalysts for selective hydrogenation of olefins in aqueous medium [161]. Garcia-Suarez et al have developed efficient and recyclable carbon-supported Pd nanocatalysts for the Suzuki-Miyaura reaction in aqueous medium [162]. Karami et al have synthesized titania-supported highly dispersed Pd nanocatalyst for Suzuki and Heck coupling reactions [163]. Zolfigol et al have prepared highly stable and active magnetically separable Pd nanocatalyst for aqueous phase coupling reaction [164].

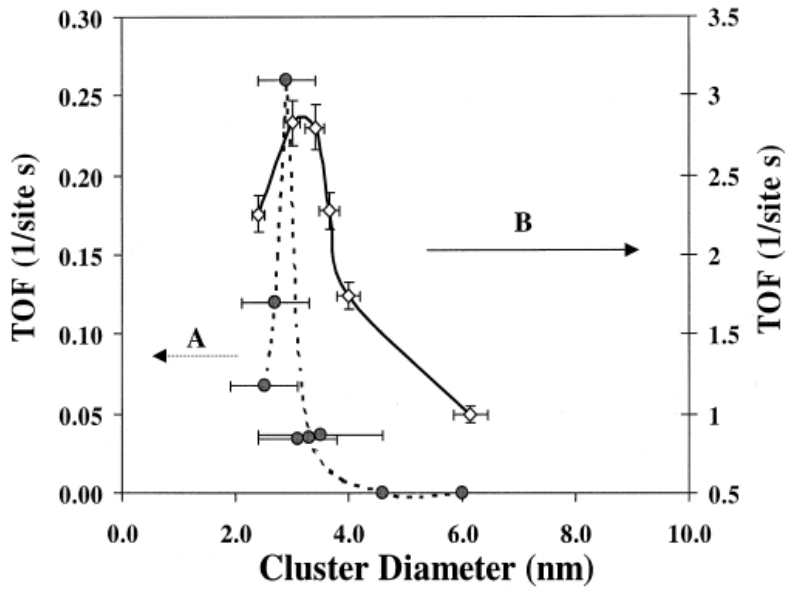

Fig. 1.6. CO oxidation turnover frequencies (TOFs). as a function of the Au cluster size supported on TiO_2 . (A) The Au/TiO2 catalysts were prepared by a precipitation method and (B) The Au/TiO_2 catalysts were prepared by vapor-deposited Au atoms on planar TiO_2 films on Mo(100). [Source Ref. 174]

Supported silver nanoparticles have long been extensively used as oxidizing catalysts and have been applied industrially to the epoxidation of ethylene [165,166]. Supported Ag nanocatalyst is a potential candidate for selective hydrogenation of chloronitrobenzenes (CNB) to the corresponding chloroanilines (CAN), important intermediates for fine chemicals such as agrochemicals, pharmaceuticals and dyestuffs [167].

Catalytic properties of nanocatalysts depend strongly on the support, particle size, shape, as well as other factors [168-170]. Many fundamental studies have been carried out to investigate how the catalytic activity depends on these factors. In case of supported noble metal catalysts, size of metal nanoparticles plays a vital role in determining the catalytic activity [171]. Noble metal nanoparticles show good catalytic activity in the size range of ≤ 10 nm [172,173]. Goodman and co-workers have performed extensive study to investigate the sensitivity of CO oxidation with respect to the size of the gold nanoparticles [174]. They have discovered that Au/TiO_2 shows maximum activity when the gold nanoparticle size is ~ 3 nm [Fig. 1.6]. Haruta et al also have found the same size dependency on catalytic activity with gold on different type of supports [175]. Many theoretical studies have been performed to investigate the reason for high catalytic activity shown by small Au nanoparticles [176,177]. Density functional theory study has suggested that low-coordinated atoms play a major role in catalytic activity of small Au nanoparticles [178]. Wilson et al have found the effect of Pd nanoparticle size on the catalytic hydrogenation of allyl alcohol [179]. Their analysis indicates that the hydrogenation kinetics is dominated by electronic effect of the smallest particles (≤ 1.5 nm diameter) and by geometric effect for larger particles (1.5-1.9 nm diameter). Bhattacharjee et al have studied the selectivity in the catalytic hydrogenation of unsaturated alcohol as function of Pd nanoparticle size [102]. They have found that smallest Pd nanoparticles (average diameter of 2.2 nm) have shown highest selectivity for hydrogenation of monosubstituted over disubstituted double bonds. Turner et al have performed selective oxidation of styrene by molecular oxygen using silica supported small Au nanoparticles of size < 2 nm [113].

Though supported metal nanocatalysts are highly active for various types of reactions, one of the major problems associated with it is deactivation of the catalyst under reaction conditions or during storage [180-182]. It is proposed that agglomeration or sintering of metal nanoparticles on the support is one of the major reasons for this deactivation [183,184]. Lie et al have investigated deactivation of Pt nanocatalyst due to sintering of mobile nanoparticles [Fig. 1.7] on alumina support [185]. Sintering of metal nanoparticles leads to decrease in metal surface area as well

as a loss in the metal-support interface area and these two factors are responsible for lowering the activity of the metal catalyst [186].

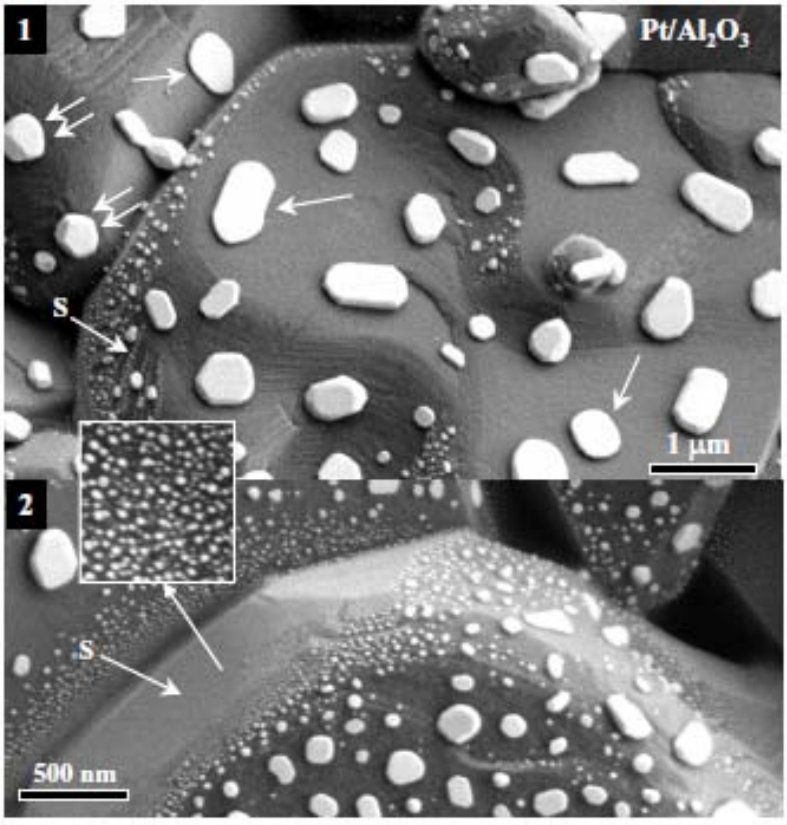

Fig. 1.7. *In situ* SEM images of Pt/Al_2O_3 catalyst showing the agglomeration of Pt articles on certain faces of the alumina support. S denotes unchanged particles. [Source: Ref.185]

Two mechanisms of particle sintering in heterogeneous catalysis have been proposed, Ostwald ripening and particle migration and coalescence [187]. The ripening process involves the emission of atoms or clusters from small particles, and the accumulation of these mobile species to larger particles. The driving force for this agglomeration is the higher surface energy of the metal atoms in small particles compared to that on larger particles. The second proposed mechanism involves the direct migration of particles on solid support followed by coalescence, leading to particle growth. These processes are shown schematically in Fig. 1.8. Sintering is one of the most important causes for loss of catalytic activity when catalysts are subjected to elevated temperatures, as in automotive exhaust or during catalytic combustion.

Datye and co-workers have performed extensive study on sintering of model catalysts at elevated temperatures. They have demonstrated that Ostwald ripening is the dominant mechanism for sintering of Pd nanoparticles on oxide support [188].

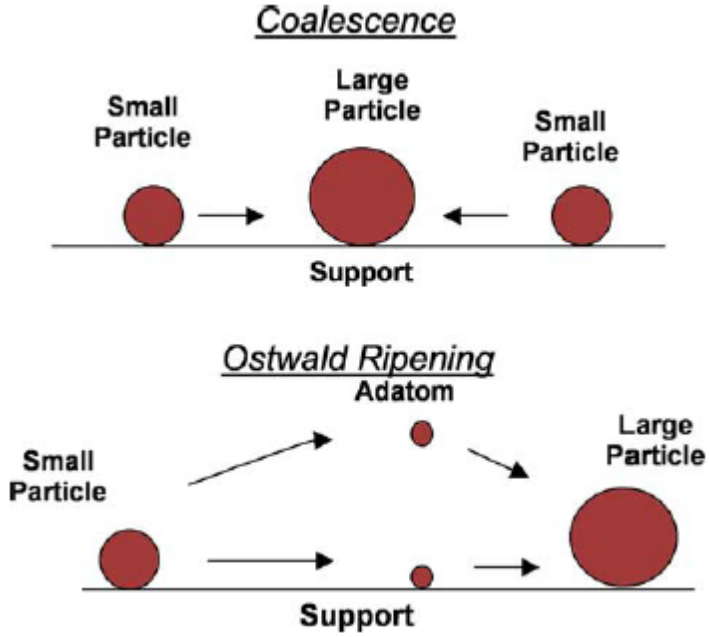

Fig. 1.8. Mechanism for metal nanoparticle sintering. [Source: Ref. 186]

Various novel ideas have been practiced to keep a check on the agglomeration and growth of particle sizes. First attempt was to use mesoporous silica like SBA-15, MCM-41 as support [189-191] by which, size could be controlled by arresting the growth of the nanoparticles inside the channels of these porous materials [192]. Song et al have prepared monodisperse Pt nanoparticles of size 1.7-7.1 nm by alcohol reduction method and incorporated into mesoporous SBA-15 silica during hydrothermal synthesis [190]. Prashar et al have developed a simple *in situ* method for Pt nanoparticle incorporation within the mesochannels of SBA-15 involving dispersion of metal precursors in surfactant-modified polymer micelles [192]. Karimi et al have synthesized a new highly recoverable and efficient palladium-based catalyst for the aerobic oxidation of alcohols [193]. Sun et al have developed an *in situ* autoreduction method for the fabrication of highly dispersed silver nanoparticles inside the channels of mesoprous silicas [194]. Li et al have performed cyclohexane oxidation over Au nanoparticles of size 3-8 nm hosted by mesoporous SBA-15 [195].

Liu et al have synthesized a highly efficient Au-Cu alloy nanocatalyst confined in SBA-15 for CO oxidation [196].

Even though mesoporous supports are better than the conventional supports, they still have some drawbacks since nanoparticles are labile inside the open channels of mesoporous silica leading to agglomeration at high temperatures. Scheuth and co-workers have demonstrated the deactivation of Au/SBA-15 catalyst due to increase in Au nanoparticle size at temperatures higher than 100 °C in CO oxidation reaction [197]. Fig. 1.9 represents the TEM image of Au/SBA-15 before and after use in CO oxidation reaction at 160 °C.

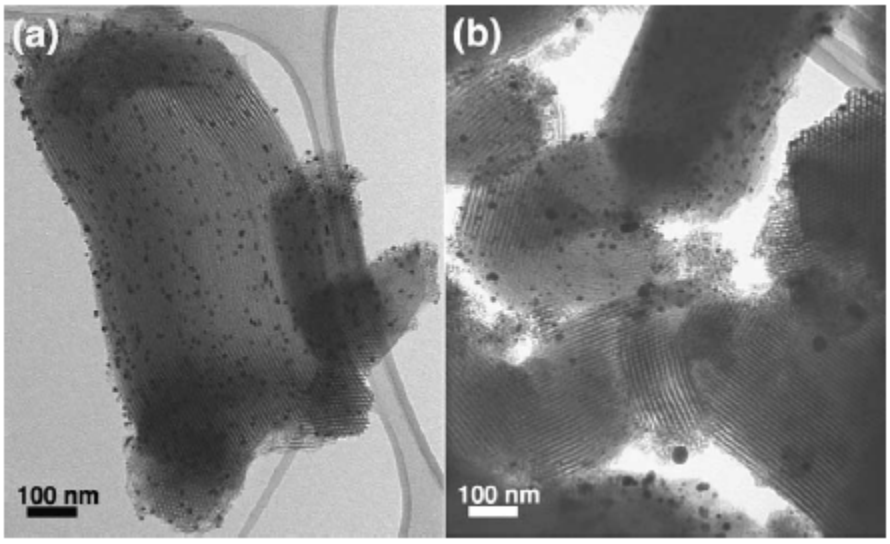

Fig. 1.9. TEM images of Au/SBA-15 a) before and b) after use in CO oxidation reaction at 160 °C. [Source Ref. 197]

1.5. POROUS SILICA ENCAPSULATION OF NOBLE METAL NANOPARTICLES

Agglomeration of nanoparticles can be prevented better by encapsulating them completely inside silica shell. In the late 1960s, Stober and co-workers developed sol-gel chemistry of silicon alkoxide for growing monodisperse spherical silica nanoparticles in basic aqueous solutions containing different alcohols such as methanol, ethanol, or isopropanol [198]. Adopting the well-established Stober method, Liz-Marzan, Mulvaney, and co-workers have performed interesting work on silica coating of metal nanoparticles [199]. Most of them are focused on dense silica coating around the metal nanoparticles to investigate their optical properties [200-204], self-assembly for photonics [205-207] or surface functionalization, conjugation for surface-enhanced Raman scattering [208-210], phototherapy [211,212] or colorimetric detection [213,214]. Liz-Marzan et al have synthesized silica encapsulated Au nanoparticles with various silica shell thickness [Fig. 1.10] and studied their optical property [199].

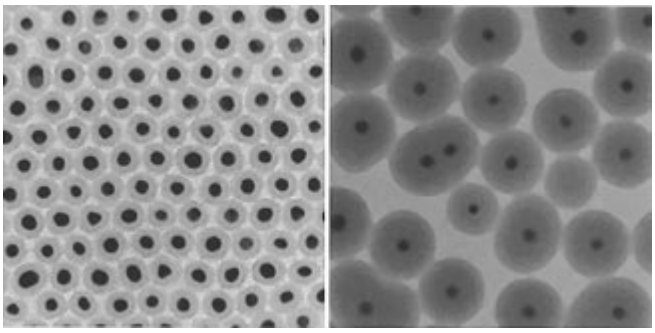

Fig. 1.10. TEM images of Au-silica core-shell particles; shell thicknesses are (left) 10 nm, and (right) 23 nm. [Source: Ref. 199]

These materials are catalytically inactive due to the presence of thick non-porous silica shell totally masking the active sites. This can be addressed if the silica shell is porous so that active sites are accessible and hence porous silica encapsulation of nanoparticles is necessary to get both activity and stability. Several attempts have been made to synthesize porous silica encapsulated nanoparticles for their catalytic application studies. For example, Corma and co-workers have successfully synthesized mesoporous silica-coated gold nanoparticles [215]. In this synthesis

procedure, first silica coated Au nanoparticle Au@SiO_2 has been prepared by using (3-aminopropyl)-trimethoxysilane (APTMS) and this is used as precursor for the synthesis of mesoporous silica coated Au nanoparticle.

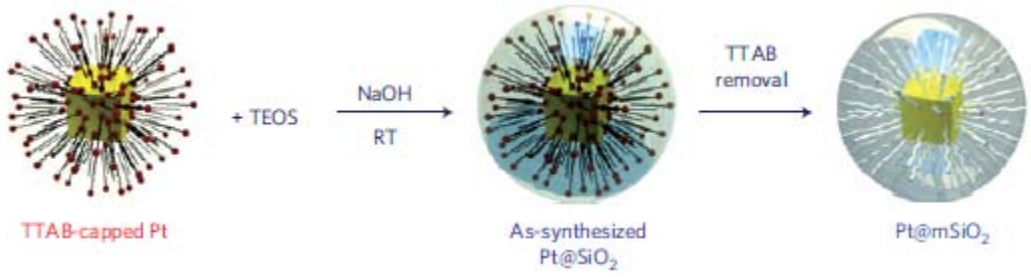

Fig. 1.11. Schematic representation of the synthesis of Pt@mSiO_2 nanoparticles. [Source: Ref. 216]

Prof. Somorjai's group from University of California, Berkeley has carried out excellent work on porous silica encapsulation of Pt nanoparticles (Pt@mSiO_2) and their CO oxidation study at high temperature [216].

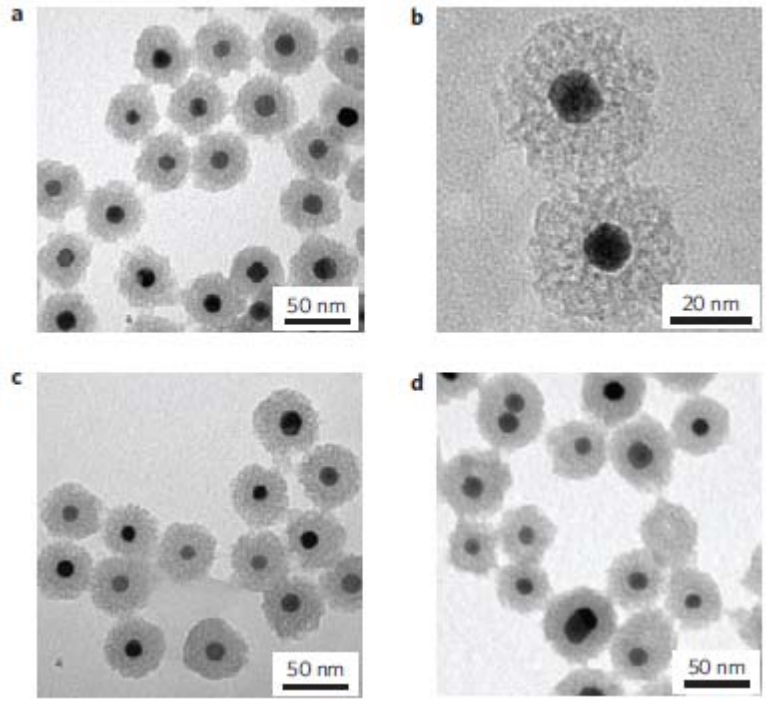

Fig. 1.12. TEM images of Pt@mSiO2 nanoparticles after calcination at 350 °C (a,b), 550 °C (c) and 750 °C (d). [Source: Ref. 216]

The core shell structured Pt@mSiO_2 nanoparticles were synthesized in three steps [Fig. 1.11]: (1) synthesis of Pt nanoparticles using tetradecyltrimethylammonium bromide (TTAB) as the capping agent, (2) silica polymerization around the Pt cores, generating the as-synthesized Pt@SiO_2 material and (3) removal of the TTAB molecules by calcination to produce porous silica encapsulated Pt nanoparticle (Pt@mSiO_2). The Pt@mSiO_2 consisted of 14 nm Pt cores and 17 nm thick mesoporous silica shells. The reacting molecules can directly access the active Pt metal cores through the mesopores within the silica shells and the product molecules can also readily exit through these mesopores. In this synthesis protocol, TTAB acts as stabilizing agent for the preparation of Pt nanoparticles and also as template for the in situ generation of mesopores during calcination by its removal.

Thermal stability study showed that Pt@mSiO_2 maintained their core-shell architecture even at temperatures up to 750 °C in air [Fig. 1.12]. This type of thermally stable silica encapsulated catalysts can be used for high-temperature reactions, such as partial oxidation and cracking of hydrocarbons and catalytic combustion. Park et al followed a similar approach to prepare highly sinter resistant Pd@SiO_2 catalyst [217]. Researchers have adopted post-synthetic approach also for the creation of pores into silica wall of as-synthesized non porous silica encapsulated metal nanoparticles. Zhang et al have described the synthesis of porous silica encapsulated Au nanoparticles by surface protected etching method [218]. In this method, PVP stabilized Au nanoparticles are silica encapsulated completely initially, then NaOH has been used to selectively etch the interior of the silica spheres for transforming solid silica sphere to a permeable porous silica shell and in this etching process silica shell would protect the nanoparticles from agglomeration.

Few other methods are also reported for the porous silica encapsulation of Au nanoparticles, for example; Wu et al have prepared nano-rattle of Au@hollow silica (Au@HSNs) catalyst by using a water-in-oil microemulsion as a template [219]. They have demonstrated the catalytic hydrogenation of 4-nitrophenol by using this catalyst.

1.6. SCOPE AND OBJECTIVE OF THE THESIS

Noble metal nanoparticles and nanoclusters are highly interesting because of their versatile application in catalysis and bioimaging. But poor stability of these nano materials has limited their applications in catalysis with even oxide supported nanocatalysts suffering serious agglomeration problems. Several approaches including silica encapsulation have been performed to minimize this agglomeration problem. Various classical methods like the Stober method, use of silane coupling agents and recently microemulsion method are employed to make silica encapsulated nanomaterials. But most of the processes are lengthy and cumbersome. So there is a good opportunity to work in the area of noble metal nanoclusters and nanoparticles and their silica encapsulation study for various applications.

Based on these observations, the objective of the present work is to synthesize water dispersible noble metal nanoclusters and further utilization of these nanoclusters as precursors for the synthesis of porous silica encapsulated metal nanoparticles and their catalytic activity study. To achieve this aim, various functionalized materials are synthesized and characterized thoroughly. Different catalytic activities are also performed by using these materials. Various properties of the ultra-small nanolcusters also are explored.

By keeping the above objectives in mind, the following specific work has been selected for the present thesis:

(i) Design of a novel alkylammonium thiol ligand capable of synthesizing water dispersible noble metal nanoclusters.

(ii) Synthesis and characterization of thiol stabilized noble metal nanoclusters and their applications and silica encapsulation.

(iii) Synthesis and characterization of porous silica encapsulated noble metal nanoparticles from silica encapsulated nanoclusters.

(iv) Catalytic activity study of these porous silica encapsulated nanomaterials.

1.7. REFERENCES

1. I. Linkov, *Nanomaterials*, Springer, New York, 2008.
2. D, Vollath, *Nanomaterials: an introduction to synthesis, properties and application*, Wiley-VCH: Weinheim, 2008
3. G. A. Somorjai, F. Tao and J. Y. Park, *Top. Catal.*, 2008, **47**, 1.
4. R. W. Murray, *Chem. Rev.*, 2008, **108**, 2688.
5. B. C. Gates, *Chem. Rev.*, 1995, **95**, 511.
6. R. Jin, *Nanotechnology Reviews*, 2012, **1**, 31.
7. H. Wang, J-G. Wang, Z-R. Shen, Y-P. Liu, D-T. Ding and T-H. Chen, *J. Cat.* 2010, **275**, 140.
8. T. Mitsudome, A. Noujima, Y. Mikami, T. Mizugaki, K. Jitsukawa and K. Kaneda, *Angew. Chem. Int. Ed.*, 2010, **49**, 5545.
9. 9. C-H. Cui and S-H. Yu, *Acc. Chem. Res.*, 2012, **46**, 1427.
10. T. Pradeep and Anshup, *Thin solid Films*, 2009, **517**, 6441.
11. B. K. Min and C. M. Friend, *Chem. Rev.*, 2007, **107**, 2709.
12. L. Dykman and N. Khlebtsov, *Chem. Soc. Rev.* 2012, **41**, 2256.
13. K. Saha, S. S. Agasti, C. Kim, X. Li and V. M. Rotello, *Chem. Rev.*, 2012, **112**, 2739.
14. G. Doria, J. Conde, B. Veigas, L. Giestas, C. Almeida, M. Assuncao, J. Rosa and P. V. Baptista, *Sensors*, 2012, **12**, 1657.
15. Y. Yu, Q. Yao, Z. Luo, X. Yuan, J. Y. Lee and J. Xie, *Nanoscale*, 2013, **5**, 4606.
16. R. Jin, *Nanoscale*, 2010, **2**, 343.
17. S. Yamazoe, K. Koyasu and T. Tsukuda, Acc. Chem. Res. 2013, DOI: 10.1021/ar400209a.
18. Y. Zhu, H. Quian, B. A. Drake and R. Jin, *Angew. Chem. Int. Ed.*, 2010, **49**, 1295.
19. J. Zheng, P. R. Nicovich and R. M. Dickson, *Annu. Rev. Phys. Chem.* 2007, **58**,
20. J. Wang, G. Zhang, Q. Li, H. Jiang, C. Liu, C. Amatore and X. Wang, *Sci. Rep.*, 2013, **3**, 1

21. C-A. J. Lin, C-H. Lee, J-T. Hsieh, H-H. Wang, J. K. Li, J-L. Shen, W-H. Chan, H- I. Yeh and W. H. Chang, *J. Med. Biol. Eng.*, 2009, **29**, 276.
22. H. Xu and K. S. Suslick, *Adv. Mater*., 2010, **22**, 1078.
23. P. L. Xavier, K. Chaudhari, A. Baksi and T. Pradeep, *Nano Rev*., 2012, **3**, 14767.
24. M. Aslam, L. Fu, M. Su, K. Vijayamohanan and V. K. Dravid, *J. Mater. Chem*., 2004, **14**, 1795.
25. P. R. Selvakannan, S. Mandal, S. Phadtare, R. Pasricha and M. Sastry, Langmuir, 2003, **19**, 3545.
26. J. Turkevich, P. C. Stevenson and J. Hillier, *Discuss. Faraday Soc.* 1951, **11**, 55.
27. B. V. Turkevich and J. Turkevich, *J. Am. Chem. Soc.* 1963, **85**, 3317.
28. J. An, B. Tang, X. Ning, J. Zhou, S. Xu, B. Zhao, W. Xu, C. Corredor and J. R. Lombardi, *J. Phys. Chem. C*, 2007, **111**, 18055.
29. W. Cheng, S. Dong and E. Wang, *Langmuir*, 2003, **19**, 9434.
30. S. Nath, S. Jana, M. Pradhan and T. Pal, *J. Colloid Interface Sci.* 2010, **341**, 333.
31. M. Brust, M. Walker, D. Bethell, D. J. Schiffrin and R. Whyman, *Chem. Commun.*, 1994, 801.
32. D. Zopes, B. Stein, S. Mathur and C. M. Graf, *Langmuir*, 2013, **29**, 11217.
33. F. Schulz, T. Vossmeyer, N. G. Bastus and H. Weller, *Langmuir*, 2013, **29**, 9897.
34. I. Javakhishvili and S. Hvilsted, *Biomacromolecules*, 2009, **10**, 74.
35. A. G. Kanaras, F. S. Kamounah, K. Schaumburg, C. J. Kiely and M. Brust, *Chem. Commun.*, 2002, 2294.
36. F. Lu, J. Ruiz and D. Astruc, *Tetrahedron Lett*., 2004, **45**, 9443.
37. M. J. Hostetler, S. J. Green, J. J. Stokes and R. W. Murray, *J. Am. Chem. Soc*., 1996, **118**, 4212.
38. M. M. Alvarez, J. T. Khoury, T. G. Schaaff, M. Shafigullin, I. Vezmar and R. L. Whetten, *Chem. Phys. Lett.*, 1997, **266**, 91.
39. S. Chen and R. W. Murray, *Langmuir*, 1999, **15**, 682.
40. C. J. Ackerson, P. D. Jadzinsky and R. D. Kornberg, *J. Am. Chem. Soc*.,

2005, **127**, 6550

41. I. Hussain, S. Graham, Z. X. Wang, B. Tan, D. C. Sherrington, S. P. Rannard, A. I. Cooper and M. Brust, *J. Am. Chem. Soc.*, 2005, **127**, 16398.
42. H. Yao, H. Kojima, S. Sato and K. Kimura, *Langmuir*, 2004, **20**, 10317.
43. Z. Wang, B. Tan, I. Hussain, N. Schaeffer, M. F. Wyatt, M. Brust and A. I. Cooper, *Langmuir*, 2007, **23**, 885.
44. M. Cargnello, N. L. Wieder, P. Canton, T. Montini, G. Giambastiani, A. Benedetti, R. J. Gorte and P. Fornasiero, *Chem. Mater*., 2011, **23**, 3961.
45. M. M. Alvarez, J. T. Khoury, T. G. Schaaff, M. Shafigullin, I. Vezmar and R. L. Whetten, *Chem. Phys. Lett*., 1997, **266**, 91.
46. J. P. Wilcoxon and P. Provencio, *J. Phys. Chem. B*, 2003, **107**, 12949.
47. J. P. Wilcoxon, J. E. Martin and P. Provencio, *Langmuir*, 2000, **16**, 9912.
48. Y. Song, V. Jimenez, C. McKinney, R. Donkers and R. W. Murray, *Anal. Chem.*, 2003, **75**, 5088.
49. V. L. Jimenez, M. C. Leopold, C. Mazzitelli, J. W. Jorgenson and R. W. Murray, *Anal. Chem.*, 2003, **75**, 199.
50. C. J. Zhong, W. X. Zhang, F. L. Leibowitz and H. H. Eichelberger, *Chem. Commun.*, 1999, 1211.
51. X. M. Lin, G. M. Wang, C. M. Sorensen and K. J. Klabunde, *J. Phys. Chem. B*, 1999, **103**, 5488.
52. S. Stoeva, K. J. Klabunde, C. M. Sorensen and I. Dragieva, *J. Am. Chem. Soc*., 2002, **124**, 2305.
53. B. L. V. Prasad, S. I. Stoeva, C. M. Sorensen and K. J. Klabunde, *Langmuir*, 2002, **18**, 7515
54. X. M. Lin, G. M. Wang, C. M. Sorensen and K. J. Klabunde, *J. Phys. Chem. B*, 1999, **103**, 5488.
55. S. Stoeva, K. J. Klabunde, C. M. Sorensen and I. Dragieva, *J. Am. Chem. Soc*., 2002, **124**, 2305.
56. M. M. Alvarez, J. T. Khoury, T. G. Schaaff, M. N. Shafigullin, I. Vezmar and R. L. Whetten, *J. Phys. Chem. B*, 1997, **101**, 3706.
57. M. J. Hostetler, S. J. Green, J. J. Stokes and R. W. Murray, *J. Am. Chem. Soc*., 1996, **118**, 4212.

58. M. M. Alvarez, J. T. Khoury, T. G. Schaaff, M. N. Shafigullin, I. Vezmar and R. L. Whetten, *J. Phys. Chem. B*, 1997, **101**, 3706.
59. R. L. Whetten, M. N. Shafigullin, J. T. Khoury, T. G. Schaaff, I. Vezmar, M. M. Alvarez and A. Wilkinson, *Acc. Chem. Res.*, 1999, **32**, 397.
60. R. L. Donkers, D. Lee and R. W. Murray, *Langmuir*, 2004, **20**, 1945.
61. V. L. Jimenez, D. G. Georganopoulou, R. J. White, A. S. Harper, A. J. Mills, D. Lee and R. W. Murray, *Langmuir*, 2004, **20**, 6864.
62. Y. Negishi, Y. Takasugi, S. Sato, H. Yao, K. Kimura and T. Tsukuda, *J. Am. Chem. Soc.*, 2004, **126**, 6518.
63. M. Zhu, H. Qian and R. Jin, *J. Am. Chem. Soc.*, 2009, **131**, 7220.
64. H. Qian, M. Zhu, U. N. Andersen and R. Jin, *J. Phys. Chem. A*, 2009, **113**, 4281.
65. H. Qian and R. Jin, *Nano. Lett.*, 2009, **9**, 4083.
66. H. Qian, Y. Zhu and R. Jin, *ACS Nano*, 2009, **3**, 3795.
67. M. Zhu, C. M. Aikens, F. J. Hollander, G. C. Schatz and R. Jin, *J. Am. Chem. Soc.*, 2008, **130**, 5883.
68. M. Zhu, E. Lanni, N. Garg, M. E. Bier and R. Jin, *J. Am. Chem. Soc.*, 2008, **130**, 1138.
69. T. U. B. Rao, B. Nataraju and T. Pradeep, *J. Am. Chem. Soc.*,2010, **132**,16304.
70. X. Yuan, Z. Luo, Q. Zhang, X. Zhang, Y. Zheng, J. Y. Lee and J. Xie, *ACS Nano*, 2011, **5**, 8800.
71. S. Eustis and M. A. El-Sayed, *Chem. Soc. Rev.*, 2006, **35**, 209.
72. A. Moores and F. Goettmann, *New. J. Chem.*, 2006, **30**, 1121.
73. D. E. Mustafa, T. Yang, Z. Xuan, S. Chen, H. Tu and A. Zhang, *Plasmonics*, 2010, **5**, 221.
74. M. A. El-Sayed, *Acc. Chem. Res*., 2001, **34**, 257.
75. Z. Wu, J. Suhan and R. Jin, *J.Mater. Chem.*, 2009, **19**, 622.
76. M. A. Habeeb Muhammed, S. Ramesh, S. S. Sinha, S. K. Pal and T. Pradeep, *Nano Res*. 2008, **1**, 333.
77. E. S. Shibu, M. A. Habeeb Muhammed, T. Tsukuda and T. Pradeep, *J. Phys.*

Chem. C, 2008**, 112**, 12168.

78. M. Zhu, C. M. Aikens, M. P. Hendrich, R. Gupta, H. Qian, G. C. Schatz and R. Jin, *J. Am. Chem. Soc.*, 2009, **131**, 2490.
79. D. Lee, R. L. Donkers, G. Wang, A. S. Harper and R. W. Murray, *J. Am. Chem. Soc.*, 2004, **126,** 6193.
80. S. Chen, R. s. Ingram, M. J. Hostetler, J. J. Pietron, R. W. Murray, T. G. Schaaff, J. T. Khoury, M. M. Alvarez and R. L. Whetten, *Science*, 1998, **280**, 2098.
81. Z. Lin, R. P. F. Kanters and D. M. P. Mingos, *Inorg. Chem.*, 1991, **30**, 91.
82. P. Apell, R. Monreal and S. Lundqvist, *Phys. Scr.*, 1988, **38**, 174.
83. J. Zheng, C. Zhang and R. M. Dickson, *Phys. Rev. Lett.*, 2004, **93**, 077402.
84. J. Zheng, C. Zhou, M. Yu and J. Liu, *Nanoscale*, 2012, **4**, 4073.
85. X. L. Guevel, B. Hotzer, G. Jung and M. Schneider, *J. Mater. Chem.* 2011, **21**, 2974.
86. X.Wu, X. He, K. Wang, C. Xie, B. Zhou and Z. Qing, *Nanoscale*, 2010, **2**, 2244.
87. Y. Wang, J-T. Chen and X-P. Yan, *Anal. Chem.* 2013, **85**, 2529.
88. B. Adhikari and A. Banerjee, *Chem. Mater.* 2010, **22**, 4364.
89. S-i. Tanaka, K. Aoki, A. Muratsugu, H. Ishitobi, T. Jin, Y. Inouya, *Opt. Mater. Express*, 2013, **3**, 157.
90. G. J. Hutchings and M. Haruta, *Appl. Catal. A*, 2005, 291, 2.
91. B. Hvolbaek, T. V. W. Janssens, B. S. Clausen, H. Falsig, C. H. Christensen and J. K. Norskov, *Nanotoday*, 2007, **2,** 14.
92. G. Li and R. Jin, *Acc. Chem. Res.* 2013, **46**, 1749.
93. Y. Chen, C. Wang, H. Liu, J. Qiu and X. Bao, *Chem. Commun.* 2005, 5298
94. K. E. Wilkinson, L. Palmberg, E. Witasp, M. Kupczyk, N. Feliu, P. Gerde, G. A. Seisenbaeva, B. Fadeel, S-E, Dahlen and V. G. Kessle, *ACS Nano*, 2011, **5**, 5312.
95. P. Gelin and M. Primet, *Appl. Catal. B*, 2002, **39**, 1.
96. A. S. Pratt and J. A. Cairns, *Platinum Met. Rev.*, 1977, **21**, 74.
97. H. S Gandhi, W. B Williamson and J. L Bomback, *Appl. Catal.*, 1982, **3**, 79.
98. J. T. Kummer, *J. Phys. Chem.* 1986, **90**, 4748.

99. V. Komanicky, H. Iddir, K-C. Chang, A. Menzel, G. Karapetrov, D. Hennessy, P. Zapol and H. You, *J. Am. Chem. Soc.*, 2009, **131**, 5732.

100. M. E. Grass, R. M. Rioux and G. A. Somorjai, *Catal. Lett.*, 2009, **128**, 1.
101. S. Cheong, J. D. Watt and R. D. Tilley, *Nanoscale*, 2010, **2**, 2045.
102. S. Bhattacharjee, D. M. Dotzauer and M. L. Bruening, *J. Am. Chem. Soc.*, 2009, 131, 3601.
103. I. Laoufi, M-C. Saint-Lager, R. Lazzari, J. Jupille, O. Robach, S. Garaudee, G. Cabailh, P. Dolle, H. Cruguel and A. Bailly, *J. Chem. Phys. Chem. C*, 2011, **115**, 4673.
104. Ilkueun Lee, Ricardo Morales, M. A. Albiter and F. Zaera, *Proc. Natl. Acad. Sci. U.S.A.*, 2008, **40**, 15241.
105. S. Mandal, A. Das, R. Srivastava, M. Sastry, *Langmuir*, 2005, **21**, 2408.
106. C. M. Park, M. S. Kwon and J. Park, *Synthesis*, 2006, 3790.
107. J. C. Garcia-Martinez, R. L. Lezutekong and R. M. Crooks, *J. Am. Chem. Soc.*, 2005, **127**, 5097.
108. N. Mjias, R. Pleixats, A. Shafir, M. Medio-Simon and G. Asensio, *Eur. J. Org. Chem.*, 2010, 5090.
109. Y. Li and M. A. El-Sayed, *J. Phys. Chem. B*, 2001, 105, 8938.
110. S. Yamazoe, K. Koyasu and T. Tsukuda, *Acc. Chem. Res.*, 2013,DOI: 10.1021/ar400209a.
111. Y. Zhu, H. Quian, B. A. Drake and R. Jin, *Angew. Chem. Int. Ed.* 2010, **49**, 1295.
112. H. Tsunoyama, H. Sakurai, Y. Negishi and T. Tsukuda, *J. Am. Chem. Soc.*, 2005, **127**, 9374.
113. M. Turner, V. B. Golovko, O. P. H. Vaughan, P. Abdulkin, A. Berenguer-Murcia, M. S. Tikhov, B. F. G. Johnson and R. M. Lambert, *Nature*, 2008, **454**, 981.
114. J. Kaspar, P. Fornasiero and N. Hickey, *Catal. Today*, 2003, **77**, 419.
115. I. Langmuir, *Trans. Faraday Soc.*, 1922, 17, 621.
116. C. T. Campbell, G. Ertl, H. Kuipers and J. A. Segner, *J. Chem. Phys.*, 1980, **73**, 5862.

117. P. J. Berlowitz, C. H. F. Peden and D. W. Goodman, *J. Phys. Chem*., 1988, **92**, 5213.
118. K. R. McCrea, J. S. Parker and G. A. Somorjai, *J. Phys. Chem*., 2002, **106**, 10854.
119. F. Zaera, *Catal. Today*, 2003, **81**, 149.
120. G. W. Huber and A. Corma, *Angew. Chem. Int. Ed*., 2007, **46**, 7184.
121. D. Ciuparu, M. R. Lyubovsky, E. Altman, L. D. Pfefferle and A. Datye, *Catal. Rev.*, 2002, **44**, 593.
122. P. Francesco, *Catal. Today*, 1998, **41**, 129.
123. M. Haruta, T. Kobayashi, H. Sano and N. Yamada, *Chem. Lett*., 1987, 405.
124. M. Haruta, N. Yamada, T. Kobayashi and S. Iijima, *J. Catal.*, 1989, **115**, 301.
125. C. T. Campbell, *Science*, 2004, **306**, 234.
126. Y. Zhang, R. W. Cattrall and I. D. McKelvie, *Gold Bull*., 2011, **44**, 145.
127. C. J. Jia, Y. Liu, H. Bongard and F. Schuth, *J. Am. Chem. Soc*., 2010, **132**, 1520.
128. S. J. Lee and A. Gavriilidis, J. Catal, 2002, **206**, 305.
129. D-S. Lee and Y-W. Chen, *J. Catal.*, 2013, doi:10.1155/2013/586364.
130. D. A. Bulushev, I. Yuranov, E. I. Suvorova, P. A. Buffat and L. Kiwi-Minsker, *J. Catal.*, 2004, **224**, 8.
131. H. Liu, A. I. Kozlov, A. P. Kozlova, T. Shido, K. Asakura and Y. Iwasawa, *J. Catal.*, 1999, **185**, 252.
132. D. Li, Y. Zhu, H. Wang and Y. Ding, *Sci. Rep.*, 2013, DOI: 10.1038/srep03015.
133. A. Manasilp and E. Gulari, *Appl. Catal. B*, 2002, **37**, 17.
134. A. Wongkaew and P. Limsuwan, *Adv. Chem. Engineer. Sci.*, 2013, **3**, 7.
135. A. Noujima, T. Mitsudome, T. Mizugaki, K. Jitsuka and K. Kaneda, *Molecules*, 2011, **16**, 8209.
136. A. K. Sinha, S. Seelan, S. Tsubota and M. Haruta, *Top. Catal.*, 2004, 29, 95.
137. A. Abad, A. Corma and H. Garcia, *Pure Appl. Chem.*, 2007, 79, 1847.
138. L. Wang, J. Zhang, X. Meng, D. Zheng and F-S. Xiao, *Cata. Today*, 2011, **175**, 404.

139. C. Marsden, E. Taarning, D. Hansen, L. Johansen, S. K. Klitgaard, K. Egeblad and C. H. Christensen, *Green Chem*., 2008, **10**, 168.
140. M. D. Hughes, Y-J. Xu, P. Jenkins, P. McMorn, P. Landon, D. I. Enache, A. F. Carley, G. A. Attard, G. J. Hutchings, F. King, E. H. Stitt, P. Johnston, K. Griffin and C. J. Kiely, *Nature*, 2005, **437**, 1132.
141. D. A. King and D. P. Woodruff, *The Chemical Physics of Solid Surfaces and Heterogeneous Catalysis*; Elsevier: Amsterdam, 1982; Vol. 4.
142. H. J. Freund, *Surf. Sci.*, 2002, **500**, 271.
143. A. K. Santra and D. W. Goodman, *Electrochim. Acta*, 2002, **47**, 3595.
144. W. J. Arblaster, *Platinum Metals Rev.*, 2005, **49**, 141.
145. N. Seriani, Z. Jin, W. Pompe and L. Colombi Ciacchi, *Phys. Rev.* B, 2007, **76**, 155421.
146. J. R. Croy, S. Mostafa, J. Liu, Y. H. Sohn, H. Heinrich, B. Roldan Cuenya, *Catal. Lett.*, 2007, **119**, 209.
147. J. R. Croy, S. Mostafa, J. Liu, Y. H. Sohn and B. Roldan Cuenya, *Catal. Lett.*, 2007, **118**, 1.
148. J. R. Croy, S. Mostafa, L. Hickman, H. Heinrich and B. Roldan Cuenya, *Appl. Catal., A*, 2008, **350**, 207.
149. J. R. Croy, S. Mostafa, H. Heinrich and B. Roldan Cuenya, *Catal. Lett.*, 2009, **131**, 21.
150. S. Mostafa, J. R. Croy, H. Heinrich and B. Roldan Cuenya, *Appl. Catal., A*, 2009, **366**, 353.
151. J. C. Serrano-Ruiz, A. López-Cudero, J. Solla-Gullon, A. Sepúlveda-Escribano, A. Aldaz and F. Rodríguez-Reinoso, *J. Catal.*, 2008, **253**, 159.
152. B. Wu, H. Huang, J. Yang, N. Zheng and G. Fu, *Angew. Chem. Int. Ed.*, 2012, **51**, 3440.
153. A. Fukuoka, J-I. Kimura, T. Oshio, Y. Sakamoto and M. Ichikawa, *J. Am. Chem. Soc*., 2007, **129**, 10120.
154. S. Huang, K. Hara and A. Fukuoka, *Energy Environ. Sci.*, 2009, **2**, 1060.
155. C-S. Chen, H-W. Chen and W-H. Cheng, *Appl. Catal.*, 2003, **248**, 117.
156. K. An, S. Alayoglu, N. Musselwhite, S. Plamthottam, G. Melaet, A. E. Lindeman, G. A. Somorjai, *J. Am. Chem. Soc.*, 2013, **135**, 16689.

157. J. Y. Park, C. Aliaga, J. R. Renzas, H. Lee and G. A. Somorjai, *Catal. Lett.*, 2009, **129**, 1.
158. N. Marin-Astorga, G. Alvez-Manoli and P. Reyes, J Mol Catal. A, 2005, 226, 81.
159. S. Somboonthanakij, O. Mekasuwandumrong, J. Panpranot, T. Nimmanwudtipong, R. Strobel, S. E. Pratsinis and P. Praserthdam, *Catal. Lett.*, 2007, **119,** 346.
160. J. Silvestre-Albero, G. Rupprechter and H-J. Freund, *Chem. Commun.*, 2006, 80.
161. M. Lim, K. A. De Castro, S. oh, K. Lee, Y-W. Chang, H. Kim and H. Rhee, *Appl. Organometal. Chem.*, 2011, ***25***, 1.
162. E. J. García-Suárez, P. Lara, A. B. García, M. Ojeda, R. Luque and K. Philippot, *Appl. Catal. A*, 2013, 468, 59.
163. K. Karami, M. B. Shehni and N. Rahimi, *Appl. Organometal. Chem.*, 2013, **27**, 437.
164. M. A. Zolfigol, V. Khakyzadeh, A. R. Moosavi-Zare, A. Rostami, A. Zare, N. Iranpoor, M. H. Beyzavi and R. Luque, *Green Chem.*, 2013, **15**, 2132.
165. D. J. Guo and H. L. Li, *Carbon*, 2005, **43**, 1259.
166. J. Q. Lu, J. J. Bravo-Suarez, A. Takahashi, M. Haruta and S. T. Oyama, *J. Catal*., 2005, **232**, 1, 85.
167. Y. Chen, C. Wang, H. Liu, J. Qiu and X. Bao, *Chem. Commun.* 2005, 5298.
168. A. Wolf and F. Schuth, *Appl. Catal. A*, 2002, **226**, 1.
169. M. Valden, X. Lai and D.W. Goodman, *Science*, 1998, **281**, 1647.
170. B. R. Cuenya, *Thin Solid Films*, 2010, **518**, 3127.
171. I. Laoufi, M-C. Saint-Lager, R. Lazzari, J. Jupille, O. Robach, S. Garaudee, G. Cabailh, P. Dolle, H. Cruguel and A. Bailly, *J. Phys. Chem.* C, 2011, **115**, 4673.
172. C.-K. Tsung, J. N. Kuhn, W. Huang, C. Aliage, L.-I. Hung and G. A. Somorjai, P. Yang, *J. Am. Chem. Soc*., 2009, **131**, 5816.
173. J. Han, L. Wang and R. Guo, *J. Mater. Chem*. 2012, **22**, 5932.
174. X. Lai and D. W. Goodman, *J. Mol. Catal. A: Chem.*, 2000, **162**, 33.
175. M. Haruta, *Catal. Today*, 1997, **36**, 153.

176. M. Mavrikakis, P. Stoltze, J. K. Nørskov, *Catal. Lett.*, 2000, **64**, 101.
177. I. N. Remediakis, N. Lopez and J. K. Nørskov, *Appl. Catal. A*, 2005, **291**, 13.
178. I. Laoufi, M-C. Saint-Lager, R. Lazzari, J. Jupille, O. Robach, S. Garaudee, G. Cabailh, P. Dolle, H. Cruguel and A. Bailly, *J. Phys. Chem. C*, 2011, **115**, 4673.
179. O. M. Wilson, M. R. Knecht, J. C. Garcia-Martinez and R. M. Crooks, *J. Am. Chem. Soc*., 2006, **128**, 4510.
180. P. Albers, J. Pietsch and S. F. Parker, *J. Mol. Catal. A-Chem*. 2001, **173**, 275.
181. F. Maillard, S. Schreier, M. Hanzlik, E. R. Savinova, S. Weinkauf and U. Stimming, *Phys. Chem. Chem. Phys*. 2005, **7**, 385.
182. M. Raphulu, J. McPherson, G. Pattrick, T. Ntho, L. Mokoena, J. Moma and E. V. D. Lingen, *Gold Bulletin*, 2009, **42**, 328.
183. J. Matos, L. K. Ono, F. Behafarid, J. R. Croy, S. Mostafa, A. T. DeLaRiva, A. K. Datye, A. I. Frenkel and B. R. Cuenya, *Phys. Chem. Chem. Phys.* 2012, **14**, 11457.
184. R. S. Goeke and A. K. Datye, *Top. Catal.*, 2007, **46**, 3.
185. J. Liu, *Microsc. Microanal.* 2003, **9** *(Suppl 2)*, 290.
186. J. P. Gabaldon, M. Bore and A. K. Datye, *Top. Catal.*, 2007, **44**, 253.
187. P. Wynblatt and N.A. Gjostein, Prog. Solid State Chem., 1975, 21.
188. Q. Xu, K. C. Kharas, B. J. Croley and A. K. Datye, *Top. Catal.*, 2012, **55**, 78.
189. L. M. Bronstein, Top Curr Chem, 2003, 226, 55.
190. H. Song, R. M. Rioux, J. D. Hoefelmeyer, R. Komor, K. Niesz, M. Grass, P. Yang and G. A. Somorjai, *J. Am. Chem. Soc*., 2006, **128**, 3027.
191. Y. Oumi, H. Oka, M. Kanehara, T. Teranishi and T. Sano, Stud. Surf. Sci. Catal., 2004, 154, 834.
192. A. K. Prashar, R. P. Hodgkins, R. Kumar and R. N. Devi, *J. Mater. Chem*., 2008, **18**, 1765.
193. B. Karimi, S. Abedi, J. H. Clark and V. Budarin, *Angew. Chem. Int. Ed.*, 2006, 45, 4776.
194. J. Sun, D. Ma, H. Zhang, X. Liu, X. Han, X. Bao, G. Weinberg, N. Pfander and D. Su, *J. Am. Chem. Soc*., 2006, **128**, 15756.
195. L. Li, C. Jin, X. Wang, W. Ji, Y. Pan, T. V. D. Knaap, R. V. D. Stoel and C.

T. Au, *Catal. Lett.*, 2009, 129, 303.

196. X. Liu, A. Wang, X. Wang, C-Y. Mou and T. Zhang, *Chem. Commun.*, 2008, 3187.
197. C-M. Yang, M. Kalwei, F. Scheuth and K-J. Chao, *Applied Catal. A,* 254 (2003) 289–296
198. W. Stober, A. Fink and E. Bohn, *J. Colloid Interface Sci.,* 1968, **26**, 62.
199. L. M. Liz-Marzan, M. Giersig and P. Mulvaney, *Langmuir* 1996, 12, 4329.
200. T. Ung, L. M. Liz-Marzan and P. Mulvaney, *J. Phys. Chem. B,* 2001, **105**, 3441.
201. Y. Kobayashi, M. A. Correa-Duarte and L. M. Liz-Marzan, *Langmuir,* 2001, **17**, 6375.
202. M. Grzelczak, M. A. Correa-Duarte, V. Salgueirino-Maceira, M. Giersig, R. Diaz and L. M. Liz-Marzan, *Adv. Mater.*, 2006, **18**, 415.
203. N. G. Liu, B. S. Prall and V. I. Klimov, *J. Am. Chem. Soc.*, 2006, **128**, 15362.
204. K. Aslan, M. Wu, J. R. Lakowicz and C. D. Geddes, *J. Am. Chem. Soc.*, 2007, **129**, 1524.
205. F. Caruso, M. Spasova, V. SalgueiriCo-Maceira and L. M. Liz-Marzan, *Adv. Mater.*, 2001, **13**, 1090.
206. D. Y. Wang, V. Salgueirino-Maceira, L. M. Liz-Marzan and F. Caruso, *Adv. Mater*., 2002, **14**, 908.
207. F. Garcia-Santamaria, V. Salgueirino-Maceira, C. Lopez and L. M. Liz-Marzan, *Langmuir*, 2002, **18**, 4519.
208. S. P. Mulvaney, M. D. Musick, C. D. Keating and M. J. Natan, *Langmuir*, 2003, 19, 4784.
209. L. O. Brown and S. K. Doorn, *Langmuir*, 2008, **24**, 2277.
210. M. Y. Sha, H. X. Xu, M. J. Natan and R. Cromer, *J. Am. Chem. Soc.*, 2008, **130**, 17214.
211. C. Radloff and N. J. Halas, *Appl. Phys. Lett.*, 2001, **79**, 674.
212. S. Lal, S. E. Clare and N. J. Halas, *Acc. Chem. Res.*, 2008, **41**, 1842.
213. S. H. Liu and M. Y. Han, *Adv. Funct. Mater.*, 2005, **15**, 961.
214. Y. Kobayashi, M. Horie, M. Konno, B. Rodriguez-Gonzalez and L. M. Liz-

Marzan, *J. Phys. Chem. B*, 2003, **107,** 420.

215. P. Botella, A. Corma and M. T. Navarro, *J. Mater Chem.*, 2009, **19**, 3168.
216. S. H. Joo, J. Y. Park, C-K. Tsung, Y. Yamada, P. Yang and G. A. Somorjai, *Nat. Mater.* 2009, **8**, 126.
217. J. N. Park, A. J. Forman, W. Tang, J. Cheng, Y. S. Hu, H. Lin and E. W. McFarland, *Small*, 2008, **4**, 1694.
218. Q. Zhang, T. Zhang, J. Ge and Y. Yin, *Nano Lett.*, 2008, **8**, 2867.
219. S-H. Wu, C-T. Tseng, Y-S. Lin, C-H. Lin, Y. Hung and C-Y. Mou, *J. Mater. Chem.*, 2011, **21**, 789.

CHAPTER 2

SYNTHESIS AND CHARACTERIZATION OF THIOL STABILIZED Au ULTRA-SMALL CLUSTERS AND NANOPARTICLES AND THEIR ENCAPSULATION IN POROUS SILICA

PART A

SYNTHESIS AND CHARACTERIZATION OF Au ULTRA-SMALL CLUSTERS AND NANOPARTICLES AND THEIR APPLICATIONS

2A.1. INTRODUCTION

Ultra-small Au clusters < 2 nm in diameter have attracted much attention due to their unusual electron confinement properties which are highly important in the area of catalysis, optoelectronics and bioimaging. The importance of Au nanoclusters and nanoparticles is discussed thoroughly in Chapter 1. Briefly, Au nanoclusters and nanoparticles can play significant role in various catalytic reactions, like CO oxidation and selective alkene epoxidation. As evident from the literature study, most of the reported nanoparticles, especially clusters, are synthesized by long chain alkyl thiol protecting agents. This substantially reduces the applicability of these clusters in biological systems as well as narrows down the possibility of further functionalization. Hence fabrication of water dispersible and stable functionalized Au ultra small clusters and particles is highly desirable.

To accomplish this goal, we have synthesized novel *N,N,N*-Tripropyl(11-mercaptoundecyl)ammonium chloride ligand which is capable of stabilising water dispersible Au nanoclusters and nanoparticles. Au nanoclusters <2 nm in diameter showing good fluorescence intensity at NIR region have been synthesized. Due to the inherent fluorescence property, these Au nanoclusters are used to fabricate fluorescence probe for bacterial cell detection. In the present chapter we have described synthesis and characterization of cation ended alkyl thiol stabilized Au ultra-small clusters and nanoparticles and their applications.

2A.2. SYNTHESIS

2A.2.1. Synthesis of N,N,N-Tripropyl(11-mercaptoundecyl)ammonium chloride (RSH) ligand

The ligand was synthesized by modifying procedures reported elsewhere [1, 2]. Synthesis procedure is given in Scheme 2A.1. 11-bromo-1-undecene (5.4 g, 23 mmol) was added to a tripropylamine (10.2 g, 71 mmol) in ethanol (40 mL) and stirred for two days under reflux condition at 80 °C. The solvent was reduced in *vacuo* resulting in the bromide salt (**S**). It was purified by washing (3 times) with hexane (100 mL) under sonication (yield: 93 %). To a solution of **S** (19.0 mmol) in 1:1

mixture of toluene:ethanol AIBN (10.0 mmol) and thioacetic acid (80 mmol) were added.

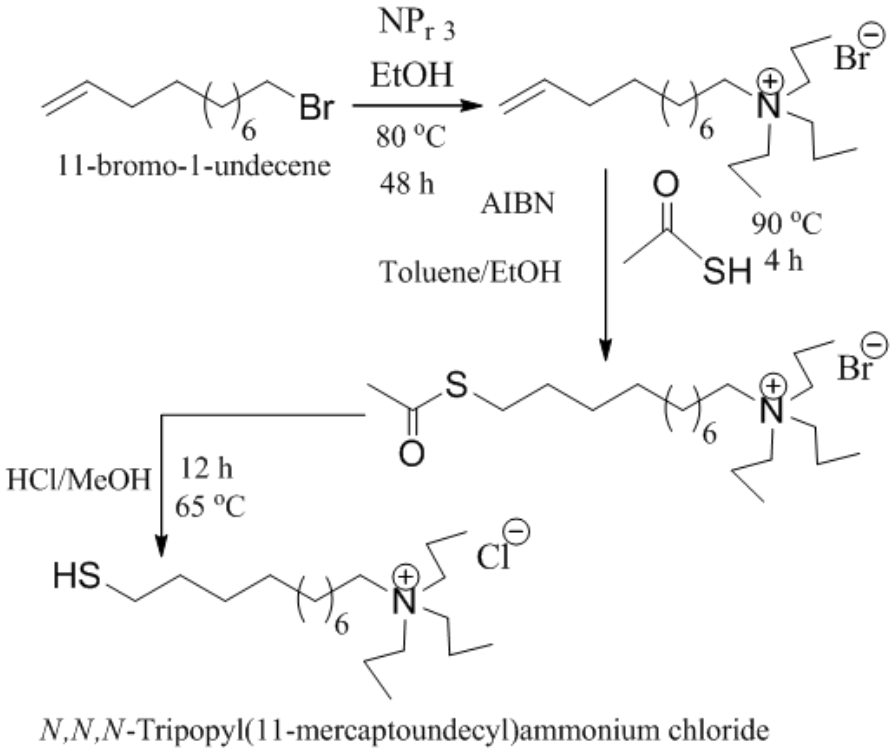

Scheme 2A.1. Scheme representing the synthesis of of *N,N,N*-Tripropyl(11-mercaptoundecyl)ammonium chloride.

The mixture was stirred under reflux for 4 h. The solvents were reduced *in vacuo* resulting in thioester (**G**). It was purified by washing (3 times) with a 9:1 mixture of hexane:ethylacetate (100 mL) under sonication. **G** was stirred with concentrated hydrochloric acid (2 mL) in methanol (40 mL) under reflux for 12 h. The solvent was then reduced *in vacuo* resulting in thiol. Thiol was purified by washing (3 times) with a 9:1 mixture of hexane:ethylactate (100 mL) under sonication (yield: 75 %).

2A.2.2. Synthesis of Au ultra-small clusters and nanoparticles stabilized by N,N,N-Tripropyl(11-mercaptoundecyl)ammonium chloride ligand

Au ultra-small clusters and nanoparticles were synthesized by using two different amounts of thiol. A stock solution of $HAuCl_4$ in acetonitrile (8.5 mL, 10 mM) was mixed with 20 mL of acetonitrile. For the preparation of nanoclusters,

higher amount of thiol (0.593 g, 1.6 mmol) in 2 mL of methanol and for nanoparticles, lower amount of thiol (0.133 g, 0.358 mmol) in 450 μL of methanol were added to this mixture separately. Then the mixture was stirred for 30 min. $NaBH_4$ solution (100 μL, 1.58 M) in methanol was added, and stirring was continued for 45 min. All the steps were carried out in ice-cooled conditions. Water (30 mL) was added to nanocluster and nanoparticle solutions. Acetonitrile was removed *in vacuo*. Aqueous solution of gold nanoclusters and nanoparticles were purified by dialysis using cellulose membrane (Aldrich, pore size 12 kDa). Lower amount of thiol produced ruby red colour gold nanoparticle solution and higher amount of thiol produced clear yellow colour gold nanocluster solution.

2A.3. INSTRUMENTS FOR CHARACTERIZATION

Many physico-chemical techniques like high resolution transmission electron microscopy (HRTEM), transmission electron microscopy (TEM), UV-Vis spectroscopy, fluorescence spectroscopy, confocal microscopy, X-ray photoelectron spectroscopy (XPS), FT-IR spectroscopy, NMR spectroscopy, zeta potential measurement and inductively coupled plasma spectroscopy (ICP) were used for the characterization of gold clusters and nanoparticles. Specification of the instruments used for these characterizations is described below. This section describes the instrumentation which is relevant to other chapters also. Detailed description of the principles of these instrumentation techniques is given in Appendix 1.

2A.3.1. High Resolution Transmission Electron Microscopy

FEI Tecnai TF-30 and T-20 electron microscope, operating at 300 and 200 kV, with an information resolution limit of 0.14 nm and 0.15 nm respectively were used for high resolution transmission electron microscopy (HRTEM) and transmission electron microscopy (TEM) sample observations. Samples for HRTEM and TEM were prepared by evaporating a droplet of the solutions onto a carbon coated copper mesh 200 grid. Solid samples were dispersed in ethanol under sonication before drop casting on grid.

2A.3.2. UV-Visible Spectroscopy

Absorption spectra were recorded on a JASCO V570 UV-Vis-NIR spectrophotometer operated with a resolution of 2 nm. UV-vis spectra were measured by using quartz cell of 10 mm path length (volume 1 mL).

2A.3.3. Fluorescence Spectroscopy

Fluorescence emission spectra were obtained on a Photon Technology International Spectrofluoremeter. Samples were taken in 3.5 mL quartz cells of 10 mm path length for fluorescence measurements. Two detectors were used: 1) R2658 PMT in PTI cooled housing with a single emission monochromator, 1200 l/mm, 400 nm blazed grating; 2) InGaAs diode with chopper and locking and a single emission monochromator, 600 l/mm, 1250 nm blazed grating. The spectra were corrected for the sensitivity of the respective emission channel and normalized. Quantum yield was calculated based on experiment in a small integrating sphere and was done using a double/single (excitation/emission) monochromator format. The lamp used was a xenon arc lamp with a chopper set for 27 Hz. The detector was a 1700 nm InGaAs. The grating used was 600 l/mm, 1.25 μm blaze angle. The bandpass was 12 nm for excitation and 48 nm for emission.

2A.3.4. Confocal Microscopy

An LSM 710 Carl Zeiss laser scanning confocal microscope (LSCM) was used to image the fluorescent samples. An Argon-ion laser (488 nm) was used for the experiments. Samples were fixed on a glass slide (not plastic) and cover slipped with a cover slip which was securely fastened to the slide. Clear nail polish was put around the edge of the slide which kept the sample compacted when focusing with an oil objective.

2A.3.5. X-ray Photoelctron Spectroscopy

X-ray photoelectron spectroscopy (XPS) measurements were carried out on a VG Micro Tech ESCA at a pressure of 10^{-9} Torr. Samples were prepared by evaporating a drop of the solution on a silicon wafer. Solid samples were dispersed in ethanol under sonication before drop casting on silicon wafer.

2A.3.6. FT-IR Spectroscopy

FTIR spectra were recorded on a Perkin-Elmer FT-IR spectrum GX instrument. KBr crystals were used as the matrix for preparing samples. Few drops of nanoparticle solution was mixed with finely powdered KBr crystals and dried under UV lamp for recording FTIR spectra. The spectra were collected for each measurement over the spectral range of 400–4000 cm^{-1} with a resolution of 1 cm^{-1}.

2A.3.7. NMR Spectroscopy

^{1}H NMR studies were performed in Bruker 400 MHz NMR spectrometer and samples were prepared by dissolving in $CDCl_3$.

2A.3.8. Dynamic Light Scattering and Zeta Potential Measurement

Dynamic light scattering and zeta potential measurement were performed on a 90 Plus particle size analyzer (Brookhaven Instruments, USA).

2A.3.9. Inductively Coupled Plasma Spectroscopy

Elemental analysis of nanoparticle solution and silica encapsulated nanoparticle material was carried out by inductively coupled plasma atomic emission spectroscopy on Spectro Arcos, FHS-12 (ICP-AES). Standard solutions were used for calibration purpose. 1 mL nanoparticle solution was dried at 100 °C, dried material was calcined at 500 °C to remove the organic ligand, the residue obtained after calcination was dissolved in 1 mL of aqua regia and diluted with 9 mL millipore water. This diluted 10 mL solution was used for the elemental analysis.

2A.4. CHARACTERIZATION

2A.4.1. Characterization of *N,N,N*-Tripropyl(11-mercaptoundecyl)ammonium chloride ligand

N,N,N-Tripropyl(11-mercaptoundecyl)ammonium chloride ligand is characterized by ^{1}H NMR and FTIR spectroscopy. Au ultra-small clusters and nanoparticles are characterized by HRTEM, UV-vis spectroscopy, fluorescence spectroscopy, confocal microscopy, FT-IR spectroscopy, DLS and zeta potential measurement.

2A.4.1.1. ^{1}H NMR Spectroscopy

N,N,N-Tripropyl(11-mercaptoundecyl)ammonium chloride ligand was characterized by ^{1}H NMR [Fig. 2A.1]. ^{1}H NMR (400 MHz, CDCl3): δ3.34-3.39 (m, 6 H, $CH_3CH_2CH_2N^+$), 2.90-3.01 (bm, 2 H,--CH_2N^+), 2.51-2.55 (m, 2 H, HS-CH_2-), 1.86-1.91 (m, 2 H, $CH_2CH_2N^+$), 1.66-1.84 (bm, 6 H, $CH_3CH_2CH_2N^+$), 1.58-1.64 (m, 2 H, HS-CH_2CH_2), 1.20-1.39 (m, 14 H, -CH_2), 1.07 (t, J = 7 Hz, 9 H, $CH_3CH_2CH_2N^+$).

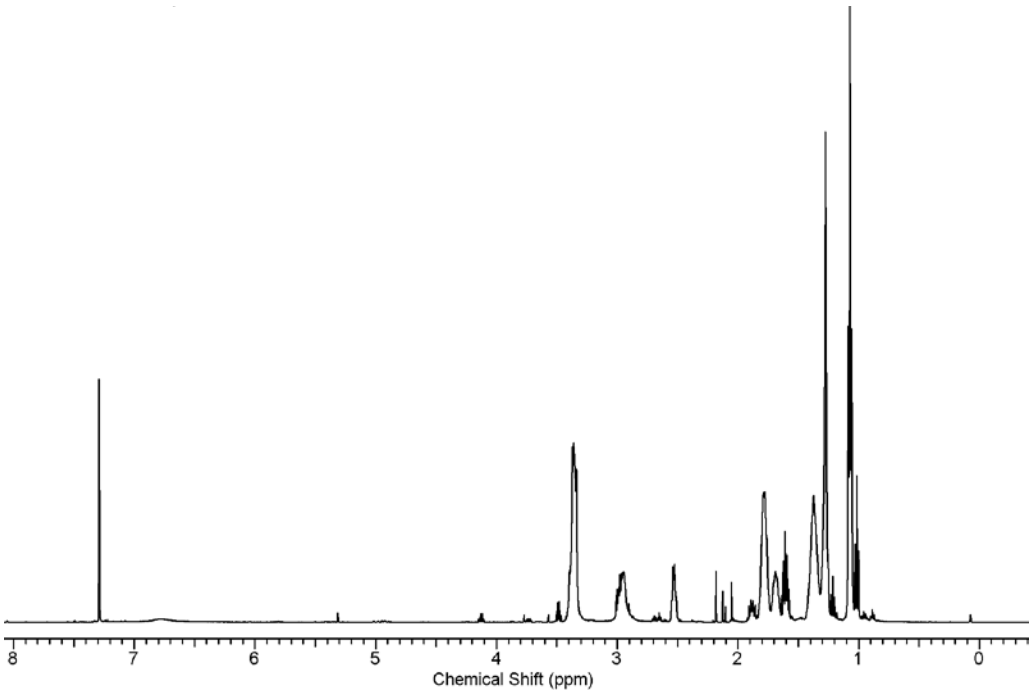

Fig. 2A.1. ^{1}H NMR spectrum of *N,N,N*-Tripropyl(11-mercaptoundecyl)ammonium chloride ligand.

2A.4.1.2. FT-IR Spectroscopy

N,*N*,*N*-Tripropyl(11-mercaptoundecyl)ammonium chloride ligand was characterized by FT-IR spectroscopy. IR (KBr): 3400, 3146, 2980, 2925, 2878, 2850, 2636, 2437, 2066, 1618, 1467, 1405, 1164, 1102, 1047, 964, 854, 758, 565 cm^{-1}. The vibrational frequencies in the C–H stretching region for the thiol molecule can be observed in Fig. 2A.2. The main features in the FT-IR spectra arising from long alkanechain thiol are the C-H stretching modes in the interval 2700-3100 cm^{-1}. The two strong peaks at 2925 and 2850 cm^{-1} arise from the asymmetric and symmetric CH_2 stretching mode. Two peaks at 2970 and 2878 cm^{-1} corresponds to the asymmetric and symmetric vibration stretching frequencies of CH_3 group. A peak position at around 2636 cm^{-1} indicates the stretching frequency of S-H bond which confirms the thiol formation.

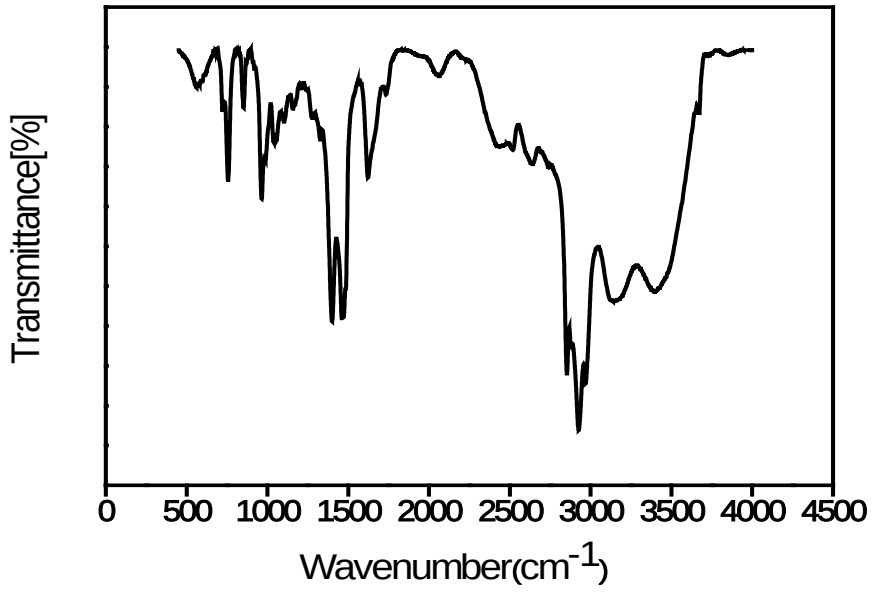

Fig. 2A.2. FT-IR spectrum of *N*,*N*,*N*-Tripropyl(11-mercaptoundecyl)ammonium chloride ligand.

2A.4.2. Characterization of *N,N,N*-Tripropyl(11-mercaptoundecyl)ammonium chloride ligand protected Au ultra-small clusters (NC) and nanoparticles (NP)

2A.4.2.1. High Resolution Transmission Electron Microscopy

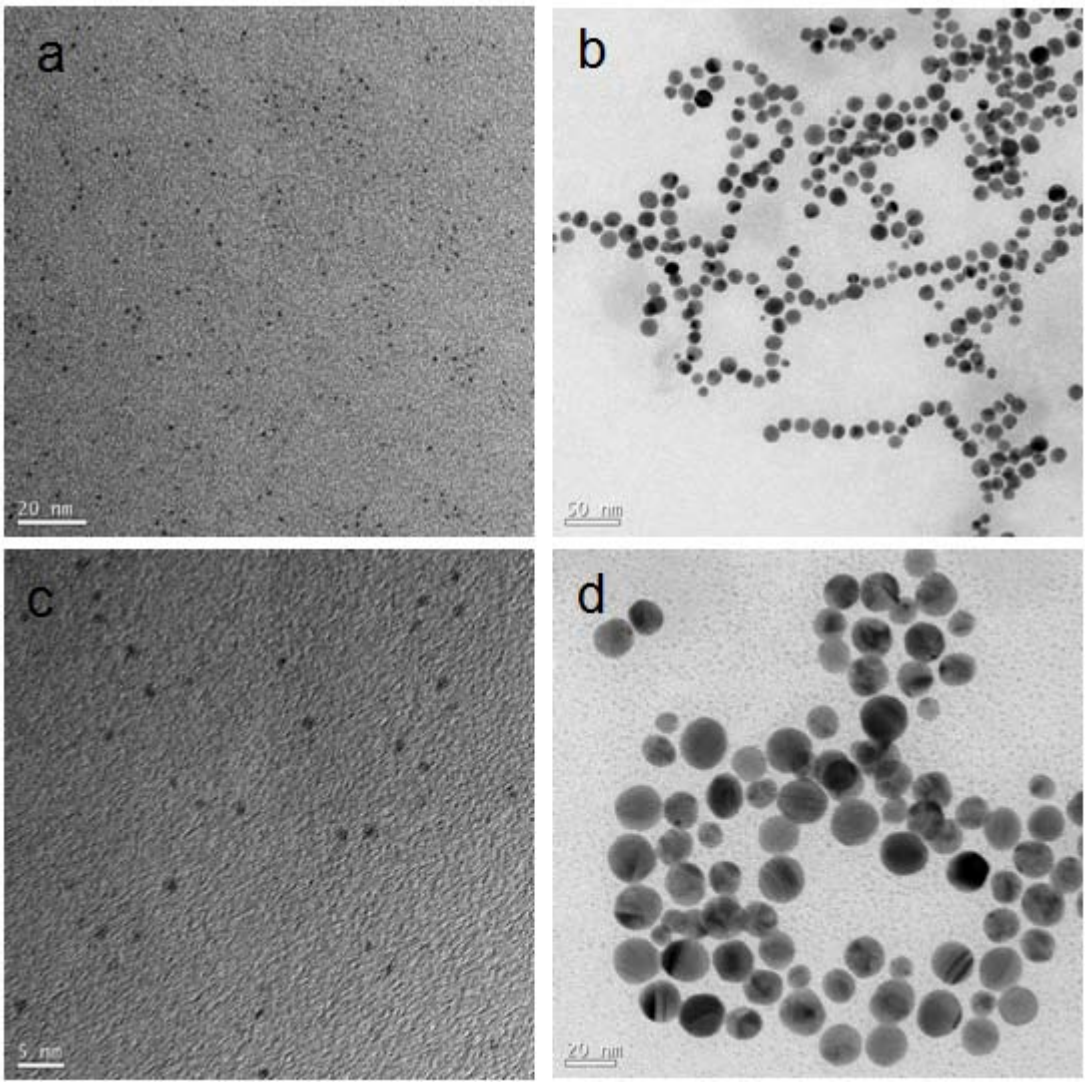

Fig. 2A.3. HRTEM images of a,c) Au ultra-small clusters and b,d) Au nanoparticles

High resolution transmission electron microscopy (HRTEM) has been employed to study the morphology and size of Au ultra-small clusters and nanoparticles. Fig. 2A.3 (a, c) and (b,d) shows the HRTEM images of Au ultra-small clusters and Au nanoparticles prepared by higher and lower amount of thiol respectively. HRTEM analysis has revealed that higher amount of thiol yields Au ultra-small clusters of diameter in the range 1-2 nm and Au nanoparticles of diameters

in the range 13-21 nm are formed in case of lower amount. Au ultra-small clusters and nanoparticles are spherical in nature and space separated nicely from each other. This space separation indicates that Au ultra-small clusters and nanoparticles are stabilized properly against aggregation by the thiol ligand. On the basis of HRTEM images the size distribution of nanoclusters and nanoparticles are calculated. The precise size distribution of nanoclusters and nanoparticles are presented in Fig. 2A.4. These size distribution histograms are made by measuring individual size of ca 100 nanoparticles.

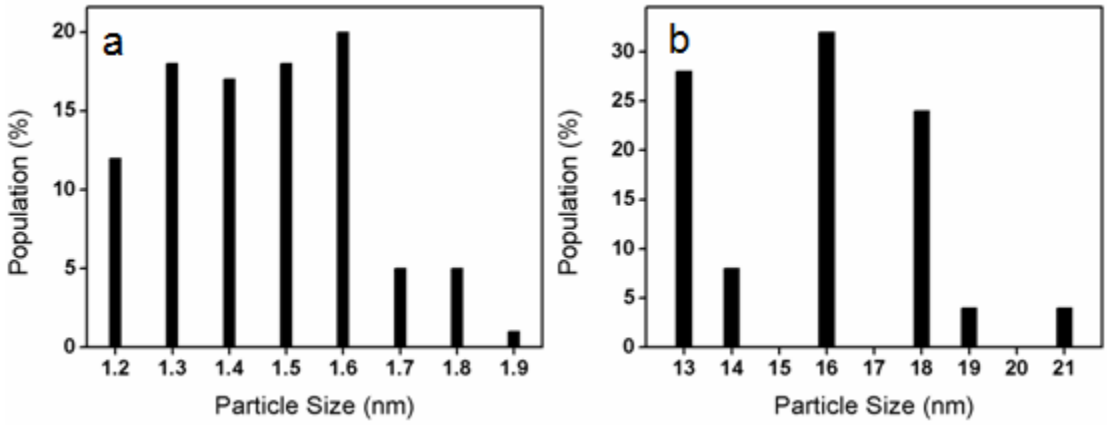

Fig. 2A.4. Particle size distribution of a) Au ultra-small clusters and b) Au nanoparticles

2A.4.2.2. UV-Vis Spectroscopy

UV–visible absorption spectroscopy is the most widely used technique for characterizing the optical properties and electronic structure of nanoparticles, since the peak position of absorption bands are strongly dependent on shape and size of metal nanoparticles [3]. The formation of gold nanoparticles can be observed by a characteristic surface plasmon resonance band (SPR). UV-vis spectra of Au nanoparticles and clusters are given in Fig. 2A.5. Curve a in Fig. 2A.5 shows the absorption band at 525 nm, which is the characteristic SPR band of gold nanoparticles [4]. The peak position of SPR band at 525 nm indicates the presence of ~ 20 nm Au nanoparticles in colloidal solution. The position of peak in the absorption spectrum predicts the size of the nanoparticles and this is in good agreement with the results obtained from direct measurements of HRTEM. UV-vis spectroscopy of ultra-small

Au clusters is quite interesting. It is completely different from the crystalline Au nanoparticles.

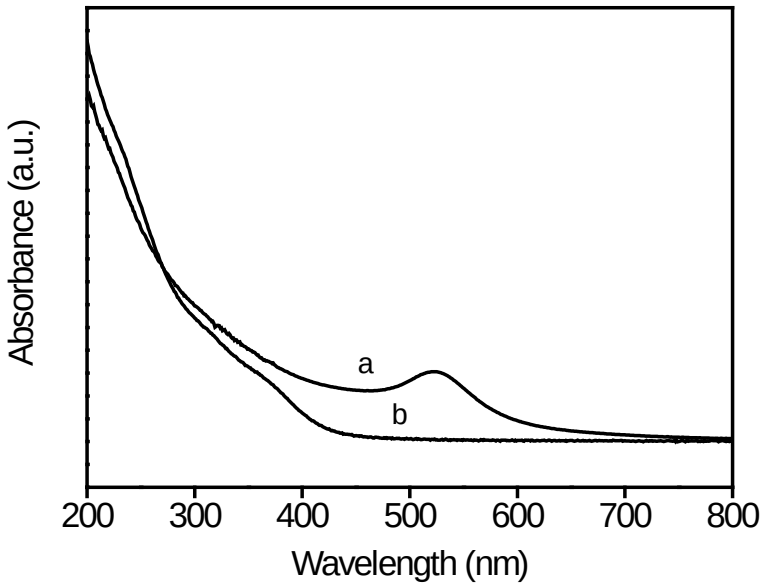

Fig. 2A.5. UV-vis spectra of a) Au nanoparticles and b) Au nanoclusters colloid solution.

It does not show any characteristic surface plasmon resonance band. Due to the ultra-small size in nature, these nanoclusters induce quantum confinement effect. As a result, nanoclusters behave like a single molecule and show HOMO-LUMO electronic transitions [5]. Because of this, ultra-small size Au nanoclusters do not show any SPR band but show an exponential decay curve with molecular level transitions appearing as distinct peaks superposed on the exponential curve. Curve b represents the UV-vis spectrum of Au nanoclusters in Fig.2A.5. It has shown an exponential decay pattern, but without any characteristic peaks representing the molecular level transitions. However, broad features in the UV region could be discerned. This broadening is attributed to the polydisperse nature of the Au nanoclusters which is also affirmed by HRTEM analysis.

2A.4.2.3. Fluorescence Spectroscopy

Fluorescence spectrum of Au cluster solution shows a broad emission peak in the NIR region at ~ 840 nm [Fig. 2A.6] when excited at 460 nm and this

photophysical property also confirms the presence of ultra-small gold clusters. Due to ultra-small size in nature Au clusters behave like single molecules and single electron transitions are possible. Because of this, ultra-small Au clusters show intrinsic photoluminescence property.

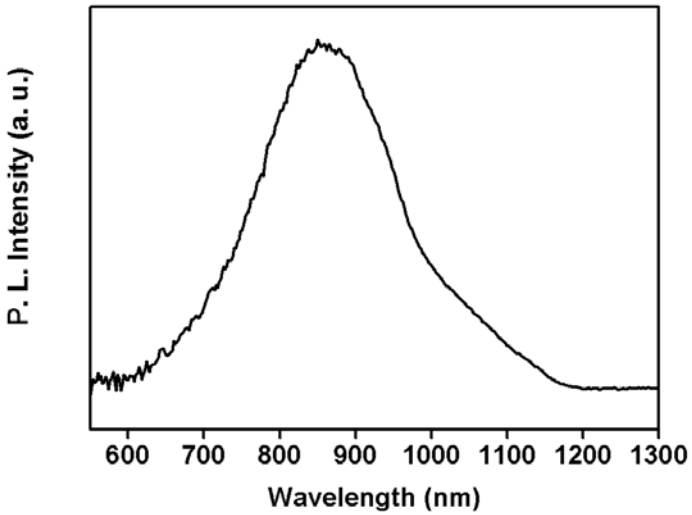

Fig. 2A.6. Fluorescence spectrum of ultra-small Au clusters solution.

The emission at 840 nm exhibited by ultra-small Au clusters is tentatively attributed to sp to sp transitions (*i.e.* intraband transitions). Quantum yield is calculated to be ~ 3 %. Details of this calculation are given in Appendix 2.1. These ultra-small Au clusters are potential candidates for biolabelling and bioimaging study because NIR fluorescence can avoid interference from biological media such as tissue auto fluorescence and scattering light. Such systems are also advantageous due to their enhanced photostability.

2A.4.2.4. Confocal Microscopy

The inherent fluorescent property of ultra-small Au clusters has been confirmed further by laser scanning confocal microscopy. Fig. 2A.7 shows fluorescence image of ultra-small Au clusters for a scan area of 140 µm X 140 µm at an excitation wavelength of 488 nm. This shows that the emission properties are intact in solid state also.

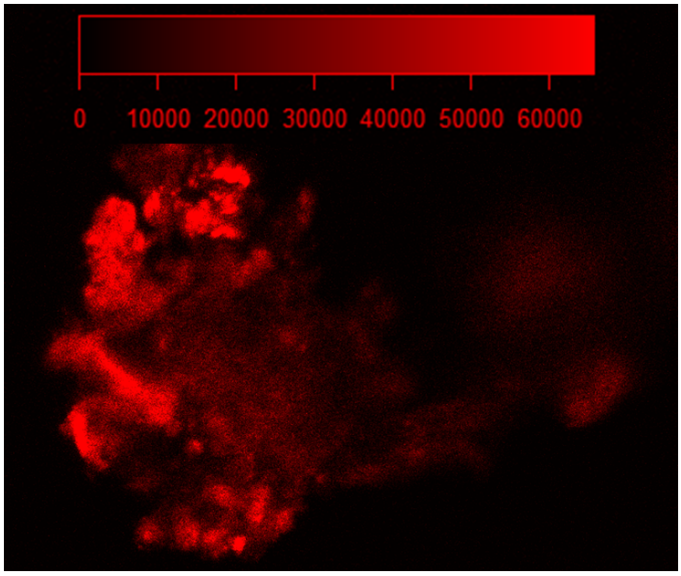

Fig. 2A.7. Fluorescence image of ultra-small Au clusters.

2A.4.2.5. FT-IR Spectroscopy

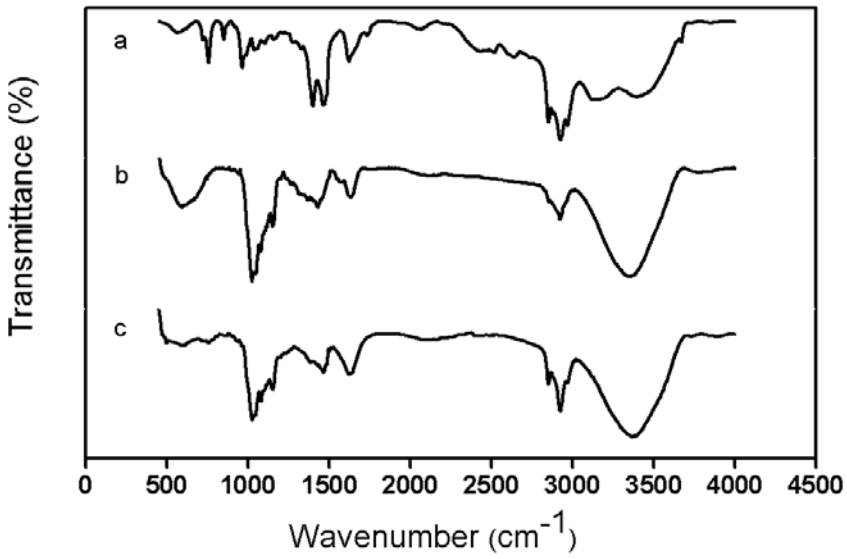

Fig. 2A.8. FT-IR spectra of a) thiol ligand, b) thiol-functionalized Au nanoparticles and c) thiol-functionalized Au nanoclusters.

FT-IR spectroscopy has been used frequently for the characterization of functionalized nanoparticles to study the metal-ligand bonding interaction [6]. Fig. 2A.8 represents the FT-IR spectra of thiol ligand, thiol functionalized Au nanoparticles and Au nanoclusters. Similar peak pattern of all the spectra has

confirmed the surface functionalization of Au nanoparticles and nanoclusters by the thiol ligand. Disappearance of S-H peak at 2636 cm^{-1} in the spectra of Au nanoparticles and nanoclusters also corroborates the Au-S bonding interaction.

2A.4.2.6. Dynamic Light Scattering and Zeta Potential Measurement

Particle size and zeta potential measurement were carried out by using DLS analyzer. Hydrodynamic diameter of nanoparticles can be determined by this method. From this measurement we can get information on aggregation of nanoparticles in solution state. Zeta potential data can predict the colloidal stability and surface functionalization of nanoparticles. Surface charge of Au ultra-small clusters and nanoparticles are found to be + 34 mV and +38 mV by zeta potential measurement. Surface charge values > + 30 mV have confirmed the stability of Au colloidal solution and positive zeta value also affirmed the surface decoration of nanoparticles by the positively charged ammonium thiol ligand. The average particle sizes, ~ 418 nm and 175 nm for nanoclusters and nanoparticles respectively, determined by this technique are much larger than that of HRTEM data. This large hydrodynamic diameter indicates the aggregation of nanoparticles due the presence of positively charged ammonium groups on terminal of the thiol ligand attached on the surface of the metal nanoparticles. But small particle size from HRTEM analysis revealed that this ionic association between the ionic groups has happened without fusion of metal core of nanoparticles.

2A.4.2.7. X-ray Photoelectron Spectroscopy

XPS analysis is performed to reveal the oxidation state of the gold component in thiol stabilized Au nanoclusters. XPS shows a doublet with binding energies of 84.4 and 88 eV corresponding to Au $4f_{7/2}$ and Au $4f_{5/2}$ respectively [Fig. 2A.9]. These are slightly deviated from bulk Au metal peak value (83.8 eV) but are characteristic of nanosized metallic Au with zero oxidation state [7].

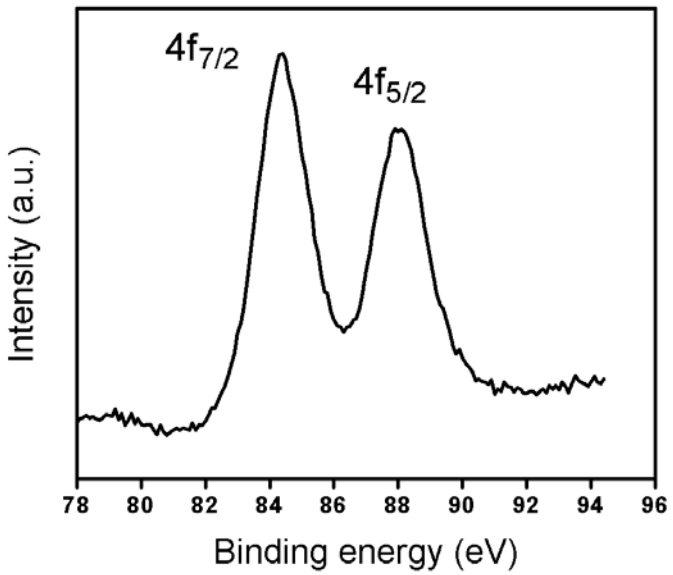

Fig. 2A.9. XPS spectrum of the gold nanoclusters showing the Au $4f_{7/2}$ and $4f_{5/2}$ doublet with binding energies of 84.4 eV and 88 eV respectively indicating Au^0.

2A.4.2.8. Inductively Coupled Plasma Spectroscopy

Concentration of Au in nanoclusters solution is estimated by ICP analysis. It shows 2 mM Au present in the as-synthesized Au nanocluster solution.

2A.5. APPLICATION OF Au NANOCLUSTERS IN BIOIMAGING OF THE BACTERIAL QUORUM SENSING PHENOMENON

Quorum sensing (QS) or the phenomenon of bacterial communication has been identified and studied in detail for more than a decade now [8-10]. Such kind of intercellular communication allows bacteria to come together and function as a single entity more or less like a multicellular organism [11]. Quorum sensing is suggested to be the mechanism by which biofilm formation takes place, which enhances the virulence, drug resistance etc. of various bacterial pathogens. QS is mediated by small easily diffusible signal molecules which regulate target gene expression and is highly dependent on the density of bacterial cells in the medium. Different categories of molecules mediate quorum sensing in different strains of bacteria which can be loosely categorized into those in gram negative and gram positive bacteria [12]. Gram positive bacteria depends on autoinduction by small peptides and in gram negative

bacteria, QS is mediated by acylated homoserine lactone (AHL) class of molecules [13,14]. These autoinducers are perceived by their complementary receptors and this process is highly selective with respect to the signal molecule and receptors. Binding of autoinducers to the specific receptor sites triggers cascade processes regulating a wide range of phenomena often detrimental to the host organisms [15-17]. In case of AHL autoinducers, receptors belong to Lux-R family of transcription regulators and they are usually located intracellularly or may be found attached to the inner leaflet of bacterial cell membrane [18].

Even though lot of biochemical information has been brought to light in recent studies regarding the mechanistic aspects of quorum sensing, attempts to visualize this phenomenon have been rare. Recently, imaging the phenomenon of quorum sensing in gram negative organisms, specifically *Pseudomonas aeruginosa* (PAO1) has been attempted, employing *in vivo* approaches whereby a quorum sensing biosensor strain was used as a probe to detect the signal [19]. However, this method is dependent on growth of both the test strain and the biosensor. Such growth associated methods are time consuming and carries the risk of a full blown infection of the host in the meantime, hence do not seem appealing enough when urgent detection of bacterial pathogens is required. Imaging and identifying bacterial pathogens at low cell numbers, before they reach a quorate state and cause havoc, seems highly desirable. Such an early detection can be envisaged if we target the receptors which are present in the bacterial cells even before the virulent quorate phase. Very recently, CepR quorum sensing receptors in live cells of *Burkholderia cenocepacia* have been tagged using signal molecules which are terminally labeled with fluorescent organic moieties [20]. However, inorganic nanomaterial based fluorescent probes emitting in near IR (NIR) spectral region like the Au nanoclusters mentioned before are understood to be superior to organic dyes due to their higher photostability, reduced background fluorescence etc [21]. Imaging quorum sensing by such fluorescent probes is as of yet unexplored. In this scenario, a simple, photostable and selective fluorescence imaging of quorum sensing based on receptors facilitating early detection of bacteria will be advantageous. Based on this, we have modified our Au NCs to obtain a fluorescence imaging probe selective to bacteria possessing AHL receptors, *Eschericia coli*. *E.coli* is a gram negative bacteria which perceives AHL signal molecule through LuxR

family of receptor SdiA but does not produce the signal molecules [22]. This method seems to have potential for species selective imaging of quorum sensing *in vivo* with the added advantage of being capable of detecting bacterial cells much before the virulent stage and at lesser populations.

2A.5.1. Strategy employed for the detection of quorum sensing receptors in bacteria

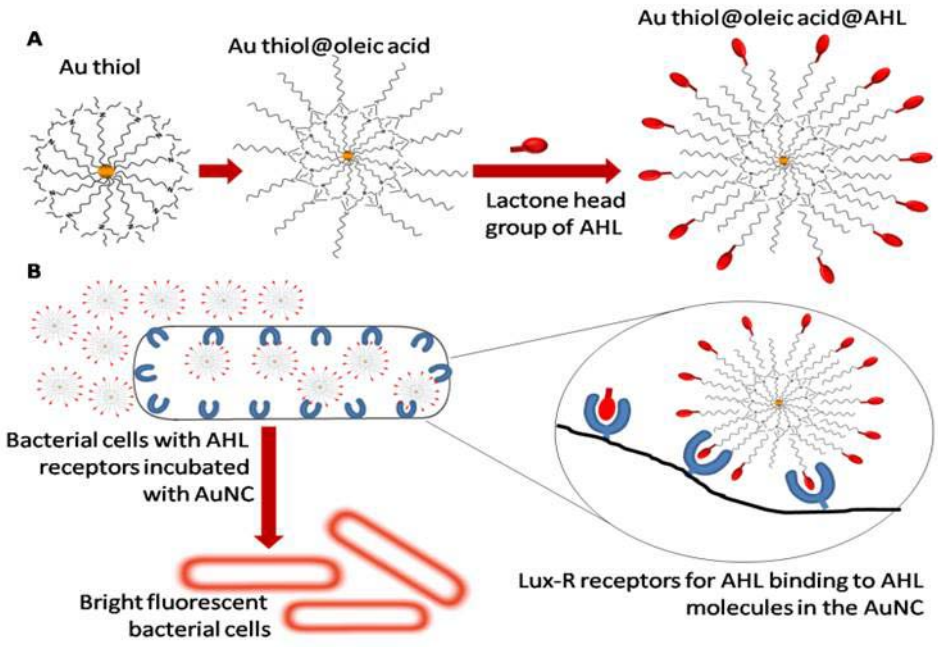

Scheme 2A.2. Interaction of the fluorescent probe with bacterial cells (A) Structure of the probe with AHL signal molecules deployed on the surface with lactone and amide moieties intact, (B) specific binding of AHL head groups to receptor sites in Lux-R regulators within bacteria. Binding sites shown schematically, actual location is not known.

The strategy employed here involves surface functionalizing fluorescent Au NCs with AHL in such a way that, capability of the signal molecules to bind to specific receptors is not compromised [Scheme 2A.2]. The AHL signal molecules consist of lactone head group and a long chain alkyl group of varying lengths. Structures of AHL molecules under study, C6-AHL and C8-AHL, with six and eight C alkyl chains are given in Fig. 2A.10. It is understood that ring carbonyl and 1-carbonyl groups of cognate AHL molecules bind to the N-terminal receptor sites of Lux R proteins through hydrogen bonding [23].

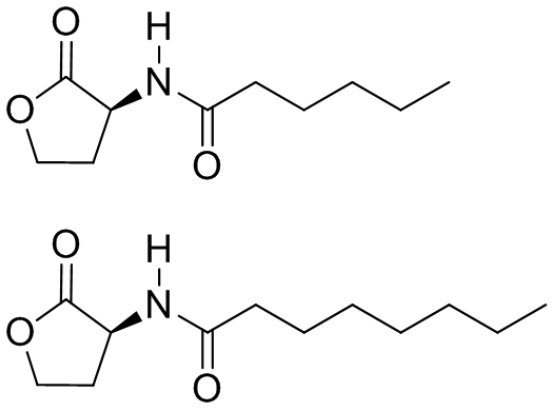

Fig. 2A.10. Chemical Structures of Acyl homoserine lactone molecules under study (top) C6 and (bottom) C8.

Hence it is imperative to leave the lactone and amide moieties intact and free to interact with the receptors. However, if pristine Au-thiolate cluster is added directly, there is a possibility of interaction between cationic head groups of NC and the lactone moiety of AHL.

Hence, further surface functionalization of the NCs is necessary to avoid any cooperative interaction between lactone and cationic head group of AuNCs. A composite is designed such that outer surface of the NC would form a hydrophobic region which would then interact with the alkyl chains of AHL molecules (Scheme 2A.2A). Accordingly, NCs are initially treated with oleic acid so that electrostatic attraction between cationic head groups and COOH groups is facilitated. Such a binding would allow the hydrophobic alkyl chains of oleic acid to decorate the outer surface of NCs rendering them ideal for interaction with the long chain alkyl groups of AHL. In this way, the lactone would be free to attach to the receptors in bacterial cells (Scheme 2A.2B). The average number of thiol molecules attached to the Au clusters are roughly estimated based on number of surface Au atoms and a methanol solution of oleic acid of equimolar concentration are added. Subsequently, lactones with varying chain lengths viz, C6 and C8 are mixed with the above Au-thiol@oleic acid composite.

2A.5.2. Synthesis and characterization of Au thiol@oleic acid@AHL

30 µL of a stock solution of oleic acid in methanol (0.6 mM) was mixed with 1 mL of the gold nanocluster solution. 10 µL of AHL in 500 µL of ethanol was added to this mixture and stirred for 4 h. This was considered as the stock solution for incubation with bacterial cells. For intermediate nanoclusters, same volumes of either AHL or oleic acid were added to 1 mL Au-thiol solution.

2A.5.2.1. FT-IR Spectroscopy

Interactions between various functionalizing molecules were ascertained by solid state FTIR spectroscopy. Electrostatic interaction between carboxylic acid group and ammonium head group based on carboxylic C=O functionality is followed in comparison to pristine oleic acid. It is known that this acid C=O stretch which is observed in 1710 cm^{-1} in pristine sample disappears in bound states with appearance of bands near 1640 and 1540 cm^{-1} corresponding to symmetric and asymmetric –COO vibrations [24]. We could also observe a strong band at 1636 cm^{-1} corresponding to symmetric and a very weak band at 1523 cm^{-1} corresponding to asymmetric –COO stretch.

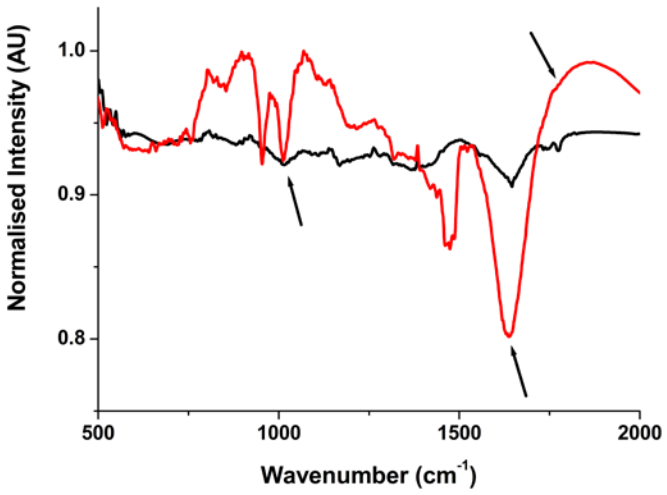

Fig. 2A.11. FTIR spectra of ethanolic solution of C6-AHL (black) and solid Au@OA@AHL (red); arrows indicate amide and lactone group bands which are intact in the composite.

This indicates a possible configuration of the cluster with COO- group interacting with ammonium group thereby deploying the alkyl functionality on the outside. IR spectrum of the composite after addition of C6-AHL in comparison to methanolic solution of AHL is given in Fig. 2A.11.

It can be seen that amide group bands are more prominent than lactone bands in both [25]. In case of pure AHL, amide group bands consist of a strong C=O stretch band at 1646 cm^{-1} and weak N-H bend at 1520 cm^{-1}[Fig. 2A.12]. Possible lactone C=O stretch could be seen at 1772 cm^{-1} and C-O stretch at 1167 and 1014 cm^{-1}corresponding to O-CO and O-CH_2 vibrations. After addition of AHL, the lactone group bands are intact at 1772 and 1011 cm^{-1} indicating that the bioactive region is free to interact with the receptor sites. O-C=O vibrations cannot be unambiguously assigned due to overlap with Au-OA bands. With these evidences we could tentatively conclude that the composite has the structure Au-thiol@oleicacid@AHL (Au@OA@AHL) with the lactone moiety on the outside of the cluster.

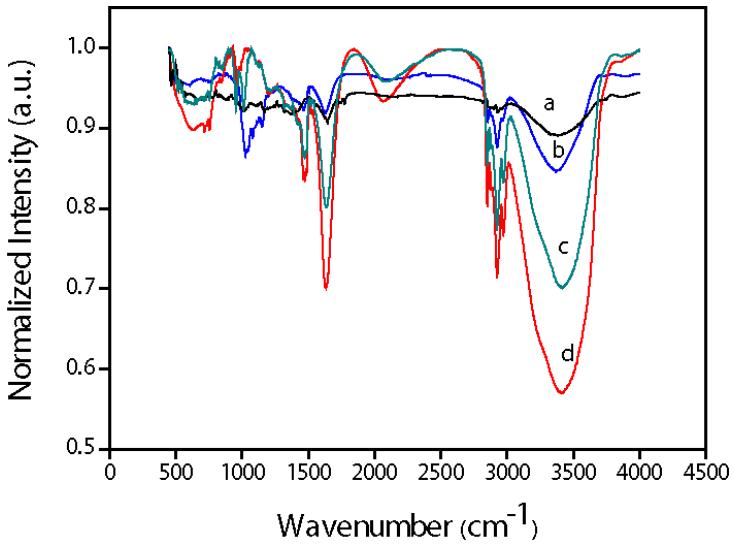

Fig. 2A.12. IR spectra of a) AHL-C6, b) Au clusters, c) Au-thiol@oleic acid@AHL-C6 and d) Au-thiol@oleic acid.

2A.5.2.2. High Resolution Transmission Electron Microscopy

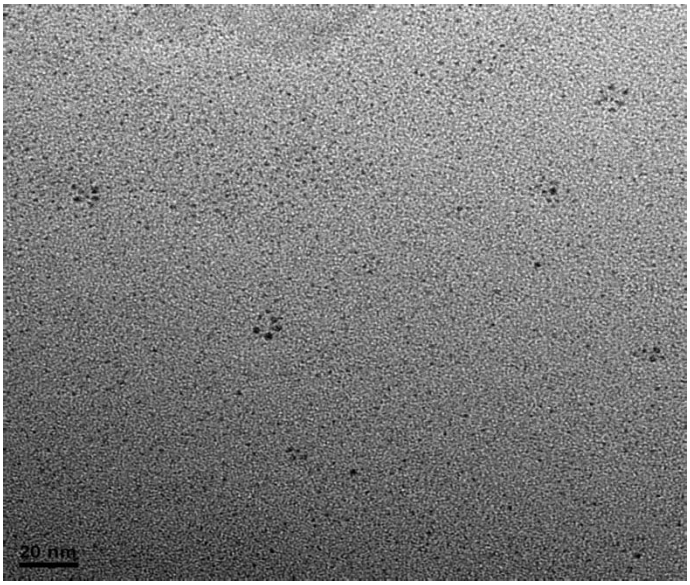

Fig. 2A.13. HRTEM images of Au-thiol@oleic acid@C6-AHL.

HRTEM analysis has been performed with Au-thiol@oleic acid@C6-AHL and this has revealed that functionalization does not affect the particle size of ultra-small clusters [Fig. 2A.13].

2A.5.2.3. Fluorescence Spectroscopy

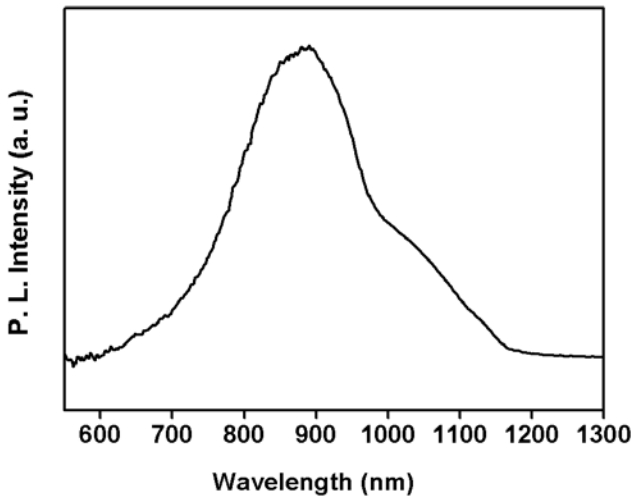

Fig. 2A.14. Fluorescence spectrum of Au-thiol@oleic acid@C6-AHL.

Fluorescence property of Au-thiol@oleic acid@C6-AHL has been measured. It shows that fluorescence emission is similar with pristine ultra-small Au clusters with an emission maximum at 860 nm and quantum yield of 1.6 % [Fig. 2A.14]. Details of quantum yield calculation are given in Appendix 2.2. This intact fluorescence property is necessary for bacteria detection study.

2A.5.3. Selective detection of Escherichia coli bacteria

We have selected representative bacteria from two distinct groups, one gram negative (*Escherichia coli*) and one gram positive (*Staphylococcus aureus*) for further fluorescence imaging. Quorum sensing receptors in *E.Coli* are of the Lux-R family but it is interesting to note that this strain does not produce AHL molecules and *S.aureus*, being gram positive does not contain the receptors. Initially, bacterial cells were suspended in saline and incubated with the Au@OA@AHL conjugates for 2 h with gentle shaking. After incubation cells were pelleted down, washed with saline and resuspended in fresh saline so that any unbound fluorescent clusters would not interfere with the imaging. Olympus Fluoview Laser Scanning Microscope was used to observe the stained bacterial cells. Confocal microscopy slides were prepared using 70% glycerol as mounting medium and this did not hamper with the fluorescence of the sample. Cover slips containing the sample and mounting medium were sealed at the sides to prevent drying by evaporation and slides were observed within 3-4 hours of sample preparation.

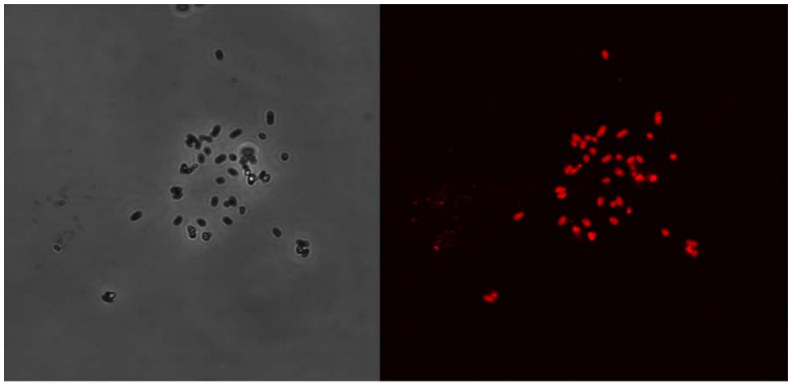

Fig. 2A.15. Confocal microscopy images of *E.coli* incubated with Au@OA@C6-AHL; (left) phase contrast image and (right) fluorescence image of the same region.

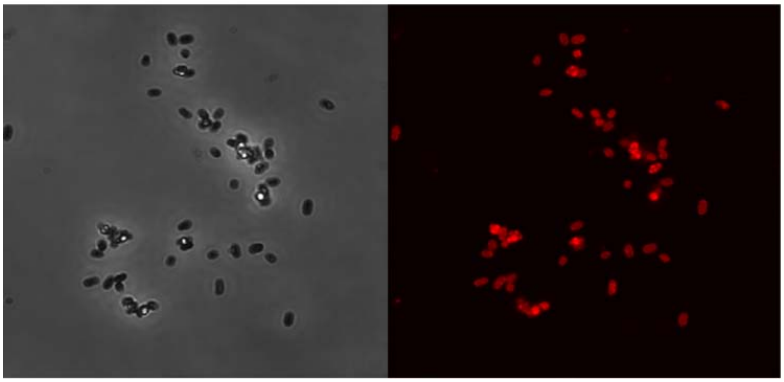

Fig. 2A.16. Confocal microscopy images of *E.coli* incubated with Au@OA@C8-AHL; (left) phase contrast image and (right) fluorescence image of the same region.

These cells in glycerol medium were observed under confocal microscope at preset excitation and emission wavelengths of 547 and 567 nm respectively. In case of *E.coli*, Au clusters decorated with both C6 (Fig. 2A.15) and C8-AHL (Fig. 2A.16) showed bright fluorescent.

Supernatant solution without the cells also has shown emission, however, in irregular agglomerated shapes pointing to unbound clusters [Fig. 2A.17.].

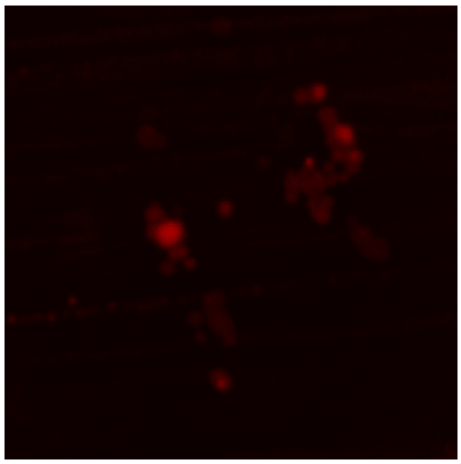

Fig. 2A.17. Confocal images of supernatant solution without bacterial cells after incubation of E.coli with Au@OA@C8-AHL for 4 h.

Since AHLs are specifically produced by gram negative bacteria, rationally the Au NCs decorated with AHL molecules should only interact with cells of *Escherichia coli* and not with *Staphylococcus aureus*, the gram positive bacterium. To establish

this hypothesis, in a separate experiment, cells of stained *S.aureus* were observed under same conditions as *E.coli*. As expected, *S.aureus* did not show fluorescence indicating that it failed to interact with Au@OA@AHL as displayed in Fig. 2A.18. This shows the inherent specificity of this conjugate to interact with only those cells which possess receptors for AHLs. This indicates that the probe conjugates are capable of accessing the receptor sites within the bacterial cells.

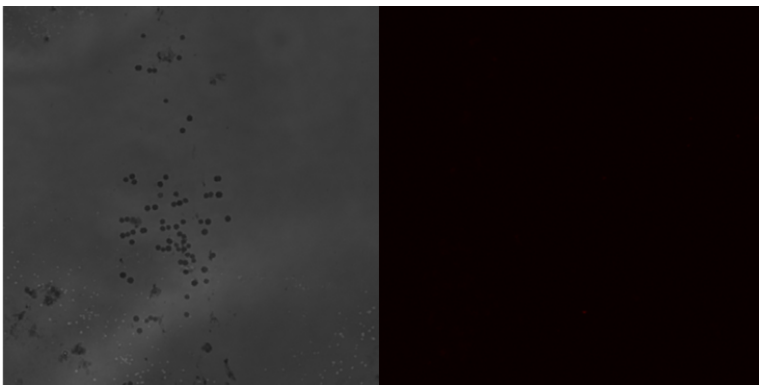

Fig. 2A.18. Confocal microscopy images of *S.aureus* incubated with Au@OA@C8-AHL; (left) phase contrast image and (right) fluorescence image of the same region.

2A.5.4. Specific interaction between lactone moiety of AHL and the receptors on bacterial cells

To further test our hypothesis of the structure of the composite and mode of binding, *E.coli* cells were also stained with two intermediate NCs, viz., Au-thiol@AHL and Au-thiol@oliec acid. These NCs were synthesized in such a way that concentrations of Au-thiol as well as AHL and oleic acid were same as that of the Au@OA@AHL conjugate. Former sample represents the situation where outer surface of Au NCs is not hydrophobic so that lactone moiety may interact with cationic ammonium head group of the thiolate layer. In such a case, we envisage non availability of the binding sites of the signal molecule and hence no detection of the bacterial cells. The latter indicates a similar case whereby a hydrophobic Au NC without the signal molecule is used. It is possible that the fluorescent Au NCs can indiscriminately access the receptors even without the signal molecules, in which case Au-thiol@oleic acid should bind to bacterial cells. Interestingly, no fluorescence could be seen [Fig. 2A.19] in either of these cases giving credence to the proposed

structure model. This clearly indicates that the structure of the fluorescent probe is Au@OA@AHL with the lactone moiety decorating the surface which can interact with the receptors on bacterial cells.

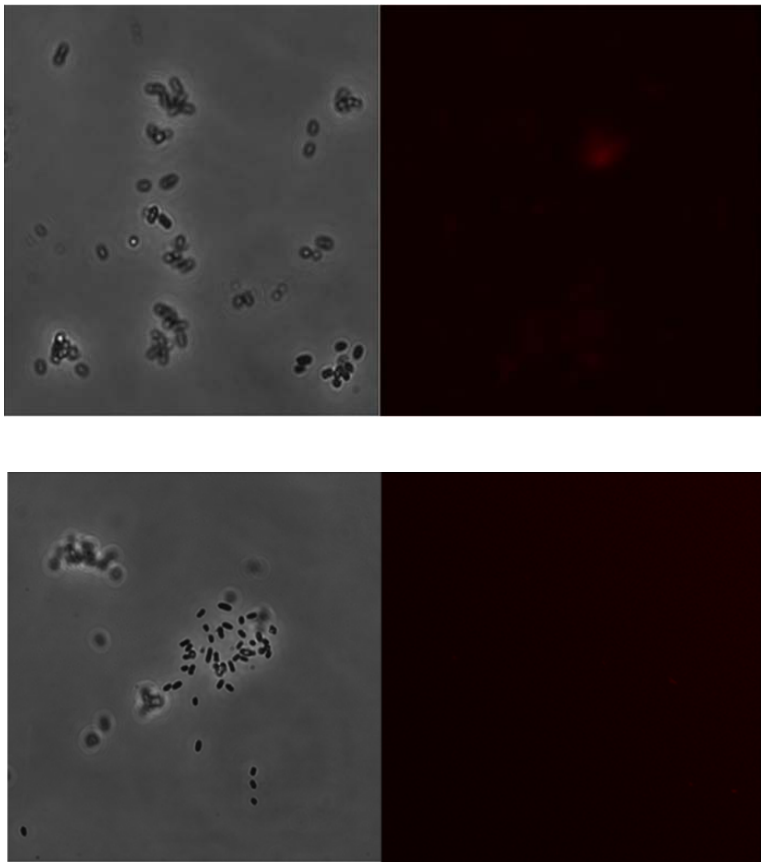

Fig. 2A.19. Confocal images of *E.coli* incubated with Au-thiol@C8-AHL (top) and Au-thiol@oleic acid (bottom).

2A.5.5. Interaction Mechanism between AHL and the receptors on bacterial cells

It is also found that in a mixed population of *E.coli* and *S.aureus*, gram negative bacterial strain *E.coli* could be exclusively observed under fluorescence imaging [Fig. 2A.20]. This could be identified due to the shape difference between the two strains of bacteria from the phase contrast image, emphasizing the enhanced specificity of the probe. An interesting point worth highlighting is that *E.coli* cells do not produce AHLs but are able to detect and respond to these QS signal molecules by eventual gene regulation. Specific detection of *E.coli* by our probe system further highlights the fact it is the possession of AHL receptor that is imperative and not the

growth stage of cell or population density for this system to function as a potential biosensor.

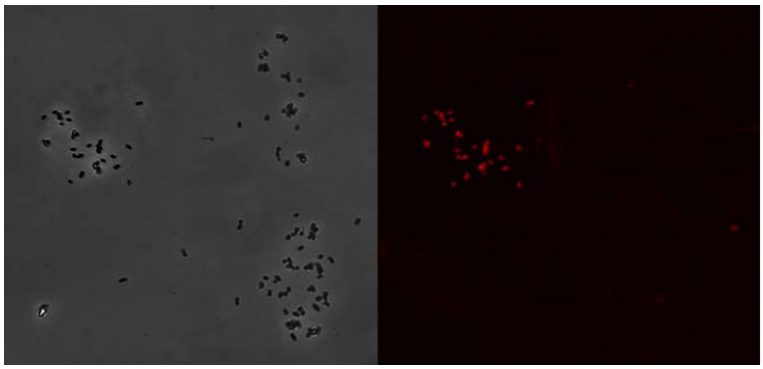

Fig. 2A.20. Confocal images of mixed population of *E.coli* and *S.aureus* incubated with Au@OA@C8-AHL; (left) phase contrast image and (right) fluorescence image of the same region.

To ascertain the interaction mechanism, we have selected another gram negative bacteria *Chromobacterium violaceum* (wild type) which is a natural producer of AHL molecules. The logic here is that if the receptor sites are already interacting with AHL in the system after the threshold concentration of signal molecules, this will prevent the interaction of the fluorescent probe to these sites. In such a case, bacterial cells incubated with the conjugate should not show any fluorescence activity and indeed this was observed [Fig. 2A.21].

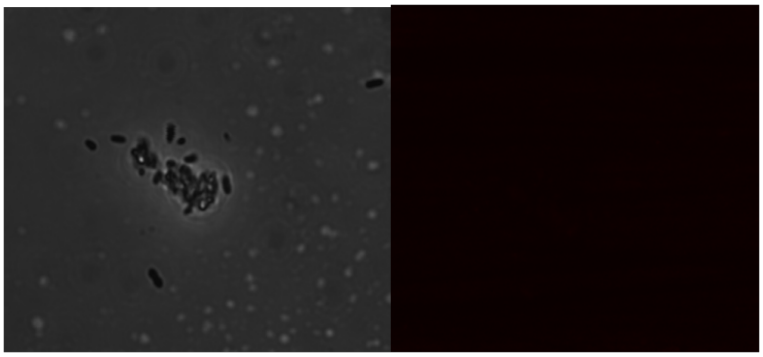

Fig. 2A.21. Confocal images of *Chromobacterium violaceum* (wild type) which produces AHL incubated with Au@OA@AHL; (left) phase contrast image and (right) fluorescence image of the same region.

Also, another test was carried out in which E.*coli* cells were first incubated with excess of free AHL so that the receptor sites are saturated and then this system was incubated with Au@OA@AHL conjugates. The confocal image does not show any indication of interaction by the probe to the bacterial cells [Fig. 2A.22]. This indicates that the receptor sites were not available for binding to Au@OA@AHL conjugate due to their saturation with excess free AHL initially added. These two observations prove that the AHL component of the conjugate interacts with the receptor sites specifically and also that these AHL molecules are strongly bound to the fluorescent Au-thiol nanoclusters. From these studies, we can also rule out any breakage of the conjugate structure.

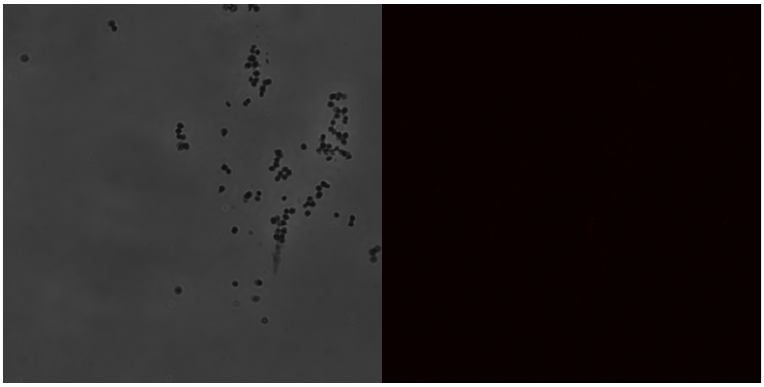

Fig. 2A.22. Confocal images of *E.coli* incubated with Au@OA@C6-AHL.

2A.6. SUMMARY

We have synthesized a novel *N,N,N*-Tripropyl(11-mercaptoundecyl)ammonium chloride thiol ligand which is capable of synthesizing stable water dispersible Au ultra-small clusters and nanoparticles. Particle size could be controlled by the thiol concentration in the synthesis medium. Ultra-small Au clusters show good fluorescence intensity at NIR region. This photophysical property has been used for imaging the phenomenon of quorum sensing in *E.coli* bacteria cell. After doing several experiments, we have concluded that we are able to develop a novel inorganic fluorescent probe capable of selectively binding to receptor sites involved in quorum sensing. The material is based on Au nanoclusters decorated with quorum sensing signal molecules for gram negative bacterial strains, acyl homoserine lactones. The structure is designed such that the bioactivity of the signal molecule,

vis-á-vis their lactone and amide groups, is intact after interacting with the fluorescent Au nanoclusters. This probe targets the binding sites for QS molecules within bacterial cells and not the concentration of signal molecules produced which is the current practice. This property makes these systems independent of cell density and can be used before the bacteria attain a virulent quorate state. This is the first time such inorganic fluorescent probes are used for bacterial detection before quorate state and the excellent specificity for binding sites renders this system indeed ideal for targeted biosensors.

2A.7. REFERENCES

1. A. Verma, J. M. Simard, J. W. E. Worrall and V. M. Rotello, *J. Am. Chem. Soc.*, 2004, **126**, 13987.
2. J. Tien, A. Terfort and G. M. Whitesides, *Langmuir*, 1997, **13**, 5349.
3. D. E. Mustafa, T. Yang, Z. Xuan, S. Chen, H. Tu and A. Zhang, *Plasmonics*, 2010, **5**, 221.
4. S. Eustis and M. A. El-Sayed, *Chem. Soc. Rev.*, 2006, **35**, 209.
5. R. Jin, *Nanoscale*, 2010, **2**, 343.
6. X. Zhou, J. M. El Khoury, L. Qu, L. Dai and Q. Li, *J. Colloid Interface Sci*, 2007, **308**, 381.
7. M. Brust, M. Walker, D. Bethell, D. J. Schiffrin and R. Whyman, *Chem. Commun.*, 1994, 801.
8. B. L. Bassler, *Cell*, 2002**, 109**, 421.
9. P. Williams, *Int. J. Med. Microbiol.*, 2006**, 296**, 57.
10. C. M. Waters, B. L. Bassler, *Annu.Rev.Cell Dev.Biol.*, 2005, **21**, 319.
11. P. Williams, *Microbiology*, 2007**, 153,** 3923.
12. N. C. Reading and V. Spreandio, *FEMS Microbiol. Lett*., 2006, **254**, 1.
13. I. Joint, D. J. Allan and P. Williams, *Philos.Trans.R.Soc.Lond B Biol.Sci.*, 2007, **362**, 1115.
14. C. Fuqua and E. P. Greenberg, *Nat.Rev.Mol.Cell Biol.*, 2002, **3**, 685.
15. P. Williams, M. Camara, A. Hardman, S. Swift, D. Milton, V. J. Hope, K. Winzer, B. Middleton, D. I. Pritchard and B. W. Bycroft, *Philos. Trans. R. Soc. Lond B Biol. Sci.* 2000, **355**, 667.

16. G. F. Kaufmann, J. Park, and K. D. Janda, *Exert.Opin.Biol.Ther.*,2008, **8**, 719.
17. L. C. Antunes, R. B. Ferreira, M. M. Buckner and B. B. Finlay, *Microbiology*, 2010, **156**, 2271.
18. P. Williams, K. Winzer, W. C. Chan and M. Camara, *Philos. Trans. R. Soc. Lond B Biol. Sci.*, 2007**, 362**, 1119.
19. L. D. Christensen, G. M. Van, T. H. Jakobsen, M. Givskov and T. Bjarnsholt, *Methods Mol. Biol*. 2011, **692**, 147.
20. J. Gomes, N. Huber, A. Grunau, L. Eberl, and K. Gademann, *Chemistry*. 2013, **19**, 9766.
21. C.-H. Quek and K.W. Leong, *Nanomaterials*, 2012, **2**, 92.
22. K. Kanamaru, K. Kanamaru, I. Tatsuno, T. Tobe, and C. Sasakawa, *Mol. Microbiol.*, 2000, 3**8**, 805.
23. B. Koch, T. Liljefors, T. Persson, J. Nielsen, S. Kjelleberg, and M. Givskov, *Microbiology*, 2005, **151**, 3589.
24. L. Zhang, R. He and H-C. Gu, *Applied Surface Science*, 2006, **5**, 2611.
25. J. Bak and J. Spanget-Larsen, *Vibrational Spectroscopy*, 2009, **49**, 237.

PART B

SYNTHESIS AND CHARACTERIZATION OF POROUS SILICA ENCAPSULATED Au NANOPARTICLES AND THEIR APPLICATIONS AS PEROXIDASE MIMIC IN HYDROGEN PEROXIDE AND GLUCOSE DETECTION

2B.1. INTRODUCTION

Gold nanoparticles with diameter < 5 nm are highly active catalysts for several reactions. One of the major problems in gold catalysis is the deactivation of the catalysts due to agglomeration of the catalytically active Au nanoparticles. Agglomeration process can be prevented and activity can be retained by porous silica encapsulation of gold nanoparticles. We have already discussed this in detail in Chapter 1 (section 1.5).

To fulfill this aim we have used thiol protected ultra-small Au clusters as precursors for silica encapsulation. The ultra-small Au clusters are synthesized by using propyl ammonium functionalized alkyl thiol making them water-dispersible and amenable for silica encapsulation. The strategy used for the synthesis of porous silica encapsulation of Au nanoparticles is described in Scheme 2B.1.

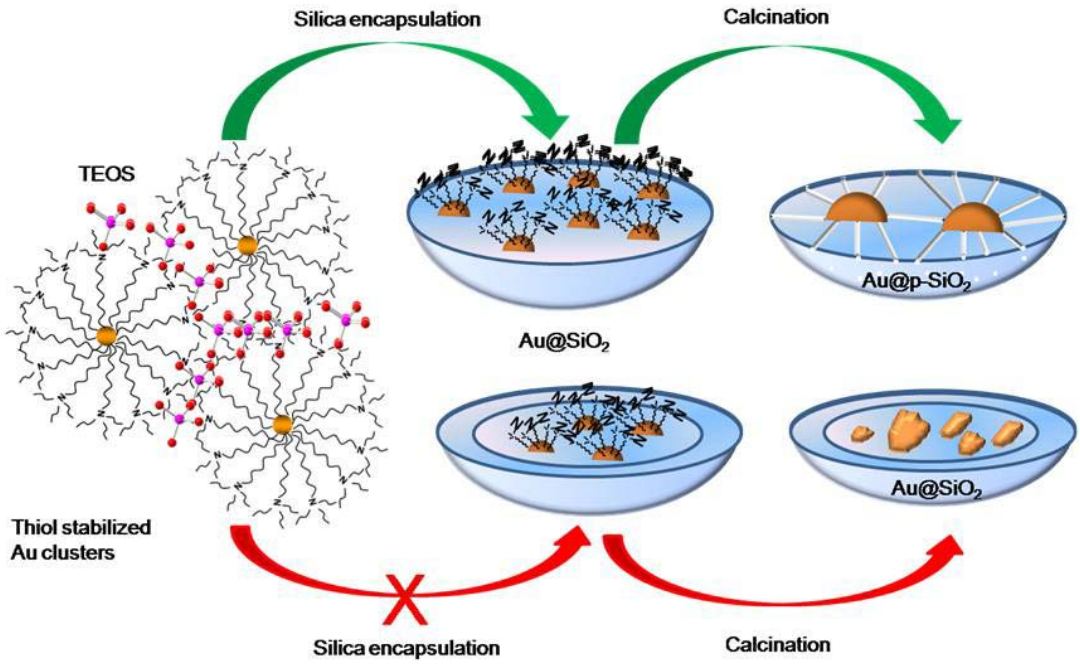

Scheme 2B.1. Encapsulation of Au nanoparticles in a space-separated manner enhances stability and reactivity compared to encapsulation in a core-shell architecture. Au@SiO_2 contains Au moieties within a dense compact matrix, which differentiates from Au@p-SiO_2, which has a porous silica matrix.

The strategy employed involves encapsulation of water dispersible ultra-small Au clusters in silica by a simple hydrolysis method. The thiol ligand designed has SH group at one end for attaching to metal and the other end is functionalised to have propyl ammonium group. The ammonium head group is proposed to help in facilitating water dispersibility and propyl groups will be sufficiently hydrophobic to direct the silica precursors to enable encapsulation of individual clusters when multiple cluster arrays are present within single silica spheres.

The abundance of organic ligands within the silica spheres has ensured the formation of pores in the silica matrix. The architecture where clusters are encapsulated individually in silica matrix enables better control of particle sizes by minimizing sintering during calcination. This porous silica encapsulated Au nanoparticles are used for the detection of H_2O_2 and glucose.

2B.2. SYNTHESIS

2B.2.1. Synthesis of porous silica encapsulated Au nanoparticles

2B.2.1.1. Syntheis of silica encapsulated Au nanoclusters

5 mL ultra-small Au clusters solution was mixed with a 1:4 mixture of water:ethanol (100 mL). 450 µL NaOH solution (0.1 M) and 150 µL tetraethyl orthosilicate (98 wt % Aldrich) were added to this mixture and stirred at room temperature for 2 d. Silica encapsulated Au nanoclusters were separated from the reaction medium by centrifuging at 14000 rpm and redispersing in water several times.

2B.2.1.2. Syntheis of porous silica encapsulated Au nanoparticles (Au@p-SiO_2)

The above as-synthesized material was calcined to remove the thiol ligand by heating with a rate of 0.8 °C/min from room temperature to 250 °C. First the temperature was increased up to 250 °C under nitrogen and then it was kept constant for 12 h under air for removing the organic ligand.

2B.3. INSTRUMENT FOR CHARACTERIZATION

High resolution transmission electron microscopy (HRTEM), transmission electron microscopy (TEM), UV-Vis spectroscopy, fluorescence spectroscopy, confocal microscopy, N_2-adsorption, X-ray photoelectron spectroscopy (XPS), N_2-adsorption and inductively coupled plasma spectroscopy (ICP-AES) were used for the characterization of silica encapsulated Au nanoclusters and porous silica encapsulated nanoparticles. Instrumental details of TEM, HRTEM, UV-Vis spectroscopy, confocal microscopy and XPS are already been described in Chapter 2 (section 2A.3).

2B.3.1. N_2 Adsorption

Nitrogen adsorption/desorption isotherm was acquired using Autosorb 1C instrument. The program consisting of both adsorption and desorption branch, typically ran at -196 ºC after the sample was degassed at 150 ºC for 2 h once the final temperature had been maintained. Specific surface area was calculated via the Brunauer-Emmett-Teller (BET) model at a relative pressure of P/P_0 = 0.05-0.2. The pore volume was estimated from the uptake of adsorbate at a relative pressure of P/P_0 = 0.99. Pore size distribution curve was obtained by using Horvath and Kawazoe (HK) method.

2B.3.2. Inductively Coupled Plasma Spectroscopy

In case of silica encapsulated nanoparticle materials, 5 mg sample was taken in a polypropylene container. Few drops of hydrofluoric acid was added to it and heated at 80 °C up to dryness to remove silica. 1 mL aqua regia was added into the container to dissolve the metal. Then 9 mL millipore water was added to it and the solution was ready for analysis.

2B.4. CHARACTERIZATION

Silica encapsulated Au nanoclusters and porous silica encapsulated nanoparticles are characterized by HRTEM, TEM, UV-vis spectroscopy, confocal microscopy, XPS and N_2 adsorption study.

2B.4.1 Characterization of silica encapsulated Au nanoclusters

2B.4.1.1. Transmission Electron Microscopy

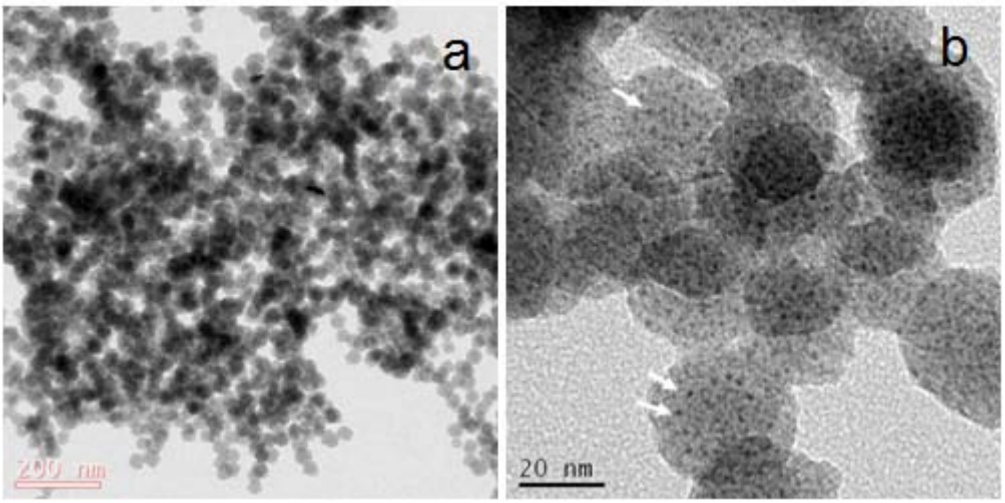

Fig. 2B.1. TEM images of silica encapsulated ultra-small Au clusters; a) at lower magnification and b) at higher magnification, arrows indicate the Au nanoclusters.

TEM analysis has revealed that arrays of ultra-small gold nanoclusters are encapsulated completely inside spherical silica shell in a space separated manner [Fig. 2B.1]. Nanoclusters are protected by thiol ligand which has both hydrophilic ammonium group and long alkyl chain hydrophobic group and because of this, silica polymerization occurs in a controlled manner to encapsulate the clusters apart from each other. The average diameter of silica shell and Au nanoclusters are ~ 30 nm and ~ 1.5 nm respectively. The average particle size of pristine Au nanoclusters is ~ 1.5 nm and this is intact even after silica encapsulation.

2B.4.1.2. UV-Vis Spectroscopy

UV-vis spectra of both pristine Au nanoclusters and silica encapsulated Au nanoclusters have shown similar pattern [Fig. 2B.2]. This indicates that particle size does not change even after silica encapsulation and nanoclusters are stable inside the silica shell.

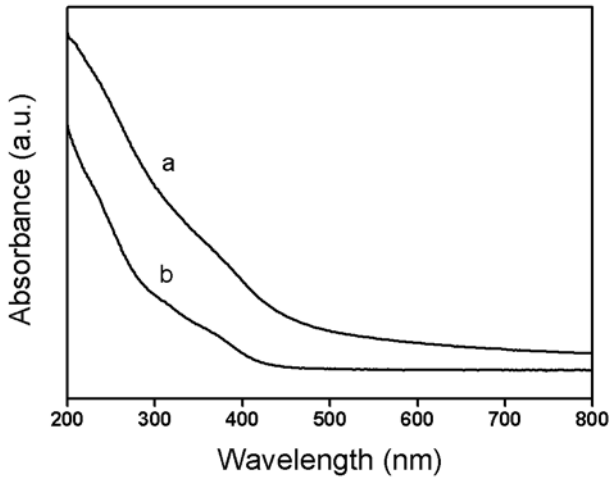

Fig. 2B.2. UV-vis spectra of a) silica encapsulated ultra-small Au clusters and b) ultra-small Au clusters

2B.4.1.3. Confocal Microscopy

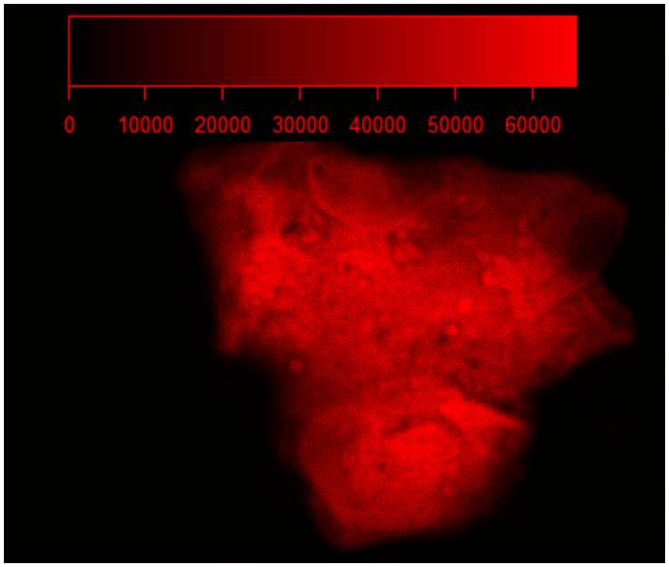

Fig. 2B.3. Fluorescence image of silica encapsulated ultra-small Au clusters.

Confocal laser scanning microscopy has shown similar fluorescence intensity to the pristine Au nanoclusters. Fig 2B.3 shows fluorescence image of silica encapsulated Au clusters for a scan area of 140 µm X 140 µm at an excitation wavelength of 488 nm. This silica encapsulated Au nanoclusters can be used further for functionalization and are potential candidates for bioimaging and biolabelling applications.

2B.4.1.4. X-ray Photoelectron Spectroscopy

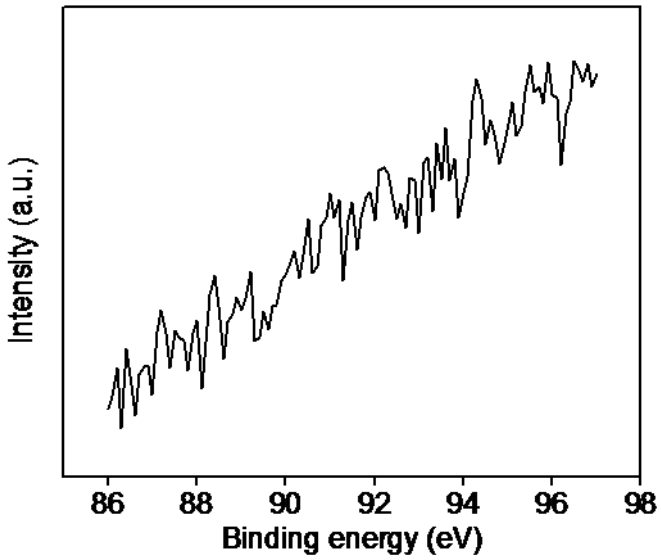

Fig. 2B.4. XPS spectrum of silica encapsulated gold nanoclusters evidencing the absence of Au $4f_{7/2}$ and $4f_{5/2}$ doublet of Au.

XPS analysis could not detect any surface concentration of Au [Fig. 2B.4]. This happens because X-ray probe depth employed for this analysis is 2-3 nm. Hence an absence of surface Au confirms the complete encapsulation of Au nanoclusters by silica sphere.

2B.4.2. Characterization of porous silica encapsulated Au nanoparticles

2B.4.2.1. High Resolution Transmission Electron Microscopy

HRTEM analysis has clearly shown that > 90 % of the Au naoparticles are of size ~ 3 nm [Fig. 2B.5]. In as-synthesized samples, Au nanoclusters are silica encapsulated individually in a space separated manner. Because of this, controlled

agglomeration happens to form ~ 3 nm nanoparticles from nanoclusters during calcination. Due to ligand removal during calcination some porosity has been generated in silica sphere which is tentatively observed in HRTEM image. But HRTEM analysis is not conclusive and porosity of the silica matrix was confirmed by N_2-adsorption study.

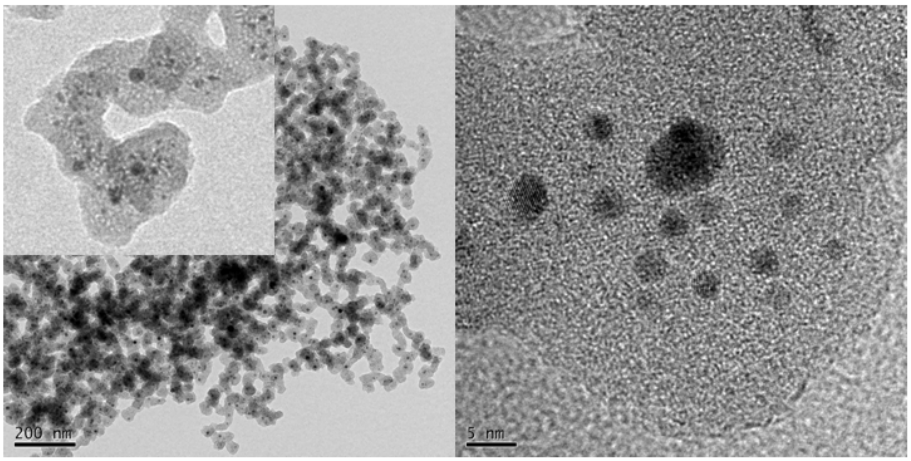

Fig. 2B.5. HRTEM images of Au@p-SiO_2 (calcined 250 °C). Magnified image (right) shows that >90% of the particles are of size ~ 3 nm. Inset shows the pore like features in silica.

2B.4.2.2. N_2 Adsorption Study

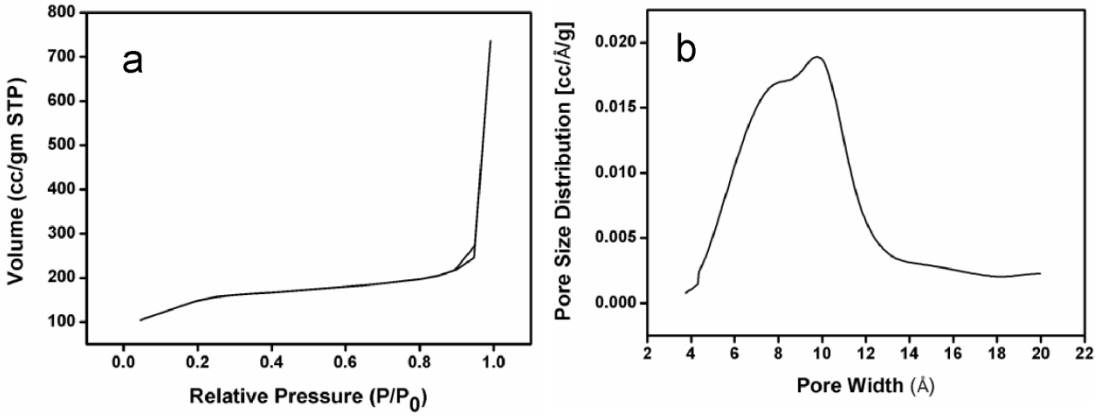

Fig. 2B.6. (a) N_2 adsorption–desorption isotherms of Au@p-SiO_2 (calcined at 250 °C) (b) Pore size distribution calculated from the adsorption branch of the isotherms by HK method.

N_2-adsorption study of calcined silica encapsulated Au nanoparticles has been performed to confirm the porosity inside the silica shell. This study indicates the presence of microporosity inside the silica shell [Fig. 2B.6]. The pore size distribution curve calculated from the adsorption branch of the isotherm has exhibited a maximum at 0.97 nm and the BET surface area of the sample calcined at 250 °C has been estimated to be 550 m^2g^{-1}. From this study it has been confirmed that Au nanoparticles are encapsulated in microporous silica matrix.

2B.4.2.3. UV-vis Spectroscopy

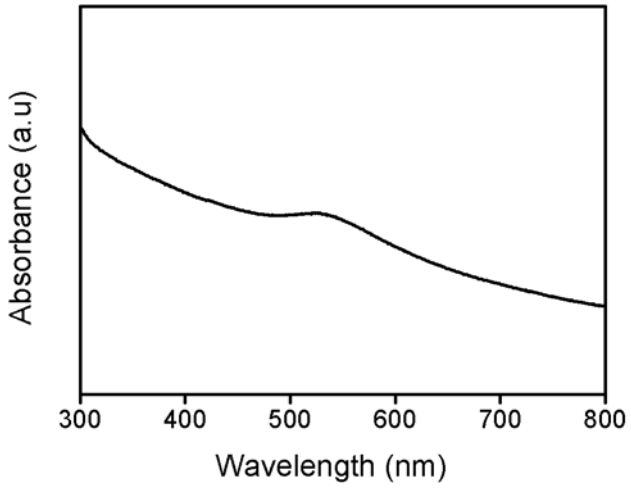

Fig. 2B.7. UV-vis spectrum of silica encapsulated Au nanoparticles.

UV-vis spectroscopy shows the characteristic surface plasmon resonance band of Au nanoparticle at ~ 530 nm [Fig. 2B.7]. This indicates Au nanoparticles formation from nanoclusters by agglomeration process during calcination.

2B.4.2.4. Inductively Coupled Plasma Spectroscopy

Concentration of Au in the porous silica encapsulated Au nanoparticles is estimated by ICP analysis. It shows that 5 wt % Au is present in the calcined material.

2B.5. POROUS SILICA ENCAPSULATED Au NANOPARTICLES AS PEROXIDASE MIMIC IN HYDROGEN PEROXIDE AND GLUCOSE DETECTION

2B.5.1. Peroxidase Activity

Enzymes form an important class of compounds catalyzing many biologically significant reactions. Peroxidases like glutathione peroxidase, horseradish peroxidase etc. constitute one such family of enzymes utilising hydrogen peroxide to oxidise a spectrum of organic compounds [1,2]. This property has lent these enzymes very useful in waste water treatment since toxic organic compounds can be oxidised easily to reduce their adverse effect on the environment [3,4]. Another important property is the production of chromogenic species during redox reactions. In the presence of H_2O_2, peroxidases facilitate one and two electron transfer processes which turn amine substrates like benzidine to blue and yellow in colour [5]. This phenomenon is exploited in detection tools for H_2O_2 and can be extended to glucose detection in tandem with glucose oxidase, employing colorimetry. However, using natural enzymes for these catalytic processes is limited due to their inherent instability and complex separation and synthesis steps. Hence inorganic materials which mimic natural enzymes have been gaining importance recently due to their stability and ease of synthesis. Oxide nanoparticles like Fe_3O_4, CuO, CeO_2 and $BiFeO_3$ nanoparticles [6-10] as well as carbon based materials [11,12] are found to be peroxidase mimics and very recently, positively charged Au nanoparticle colloids are reported to possess intrinsic peroxidase activity [13]. Interestingly, surface charge and nature of the grafted ligand were found to play an important role in the peroxidase mimicking and a two-step assay is employed for glucose detection.

2B.5.2. Strategy used for the detection of H_2O_2 and glucose by porous silica encapsulated Au nanoparticles

The encapsulated Au in porous silica, henceforth mentioned as Au@p-SiO_2, is tested for catalytic activity in H_2O_2 reduction and subsequent glucose sensing. Au NPs act as peroxidase mimics and provide H_2O_2 adsorption sites.

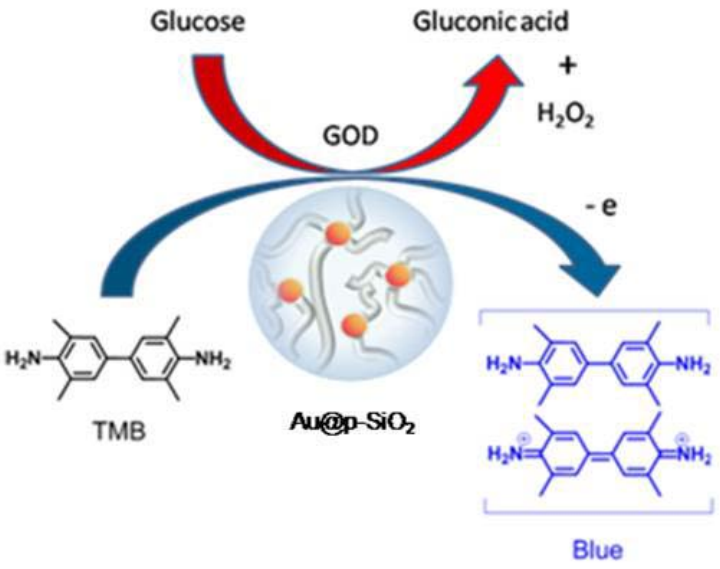

Scheme 2B.2. Detection of glucose by using Au@p-SiO_2 in a one pot reaction.

In the presence of a chromogenic electron donor like 3,3,5,5-Tetramethylbenzidene (TMB), H_2O_2 reduction is proposed to take place aided by partial electron transfers to the Au surface [14]. The consequent change in colour of the oxidation product of TMB by one electron transfer is followed easily by UV-vis spectroscopy. Oxidation of the peroxidase substrate TMB turns the reaction mixture blue and the absorbance at 650 nm corresponding to the oxidised intermediate of TMB can be followed easily by UV-vis spectroscopy. This catalytic ability of Au NPs to act as peroxidase mimic can be put to use for a range of applications in environmental and biological detection tools. One such use is in glucose detection in tandem with enzyme glucose oxidase [Scheme 2B.2]. Glucose oxidase (GOD) is the enzyme responsible for oxidizing glucose to gluconic acid and H_2O_2. Even very small concentrations of glucose can be detected by following the H_2O_2 produced during its oxidation. These consecutive reactions are exploited in designing a detection tool for H_2O_2 and glucose.

2B.5.3. Peroxidase activity by Au@p-SiO_2

To investigate the peroxidase like activity of Au@p-SiO_2, the catalytic oxidation of 3,3,5,5-tetramethylbenzidine (TMB) in the presence of hydrogen peroxide has been performed. Catalytic oxidation of TMB by Au@p-SiO_2 in presence of hydrogen peroxide produces a blue coloured solution. The blue coloured solution

results from the oxidation of TMB solution which shows an absorption maximum at 650 nm in the UV-vis spectrum. To confirm the oxidation of TMB occurs because of Au@p-SiO_2, a series of control experiments are carried out with silica material as catalyst and without catalyst. None of the experiments show colour change of TMB, only it happens in presence of Au@p-SiO_2 [Fig. 2B.8]. From these experiments, it has been confirmed that Au@p-SiO_2 possesses peroxidase mimicking activity.

In a typical experiment 294 10 µL of 9.41 X 10^{-4} M TMB, 35 µL Au catalyst (stock solution 1mg/mL, for c), no catalyst (for b), 1 mg silica (for a), 350 µL H_2O_2 of 10 mM, 16 µL of 160 mM phosphate buffer of pH 4 were added and incubated in a 40 $^{\circ}$C water bath for 10 min. Final pH of the solution was 4.5.

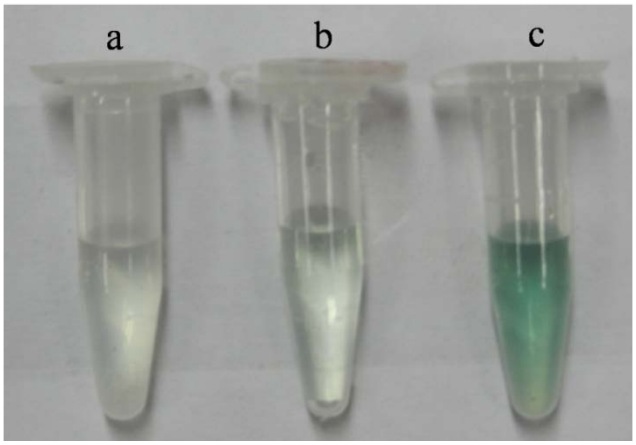

Fig. 2B.8. Images for TMB oxidation using Au@p-SiO_2 and silica; a) silica, b) without catalyst and c) Au@p-SiO_2.

2B.5.4. H_2O_2 detection using Au@p-SiO_2 mimicking peroxidase activity

The activity of the catalyst was first tested with appropriate concentrations of H_2O_2 and TMB to observe the blue colour. Calibration studies were carried out with various concentrations of H_2O_2 to estimate the potential of using this material in H_2O_2 detection [Fig. 2B.9]. It was found that concentrations as low as 10 µM could be detected which is comparable to other Au based systems reported [15]. To show the peroxidase like activity of the Au@p-SiO_2, catalytic oxidation of peroxidase substrate, 3,3,5,5-tetramethylbenzidine (TMB) was done in presence of H_2O_2.

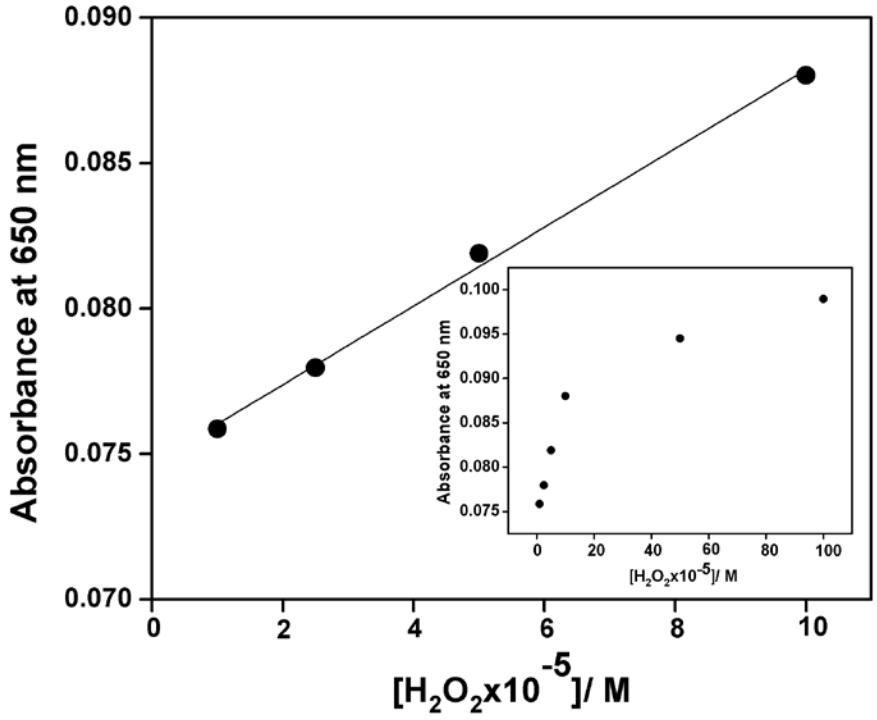

Fig. 2B.9. Linear calibration plot of the absorbance at 650 nm against concentration of H_2O_2. The inset shows the dependence of the absorbance at 650 nm on the concentration of H_2O_2 in the range 10 μM to 10 mM.

A stock solution was prepared by dispersing 1 mg of the catalyst 1 mL double distilled water. In a typical experiment 294 μL of 9.41×10^{-4} M TMB, 35 μL of stock catalyst solution, 350 μL with different concentrations of H_2O_2 and 16 μL of 160 mM phosphate buffer of pH 7.0 were added and incubated in a 40 °C water bath for 10 min. Then the resulting solution was used for absorbance measurement at 650 nm (one of the absorption peaks of oxidation product of TMB) using Perkin-Elmer –λ35 UV-vis spectrophotometer.

2B.5.5. Glucose detection using Au@p-SiO_2 in a one-pot reaction

As mentioned earlier, H_2O_2 detection can be extended to design glucose detection tools. Au@p-SiO_2 could be used in a simple one-pot reaction to detect glucose. The colorimetric response of the assays was observed after incubation of the catalyst, TMB, GOD and different concentrations of glucose at 55 °C and pH 2.5 for 15 min. GOD is reported to be stable at these conditions [16].

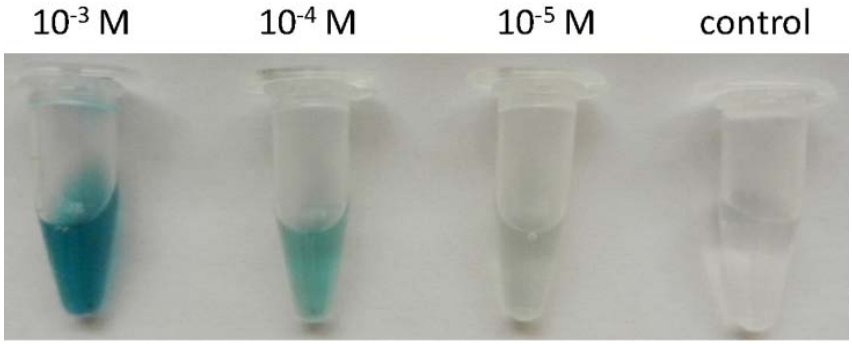

Fig. 2B.10. Typical images of detection of glucose at different concentration: a) 10^{-3} M, b) 10^{-4} M, c) 10^{-5} M and d) 10^{-3} M mannose.

The response with variations in glucose concentrations in comparison to control solutions without catalysts was even visible by naked eye. Also, the assay was found to be very specific to glucose and control experiments with another sugar, mannose did not produce any blue colour [Fig. 2B.10].

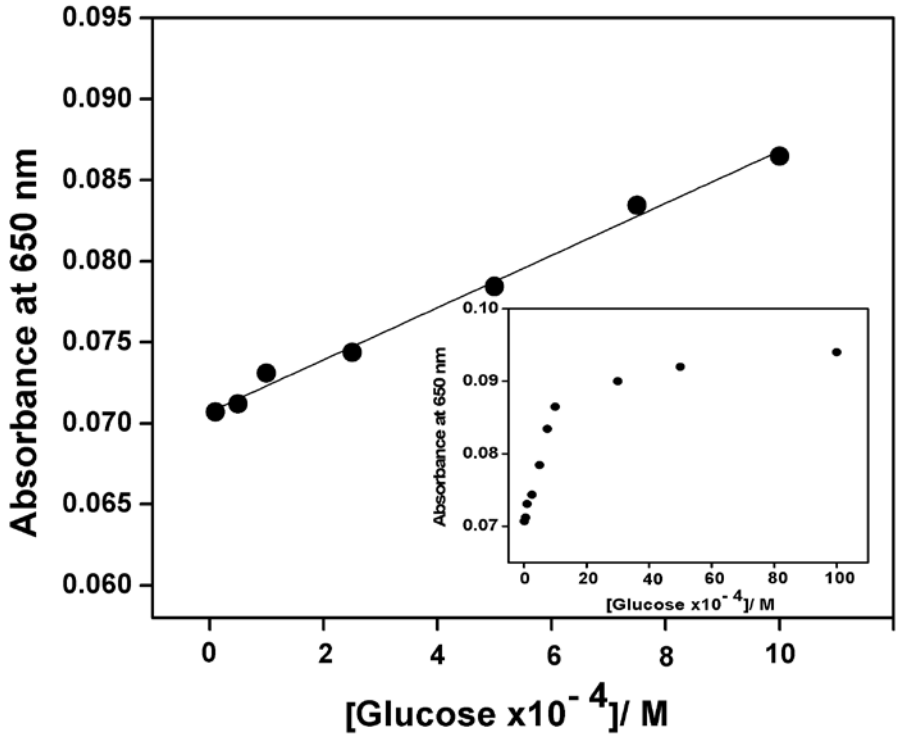

Fig. 2B.11. Linear calibration plot between the absorbance at 650 nm and concentration of glucose. The inset shows the dependence of the absorbance at 650 nm on the concentration of glucose in the range 20 µM to 2.5 mM.

In the experiment 60 µL of 5.5 mg/mL Glucose Oxidase and 600 µL glucose with different concentrations, 270 µL TMB of 20 mM TMB in 0.1 M HCl, 30 µL of stock catalyst solution (1 mg/mL) and 40 µL 500 mM phosphate buffer 4.0 were incubated at 55 °C water bath for 15 minutes.

The calibration was carried out by following the 650 nm absorbance peak in the UV-vis spectra as in the case of H_2O_2 calibration. The result shows a linear increase in the absorbance in the range 20 µM to 0.5 mM and reaches a saturation point after 1 mM [Fig. 2B.11]. The linear response region shows that the lower detection limit for glucose for this material is 20 µM. which is comparable to other nanomaterial based catalysts [6-13]. It is noteworthy here that Au@p-SiO_2 has high activity in a one-pot reaction as compared to a complicated two-step method reported for other Au NP based materials. The material has shown saturation in activity at physiological condition of 2.5 mM of glucose under the concentration levels of TMB used in the current study. However, these studies show the potential of using this catalyst in glucose detection in biological systems like blood with appropriate changes in concentration levels of TMB.

2B.5.6. Kinetic study of TMB oxidation

We have proceeded with kinetic studies to understand enzyme mimetic behaviour of the system by following the peak at 650 nm in UV-vis spectrum which indicates one of the oxidation products of TMB. Initial rates of TMB oxidation are calculated from the linear absorbance versus time plots using the extinction coefficients of 39000 $M^{-1}cm^{-1}$ which stands for oxidation product of TMB [17] at 650 nm when the conversion of the TMB does not exceed 10-20 %. Concentrations of H_2O_2 and TMB were varied and the effect followed as above [Fig. 2B12 a & b]. The range of concentration of TMB was fixed between 1-8 mM to obtain better calibration data. To solubilise TMB in these concentrations, highly acidic solutions were used and the kinetic studies were carried out at a pH of 2.5 and at room temperature using 0.25 mM of Au (1 mg/mL of 5 wt% Au@p-SiO_2). The experimental points in the above studies are fitted perfectly to Michaelis-Menten equation defining enzyme kinetics:

$$v = V_{max} \times [S]/(K_m + [S])$$

where v stands for initial rate or initial velocity, V_{max} is the maximal velocity, [S] is the concentration of the substrate and K_m is the Michaelis constant.

For both [H_2O_2] and [TMB] variations, the rates are found to follow the above equation to a very good fit and the kinetic parameters calculated from the curve are given in Table 2B.1. The Michaelis-Menten constant K_m indicates enzyme affinity towards substrate while V_{max} stands for maximal initial velocity. The K_m values with respect to H_2O_2 as substrate is much lower than those reported for HRP as well as other nanoparticles systems [6-13].

Table 2B.1. Kinetic parameters for TMB Oxidation by peroxidise mimic Au@p-SiO_2

Substrate	V_{max}/ Ms^{-1}	K_m/ mM
TMB	4.21×10^{-9}	8.70
H_2O_2	5.24×10^{-9}	0.156

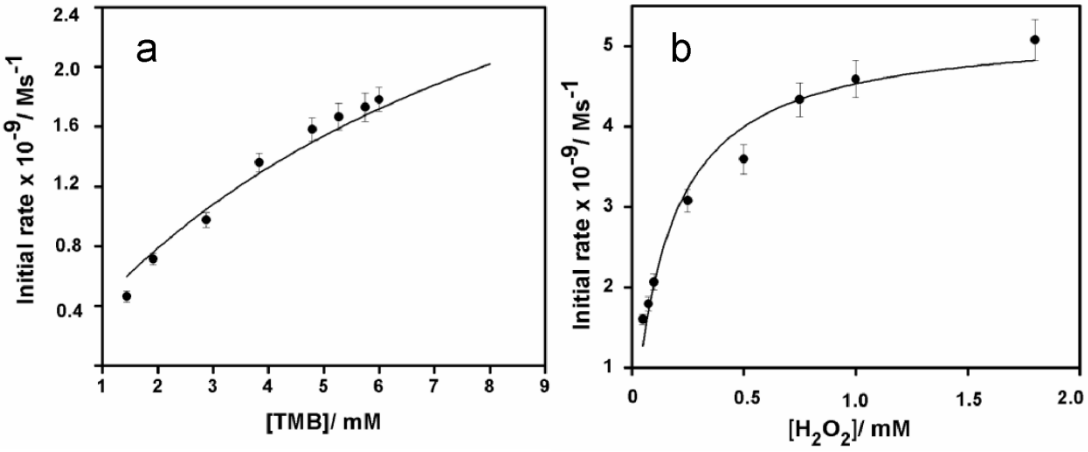

Fig. 2B.12. Steady-state kinetic assays of Au@p-SiO_2. a, b) The initial rate of the reaction was measured using 30 µg mL^{-1} Au@p-SiO_2 in a reaction volume of 1 mL (pH 2.5) at 25 °C. Error bars represent the standard error derived from three repeated measurements. a) The concentration of H_2O_2 was 5.0×10^{-5} M and TMB concentration was varied. b) The concentration of TMB was 5.75×10^{-3} M and H_2O_2 concentration was varied.

Table 2B.2 Comparison of the Michaelis constant (K_m) between Au@p-SiO_2, other nanoparticles and HRP

Catalyst	Substrate	K_m (mM)
Au@p-SiO_2	TMB	8.70
	H_2O_2	0.156
HRP	TMB	0.434
	H_2O_2	3.70
Fe_3O_4 MNPs	TMB	0.098
	H_2O_2	154
CuO NPs	TMB	0.013
	H_2O_2	85.6

A comparison of this kinetic value is given in Table 2B.2 and this indicates a higher affinity of the catalyst to H_2O_2 which suggests that detection capability is higher for much lower concentrations of H_2O_2 when compared to other reported systems. However, with respect to TMB, the trend is reversed. The results also prove that the catalytic activity of Au NPs in H_2O_2 reduction is enzyme mimicking with respect to both the substrates, H_2O_2 and TMB. So, a mechanism of two electron transfer similar to peroxidise enzymes can be envisaged for the Au@p-SiO_2 catalysts [18].

2B.5.7. Dependence of peroxidase like activity of Au@p-SiO_2 on pH and temperature

Au NPs reported hitherto have shown optimal activity in the acidic range and we have also tested the activity of our system in the pH range 2-6. Further pH increase is not amenable due to high concentrations of TMB used. The material has shown highest activity at a pH of 4.5 and the activity was found to increase exponentially with temperature [Fig. 2B.13]**.**

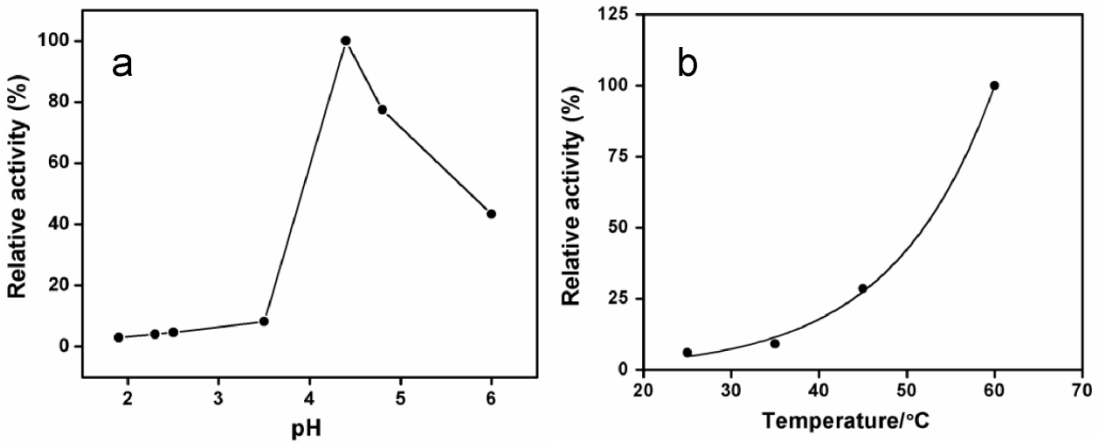

Fig. 2B.13. a) Dependence of peroxidase like activity of Au@p-SiO_2 on pH and b) on temperature. The maximum point was set as 100% in terms of intial rate.

2B.5.8. Stability and activity of Au@p-SiO_2 after treatment at various temperatures and pH values

Natural enzymes are known to be stable only in a narrow range of pH and temperature which restricts their utilization in applications involving harsh conditions. Rate of thermal denaturation of HRP is very high above 70 °C [19] and its protein structure is reported to be unstable below pH 4.5 [20]. Hence any alternative new material, stable at a wide range of temperatures and pH can replace these natural enzymes. Recently inorganic nanomaterials are proposed to be good alternatives and such nanomaterials like Fe_3O_4, CuO and positively charged Au NPs are found to be stable at a reasonable range of these conditions. Peroxidase activity was tested for Au@p-SiO_2 by incubating the catalyst at pH values from 2.5 to 10 as well as temperatures till 90 °C and further following the H_2O_2 reduction using TMB at 30 °C. Interestingly, this material was found to be stable and active even after treatments at pH 10 [Fig.2B.14] and 90 °C [Fig. 2B.15]

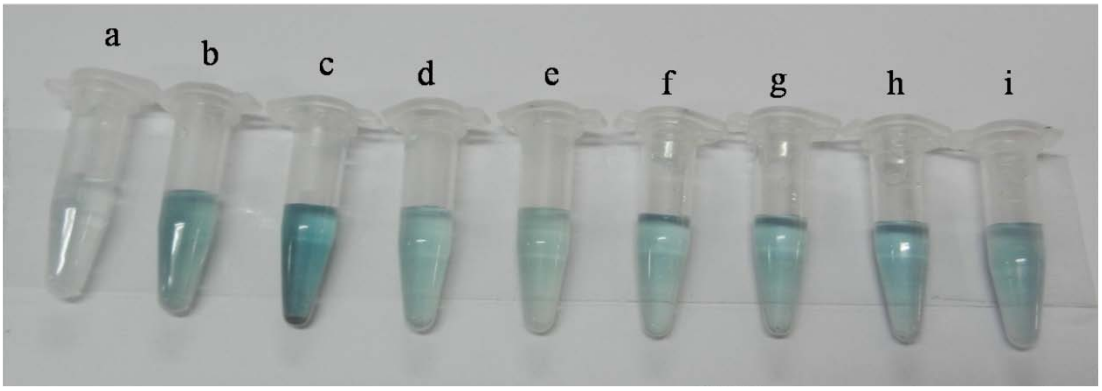

Fig. 2B.14. Images for TMB oxidation after incubation of the Au@p-SiO_2 at a range of pH.

a=without catalyst, 1 mg of catalyst was incubated in 1 mL of (50 mM) phosphate buffer solution of different pH (b=2.5, c=4, d=5, e=6, f=7, g=8, h=9, i=10) for 2 h. Then the catalyst was collected by centrifugation and washed with water. Stock solutions of catalyst were prepared by dispersing the incubated catalysts in 1 mL of water. In a typical experiment 50 µL of 20 mM TMB in 0.1 N HCl, 25 µL of stock catalyst solution, 50 µL of 2 mM H_2O_2 and 200 µL 160 mM phosphate buffer of pH 4 were added and incubated in 30 ^{0}C water bath for 20 min.

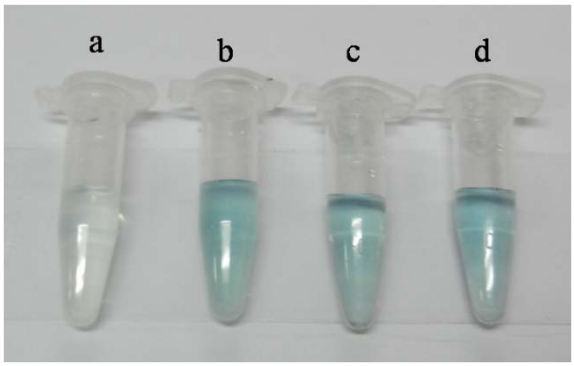

Fig. 2B.15. Images for TMB oxidation after incubation of the Au@p-SiO_2 at a range of temperature.

a=without catalyst, 1 mg of catalyst was incubated in 1 mL of water at a range of temperature (b=70 ^{0}C, C=80 ^{0}C, d=90 ^{0}C). These incubated catalysts were used for doing TMB oxidation. In a typical experiment 50 µL of 20 mM TMB in 0.1 N HCl,

25 µL of stock catalyst solution, 50 µL of 2 mM H_2O_2 and 200 µL 160 mM phosphate buffer of pH 4 were added and incubated in 30 ^{0}C water bath for 20 min.

2B.5.9. Recyclability study of the Au@p-SiO_2 catalyst

Recyclability of this catalyst was tested for three colorimetric detection cycles with repeated centrifugation and washing [Fig. 2B.16]. The activity is found to be intact which indicates Au@p-SiO_2 catalyst structure is stable under reaction condition.

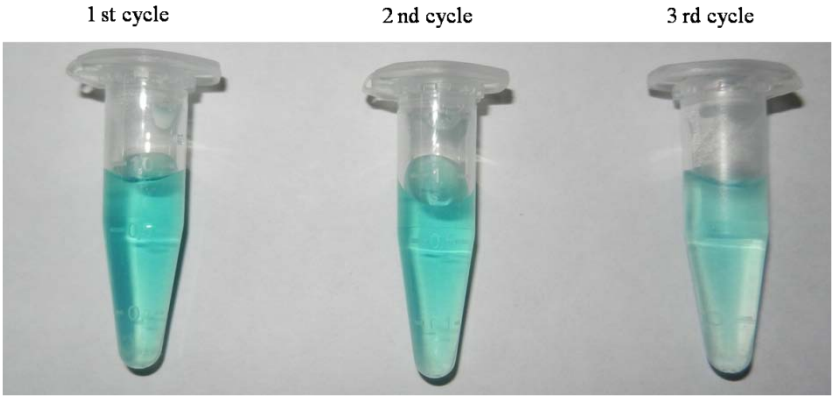

Fig. 2B.16. Images for TMB oxidation by fresh and recycled catalysts.

In a typical experiment 200 µL 20 mM TMB in 0.1 M HCL, 300 µL 0.1 mM H_2O_2, 50 µL 500 mM phosphate buffer at pH 4.0 and 0.3 mg catalyst dispersing in 450 µL of double-distilled water were incubated at 40 °C in a water bath for 20 min. Resulting solution became colourless to blue. Two consecutive reactions were done by using the same catalyst after collecting by centrifugation and giving washing by water.

2B.6. SUMMARY

In summary, a stable and novel catalyst based on Au nanoparticles encapsulated in porous silica sphere (Au@p-SiO_2) has been developed and used for H_2O_2 and glucose detection. Thiolate protected ultra-small Au clusters are used as precursors for the preparation of porous silica encapsulated Au nanoparticle catalysts. The catalyst is found to be a peroxidase mimic nanomaterial following Michaelis-Menten kinetics for enzyme catalyzed reactions. The activity is found to be the highest at a pH of 4.5 and increase exponentially with temperature. Incubation stability is also

found to be reasonably high in the range of pH 2.5-10 and temperature till 90 °C. Kinetic parameters reveal that the affinity of the catalyst to H_2O_2 is very high compared to other reported systems leading to a minimal concentration for maximum activity. So this Au@p-SiO_2 is a good alternative of natural peroxidase enzyme based on its activity and stability. Combined effect of porosity inside the silica layer and control of particle size of active Au nanoparticles has rendered this material ideal for catalysis. Also, the silica layer protecting the active Au particles is advantageous for the stability of the catalyst.

2B.7. REFERENCES

1. M. Hamid and K. ur. Rehman, *Food Chem.*, 2009, **115**, 1177.
2. L. Flohe, in Free Radicals in Biology, ed. W. A. Pryor, Academic Press, New York, 1982, vol. **5**, pp. 223–253.
3. Z. Tong, Z. Qingxiang, H. Hui, L. Qin and Z. Yi, *Chemosphere*, 1997, **34**, 893.
4. L. Al-Kassim and K. E. Taylor, *J. Chem. Technol. Biotechnol.*, 1994, **61**, 179.
5. P. D. Josephy, T. Elings and R. P. Mason, *J. Biol. Chem.*, 1982, **257,** 3669.
6. L. Zao, J. Zhuang, L. Nie, J. Zhang, Y. Zhang, N. Gu, T. Wang, J. Feng, D. Yang, S. Perrett and X. Yan, *Nat. Nanotechnol*., 2007, **2**, 577.
7. W. Chen, J. Chen, A.-L. Liu, L.-M. Wang, G.-W. Li and X.-H. Lin, *ChemCatChem*, 2011, **3**, 1151.
8. M. Ornatska, E. Sharpe, D. Andreescu and S. Andreescu, *Anal. Chem.*, 2011, **83**, 4273.
9. W. Luo, Y.-S. Li, J. Yuan, L. Zhu, Z. Liu, H. Tang and S. Liu, *Talanta*, 2010, **81**, 901
10. A. Asati, S. Santra, C. Charalambos, S. Nath and J. M. Perez, *Angew. Chem., Int. Ed.*, 2009, **48**, 2308.
11. Y. Song, K. Qu, C. Zhao, J. Ren and X. Qu, *Adv. Mater.*, 2010, **22**, 2206.
12. W. Shi, Q. Wang, Y. Long, Z. Cheng, S. Chen, H. Zheng and Y. Huang, *Chem. Commun*., 2011, **47**, 6695.
13. Y. Jv, B. Li and R. Cao, *Chem. Commun*., 2010, **46**, 8017.
14. Z. Zhang, A. Berg, H. Levanon, R. W. Fessenden and D. Meisel, *J. Am. Chem. Soc.*, 2003, **125**, 7959.

15. Y. Jv, B. Li and R. Cao, *Chem. Commun.* 2010, **46**, 8017.
16. M. H. Rashid and K. S. Siddiqui, *Process Biochem.*, 1998, **33**, 109.
17. G. P. Bienert, A. L. B. Møller, K. A. Kristiansen, A. Schulz, I. M. Møller, J.K. Schjoerring andT. P. Jahn, *J. Biol. Chem.*, 2007, **282**, 1183.
18. N. C. Veitch, *Phytochemistry*, 2004, **65**, 249.
19. J. H. Bovaird, T. T. Ngo and H. M. Lenhoff, *Clin. Chem.*, 1982, **28**, 2423.
20. Z. Temocin and M. Yigitoglu, *Bioprocess Biosyst. Eng.*, 2009, **32**, 467.

CHAPTER 3

THIOL STABILIZED Pd ULTRA-SMALL CLUSTERS AND NANOPARTICLES AND THEIR ENCAPSULATION IN POROUS SILICA APPLIED IN DYE DEGRADATION AND HYDROGENATION REACTION

3.1. INTRODUCTION

Supported Pd catalysts show excellent catalytic activity for a range of reactions from hydrogenation to C-C bond coupling in fine chemical synthesis as well as high temperature reforming processes [1-3] and any enhancement in the thermal stability and resistance to deactivation of such catalysts will make a step change in their utilization. Even though encapsulated Pd systems have been reported earlier, they are characterized by a wide range of particle size distribution and lack of uniform porosity in the silica matrix [4-8]. In this scenario, simple one step method of synthesis and thermal stability of materials are highly desirable.

In this context, we have further utilized our *N*,*N*,*N*-Tripropyl(11-mercaptoundecyl)ammonium chloride ligand to prepare highly stable and water dispersible Pd nanoparticles ranging from nanoclutsers to nanoparticles. Fine tuning of particle size has been achieved by systematically varying the thiol concentration in the reaction mixture. Various characterization techniques are used to ascertain the formation of Pd thiolate nanoparticles and evolution of the nanoparticle structure is followed. As expected, size of the particle decreases with increase in thiol concentration during synthesis. Also with increase in thiol concentration, the particle characteristics move towards Pd-thiolate complexes whereas with decrease in thiol concentration the particle characteristics incline more towards metallic nature. Methyl orange dye degradation study is performed by using Pd nanoparticles of varying sizes to understand the metal-ligand interaction.

A strategy similar to that of Au nanoparticles described in Chapter 2 (section 2B.1) has been employed for the synthesis of porous silica encapsulated Pd nanoparticles. Pd nanoclusters are used as precursors for the preparation of porous silica encapsulated Pd nanoparticles. Catalytic activity of this porous silica encapsulated Pd nanoparticles (Pd@p-SiO_2) has been tested for hydrogenation reaction of *trans*-stilbene. The catalyst is also found to be highly sinter-resistant with particle size controlled to ~ 3 nm even at high temperatures in the range of 750 °C.

3.2. SYNTHESIS

3.2.1. Synthesis of N,N,N-Tripropyl(11-mercaptoundecyl)ammonium chloride stabilized Pd ultra-small clusters and nanoparticles

The strategy employed for synthesizing water dispersible Pd nanoparticles (Pd NPs) involves surface protection by a bifunctional thiol, *N,N,N*-Tripropyl(11-mercaptoundecyl)ammonium chloride, similar to that of Au nanoparticles. The thiolate group binds to the metal and the ammonium head group decorating the surface of the particles helps in enhancing hydrophilicity. From extensive synthetic studies on AuNP systems, it is understood that reduction of precursor salts to some extent and metal-ligand complex formation happen during the thiol addition step and metallic nanoparticles formation happen as a consequence of addition of strong reducing agents like $NaBH_4$ [9]. However, in case of Pd, the nanoparticle formation is suggested to go through more complicated steps including Pd thiolate complexes. Scheme 3.1 describes the formation of Pd (II) thiolate complex and metallic Pd nanoparticle. At higher concentrations of thiols, these Pd-thiolate complexes are found to be stable towards reduction even by $NaBH_4$ [10, 11].

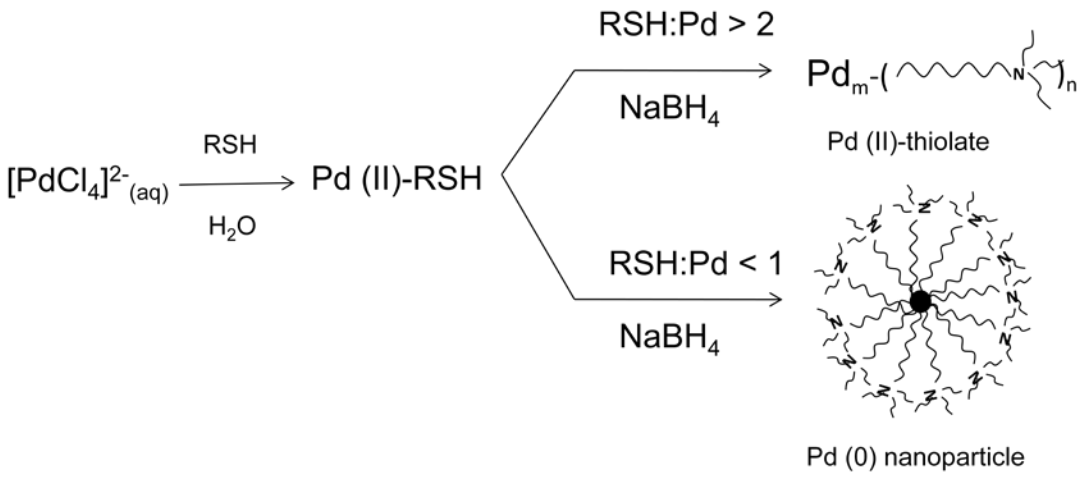

Scheme 3.1. Formation of Pd-thiolate complexes and their reduction by $NaBH_4$ to Pd(0)NPs depending on thiol concentration in the reaction mixture.

With this in mind, we followed $NaBH_4$ reduction of K_2PdCl_4 salt precursor by varying only the concentration of thiol so that thiol:Pd ratio is progressively changed. For constant molar concentrations of Pd precursor and reducing agent ie. $NaBH_4$, thiol concentration was varied as 0.4, 0. 2, 0.1, 0.05 and 0.01 mmol, corresponding to thiol:Pd ratios of 4.8, 2.4, 1.2, 0.6 and 0.12 respectively. An aqueous stock solution of K_2PdCl_4 in water (2.8 mL, 30 mM) was mixed with water (30 mL). Appropriate amount of stock solution of thiol in methanol (0.4 M) was added to this solution.

Table 3.1. Pd and thiol concentrations in the initial reaction mixtures and the results of visual comparison of the obtained samples

Sr No	Name	Thiol added (mmol)	Thiol : Pd molar ratio	Colour of the solution		
				Before adding thiol	After adding thiol	After adding $NaBH_4$
1	PdNP1	0.4	4.76	yellow	Dark orange	Brownish Yellow
2	PdNP2	0.2	2.38		Dark orange	Brown
3	PdNP3	0.1	1.19		Orange	Dark brown
4	PdNP4	0.05	0.595		Orange	Blackish brown
5	PdNP5	0.01	0.119		Orange	Black
6	PdS*R	0.4	4.76		Dark Orange	

*Without $NaBH_4$

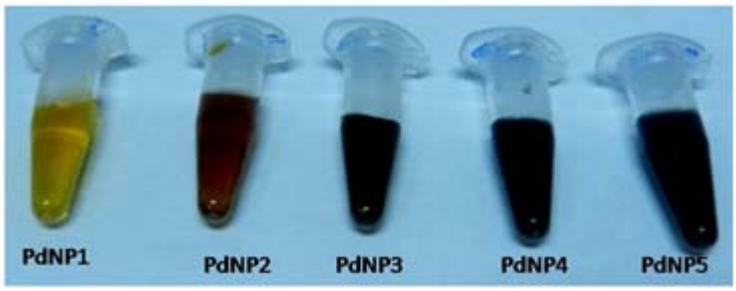

Fig. 3.1. Images of thiolate protected Palladium Nanoparticles.

The mixture was stirred for 2 h. $NaBH_4$ solution (450µL, 1.58 M) in methanol was added and stirring was continued for 45 min. All the steps were performed at RT.

Aqueous solution of Pd nanoparticles were purified by dialysis through a cellulose membrane (Aldrich, pore size 12 kDa). When the thiol ligand was added to K_2PdCl_4, the solution colour changed from yellow to orange and on addition of $NaBH_4$, the colour of the solution again changed to a range from orange yellow to black depending on the thiol concentration. The quantity of the final solution was maintained to 35 mL by adjusting with water. Details of these observations are given in Table 3.1 Pd nanoparticles corresponding to thiol:Pd ratio of 4.8, 2.4, 1.2, 0.6 and 0.12 are mentioned as PdNP1, PdNP2, PdNP3, PdNP4 and PdNP5. Images of PdNPs are given in Fig. 3.1.

3.2.2. Synthesis of porous silica encapsulated Pd nanoparticles (Pd@p-SiO_2)

3.2.2.1. Syntheis of silica encapsulated Pd nanoclusters (Pd@SiO_2)

The Pd nanocluster (PdNP1) solution (10 mL) was mixed with a 1:4 water/ethanol mixture (200 mL). 0.1 M NaOH solution (0.9 mL) and tetraethyl orthosilicate (300 mL, Aldrich, 98%) were added to this mixture and stirred at RT for 3 d. Silica-encapsulated palladium nanoclusters were separated from the reaction medium by centrifugation at 14000 rpm and redispersion in water several times.

3.2.2.2. Syntheis of porous silica encapsulated Pd nanoparticles (Pd@p-SiO_2)

The above as-synthesized material was calcined to remove the thiol ligand by heating with a rate of 0.8 °C/min from room temperature to 350 °C. First the temperature was increased up to 350 °C under nitrogen and then it was kept constant for 12 h under air for removing the organic ligand.

3.2.3. Synthesis of Pd@p-SiO_2 calcined at high temperature

The above calcined material was again heated separately under air at temperature 550 °C and 750 °C separately to study the thermal stability of the material.

3.2.4. Synthesis of SBA-15 supported Pd nanoparticle (Pd@SBA-15)

3.2.4.1. Synthesis of SBA-15

Silica SBA-15 was prepared according to the method reported in literature [12]. Pluronic P123 (2.04 g) was dissolved in 15 g of water and 60 g of 2 mM HCl solution with stirring at RT for 30 minute. Tetraethyl orthosilicate (4.4 g, Aldrich, 98 %) was added to the P123 solution with stirring at 40 °C for 24 h. The mixture was kept for aging at 100 °C for 48 h. The white powder was recovered through filtration, washed with water and ethanol thoroughly, and dried in air. The as-synthesized material was calcined to remove the organic P123 polymer by heating with a rate 0.8 °C/min from room temperature to 550 °C. First the temperature was increased up to 550 °C under nitrogen and then it was kept constant for 12 h under air for removing the organic polymer.

3.2.4.2. Synthesis of Pd@SBA-15

The above calcined SBA-15 (5 mg) was mixed with the 0.5 mL of Pd nanoclusters solution (PdNP1) thoroughly under sonication for 15 minute. The mixture was dried at 100 °C for 24 h. The material was calcined to remove the thiol ligand from the Pd clusters by heating with a rate 0.8 °C/min from room temperature to 550 °C. First the temperature was increased up to 550 °C under nitrogen and then it was kept constant for 12 h under air for removing the organic ligand. Finally SBA-15 supported Pd nanoparticle was obtained.

3.3. INSTRUMENTS FOR CHARACTERIZATION

Many physico-chemical techniques like high resolution transmission electron microscopy (HRTEM), scanning electron microscopy (SEM), UV-Vis spectroscopy, N_2-adsorption, X-ray photoelectron spectroscopy (XPS), FT-IR spectroscopy, powder X-ray diffraction, thermogravimetric analysis (TGA), CHNS analysis and inductively coupled plasma spectroscopy (ICP) were used for the characterization of Pd nanoparticles and silica encapsulated nanoparticles. Instrumental details of HRTEM, UV-Vis spectroscopy, FT-IR, ICP and N_2-adsorption are already been described in Chapter 2 (section 2A.3 and section 2B.3).

3.3.1. Scanning Electron Microscopy

The scanning electron micrographs of the samples were obtained in dual beam scanning electron microscope (FEI company, model Quanta 200 3D) operating at 30 kV with energy dispersive X-ray spectroscopy (EDS) and a resolution limit of 3.5 nm. Samples were mounted on stubs and kept inside the SEM chamber for analysis.

3.3.2. X-ray Photoelectron Spectroscopy

XPS measurements were conducted on a VG Scienta R3000 Analyzer at a pressure of 10^{-9} mbar. The sample was prepared by evaporating a drop of solution on a silicon wafer in air.

3.3.3. Thermogravimetric Analysis

Thermogravimetric analysis was carried out on a Mettler Toledo thermogravimetric analyzer. Accurately weighed 5–6 mg of the sample was heated from room temperature to 400 °C under air (50 mL min^{-1}) with a ramping temperature rate of 5 °C min^{-1}.

3.3.4. CHNS analysis

CHNS analysis was performed by using FLASH EA 1112 series CHNS(O) analyzer. Nanoparticle solutions are evaporated completely to remove water and and dried samples were used for analysis.

3.3.5. Powder X-ray Diffraction

All the samples were characterized using a PANalytical X'pert Pro dual goniometer diffractometer. An X'celerator solid state detector was employed in wide angle experiments. The radiation used was Cu Kα (1.5418Å) with a Ni filter and the data collection was carried out by mounting sample on glass plate.

3.4. CHARACTERIZATION

Pd ultra-small clusters, nanoparticles and silica encapsulated nanoparticles are characterized by HRTEM, UV-vis spectroscopy, FT-IR, XRD, XPS, TGA, N_2-adsorption study and SEM-EDAX analysis.

3.4.1. Characterization of thiol ligand protected Pd ultra-small clusters and nanoparticles

3.4.1.1. High Resolution Transmission Electron Microscopy

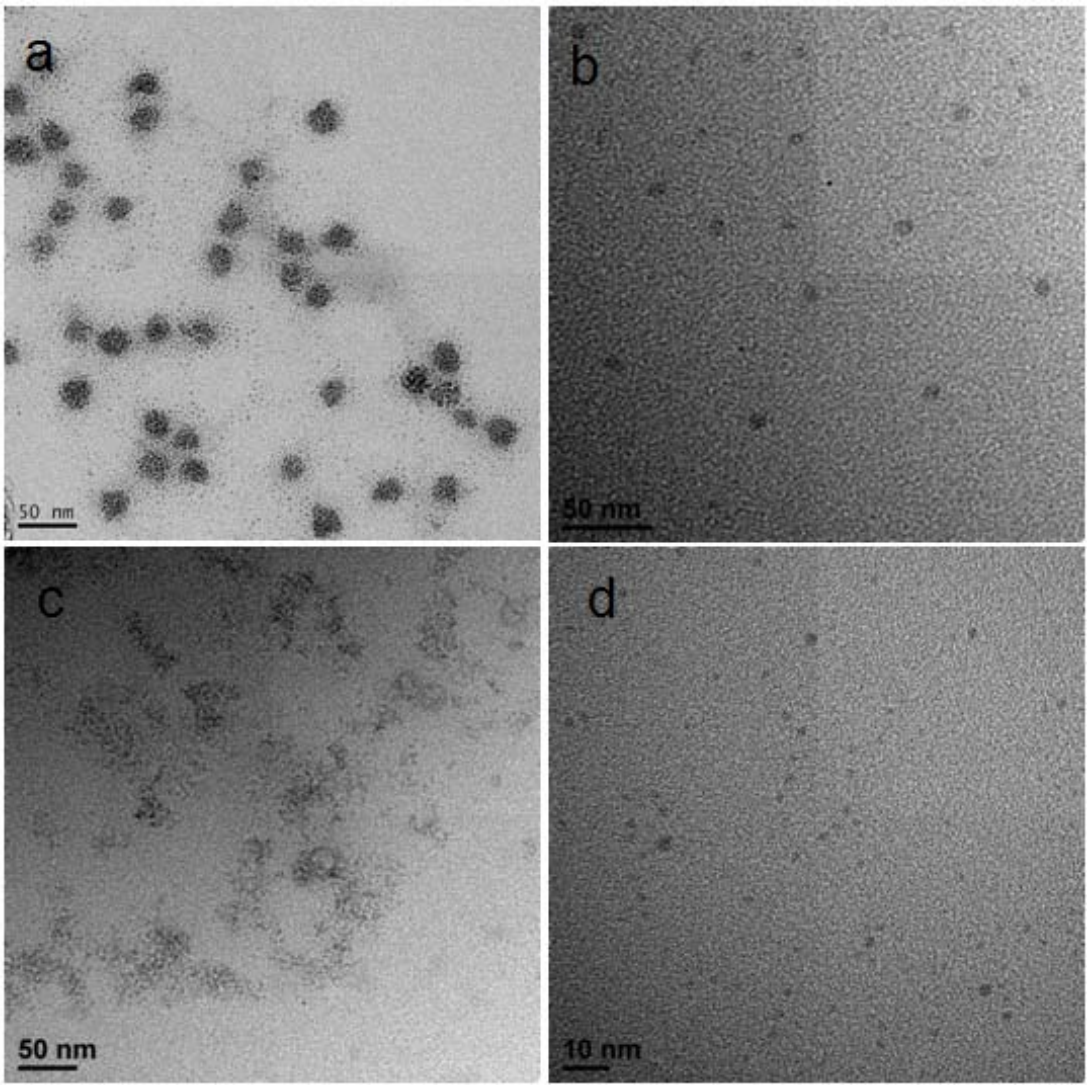

Fig. 3.2. HRTEM images of a) PdNP1, b) PdNP2, c) PdNP3 and d) PdNP4

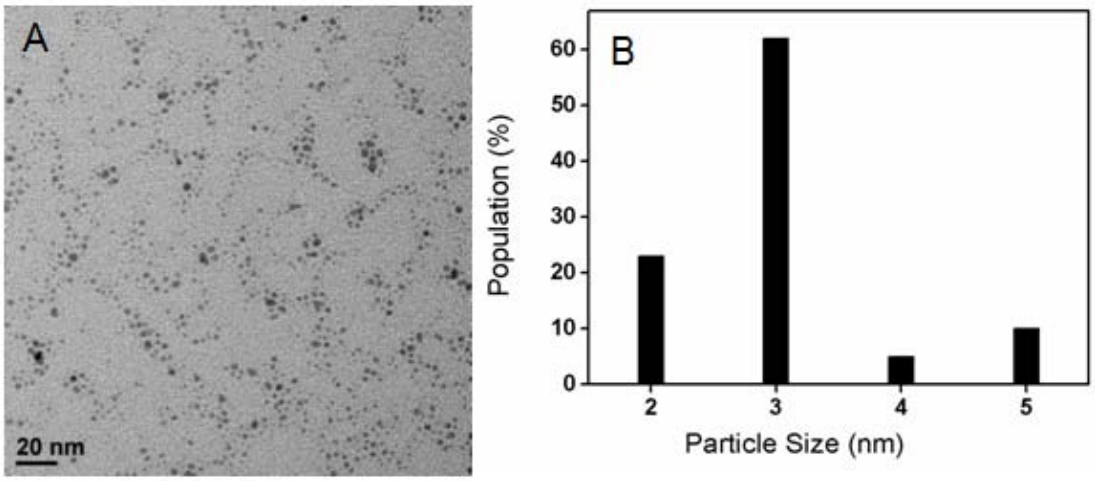

Fig. 3.3. A) HRTEM image of PdNP5 and B) particle size distribution of PdNP5

HRTEM analysis has revealed the shape and size of Pd nanoclusters and nanoparticles. Unfortunately, the nanoclusters were highly unstable under electron beam and agglomerated during imaging; hence HRTEM could not give any useful information for PdNP1-4 [Fig. 3.2].

However, some of the materials have shown spongy agglomerations with individual particles in the range of 2 nm. In case of PdNP5 with Pd:thiol ratio 1:0.119, HRTEM image shows discrete particles as displayed in Fig. 3.3A. The histogram [Fig. 3.3B] is made by analyzing 100 particles from the images. From this analysis, it is evident that the particles obtained are spherical in shape with diameter range from 2 nm to 4 nm. Also some particles of size ~ 5 nm are also present.

3.4.1.2. UV-Vis Spectroscopy

Further, UV-vis spectroscopic studies were carried out for all the samples in comparison with PdSR [Fig. 3.4]. It can be seen that PdNP1 has same spectral characteristics as PdSR complex with a sharp peak at 270 nm attributed to ligand centered transitions and two broad features at 340 and 410 nm which can be attributed to metal centered transition and ligand to metal charge transfer. As the thiol concentration reduces, these peaks also start disappearing and in PdNP3, they completely disappear and the spectra take up the shape expected for ultra-small

particles with an exponential decay in case of PdNP3 and PdNP4. In case of PdNP5, the spectrum does not show any features as expected for bigger Pd nanoparticles.

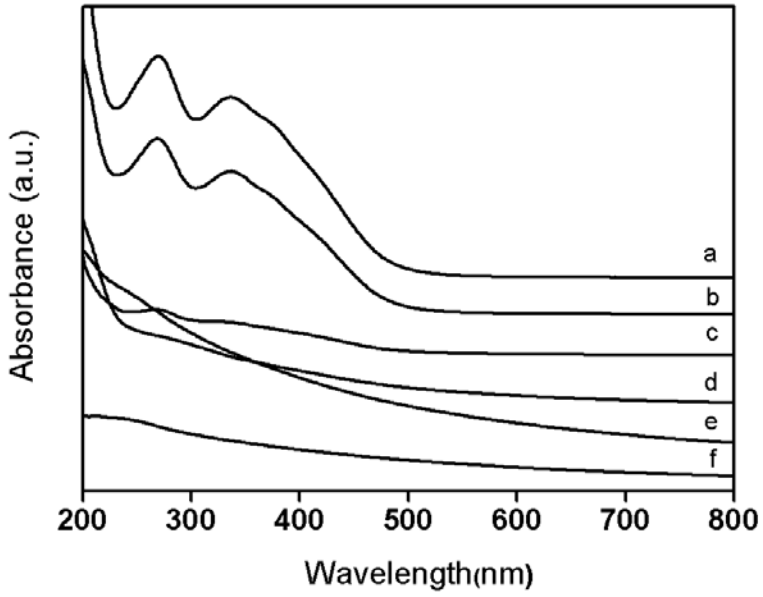

Fig. 3.4. UV-vis spectra of palladium nanoparticles with different thiol to palladium ratio; a) PdSR, b) PdNP1, c) PdNP2, d) PdNP3, e) PdNP4, f) PdNP5.

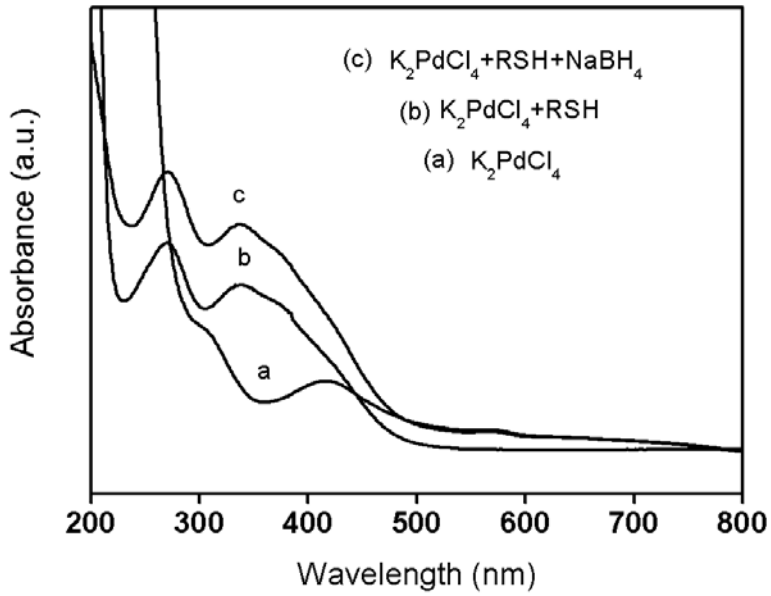

Fig. 3.5. UV-vis spectra of a) K_2PdCl_4 solution, b) K_2PdCl_4 and RSH (thiol ligand) mixture and c) and after the addition of $NaBH_4$ into the mixture.

This indicates the evolution of Pd NPs and departure of the palladium nanoparticles from complex characteristics to metallic characteristics with the reduction in the thiol concentration during synthesis.

From these observations, it is clear that presence of excess thiol in the reaction mixture contributes to the stability of the Pd-thiolate complexes. So it is possible that stable PdSR complexes formed in the solution. However, as the thiol concentration becomes less than 2x (two fold) which is necessary for the formation of a simple ion pair, $[PdCl_4]^{2-}$ precursors are also present in the reaction mixture which on addition of $NaBH_4$, form nuclei leading to further enlargement of the NPs.

Formation of PdNP1 clusters were investigated through UV-vis spectroscopy. K_2PdCl_4 spectrum in Fig. 3.5 matches reported profiles for square planar $[PdCl_2(H_2O)_2]$ complexes with partly exchanged aqua ligands showing the peaks at 420 nm and 310 nm due to d-d and ligand-to-metal charge-transfer transitions respectively [13]. On addition of the thiol ligand, an intense sharp peak at 270 nm and a broad peak at 342 nm appear which can be clearly assigned to ligand-centered and metal-centered transition transition respectively based on earlier reports [14]. An additional small shoulder at 420 nm may be attributed to contribution from ligand to metal charge transfer [11]. After adding the reducing agent, the absorbance spectra peripherally remain the same even though colour change from orange yellow to brown yellow indicates formation of clusters. In light of HRTEM and UV-vis data, the PdNP1 system we have synthesised can be considered as more of Pd-thiolate ultra-small clusters closer in characteristics to multicentered ionic complexes.

3.4.1.3. FT-IR Spectroscopy

FTIR spectroscopy was used to verify the presence of thiol as well as thiol binding following the disappearance of S-H band, supported by earlier observation as in case of Au nanoparticles. All the samples have similar IR spectra with many characteristic peaks of the ligand indicating presence of ligand in the Pd nanoparticles [Fig. 3.6]. It is clear that the peak at 2636 cm^{-1} characteristic of S-H vibration of thiol is not present in PdNPs sample. This indicates the breaking of S-H bond and bonding of the S to Pd. These are clear evidences of the attachment of the ligand to the Pd

atom. The spectra are similar to thiol protected Au nanoparticles, already discussed in Chapter 2A (section 2A.4.2.5).

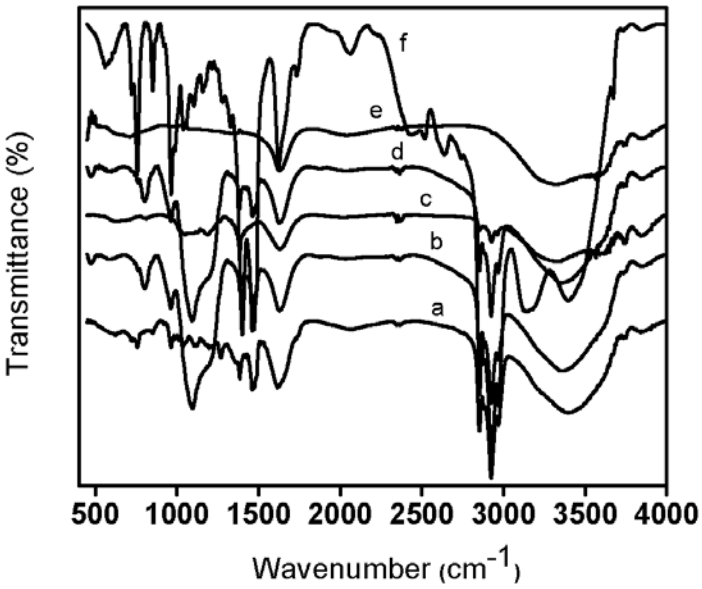

Fig. 3.6. FT-IR spectra of a) PdNP1, b)PdNP2, c) PdNP3, d) PdNP4, e) PdNP5 and f) RSH thiol.

3.4.1.4. Powder X-ray Diffraction

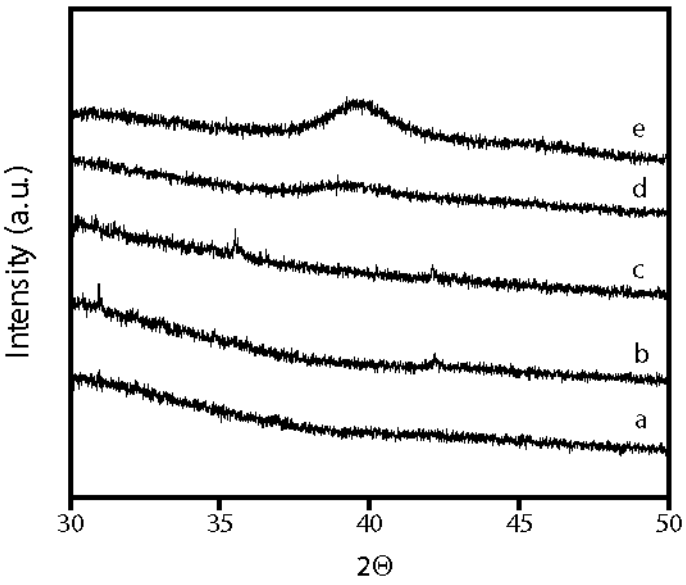

Fig. 3.7. Powder XRD patterns of Palladium Nanoparticles; a) PdNP1, b) PdNP2, c) PdNP3, d) PdNP4 and e) PdNP5.

Structural evolution of these NPs was followed by powder x-ray diffraction. Powder XRD patterns of PdNP1-3 do not show any evidence of metallic Pd; however, PdNP4 shows a small peak at 39.5° corresponding to (111) plane of fcc phase of Pd metal [Fig. 3.7]. In PdNP5, the peak has evolved into a more intense and sharp peak. This shows that particle size and attendant crystallinity starts evolving in PdNP4, albeit as ultra-small particles.

3.4.1.5. X-ray Photoelectron Spectroscopy

XPS analysis is performed to reveal the oxidation state of the Pd component in thiol stabilized Pd nanoclusters. XPS spectrum of PdNP1 shows double peaks with binding energies of 337.3 and 342.6 eV, corresponding to Pd $3d_{5/2}$ and Pd $3d_{3/2}$ respectively [Fig. 3.8].

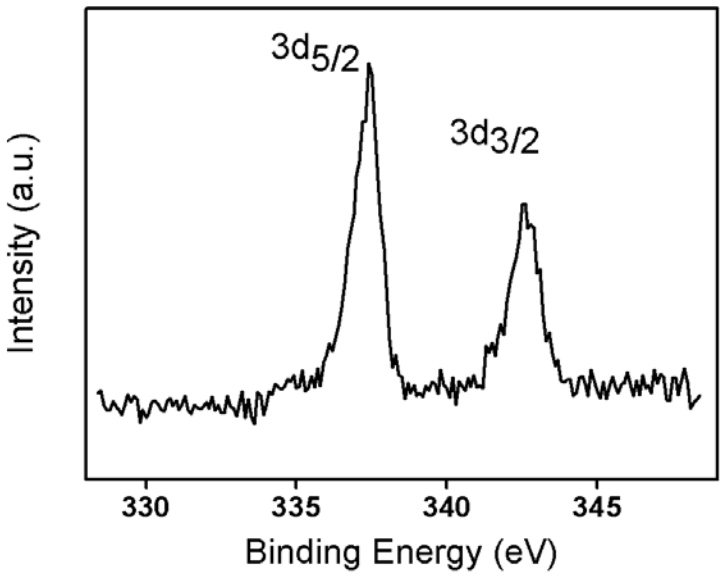

Fig. 3.8. XPS spectrum of the PdNP1 showing the Pd $3d_{5/2}$ and Pd $3d_{3/2}$ doublet with binding energies of 337.3 and 342.6 eV respectively.

These binding energy values confirm the presence of Pd (II) in nanocluster materials [15]. This also corroborates the formation of discrete transitions observed in UV-vis spectroscopy, indicating a molecular state with Pd in ionic form.

3.4.1.6. Thermogravimetric Analysis

Thermogravimetric analysis of Pd nanoclusters (PdNP1) was carried out to understand the nature of bonding between Pd and thiol ligand. Fig. 3.9 shows the weight loss of the nanoclusters with temperature. This analysis has revealed a Pd:thiol ratio of 2.5:1 which rules out the presence of simple Pd-thiol complexes which are expected at a ratio of 1:2. The extra Pd can be assumed to be not bonded to S and hence inside the cluster leading to a probable multinuclear Pd complex with outer Pd atoms bonded to the thiol ligands. Detalis of the calculation is given in Appendix 3.

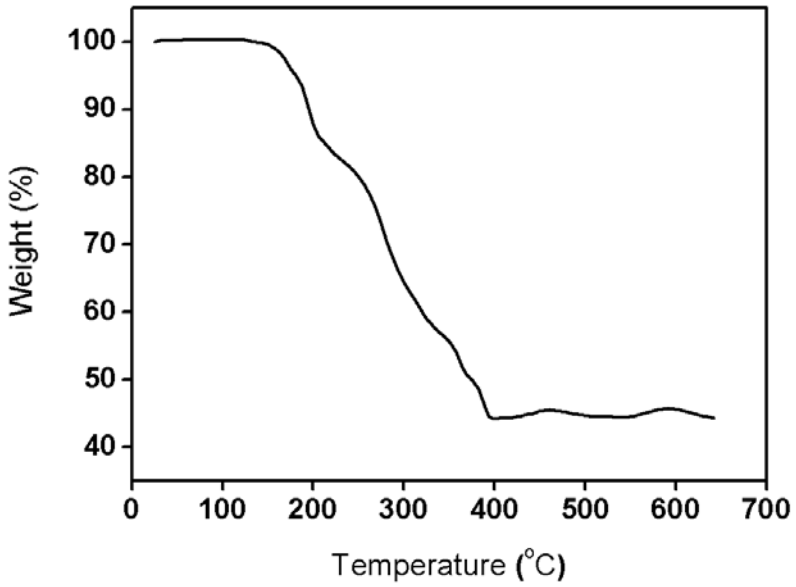

Fig. 3.9. Thermogravimetric analysis (TGA) of Pd nanocluster (PdNP1) under air with a ramping temperature rate of 5 °C/Minute.

3.4.1.7. Composition analysis

Elemental analysis of the dried samples by CHNS analysis is summarized in Table 3.2 considering after C,H,N,S remnant is Pd. It is possible to consider atom % of S to be equivalent to mole % of the ligand and the calculated thiol:Pd ratios show a vast difference in the amount of thiol present in the final product compared to the amount of thiol added to the reaction mixture. However, the trend of decreasing thiol concentration is more or less intact in the final products also.

Table 3.2. CHNS analysis of Pd nanoparticles

Sr.No.	Sample Name	Thiol conc. (mmol)	Thiol to Pd ratio (added)	At.% (by CHNS analysis)				
				C	H	N	S	Pd*
1	PdNP1	0.4	4.76:1	29.64	65.81	1.64	1.26	1.633
2	PdNP2	0.2	2.38:1	22.07	72.61	1.29	0.903	3.11
3	PdNP3	0.1	1.19:1	28.24	65.1	1.67	1.67	3.3
4	PdNP4	0.05	0.595:1	27.73	63.67	1.66	0.66	6.267
5	PdNP5	0.01	0.119:1	25.34	55.14	4.5	1.218	13.81
6	PdSR	0.4	4.76:1	28.52	67.25	1.37	1.44	1.76

*Considering after C,H,N,S remnant is Pd. Another interesting observation here is that the extent of difference in the thiol concentration between reaction mixture and final product is much greater at higher concentrations of thiol. For eg. in PdNP1, ~ 5x thiol was added to the reaction mixture whereas the final product has < 1x thiol concentration. However, as we go across to PdNp5, reaction mixture contained only 0.12x thiol and the resultant NPs had 0.088x thiol on the surface; displaying a 10 fold decrease in thiol concentration when compared to PdNP1. It is worth noting here that whatever be the added thiol concentration, final PdNPs have < 1x thiol bound to Pd. This indicates that the final product is not just a 1:2 ion pair of Pd(II) and thiolate but a complex with definite structures. Moreover, this also shows the influence of unbound thiol on the extent of reduction; mere presence of excess of thiol seems to be important even though the whole amount is not binding to the Pd species. If we consider the case of PdNP1, the formula of the complex can be considered as $Pd(S\text{-}R)_{0.77}$ leading to an excess charge of + 1.23 on Pd. So we can assume that part of the Pd is in partial oxidation states possibly resulting in Pd-Pd bonds. It is also noteworthy here that PdSR, the sample prepared without adding $NaBH_4$, had 0.82x thiol indicating partial reduction under the high concentrations of thiol used. At and above 2x thiol concentrations, where stable $Pd(S\text{-}R)_2$ complexes are reported for long chain alkyl thiols, partial reduction is observed in the current study.

Concentration of Pd in nanoclusters (PdNP1) solution is estimated by ICP analysis. It shows 2.1 mM Pd present in the as-synthesized Pd nanocluster solution.

3.5. METHYL ORANGE DYE DEGRADATION BY Pd NANOPARTICLES

We further used catalytic activity of these Pd nanoparticles as a probe to understand the effect of varying concentration of thiol on the particle size. Very recently, Pd NPs are reported to be active for environmentally benign processes like dye degradation [16,17]. However, catalytic activity of nanoparticles depends on access of surface active sites to the reactant molecules.

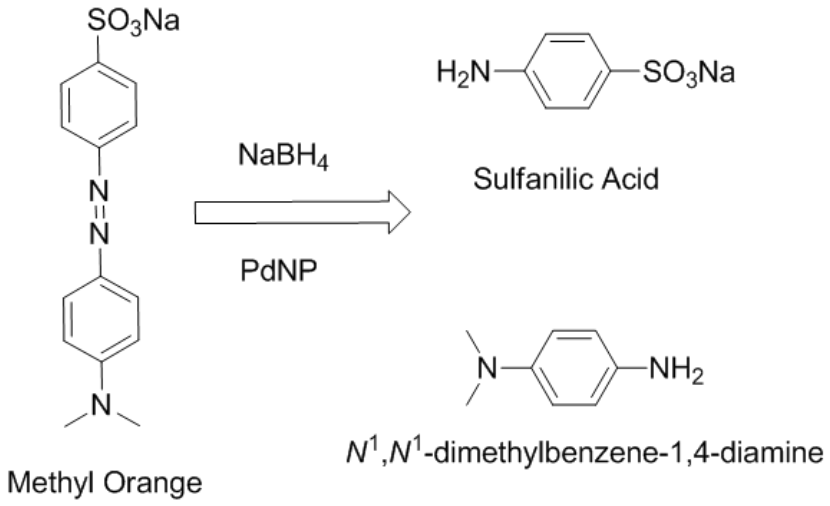

Scheme 3.2. Reductive degradation of Methyl Orange catalyzed by PdNP.

Hence, surface protection with organic molecules, especially with S which is known to poison metal catalysts, can affect the catalytic activity. It is possible that the extent of catalytic activity can also give an insight into the surface coverage of nanoparticles with protecting ligands. We selected methyl orange dye as the substrate and visually followed the changes in colour after addition of same amount of various Pd NPs. The reductive dye degradation process catalyzed by Pd naoparticles has been represented in Scheme 3.2.

For catalytic dye degradation experiments, aqueous stock solution of methyl orange of 0.75 mM concentration in pH 7 (approx) and 30 mM of $NaBH_4$ was prepared. Then in a 5 mL glass vial, 140 µL of methyl orange and 100 µL of sodium borohydride and a

20 µL of palladium nanoparticles as catalyst was taken and total solution was made up to 1.5 mL and the degradation was monitored by UV-vis Spectroscopy. This study was carried out on all Pd nanoparticles.

As the thiol concentration increases, dye degradation activity of PdNPs obviously decreases. The time taken for the discoloration of the dye, which indicates breaking of azo groups into less toxic components [18], decreases with decrease in thiol concentration. In other words, catalytic activity increases as particle size increases consequently decreasing the thiol binding on the surface. This observation was ascertained by UV-vis absorption spectroscopy. Absorption spectrum of methyl orange exhibits a broad peak at 465 nm and a small peak at 272 nm. The peak at 465 nm is typical of substituted azobenzenes [19] and changes to this peak were followed. To understand the effect of catalyst as well as $NaBH_4$, experiments were carried out on reaction mixtures without catalyst and $NaBH_4$ [Fig. 3.10]. It is evident that there is very slow degradation of the dye without the addition of catalyst or of $NaBH_4$ in the concentrations we used, not inducing any drastic degradation.

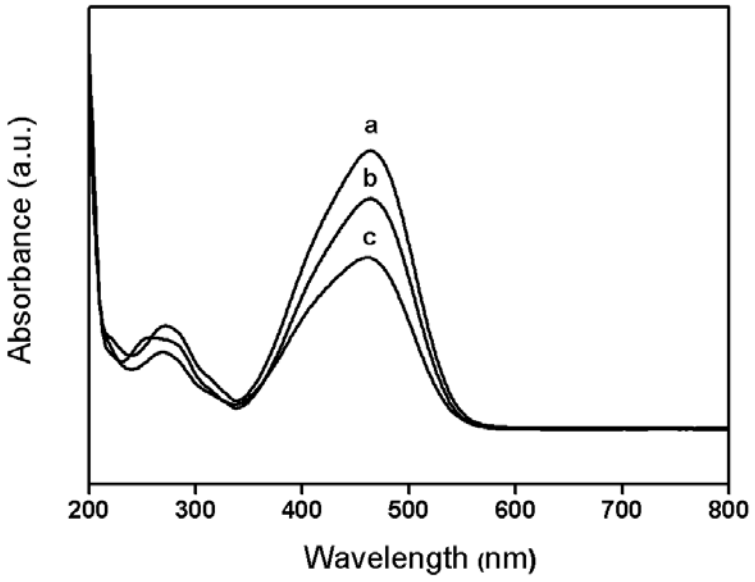

Fig. 3.10. Absorption spectra of (a) pure methyl orange dye; (b) in reaction mixture without catalyst and (c) reaction mixture without $NaBH_4$.

But it is quite clear that sodium borohydride does play a role in degradation of methyl orange in the presence of catalyst. UV-vis spectra of reaction mixtures with different

PdNPs in comparison to the sample without catalyst are displayed in Fig. 3.11. This also corroborates the observations from visual comparison. PdNP4 and PdNP5 with low thiol ratio are shown to be effective as catalysts for methyl orange degradation. Thus it is quite evident that if the thiol binding on palladium nanoparticles surface is high, there is hindrance to dye degradation. However, there is no hindrance to dye degradation on PdNPs with less concentrations of thiol.

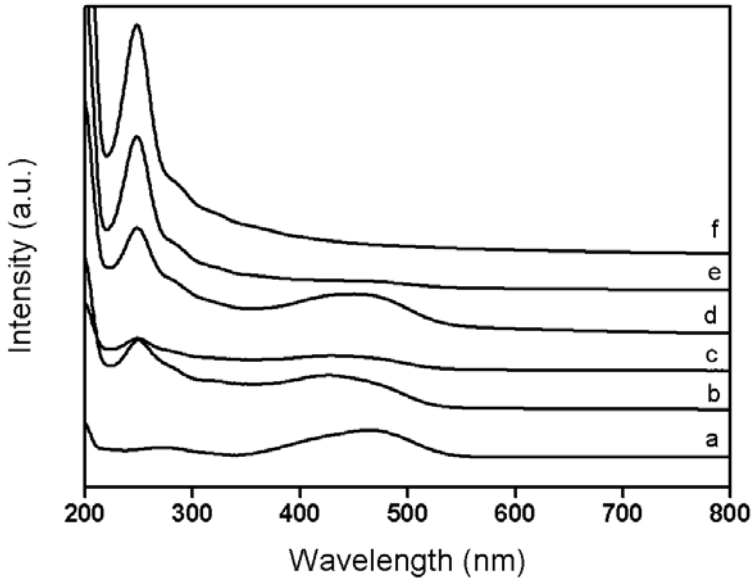

Fig. 3.11. UV-vis spectra of solutions containing methyl orange, $NaBH_4$ and different palladium nanoparticles as catalyst; a) without catalyst, b) PdNP1, c) PdNP2, d) PdNP3, e) PdNP4 and f) PdNP5.

3.4.2. Characterization of silica encapsulated Pd nanoclusters ($Pd@SiO_2$)

3.4.2.1. High Resolution Transmission Electron Microscopy

HRTEM images of silica coated Pd clusters show reasonably monodisperse silica spheres, apparently interconnected, of size 25-30 nm [Fig. 3.12]. Due to ultra-small size in nature, Pd clusters are not visible through the silica sphere.

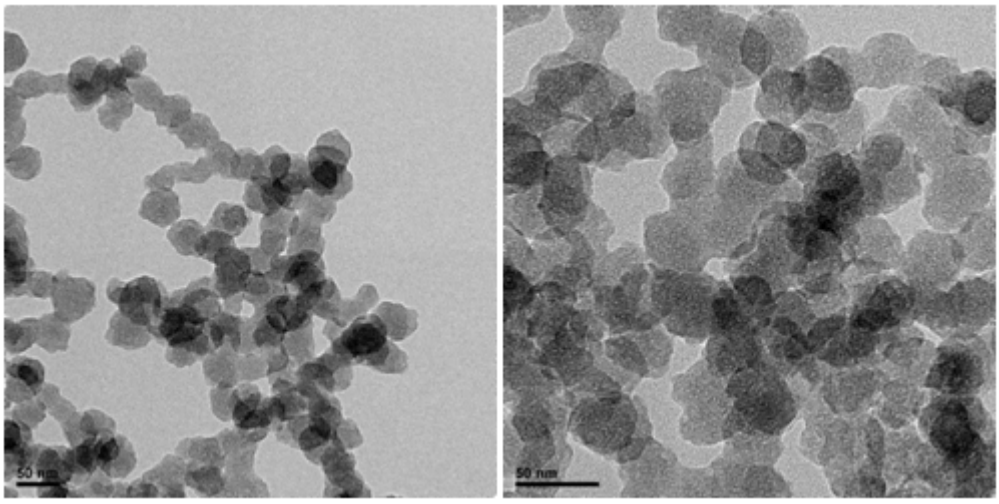

Fig. 3.12. HRTEM image of silica encapsulated Pd nanocluster.

3.4.2.2. UV-Vis Spectroscopy

As synthesised $Pd@SiO_2$ has a spectrum very similar to pristine clusters showing molecular transition peaks overlapped with the exponentially decaying peak [Fig. 3.13]. This clearly indicates that the water dispersible clusters are stable enough under the conditions employed for silica encapsulation.

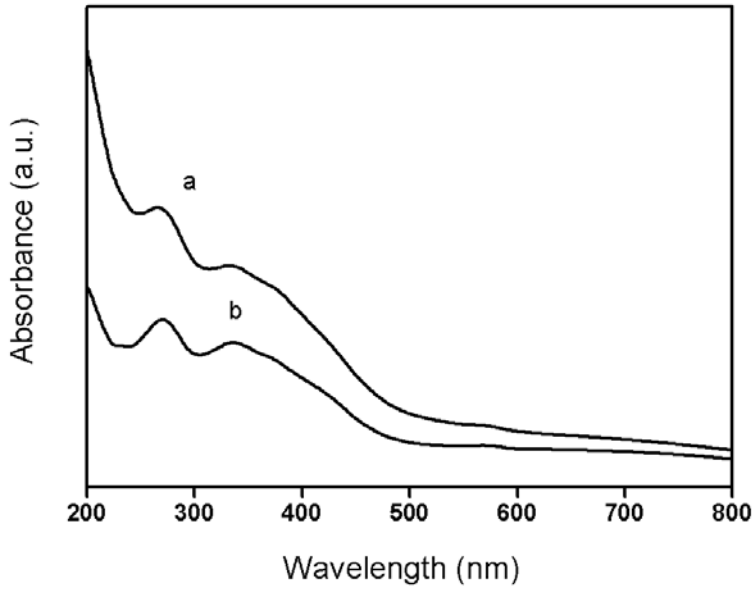

Fig. 3.13. UV-vis spectra of a) silica encapsulated Pd nanoclusters and b) Pd nanoclusters.

3.4.2.3. Thermogravimetric Analysis

Thermogravimetric analysis of as-synthesized silica encapsulated Pd clusters show weight loss of 25 % because of the removal of the organic thiol ligand [Fig. 3.14].

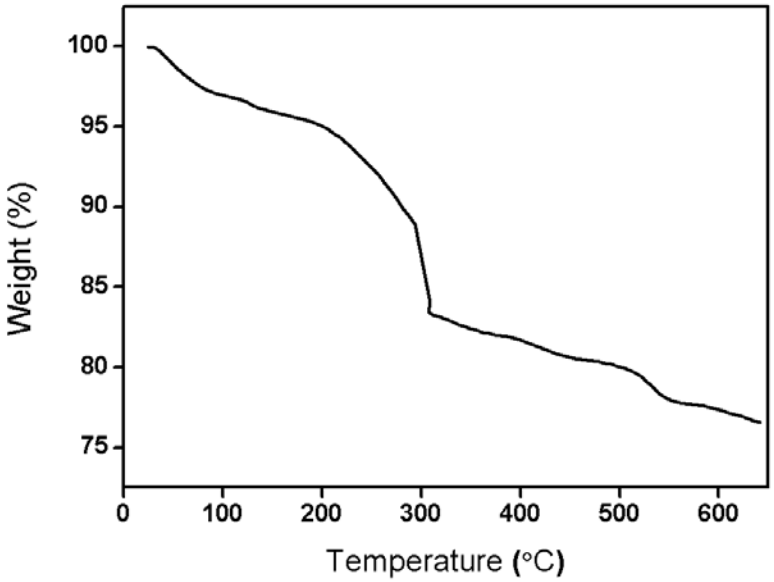

Fig. 3.14. Thermogravimetric analysis (TGA) of silica encapsulated Pd nanoclusters under air with a ramping temperature rate of $5\,^{0}$C/Minute.

3.4.2.4. SEM-EDAX Analysis

SEM-EDAX analysis was performed to do the elemental analysis of as-synthesized silica encapsulated Pd nanoclusters. Fig. 3.15 represents the EDAX spectra of the material. It shows that Pd ~ 3 % and S ~ 2 % are present in the material.

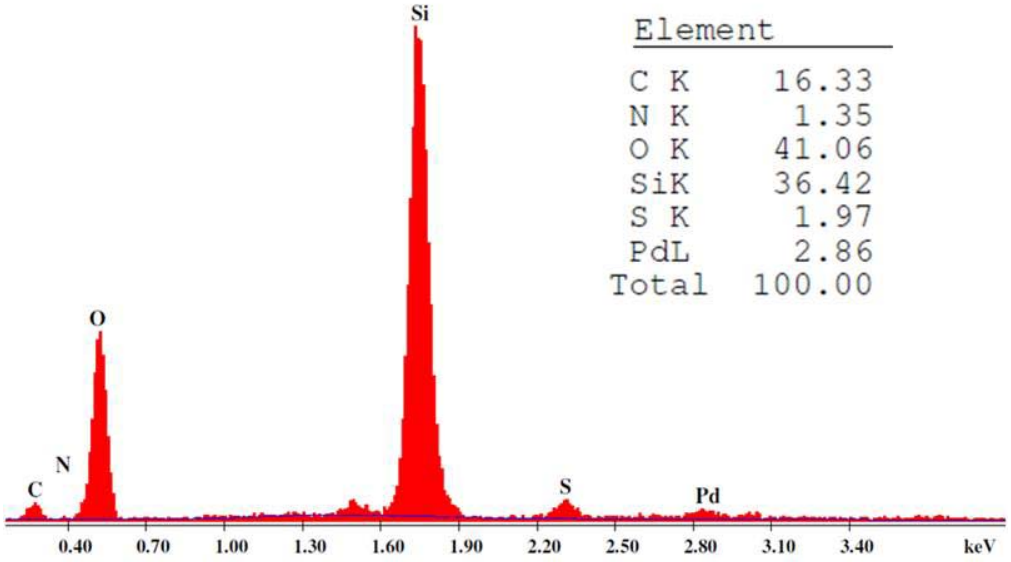

Fig. 3.15. EDAX spectra of silica encapsulated Pd nanoclusters and microanalysis (inset) (wt %)

3.4.3. Characterization of porous silica encapsulated Pd nanoparticles (Pd@p-SiO_2)

3.4.3.1. High Resolution Transmission Electron Microscopy

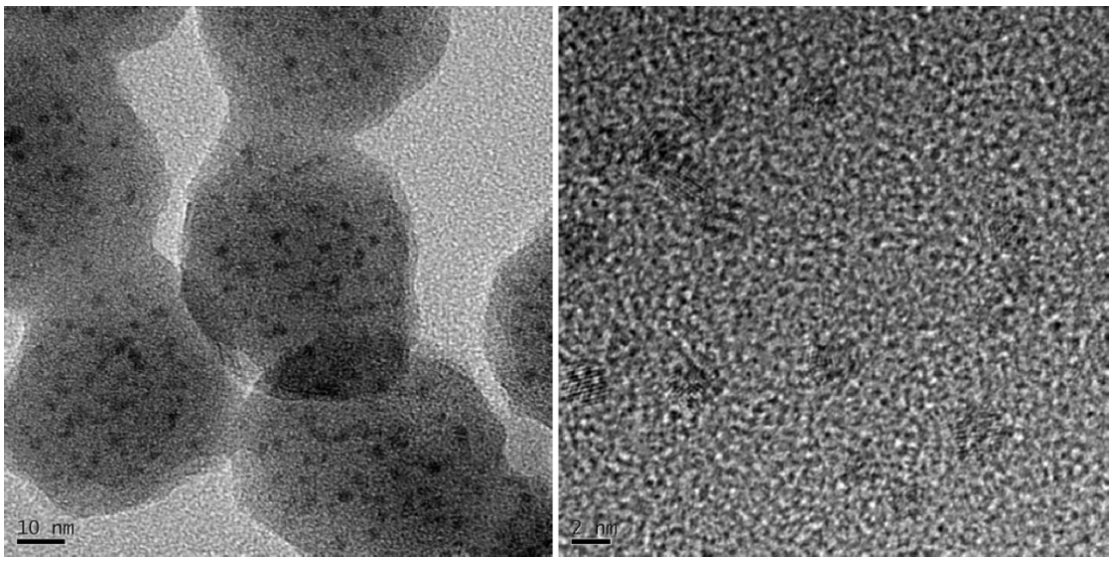

Fig. 3.16. HRTEM images of calcined silica encapsulated Pd nanoparticles. Higher magnification shows cubooctahedral shape of the Pd nanoparticle (right). Scale bars = 10 nm (left) and 2 nm (right)

HRTEM image has shown highly monodisperse Pd particles of size 2.6±0.7 nm arranged spatially separated from each other within the silica spheres [Fig. 3.16]. Moreover, no agglomerated big particles could be seen on the outer surfaces of the silica spheres. This also rules out any surface adsorption of Pd precursors and indicates a complete encapsulation. On higher magnification, a better picture of the nanoparticle structure emerged. They seem to be not only highly monodisperse at ~ 3 nm but also very crystalline with cubooctahedral shape. HRTEM has revealed that Pd nanoparticles formed from ultra-small Pd nanoclusters during calcination.

3.4.3.2. UV-Vis Spectroscopy

UV-vis spectrum of the calcined sample shows the continuous decay from UV region to visible region but also some less pronounced features corresponding to molecular transitions [Fig. 3.17]. This indicates that after calcination, the Pd characteristics are not of ultra-small clusters or complexes but of very small nanoparticles and probably a mixture of clusters and nanoparticles is formed.

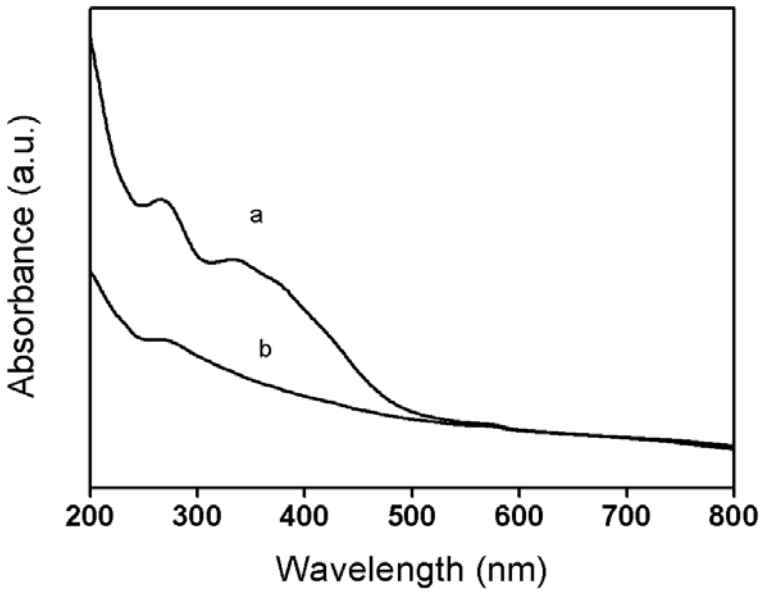

Fig. 3.17. UV-vis spectra of a) as-synthesized Pd@SiO_2 and b) calcined Pd@p-SiO_2

3.4.3.3. Thermogravimetric Analysis

Thermogravimetric analysis of the Pd@p-SiO_2 in comparison with the as synthesized encapsulated clusters also indicates loss of organics but the weight loss of 25 % in as synthesized sample decreased drastically to 6 % in case of the calcined Pd@p-SiO_2 [Fig. 3.18]. This indicates that the calcined sample contains very less amount of organics compared to as-synthesized sample.

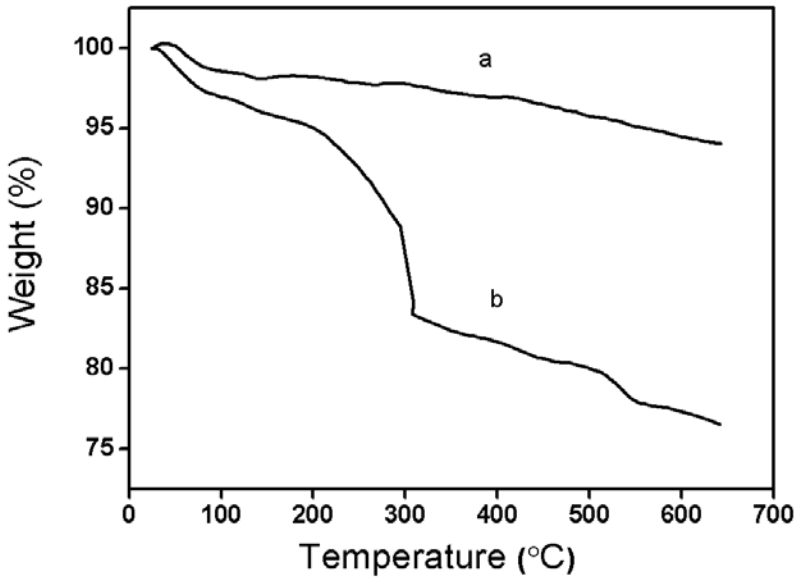

Fig. 3.18. Thermogravimetric analysis (TGA) of a) as-synthesized Pd@SiO_2 and b) calcined Pd@p-SiO_2.

3.4.3.4. SEM-EDAX Analysis

SEM-EDAX analysis was performed to do the elemental analysis of calcined Pd@p-SiO_2 material. Fig. 3.19 represents the EDAX spectra of the material. It shows that ~ 3 % of Pd and ~ 0.2 % of S are present in the material. The amount of sulphur present is very less compared to as-synthesized material. This proves that in the as-synthesized material, calcination has resulted in complete removal of the thiol ligand.

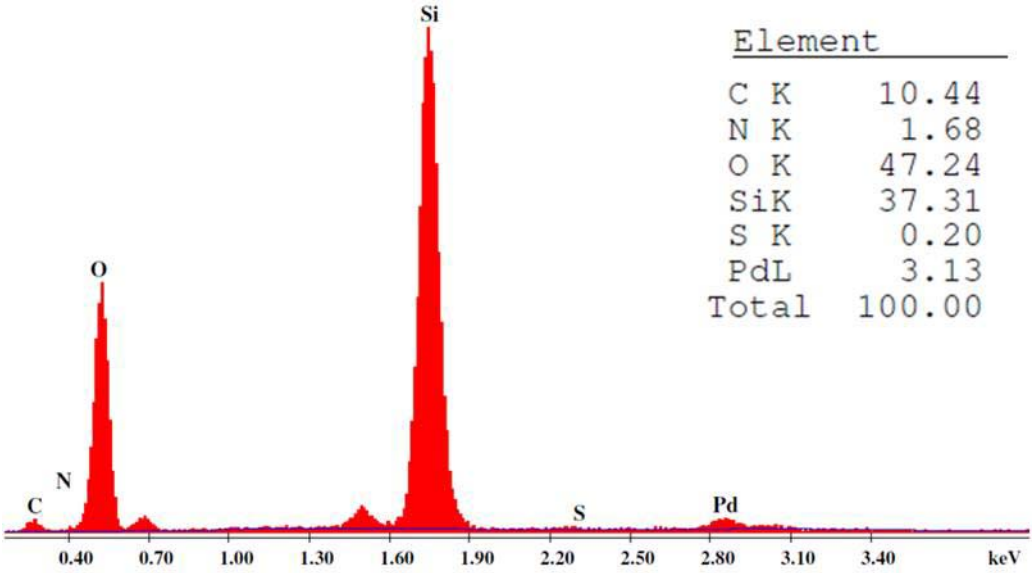

Fig. 3.19. EDAX spectra of porous silica encapsulated Pd nanoparticles (Pd@p-SiO_2) and microanalysis (inset) (wt %)

3.4.3.5. N_2 Adsorption Study

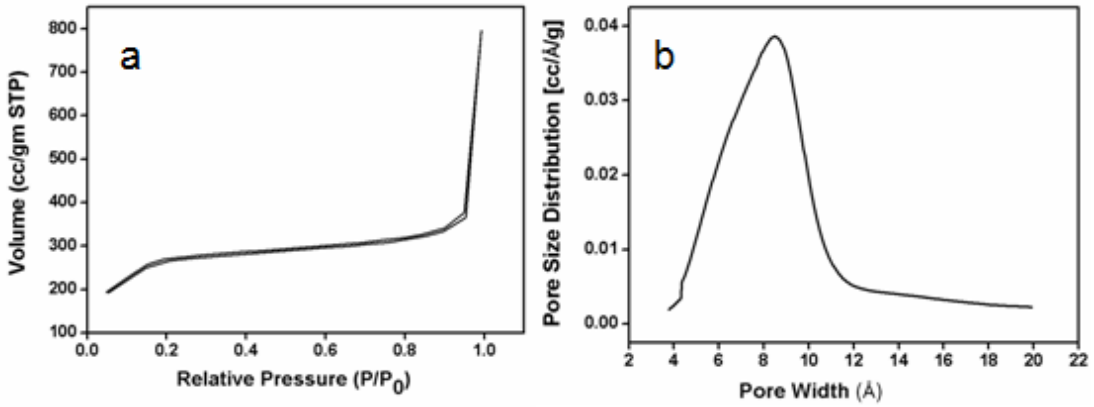

Fig. 3.20. a) N_2 adsorption–desorption isotherms of Pd@p-SiO_2 calcined at 350 °C and b) Pore size distribution calculated from the adsorption branch of the isotherms by HK method.

As discussed earlier, a complete encapsulation in dense oxides can be detrimental to catalysis due to inaccessibility of the reactant molecules to the active nanoparticles surface. Hence, for this material to be useful as a stable catalyst, porosity of the silica coating is a prerequisite. N_2 adsorption studies showed that the

silica matrix is microporous with a slightly broad distribution peaking at 0.85 nm and BET surface area of the material calcined at 350 °C was estimated to be 480 m^2g^{-1} [Fig. 3.20].

3.4.3.6. Inductively Coupled Plasma Spectroscopy

Concentration of Pd in the porous silica encapsulated Pd nanoparticles is estimated by ICP analysis. It shows that 2.3 wt % Pd is present in the calcined material.

3.6. THERMAL STABILITY STUDY OF THE POROUS SILICA ENCAPSULATED Pd NANOPARTICLES

The phenomenon of agglomeration or sintering on supported catalysts and various mechanisms for this process have been studied and the mobility of nanoparticles over support surfaces is proposed to be the main cause, especially severe at temperatures nearing Tamman temperature.

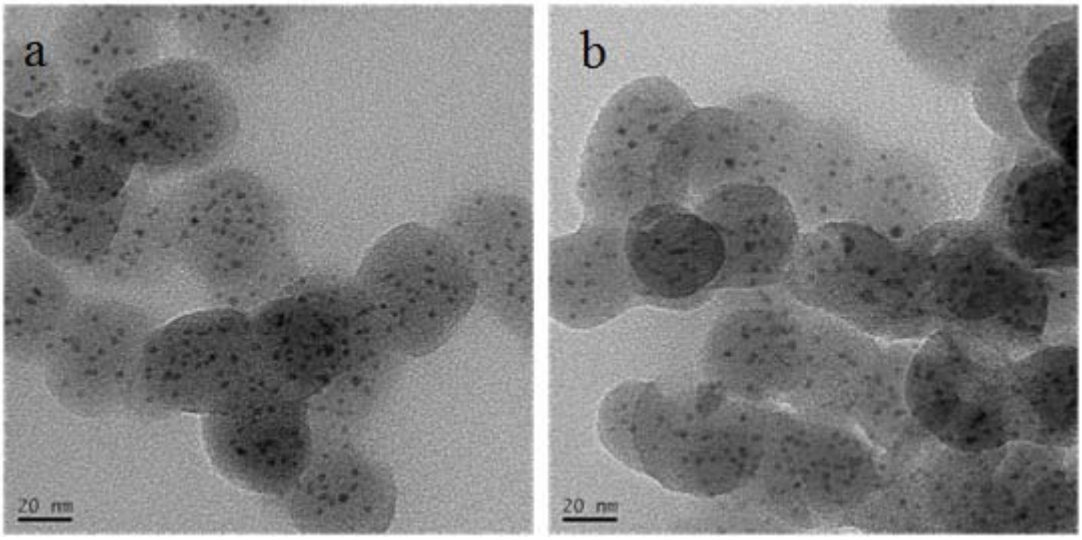

Fig. 3.21. HRTEM images of calcined Pd@p-SiO_2 material after treatment at different temperatures; a) 550 ^oC and b) 750 ^oC.

In such a scenario, a catalyst like Pd@p-SiO_2, in which nanoparticles are well separated and completely encapsulated individually within a porous matrix can be envisaged to be stable against sintering due to the confinement of metal nanoparticles

preventing mobility and coalescence. This was indeed found to be the case when Pd@p-SiO_2 was subjected to high temperature calcination. Thermal stability of the material was tested by heating it to 550 and 750 °C and observing the resulting samples under HRTEM. Very interestingly, HRTEM images showed that the particle size could be controlled at ~ 3 nm even at such high temperatures [Fig. 3.21]. Activation of this catalyst was carried out at 350 °C under hydrogen and HRTEM shows that there is no variation in particle size even after treatment at reducing condition also [Fig. 3.22a.]. To investigate the effect of high temperature on supported Pd catalysts, Pd@SBA-15, which was synthesized by supporting Pd ultra-small clusters on high surface area mesoporous silica, SBA-15, was calcined at 550 °C. HRTEM image [Fig. 3.22b.] shows severe agglomeration as expected. It is noteworthy here that near Tamman temperature of Pd wherein such sintering occurs, Pd@p-SiO_2 material exhibited complete resistance to this phenomenon. This thermal stability study has proved that Pd@p-SiO_2 material is sinter resistant and can be used for high temperature catalytic conversion reactions.

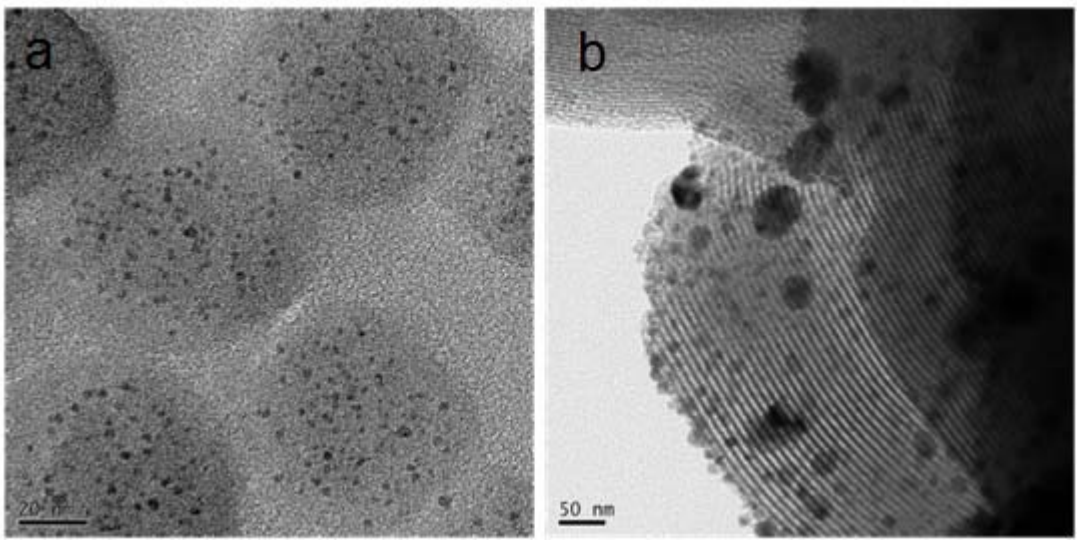

Fig. 3.22. HRTEM of a) activated silica encapsulated Pd nanoparticle (Pd@p-SiO_2) and b) SBA-15 supported Pd nanoparticle (Pd@SBA-15) synthesized by calcination method using Pd nanoclusters at 550 °C.

3.7. HYDROGENATION OF *TRANS*-STILBENE BY Pd@p-SiO_2

Catalytic study on this Pd@p-SiO_2 material was carried out by model reaction of trans-stilbene hydrogenation at room temperature. Main aim of this study was to confirm the accessibility of reactant molecules to the metal sites.

Pd@p-SiO_2 (3.1 mg, 2.3 wt % Pd) was pre-activated at room temperature for 3 h in THF (3 mL) under a H_2 balloon pressure before the reaction. *trans*-Stilbene (60 mg, 0.33 mmol) was added to the catalyst-solvent mixture and the progress of reaction was studied from time ranging 15-60 min. Reaction progress as a function of time on the *trans*-Stilbene hydrogenation using Pd@p-SiO_2 is given in Fig. 3.23.

Reaction mixture was analyzed for the product formation by gas chromatography (GC) using Varian 3800 model GC, with flame ionization detector (FID). It has CPSIL 8CB capillary column (5% phenyl 95% dimethyl polysiolxane) (30 m length, 0.25 mm diameter). N_2 (30 mLmin-1) is used as a carrier gas, H_2 (25 $mLmin^{-1}$) is used for flame and air as oxidizer (300 $mLmin^{-1}$). N_2 (1.6 $mLmin^{-1}$) was used in column. Temperature of Injector and Detector was 275 $^{\circ}C$ and 280 $^{\circ}C$ respectively. Sample was analyzed with a column oven program starting from 100 $^{\circ}C$ to 280 $^{\circ}C$ at a rate of 10 $^{\circ}Cmin^{-1}$ and a hold time of 20 min.

For comparison, activity of commercial 5 % Pd/C for the same reaction was tested. Catalyst amount was selected such that Pd mole % is same in both cases. Commercial catalyst showed 100 % conversion of the *trans*-Stilbene by 15 minutes but Pd@p-SiO_2 took 1 h for the complete conversion. This happened because of the mass transfer limitation by the porous silica structure. This also shows that the active metal particles are as easily accessible to reactant molecules as in the case of a supported catalyst where the nanoparticles are deployed on the surface of the support. However, the disadvantage of such supported catalysts is their propensity for active particle agglomeration which has been understood to be the reason for deactivation in many industrially important reactions.

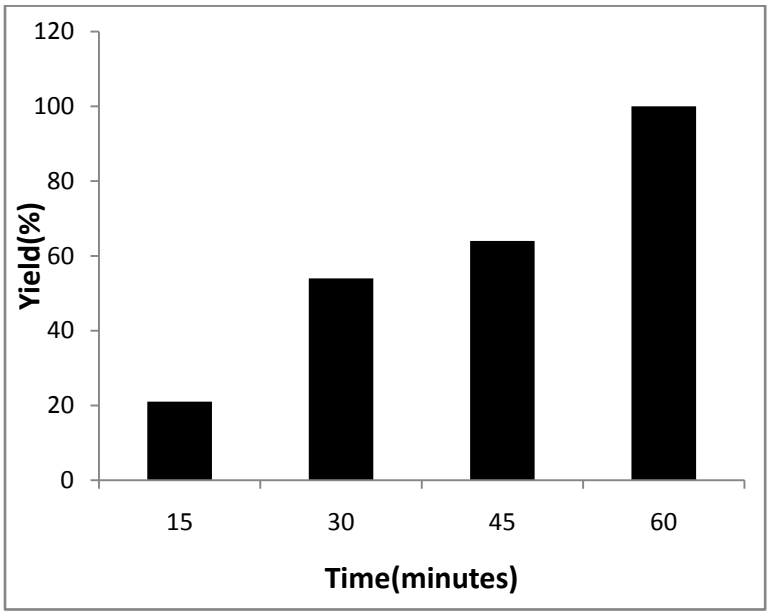

Fig. 3.23. Reaction progress as a function of time on the *trans*-stilbene hydrogenation using Pd@p-SiO_2.

3.8. SUMMARY

Highly stable and water dispersible Pd nanoparticles ranging from nanoclutsers to nanoparticles were prepared by using a bifunctional alkyl ammonium thiol ligand. Fine tuning of particle size was achieved by systematically varying the thiol concentration in the reaction mixture. Various characterization techniques were used to ascertain the formation of Pd thiolate nanoparticles and evolution of the NP structure was followed. As expected, size of the particle decreases with increase in thiol concentration during synthesis. Also with increase in thiol concentration, the particle characteristics move towards Pd-thiolate complexes whereas with decrease in thiol concentration the particle characteristics incline more towards metallic nature. Sulphur is considered as poison for the catalyst and hence limits the application of thiolate capped palladium nanoparticles as catalysts. But in case of thiol ligand used here, the palladium nanoparticles with less concentrations of thiol are shown to be effective catalysts. Also we see that at higher thiol concentrations (approximately more than 0.5:1) there is hindrance to the catalyst effect possibly due to lowering of the active sites on the nanoparticles as in case of PdNP1 to PdNP3.

Further silica encapsulation of the ultra-small Pd clusters (PdNP1) was successful in a simple condensation process. Calcination and subsequent removal of organics led to the formation of nanocatalyst with arrays of ~ 3 nm Pd particles individually encapsulated within porous silica spheres. These nanocatalysts exhibited excellent catalytic activity as well as thermal stability. Even at 750 °C near Tamman temperature of Pd, sintering was highly controlled and particle size remained intact at ~ 3 nm. Such nanocatalysts with efficient catalytic activity as well as stability against deactivation can be envisaged to be highly useful in many industrially important reactions including high temperature processes.

3.9. REFERENCES

1. S. Kidambi, J. Dai, J. Li and M. L. Bruening, *J. Am. Chem. Soc.*, 2004, **126**, 2658.
2. S. Proch, Y. Mei, J. M. R. Villanueva, Y. Lu, A. Karpov, M. Ballauff and R. Kempe, *Adv. Synth. Catal.*, 2008, **350**, 493.
3. A. Yamaguchi and E. Iglesia, *J. Catal.*, 2010, **274**, 52.
4. Y. Wang, A. V. Biradar, C. T. Ducan and T. Asefa, *J. Mater. Chem.*, 2010, **20**, 7834.
5. K.-T. Li, M.-H. Hsu and I. Wang, *Catal. Commun.*, 2008, **9**, 2257.
6. D.-S. Bae, K.-S. Han and J. H. Adair, *J. Mater. Chem*., 2002, **12**, 3117.
7. A. J. Forman, J.-N. Park, W. Tang, Y.-S. Hu, G. D. Stucky and E. W. McFarland, *ChemCatChem*, 2010, **2**, 1318.
8. J.-N. Park, A. J. Forman, W. Tang, J. Cheng, Y.-S. Hu, H. Lin and E. W. McFarland, *Small*, 2008, **4**, 1694.
9. M. Cargnello, N. L. Wieder, P. Canton, T. Montini, G. Giambastiani, A. Benedetti, R. J. Gorte and P. Fornasiero, *Chem. Mater*., 2011, **23**, 3961.
10. G. Corthey, A. A. Rubert, A. L. Picone, G. Casillas, L. J. Giovanetti, J. M. Ramallo-Lopez, E. Zelaya, G. A. Benitez, F. G. Requejo, M. Jose-Yacaman, R. C. Salvarezza and M. H. Fonticelli, *J. Phys. Chem. C*, 2012, **116**, 9830.
11. F. P. Zamborini, S. M. Gross and R. W. Murray, *Langmuir*, 2001, **17**, 481.
12. D. Y. Zhao, Q. Huo, J. Feng, B. F. Chmelka and G. D. Stucky, *J. Am. Chem. Soc.*, 1998, **120**, 6020.

13. L. I. Elding and L. F. Olsson, *J. Phys. Chem.*, 1978, **82**, 69.
14. Z. Yang, A. B. Smetana, C. M. Sorensen, K. J. Klabunde, Inorg. Chem. 2007, **46**, 2427.
15. G. Liu, M. Hou, J. Song, T. Jiang, H. Fan, Z. Zhang and B. Han, *Green Chem*., 2010, **12**, 65.
16. L. Xu, X-C. Wu and J-J. Zhu, *Nanotechnology*, 2008, **19**, 1.
17. A. Safavi and S. Momeni, *J.Hazard Mater*., 2012, **201**, 125.
18. A. Johnson, G. Merilis, J. Hastings, M. E. Palmer, J. P. Fitts and D. Chidambaram, *J. Electrochem. Soc*., 2013, **160**, 27.
19. J. Oakes and P. Gratton, *J. Chem. Soc., Perkin Trans.*, 1998, **2**, 2563.

CHAPTER 4

POROUS SILICA ENCAPSULATED Au-Pd ALLOY NANOPARTICLES FOR CO OXIDATION REACTION

4.1. INTRODUCTION

Bimetallic alloys are known to have superior properties when compared to the individual metal components due to synergistic electronic effects [1-4]. When translated into the nanoregime, alloys exhibit enhanced properties especially conducive for catalysis, exploiting the characteristic changes occurring on surfaces as a consequence of decrease in particle size. There has been particular interest in catalytic properties of Au-Pd bimetallic systems due to their application in various industrially important reactions like direct H_2O_2 production, low temperature CO oxidation, vinylacetate monomer synthesis etc [5-12]. Most of the studies on Au-Pd colloidal systems report core-shell models synthesized by simultaneous or sequential reduction of the metal precursors [13-17]. Control of size to catalytically active regime of $\leq$ 5 nm is also achieved by dendrimer encapsulation or microemulsion methods [18-20]. However, one of the drawbacks of these materials is that the protecting capping agents may prevent access of reactant molecules to active surface sites. Hence complex methods need to be designed to remove the capping agents preferably at low temperatures to avoid sintering of the nanoparticles. Another major hurdle is that these methods lead to mostly core-shell architectures or quasialloying at the best, since any conditions like increase in temperature to facilitate diffusion and better alloying will destroy the ensemble structure.

It becomes clear at this juncture that for practical catalysis applications, these bimetallic colloidal NPs need to be supported on stable high surface area materials, as in the case of monometallic NPs discussed till now. Conventional methods as well as post synthetic grafting have been explored [21,22]; latter again demanding complex steps to remove capping agents prior to grafting. Conventional methods, even though simple, lead to highly non-uniform particles in terms of size as well as composition. Most of the time, mixtures of individual metal NPs and bimetallic particles, with a range of Au-Pd compositions are present in the same catalyst. Phase segregation into the individual metal components is also observed due to the differences in Tammann temperatures of Au and Pd [23]. In this scenario, formation of uniform bimetallic alloy nanoparticles based supported catalysts stable at high temperatures is highly challenging. For any synthetic method to succeed in fabricating such catalysts, it

should primarily address the stability issue. This is especially true in case of automotive catalysts, wherein the operating temperatures vary over a wide range in oxidising and reducing conditions.

We have employed a very simple strategy similar to Au and Pd, described in Chapter 2 and 3 (section 2B.1 and section 3.1). For bimetallic system, a mixture of Au and Pd nanoclusters are used as precursors instead of single nanocluster precursors for silica encapsulation as in case of simple Au or Pd [Scheme 4.1]. Prior to hydrolysis, a random mixing of Au and Pd nanoclusters can be expected since interparticle interactions will be similar due to same outer surface functionality, viz., propyl ammonium group. Presence of intimate mixtures of the clusters within the silica encapsulation ensures the formation of fully alloyed nanoparticles at high temperatures, at the same time controlling further growth and sintering.

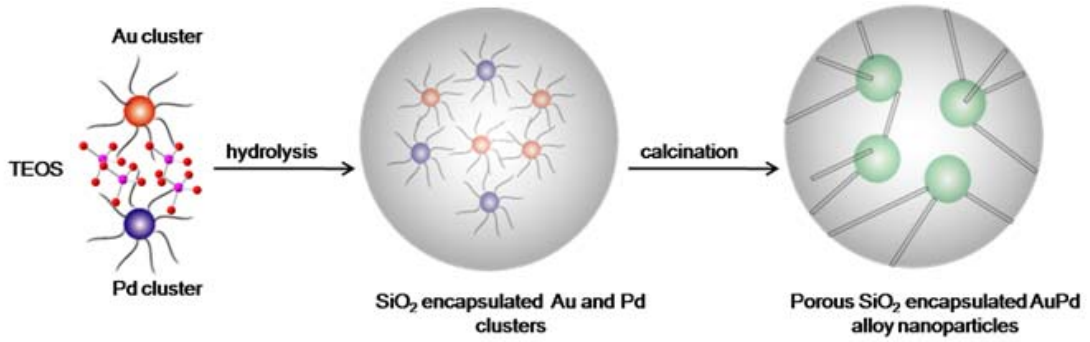

Scheme 4.1. Synthesis of porous silica encapsulated Au-Pd alloy nanoparticle

4.2. SYNTHESIS

4.2.1. Synthesis of porous silica encapsulated Au-Pd alloy nanoparticles

4.2.1.1. Synthesis of silica encapsulated Au & Pd nanoclusters

Synthesis of Au and Pd nanoclusters (PdNP1) are described in Chapter 2 (section 2A.2.2) and Chapter 3 (section 3.2.1) respectively. 10 mL mixtures of Au and Pd nanoclusters (PdNP1) solutions in three different ratios (Au: Pd; 3:1, 1:1 and 1:9) were sonicated for 1 h. The sonicated nanocluster solution (10 mL) was mixed with a 1:4 water/ethanol mixture (200 mL). 0.1 M NaOH solution (0.9 mL) and tetraethyl orthosilicate (TEOS) (300 µL, Aldrich, 98%) were added to this mixture and stirred at

RT for 3 d. Silica-encapsulated gold-palladium nanoclusters were separated from the reaction medium by centrifugation at 14000 rpm and redispersed in water several times. Here, we have started with three different initial concentration regimes aiming at Au rich (2.85:1-Au3Pd), equivalent (0.95:1-AuPd) and Pd rich (0.1:1-AuPd10) alloys. The samples henceforth will be represented as Au3Pd@SiO_2, AuPd@SiO_2 and AuPd10@SiO_2 based on the initial metal concentrations added.

4.2.1.2. Synthesis of porous silica encapsulated Au-Pd alloy nanoparticles

The above as-synthesized materials were calcined to remove the thiol ligand and for the intimate mixing of nanclusters to form alloy nanoparticles by heating with a rate of 0.8 °C/min from room temperature to 550 °C. First the temperature was increased up to 550 °C under nitrogen and then it was kept constant for 12 h under air for removing the organic ligand.

4.3. INSTRUMENTS FOR CHARACTERIZATION

Many physico-chemical techniques like high resolution transmission electron microscopy (HRTEM), scanning electron microscopy (SEM), UV-vis spectroscopy, N_2-adsorption, photoelectron spectroscopy (XPS), powder X-ray diffraction (XRD), and inductively coupled plasma spectroscopy (ICP) were used for the characterization of silica encapsulated AuPd alloy nanoparticles. Details of HRTEM, UV-Vis spectroscopy, XPS and SEM have already been described previously in Chapter 2 (section 2A.3) and Chapter 3 (section 3.3) respectively.

4.3.1. Powder X-ray Diffraction (XRD)

Powder X-ray diffraction (XRD) for all the samples was carried out in a PANalytical X'pert Pro dual goniometer diffractometer working under 40 kV and 30 mA. The radiation used was Cu Kα (1.5418 Å) with a Ni filter, and the data collection was carried out using a flat holder in Bragg-Brentano geometry with 1° slit at the source side. An X'celerator solid-state detector with a scan speed of 0.078 ° min^{-1} was employed. Powder XRD profile refinement was done using Rietveld method by means of the GSAS-EXPGUI program [24]. Initially, background and scale factors were refined followed by cell parameters and profile parameters.

4.3.2. N_2 Adsorption Study

Nitrogen adsorption/desorption isotherm was acquired using Quadrasorb instrument model from Quantachrome. The program consisting of both an adsorption and desorption branch typically ran at -196 °C after sample was degassed at 300 °C for 3 h once the final temperature had been maintained. Specific surface area was calculated via BET model at a relative pressure of P/P_0 = 0.05-0.2. The pore volume was estimated from the uptake of adsorbate at a relative pressure of P/P_O = 0.99. Pore size distribution curve was obtained by using Density Functional Theory (DFT) method.

4.4. CHARACTERIZATION

Silica encapsulated Au, Pd nanoclusters and porous silica encapsulated AuPd alloy nanoparticles are characterized by HRTEM, UV-vis spectroscopy, XRD, XPS, N_2 adsorption study and SEM-EDAX analysis.

4.4.1. Characterization of silica encapsulated mixture of Au & Pd nanoclusters

High Resolution Transmission Electron Microscopy

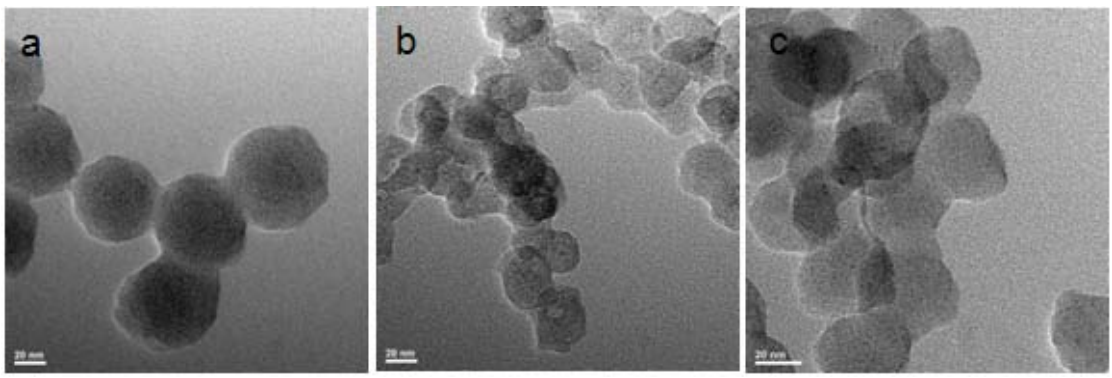

Fig. 4.1. HRTEM images of as-synthesized a) Au3Pd@SiO_2, b) AuPd@SiO_2 and C) AuPd10@SiO_2. Scale bars = 20 nm.

HRTEM images of as-synthesized materials before calcination shows ~ 1 nm particles within the silica matrix [Fig. 4.1]. Similar behaviour was observed in case of

encapsulation of individual Au and Pd clusters discussed in Chapter 2 (section 2B.4.1.1) and Chapter 3 (section 3.4.2.1).

4.4.2. Characterization of porous silica encapsulated Au-Pd alloy nanoparticles

4.4.2.1. High Resolution Transmission Electron Microscopy

HRTEM analysis of the samples calcined at 550 °C has shown highly monodisperse particles of size ~ 3.5 nm spatially separated from each other arrayed within the silica matrix [Fig. 4.2].

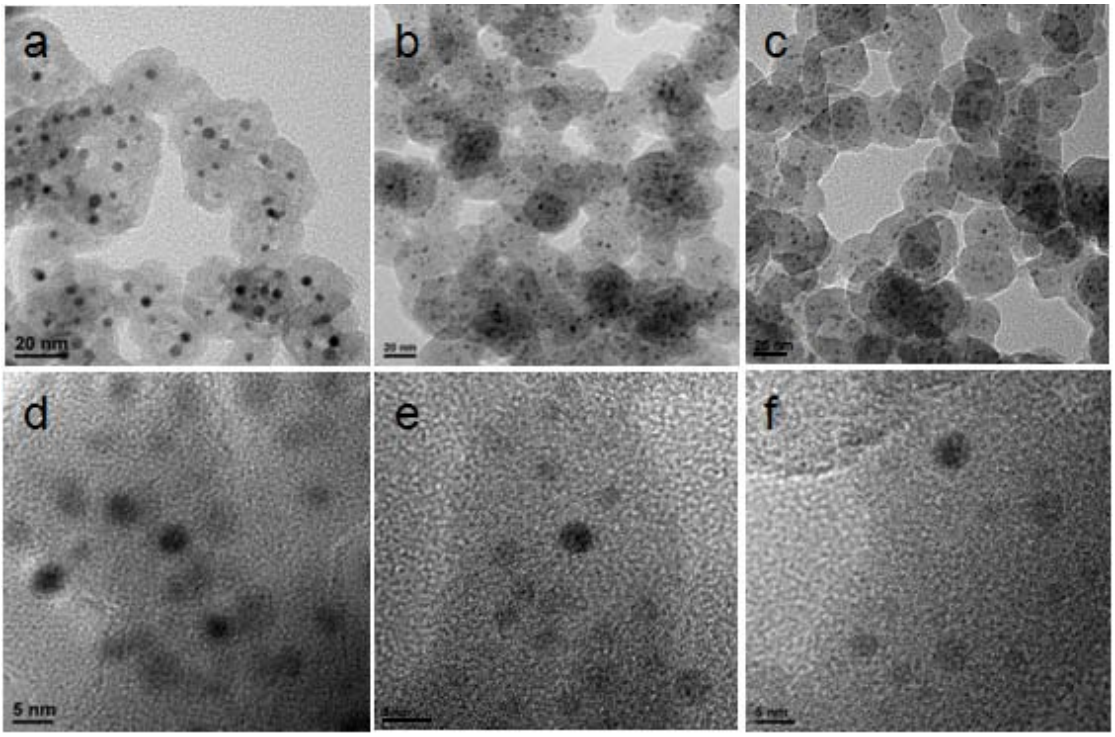

Fig. 4.2. HRTEM images of a,d) Au3Pd@SiO_2, b,e) AuPd@SiO_2 and c,f) AuPd10@SiO_2. Scale Bars = 20 nm (top) and 5 nm (bottom)

No particle is observed at the outside of the silica sphere. This indicates nanoparticles are formed from nanoclusters through agglomeration process during calcination but in a controlled manner and nanoparticles are stabilized successfully inside silica matrix. Particle size distribution is made by measuring individual size of ca 100 nanoparticles [Fig. 4.3]. In Au3Pd@SiO_2, the average particle size is found to be ~ 4.2 nm and in

$AuPd@SiO_2$ and $AuPd10@SiO_2$, the average size could be controlled to ~ 3.6 nm and 3.3 nm respectively.

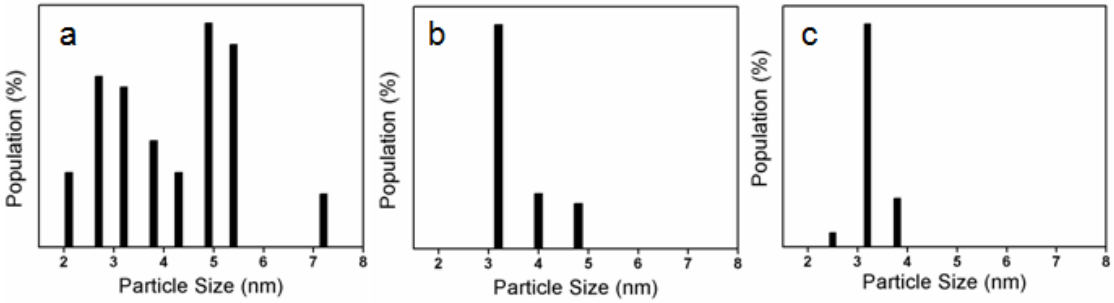

Fig. 4.3. Particle size distribution graph of a) $Au3Pd@SiO_2$, b) $AuPd@SiO_2$ and C) $AuPd10@SiO_2$ calcined at 550 °C.

4.4.2.2. Inductively Coupled Plasma Spectroscopy (ICP)

Metal compositions of the final silica encapsulated alloy materials could be controlled by the initial concentrations of metal nanoclusters. Elemental analysis of the final products by ICP-AES [Table 4.1] revealed compositions of 2.77:1, 1.06:1 and 0.07:1 respectively for the above alloys indicating a correspondence of final composition and initial metal precursor concentrations.

Table 4.1. Elemental composition of silica encapsulated Au-Pd and Pd catalysts

Catalysts	Au:Pd atomic ratio from ICP analysis		Wt %	
	Initial synthesis solution	Final Au-Pd@SiO_2	Au	Pd
Au3Pd	2.85:1	2.77:1	5.4	1.1
AuPd	0.95:1	1.06:1	3.3	1.6
AuPd10	0.1:1	0.07:1	0.36	2.48
Pd				2.62

4.4.2.3. SEM-EDAX Analysis

Elemental analysis by SEM-EDAX also corroborated the trend obtained for ICP analysis and elemental mapping over a range of 512 μm x 400 μm provided evidence of intimate mixing and no sign of segregation at this scale could be observed

[Fig. 4.4 and 4.5]. However, at this stage, we do not have a clear picture of the extent of alloying within the nanoparticles.

a

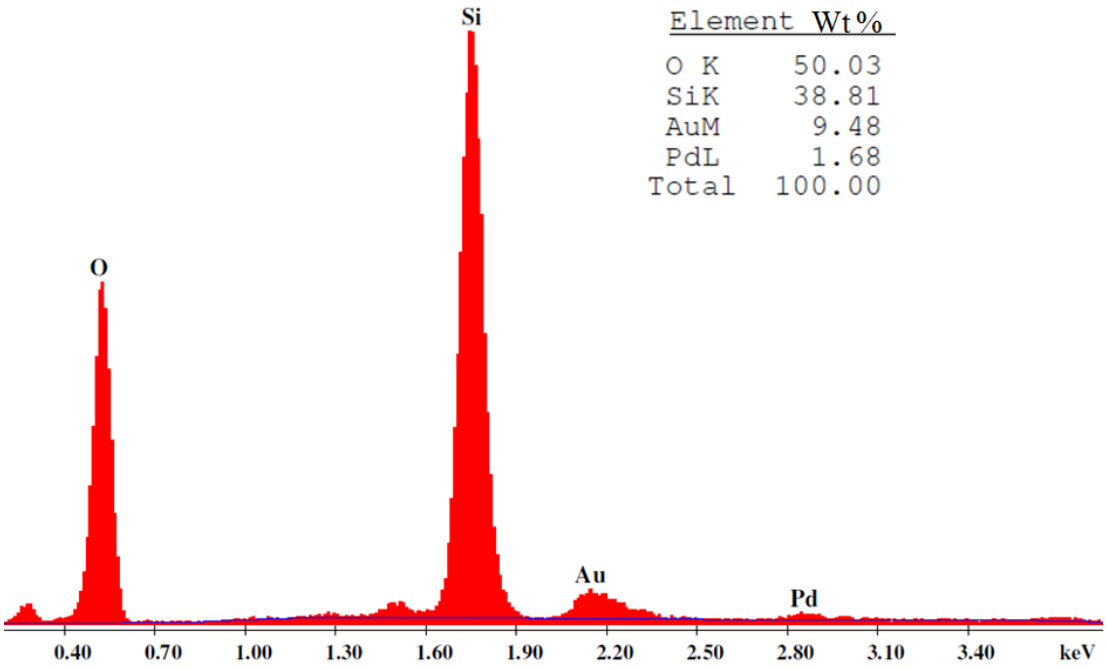

b

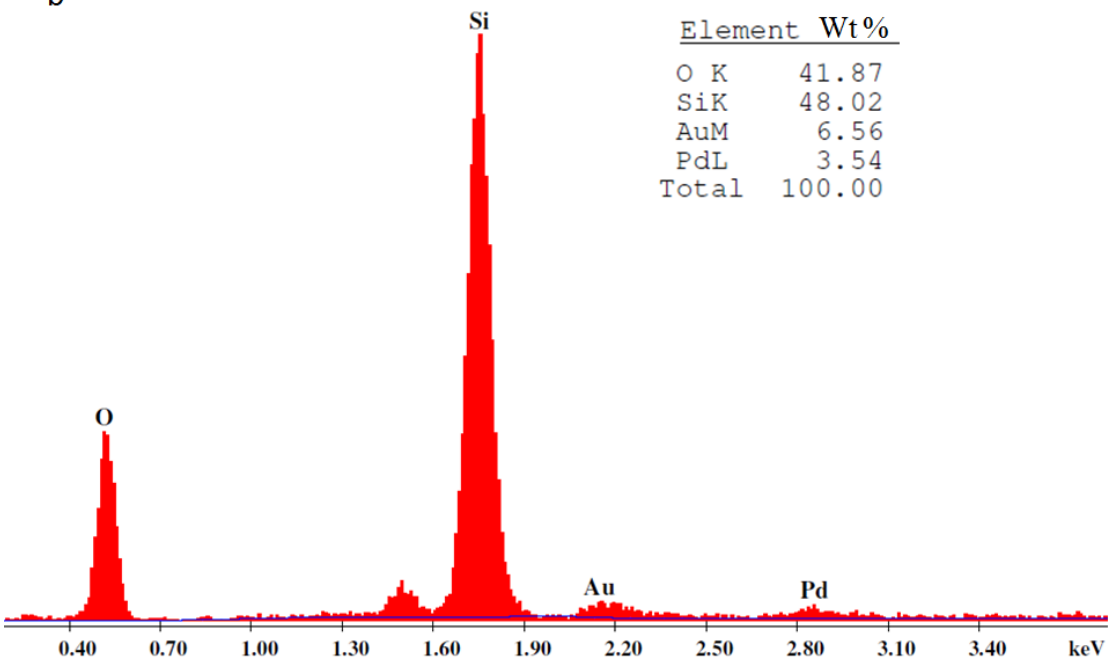

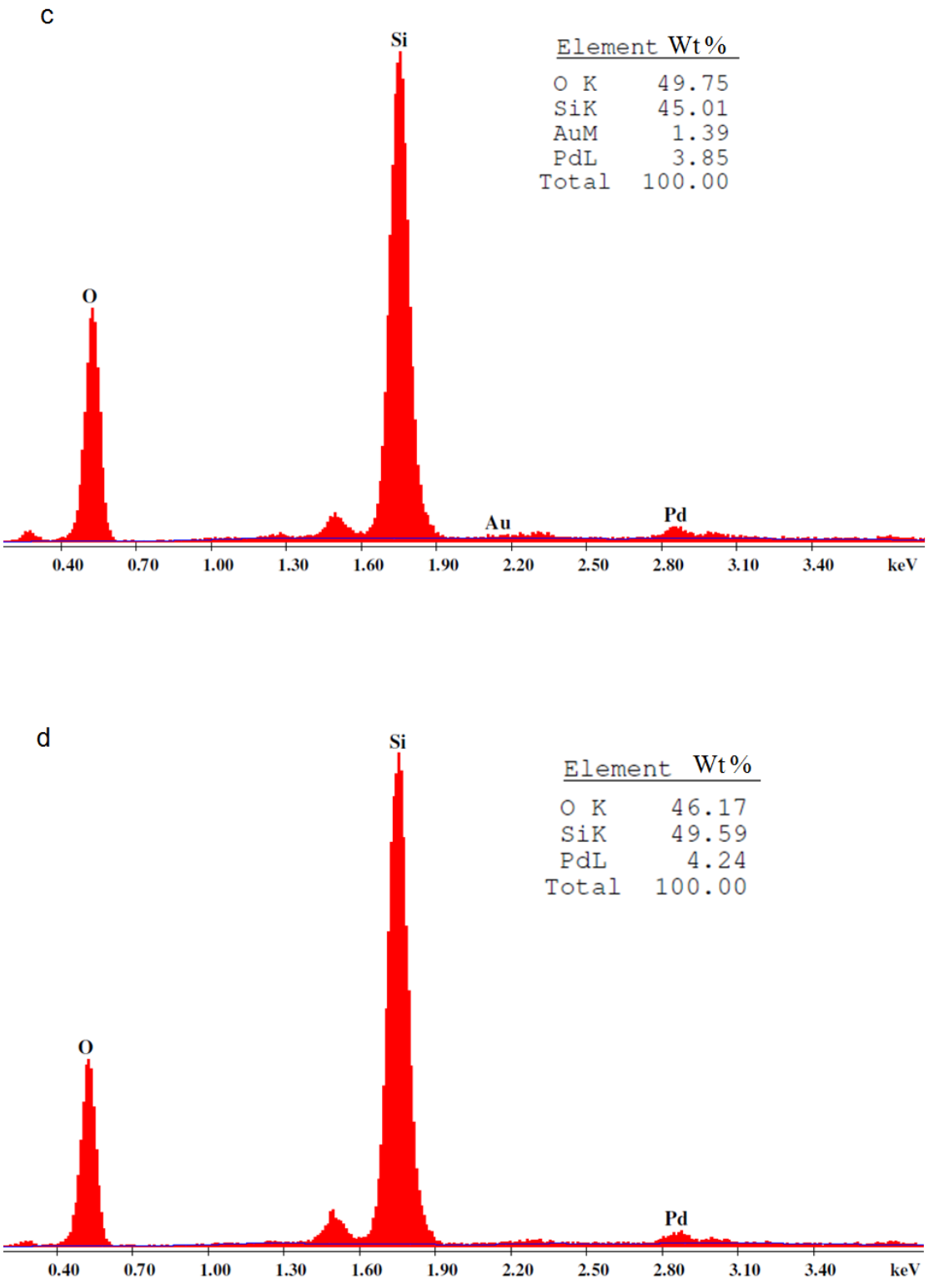

Fig. 4.4. EDAX spectra of a) Au3Pd@SiO_2, b) AuPd@SiO_2, C) AuPd10@SiO_2, d) Pd@SiO_2 and respective microanalysis (insets).

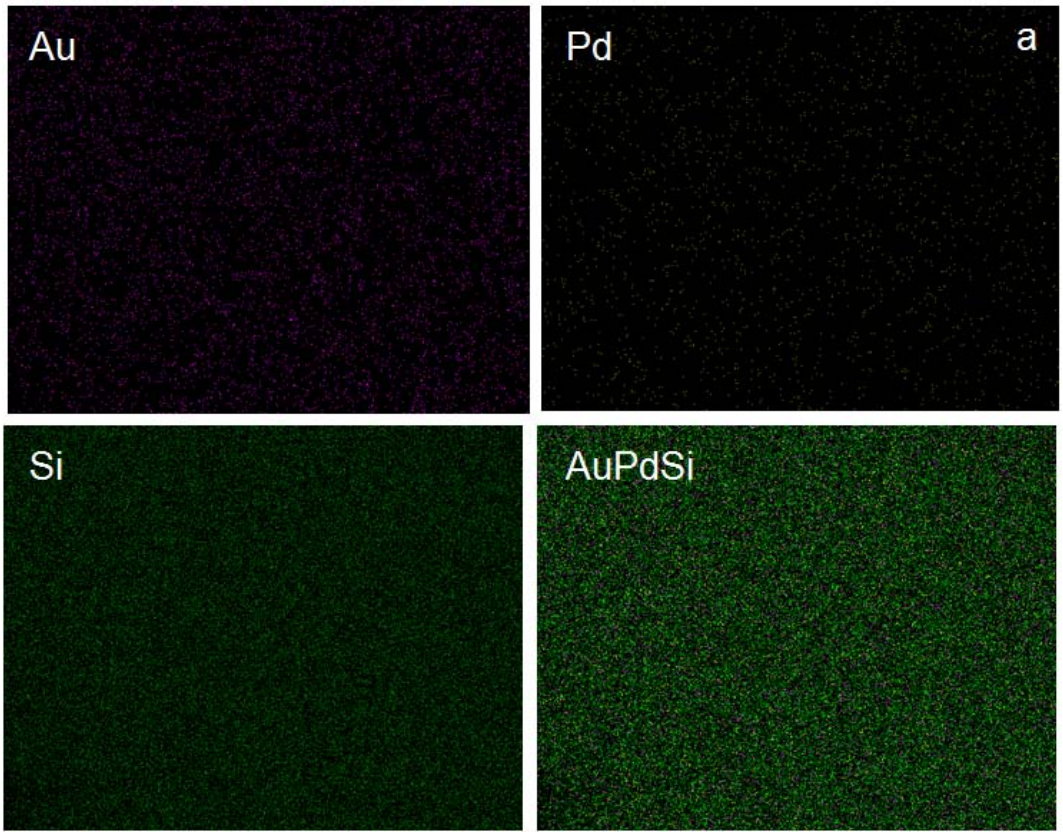
Au
Pd
a
Si
AuPdSi

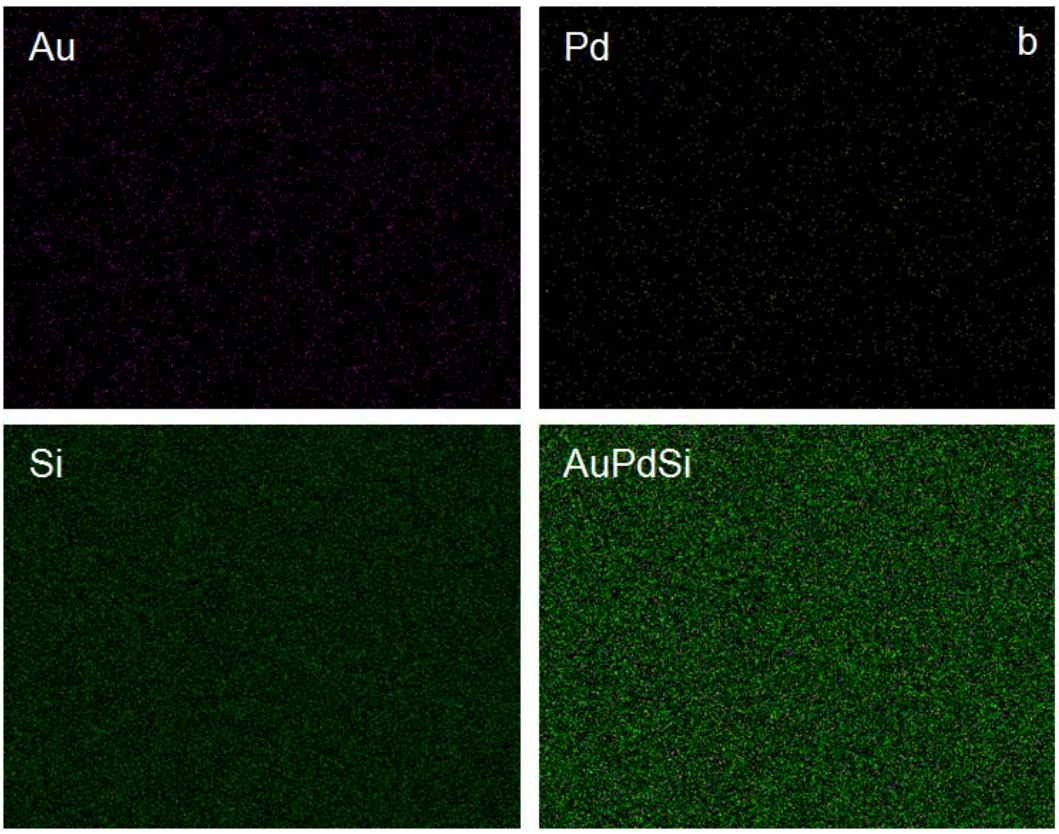
Au
Pd
b
Si
AuPdSi

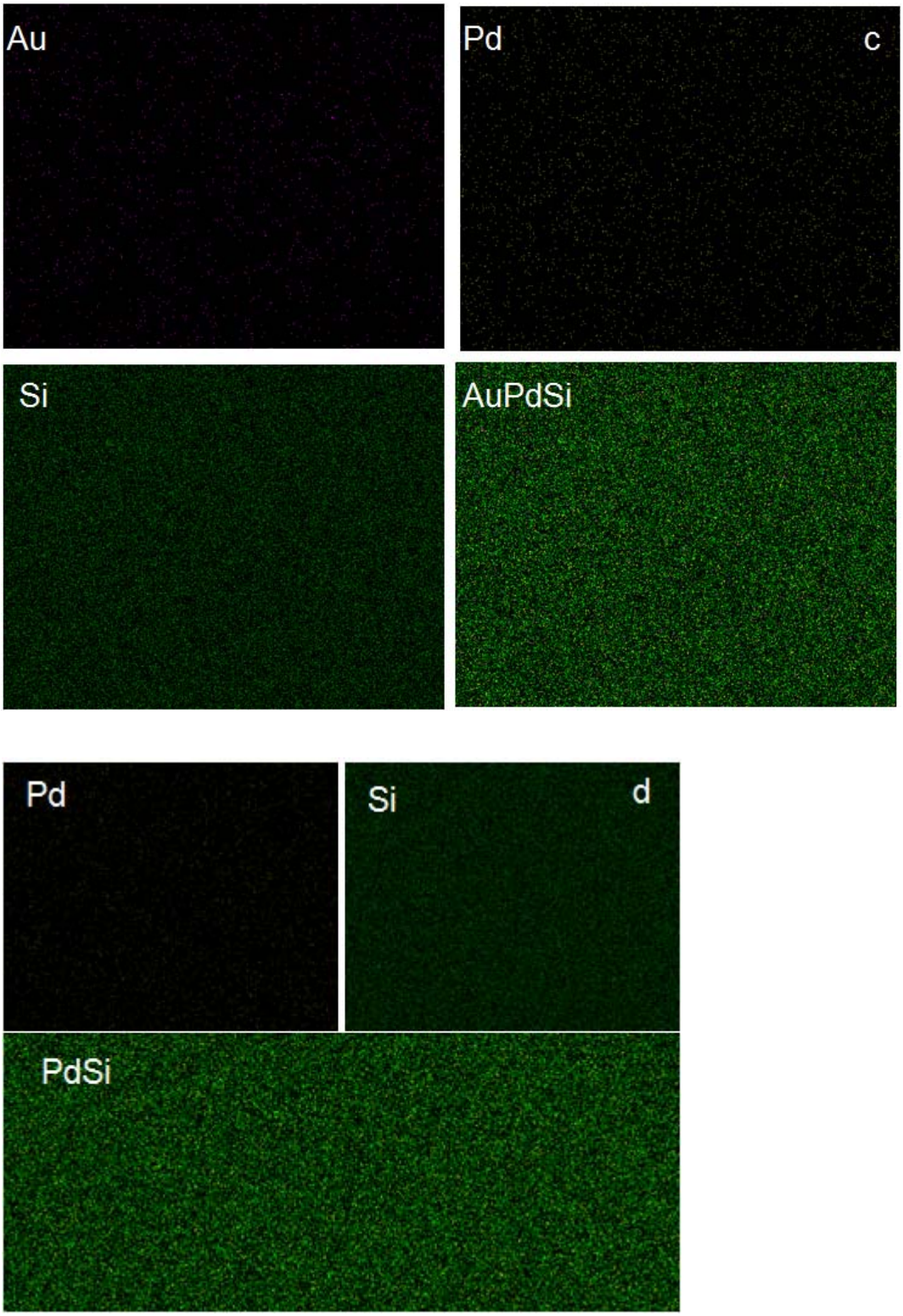

Fig. 4.5. SEM elemental mapping analysis of a) Au3Pd@SiO_2, b) AuPd@SiO_2, C) AuPd10@SiO_2 and d) Pd@SiO_2.

4.4.2.4. TEM-EDAX Analysis

Selected area TEM-EDX analysis shows the presence of both Au and Pd element in nanometer regime [Fig. 4.6]. This supports the intimate mixing of Au and Pd atom in nanometer regime. But this is not conclusive to prove the alloy formation and further characterizations are necessary.

a)

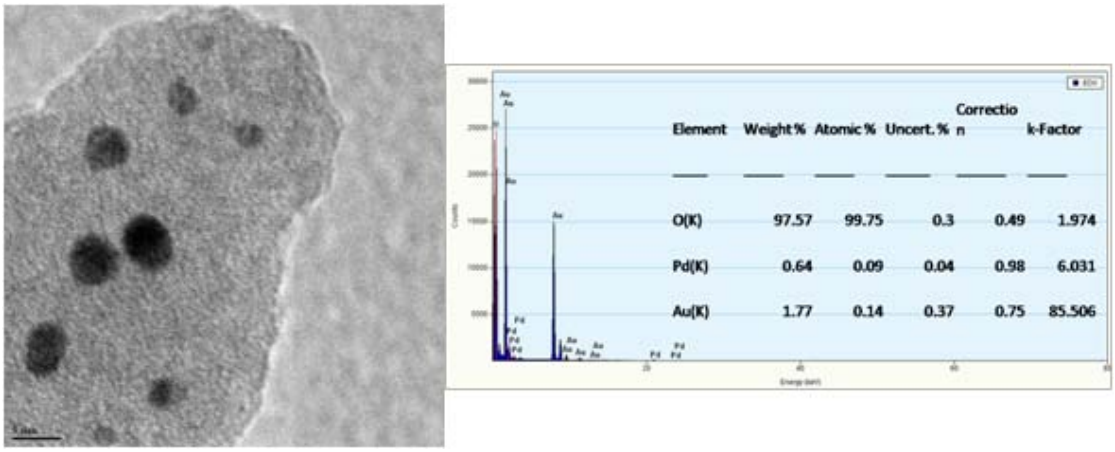

b)

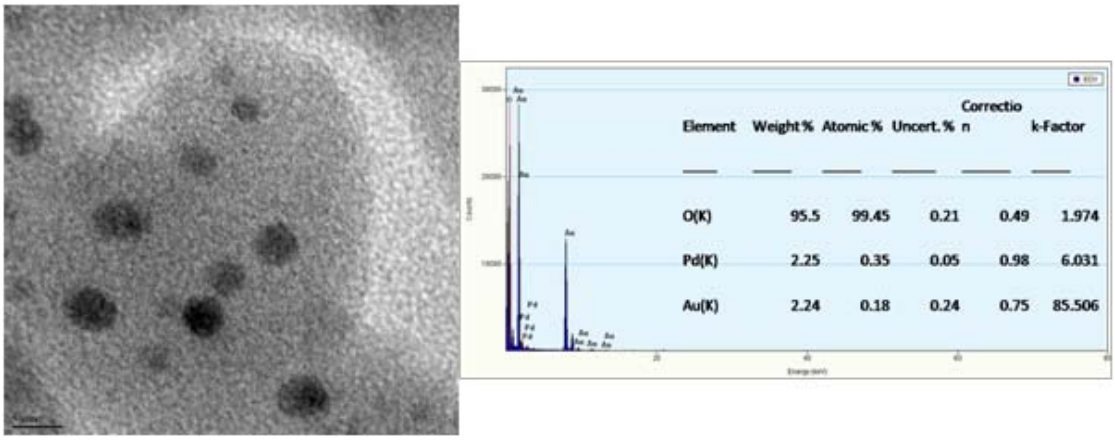

C)

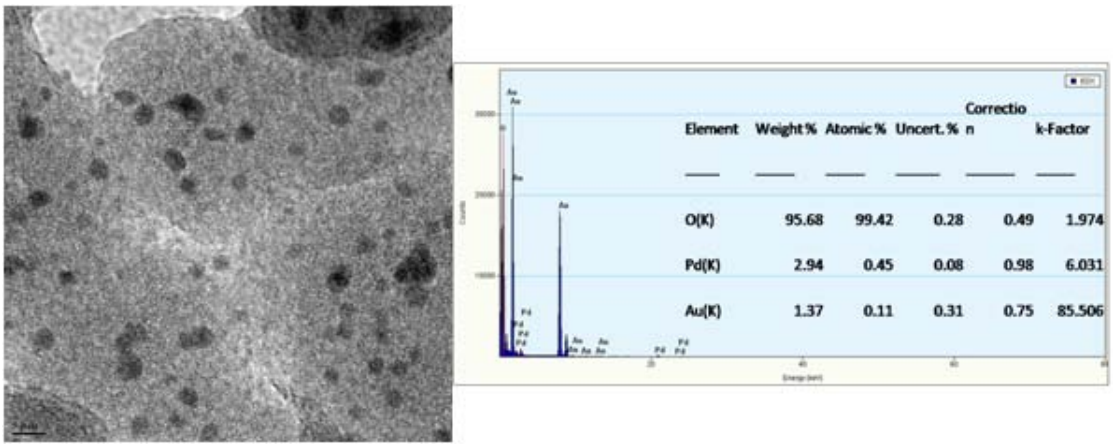

Fig. 4.6. Selected area TEM-EDX analysis of a) Au3Pd@SiO_2, b) AuPd@SiO_2 and C) AuPd10@SiO_2 and respective microanalysis (right).

4.4.2.5. UV-Vis Spectroscopy

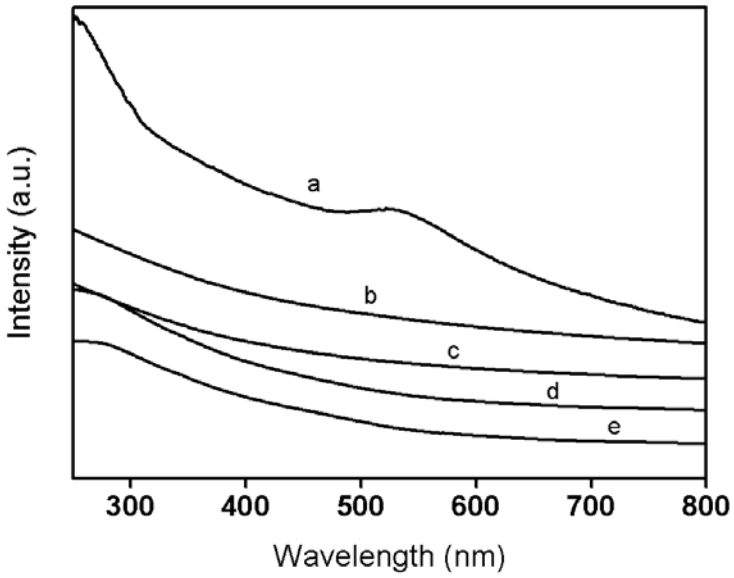

Fig. 4.7. UV-visible spectra of a) Au@SiO_2, b) Au3Pd@SiO_2, c) AuPd@SiO_2, d) AuPd10@SiO_2 and e) Pd@SiO_2.

Optical properties of Au nanoparticles are known to be affected by alloying with metals which do not exhibit such properties [22,25]. Au nanoparticles display Surface Plasmon Resonance (SPR) bands in the visible region whereas Pd

nanoparticles show an exponential decay in case of clusters which flats out in the visible region as size increases. A comparison of the UV-vis spectra of the alloy catalysts with that of the $Au@SiO_2$ indicates, tentatively, alloy formation in these catalysts [Fig. 4.7] as evident from the absence of SPR band at ~ 535 nm.

4.4.2.6. Powder X-ray Diffraction

Further structural analysis of the materials was carried out by Powder XRD. XRD patterns of the three alloy samples are given in Fig. 4.8 and extremely small particle sizes are indicated by the broadness of the peaks.

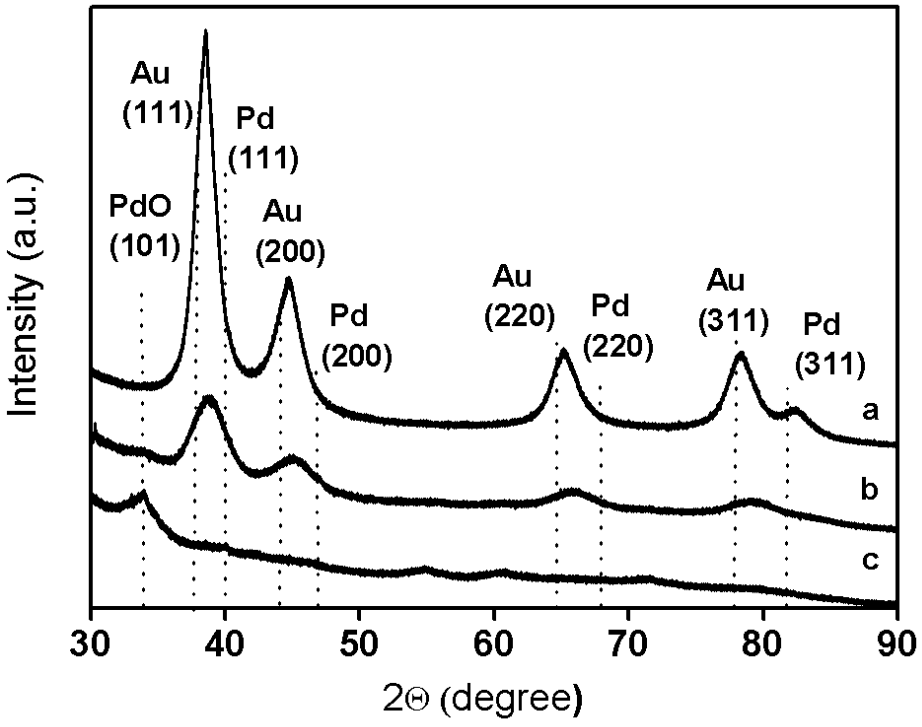

Fig. 4.8. XRD patterns of a)$Au3Pd@SiO_2$, b) $AuPd@SiO_2$ and c) $AuPd10@SiO_2$; the dotted lines indicate the position of $Au@SiO_2$, $Pd@SiO_2$ and $PdO@SiO_2$.

For comparison, peak positions of pure $Au@SiO_2$ and $Pd@SiO_2$ calcined at 250 °C and 550 °C respectively and $Pd@SiO_2$ heated under H_2 at 400 °C are also given, corresponding to pure Au, PdO and Pd. It is to be noted that pattern of calcined $Pd@SiO_2$ indicates that Pd is present as PdO. However, on treating with a flow of H_2 at 400 °C, complete reduction to metallic Pd phase could be observed. These two

patterns were used as standards for estimating the alloy compositions. As evident from the figure, the (111) peak for pure Au is at 38.2 ° whereas it is at 40.1 ° in case of pure Pd metal. On the outset, a trend is seen in case of Au3Pd@SiO_2 and AuPd@SiO_2 with (111) peaks shifting to higher theta values as Pd amount increases. In case of AuPd@SiO_2, traces of PdO phase could be detected. It is noteworthy here that Pd rich sample AuPd10 shows the presence of PdO with trace amounts of metallic phase. Formation of PdO phases in oxide supported systems is often observed and attributed to oxidation facilitated by interactions with the support [26].

Further analysis and quantification of multiple phases in each of these compounds by Rietveld refinement [Appendix 4.1] was undertaken and the parameters are given in Table 4.2.

Table 4.2. Alloy composition analysis by Rietveld method

	Au	Pd	Au3Pd	AuPd	AuPd10
Lattice parameter, Å	4.0754(1)	3.8982(2)	4.0499(0)	4.0149(1)	3.9156(7)
Au-Pd alloy phase (wt%)			100	94.905	7.707
PdO phase (wt%)			0	5.095	92.293
Cell volume , $Å^3$	67.687(6)	59.239(11)	66.425(2)	64.717(5)	60.035(32)
$\chi 2$	4.019	1.17	3.593	1.066	1.329
wRp (%)	3.57	2.20	3.22	1.92	2.23
Rp(%)	2.90	1.74	2.63	1.51	1.74
Alloy composition			$Au_{86}Pd_{14}$	$Au_{66}Pd_{34}$	$Au_{10}Pd_{90}$

Earlier report of supported AuPd alloy nanoparticles synthesized by oxidation-reduction treatment suggested the formation of Au and Pd rich alloys in the whole range of compositions [11]. However, we have not observed this; rather, unalloyed Pd was found to exist as PdO phase. The unit cell length of the alloy phase in the three compounds varied within the range of pure Au and Pd calculated as 4.0754 Å to 3.8982 Å respectively. The amounts of PdO phase in Au3Pd@SiO_2 and AuPd@SiO_2 were found to be 0 % and 5.1 % indicating a very high percentage of alloying. Au and Pd are reported to be completely miscible in all composition ranges and lattice parameters of the alloy phases hold a linear relation with composition according to Vegard's law. Taking the cell parameters of pure Au@SiO_2 and Pd@SiO_2 as the end members of the bimetallic system, their linear relation to composition was reached by

the equation y=0.00178x+3.8982 (Appendix 4.2). Based on this, the alloy compositions were estimated and are tabulated in Table 4.2.

In Au3Pd@SiO_2 only one phase could be observed, which is an alloy whose composition was estimated to be $Au_{86}Pd_{14}$ and no PdO formation was detected. In AuPd@SiO_2, the metallic phase was estimated to be of composition, $Au_{66}Pd_{34}$ and was present at 95% and PdO was present at 5 %. However, in case of AuPd10@SiO_2, 93% PdO was present along with 7.7 % of alloy with composition $Au_{10}Pd_{90}$.

If we consider the amount of PdO as an estimate of unalloyed Pd in each sample, it can be observed that extent of alloying depends on the Au amount, in other words, Au seems to be more amenable for alloying than Pd. Unalloyed Pd is present only in traces in case of AuPd@SiO_2 but drastically increases when Au amount is reduced by tenfold in AuPd10@SiO_2. This gives credence to the fact that oxidation of Pd is more facile than Au and hence Pd may be segregating into PdO phase on the metal-support interface.

4.4.2.7. X-ray Photoelectron Spectroscopy

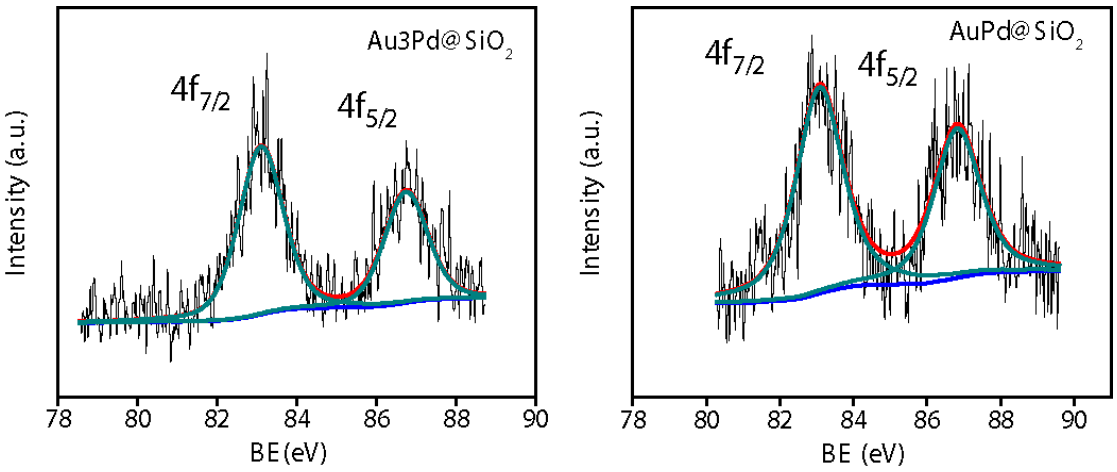

Fig. 4.9. $4f_{7/2}$ and $4f_{5/2}$ XPS spectra of (left) Au3Pd@SiO_2 and (right) AuPd@SiO_2

Evidence of alloying was also obtained from observing the binding energy differences of Au and Pd in these samples by X-ray photoelectron spectroscopy. Even though encapsulation within SiO_2 is expected to decrease the signal to noise ratio due to limitations of probing depth, we could obtain some indicators in case of Au due to

its higher scattering capacity. Au $4f_{7/2}$ peak in case of monometallic Au is expected at 84 eV. As a consequence of alloying, electronic effects referred to as "ligand effect" come into play because of electron transfer from Pd to Au thereby shifting the binding energy to lower values [21,22]. In $Au3Pd@SiO_2$ and $AuPd@SiO_2$ catalysts, this effect is clearly seen with binding energies shifting to 83.08 and 83.06 eV respectively [Fig. 4.9].

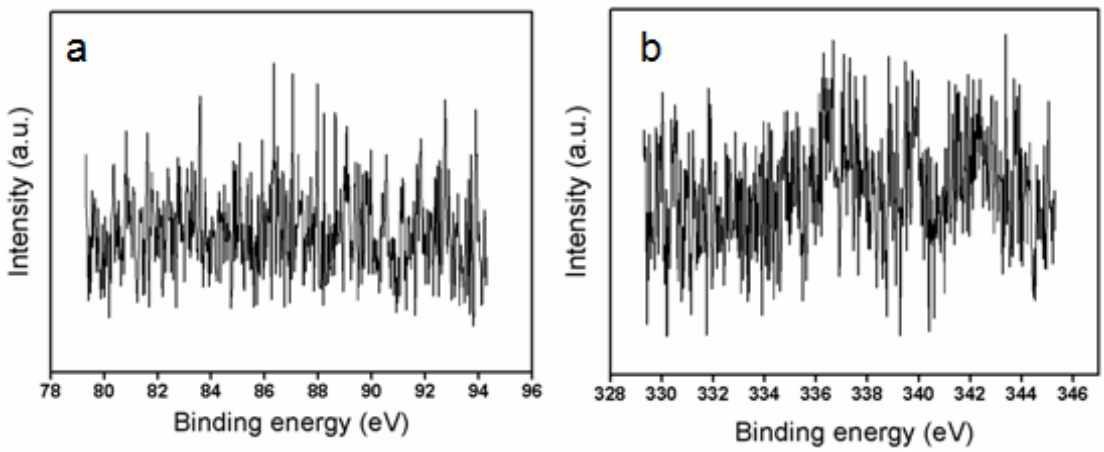

Fig. 4.10. a) Au XPS spectrum and b) Pd XPS spectrum of $AuPd10@SiO_2$.

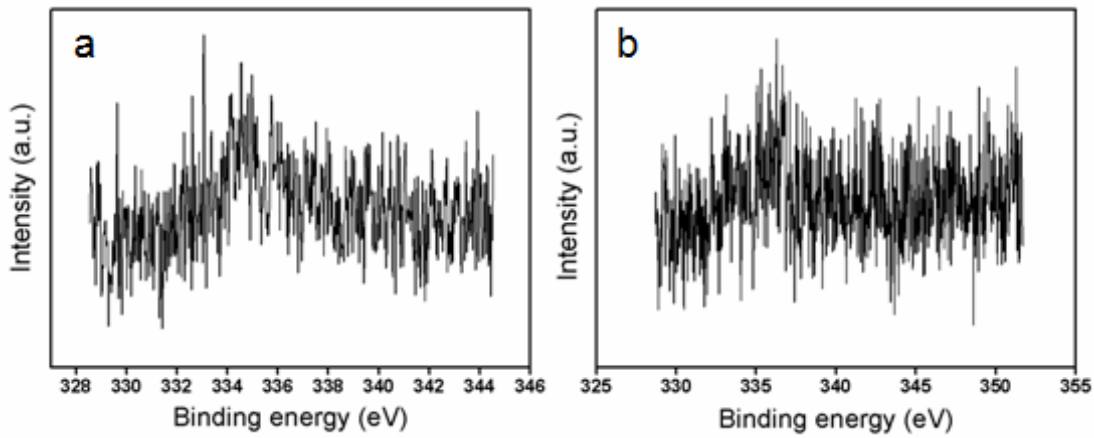

Fig. 4.11. Pd XPS spectrum of a) $Au3Pd@SiO_2$ and b) $AuPd@SiO_2$.

$AuPd10@SiO_2$ does not show the characteristic $Au4f_{7/2}$peak in XPS spectrum due to presence of very low amount of gold [Fig. 4.10 a]. However, we were unable to detect Pd peak which is expected due to the lower scattering capacity of Pd atom compared to Au atom [Fig. 4.10 b and Fig. 4.11]

4.4.2.8. N_2 Adsorption Study

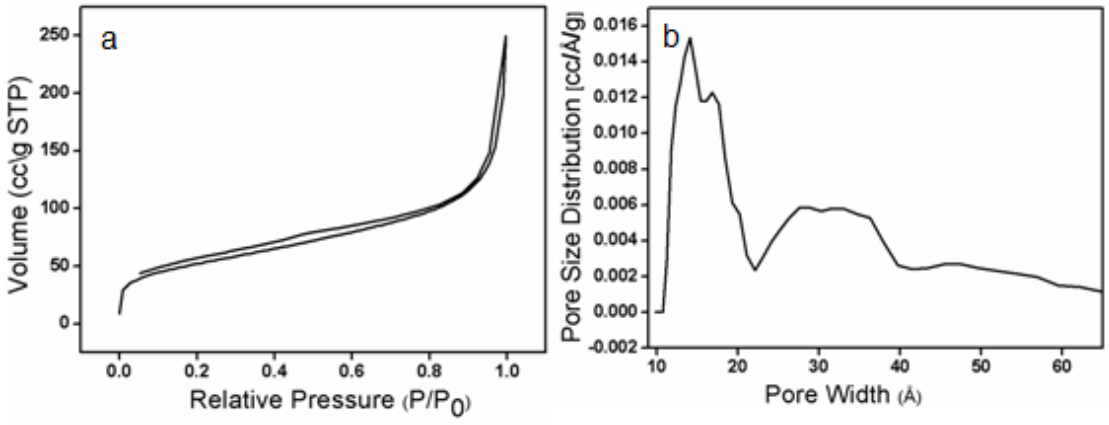

Fig. 4.12. a) N_2 adsorption–desorption isotherms of the sample Au3Pd@SiO_2 calcined at 550 °C and b) Pore size distribution calculated from the adsorption branch of the isotherms by DFT method.

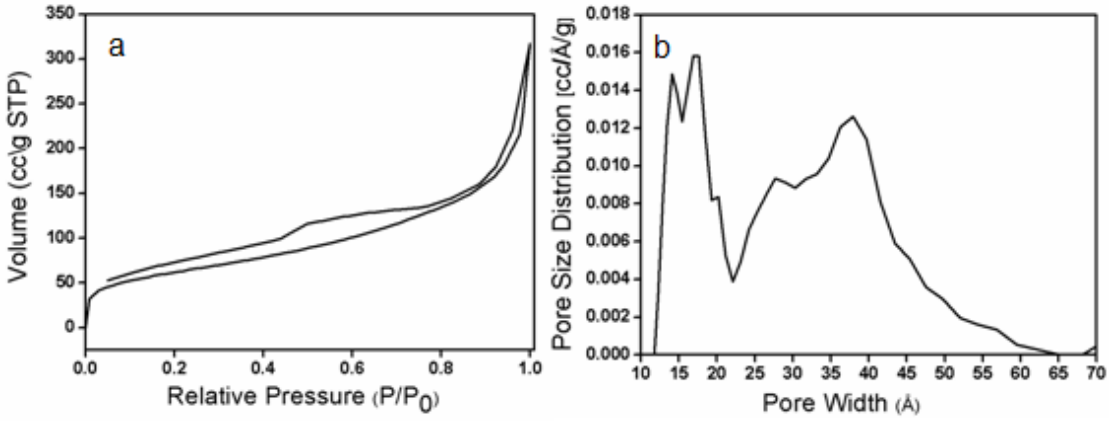

Fig. 4.13. a) N_2 adsorption–desorption isotherms of the sample AuPd@SiO_2 calcined at 550 °C and b) Pore size distribution calculated from the adsorption branch of the isotherms by DFT method.

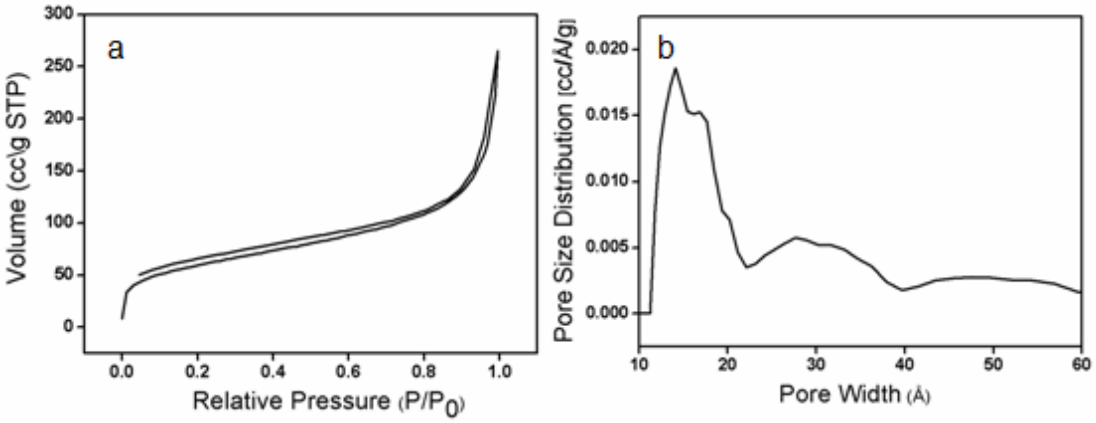

Fig. 4.14. a) N_2 adsorption–desorption isotherms of the sample AuPd10@SiO_2 calcined at 550 °C and b) Pore size distribution calculated from the adsorption branch of the isotherms by DFT method.

N_2-adsorption studies indicate the presence of micro and mesoporosity [Fig. 4.12, 4.13 and 4.14]. The pore size distribution curve calculated from the adsorption branch of the isotherm exhibited a distribution from 1.5 to 3 nm and the BET surface areas of the samples calcined at 550 °C were estimated to be 190, 220 and 215 m^2 g^{-1} for Au3Pd@SiO_2, AuPd@SiO_2 and AuPd10@SiO_2 respectively. This study confirmed the porous nature of the silica matrix necessary for getting access of the active metal centre.

4.5. THERMAL STABILITY STUDY OF THE POROUS SILICA ENCAPSULATED Au-Pd ALLOY NANOPARTICLES

To compare the thermal stability of pure silica encapsualed Au nanoparticle with alloy AuPd nanoparticles, Au@SiO_2 was synthesized by following the method which is already described in Chapter 2 (section 2B.2.1). Material was synthesized by using excess TEOS and as-synthesized sample was calcined at 500 °C. We observed agglomeration to some extent in the catalyst system consisting of pure Au, viz., Au@SiO_2 after calcination at 500 °C, leading to average particle size of ~ 7 nm [Fig. 4.15]. However, in case of bimetallic systems, presence of Pd has assisted immensely in controlling the particle growth of Au as revealed by particle size analysis.

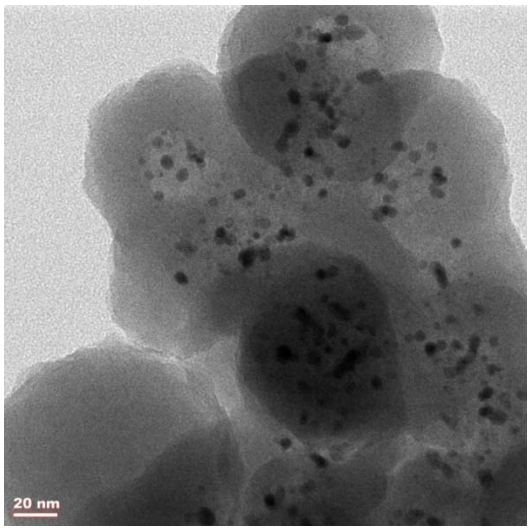

Fig. 4.15. TEM image of silica encapsulated gold nanoparticles.

Tamman temperature of Au is low compared to that of Pd, hence an enhanced sinter resistance is observed in Pd. This trend can also be expected in case of alloys and was indeed observed in thermal stability testing of the three alloy samples.

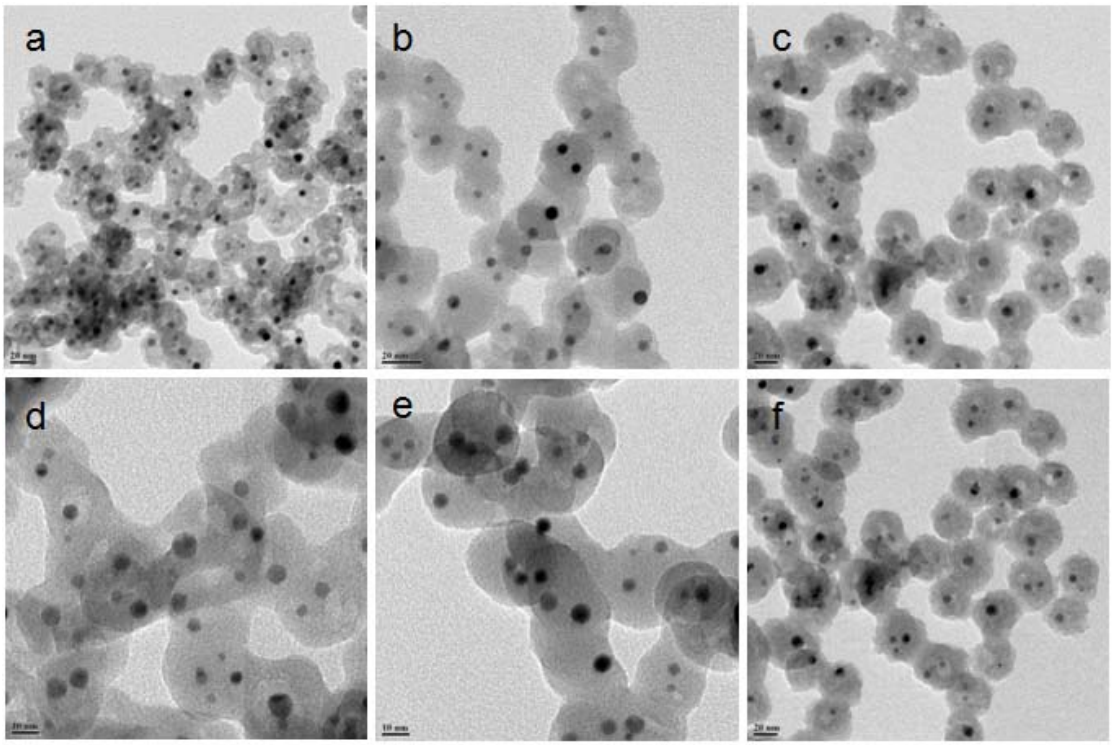

Fig. 4.16. TEM images of a, d) Au3Pd@SiO_2, b,e) AuPd@SiO_2 and c, f) AuPd10@SiO_2 calcined at 750 °C under air for 6 h. Scale bars for images a, b, c and f = 20 nm and for images d and e = 10 nm.

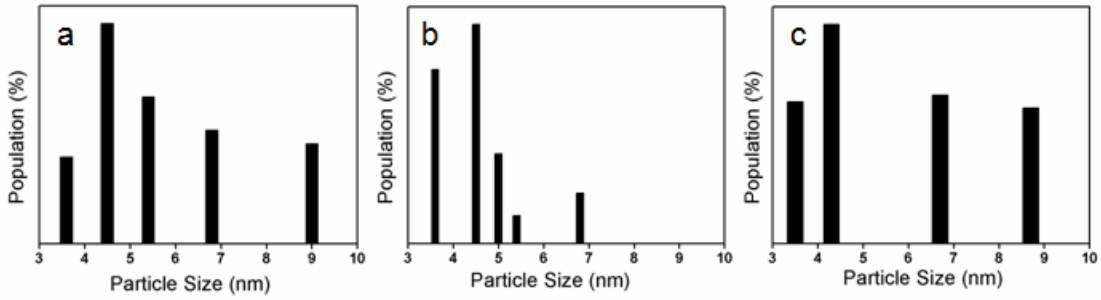

Fig. 4.17. Particle size distribution graph of a) Au3Pd@SiO_2, b) AuPd@SiO_2 and C) AuPd10@SiO_2 catalysts calcined at 750 ºC.

This was carried out by TEM analysis of the samples heated at 750 °C under air for 6 h [Fig. 4.16] which revealed that the average particle size was ~ 5.6 nm for Au3Pd@SiO_2 and AuPd10@SiO_2, and ~ 4.5 nm for AuPd@SiO_2 [Fig. 4.17]. This shows that silica encapsulated AuPd alloy materials with appropriate concentrations of Au and Pd are sinter resistant and present themselves as potential candidates as pollution abatement catalysts.

4.6. CO OXIDATION BY POROUS SILICA ENCAPSULATED Au-Pd ALLOY NANOPARTICLES

4.6.1. CO Oxidation

CO oxidation is an important reaction in abatement of vehicular pollution. Two parameters are important in this process (i) low light-off temperature at which CO is fully converted to CO_2 to reduce the CO emission on cold starts and (ii) sinter resistance at high temperatures under oxidizing conditions as a consequence of heating up of the catalysts during operation. Currently, Pt based catalysts are used mainly due to better stability under oxidizing conditions when compared to more cost effective Pd based catalysts [27]. It is known that reducibility as well as activity of Pd can be enhanced with alloying. CO oxidation proceeds through Langmuir-Hinshelwood mechanism [Fig. 4.18] and co-adsorption of both reactants CO and active oxygen is the most fundamental step [28].

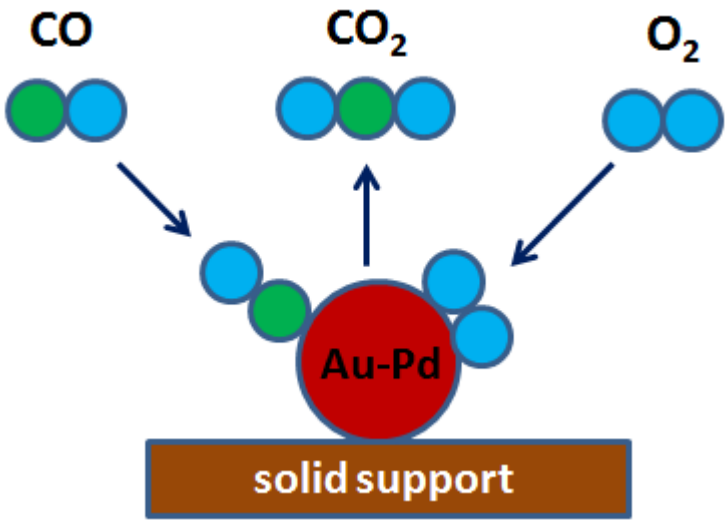

Fig. 4.18. CO oxidation on supported noble metal catalyst through Langmuir-Hinshelwood mechanism.

It is well known that Au particles as well as bulk Au can absorb CO under reaction conditions, but cannot activate molecular O_2. Pure Pd catalyst is capable of O_2 activation, but it is active for CO oxidation reaction only at higher temperatures (≥400 K) under steady-state conditions [29,30]. For pure Pd, the metal surfaces are fully covered with a layer of chemisorbed CO at relatively low temperatures which prevents the adsorption of O_2, thereby reducing the reaction rate [2].

AuPd alloy surface, on the other hand, has lower CO binding energy compared to pure Pd because of charge transfer from Pd to Au. It also has the O_2 dissociation capability because of contiguous Pd sites. So Au-Pd alloys can perform the CO oxidation more efficiently than pure Au and pure Pd catalysts at lower temperatures. However, Pd contiguous sites are disrupted due to the introduction of excess Au atom and hence optimum Au concentrations have to be arrived at for efficient CO oxidation. Moreover, an efficient catalyst system should also address sintering problems effectively, by controlling particle sizes to < 5 nm at elevated temperatures. In continuation to this train of logic, we hypothesize an enhancement in activity if alloying is made synergistic to sinter resistance, thereby giving an advantage to encapsulated alloy nanoparticles.

4.6.2. Experimental set up and reaction condition

For catalytic activity testing, catalysts were pre-treated prior to reaction. Catalysts were kept under 20 % O_2 in N_2 for 2 h at 100 °C. The catalyst tests were carried out under atmospheric pressure in a fixed bed reactor of diameter 3 mm. Mass flow controllers (Brooks) were used to control the gas flow from the respective cylinders N_2, O_2 and CO. The reactor was placed in a tubular furnace with a uniform heating zone of 4 cm and temperature of the furnace was controlled using Radix 6400 temperature controller. A K-type thermocouple placed in a thermowell over the catalyst was used to measure the catalyst bed temperature. A reaction gas containing 4.6 % v/v CO was passed over 17 mg of the pretreated catalyst. The flow rate of the reaction gas mixture was 25 $mLmin^{-1}$ (1:5:15.7, $CO:O_2:N_2$) and the calculated GHSV was 15000 $cm^3g^{-1}h^{-1}$. The conversion reported here is carried out in the steady state where catalyst temperature is ramped at 2 °C min^{-1} and held at various temperatures for 10 min for equilibration. After the equilibration, data was checked for consistency by noting the conversion at 5 min interval (thrice) at the specific temperature. The reactor outflow was analyzed using a NUCON gas chromatograph equipped with a Carbosphere column and a thermal conductivity detector. All the catalytic test runs were carried out from room temperature to 200 °C.

4.6.3. Catalytic activity

Catalytic activities of the three samples were tested for CO oxidation and the results support the observations from the above characterizations. AuPd@SiO_2catalyst showed 100 % CO conversion at the lowest temperature indicating the composition to have optimum surface Au among the three catalysts [Fig. 4.19 a]. The catalytic results in terms of moles of CO converted with respect to moles of total Pd is shown in Fig. 4.19 b. For comparison study pure porous silica encapsulated Pd nanoparticles (Pd@p-SiO_2) was synthesized. Details of the synthesis is given in Chapter 3 (section 3.2.2), only one change was employed; as-synthesized materials was calcined at 550 °C instead of 350 °C.

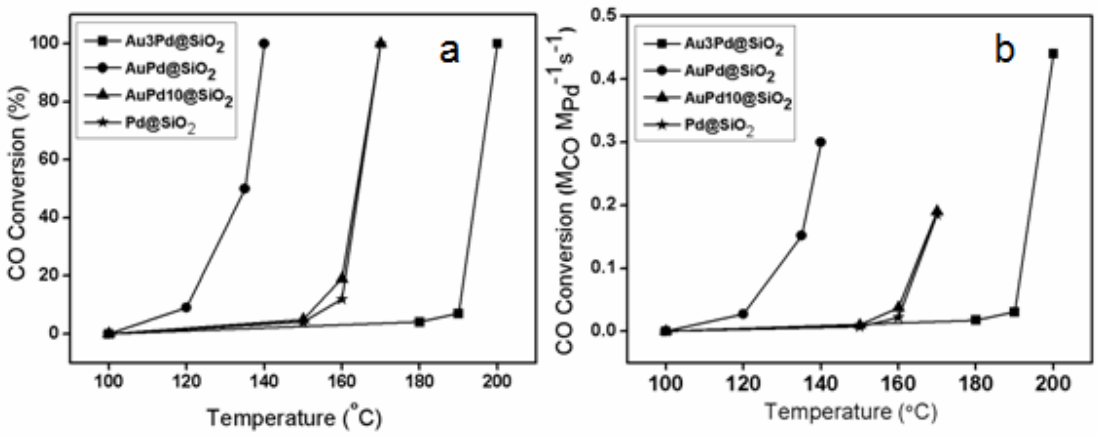

Fig. 4.19. a) CO conversion with temperature by the four catalysts and b) CO conversion vs. temperature plot for the alloy catalysts in comparison to pure Pd@SiO_2. Activity is measured based on moles of CO converted with respect to total concentration of Pd

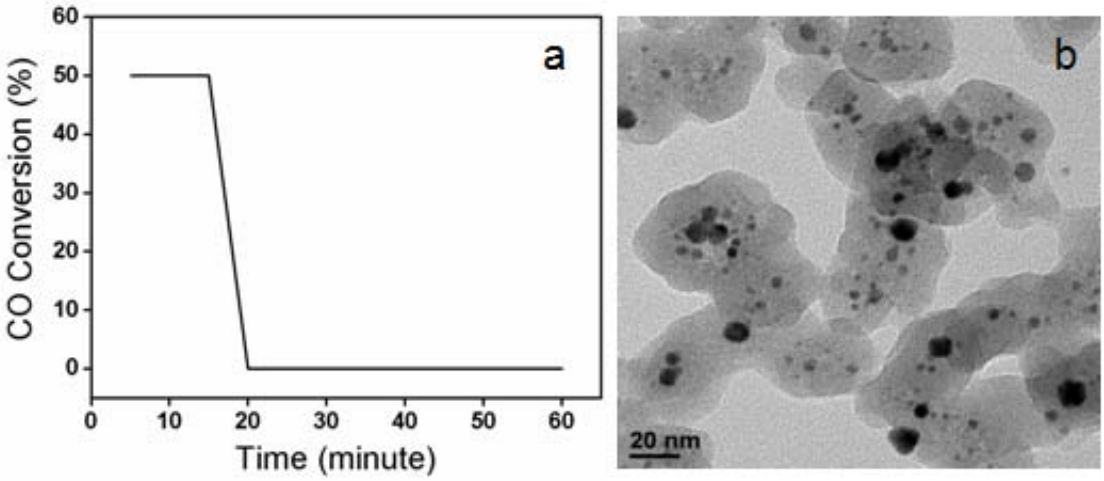

Fig. 4.20. a) CO conversion as a function of time-on-stream by Au@SiO_2 at room temperature (28 °C) and b) HRTEM image of Au@SiO_2 catalyst after CO oxidation study.

Total number of Pd atom of each catalyst was calculated based on ICP-AES studies of the materials. Details of the calculations are given in the Appendix 4.3. Pure Au catalyst Au@SiO_2, even though very highly active at lower temperatures, showed a drastic deactivation immediately on stream [Fig.4.20 a]. It showed 50 % CO

conversion at room temperature (28 °C) which can be attributed to the presence of ~ 3 nm Au particle [Chapter 2, section 2B.4.2.1].

But under the reaction conditions, agglomeration of the particles was revealed by HRTEM analysis [Fig. 4.20 b] consequent to which, immediate deactivation occurred. On the other hand, Pd@SiO_2 showed reasonable activity with a light-off at ~ 160 °C. Even though full conversion of CO to CO_2 occurred at 170 °C [Fig. 4.19 a], turnover frequency based on activity per Pd site was only 0.185. Catalyst AuPd10 also showed similar activity understandably due to the excess of Pd practically rendering the surface similar to pure Pd catalyst. The very small percentage of alloying with low concentration of Au (10 %) apparently does not affect the activity much. However, the other two catalysts, Au3Pd@SiO_2 and AuPd@SiO_2 showed drastic difference in activities with AuPd presenting a light-off temperature as low as 120 °C. At the same time, we observe an increase in light off temperature to 190 °C in case of Au3Pd@SiO_2. Turnover frequencies at maximum conversion remained more or less same in all catalysts, except, Au3Pd@SiO_2 showing a marginal increase. Particle size may have played an important role in the activity profile along with electronic and ensemble effects. The average particle size and particle distribution was found to be higher for Au3Pd (4.2 nm) when compared to AuPd (3.3 nm). It is also plausible that with 85 % Au in the alloy, surface structure is not conducive for adjacent Pd islands. These two factors may have contributed to the comparatively less activity in Au3Pd.

Tamman temperature of Au is low compared to that of Pd, hence an enhanced sinter resistance is observed in Pd. This trend can also be expected in case of alloys and was indeed observed in thermal stability testing of the three alloy samples. This was carried out by TEM analysis of the samples heated at 750 °C under air for 6 h [Fig. 4.16] which revealed that the average particle size was ~ 5.6 nm for Au3Pd@SiO_2 and AuPd10@SiO_2, and ~ 4.5 nm for AuPd@SiO_2 [Fig. 4.17]. All the four catalysts are characterized by TEM after CO oxidation experiment [Fig. 4.21]. This shows particle sizes are more intact in the catalysts containing more amounts of Pd.

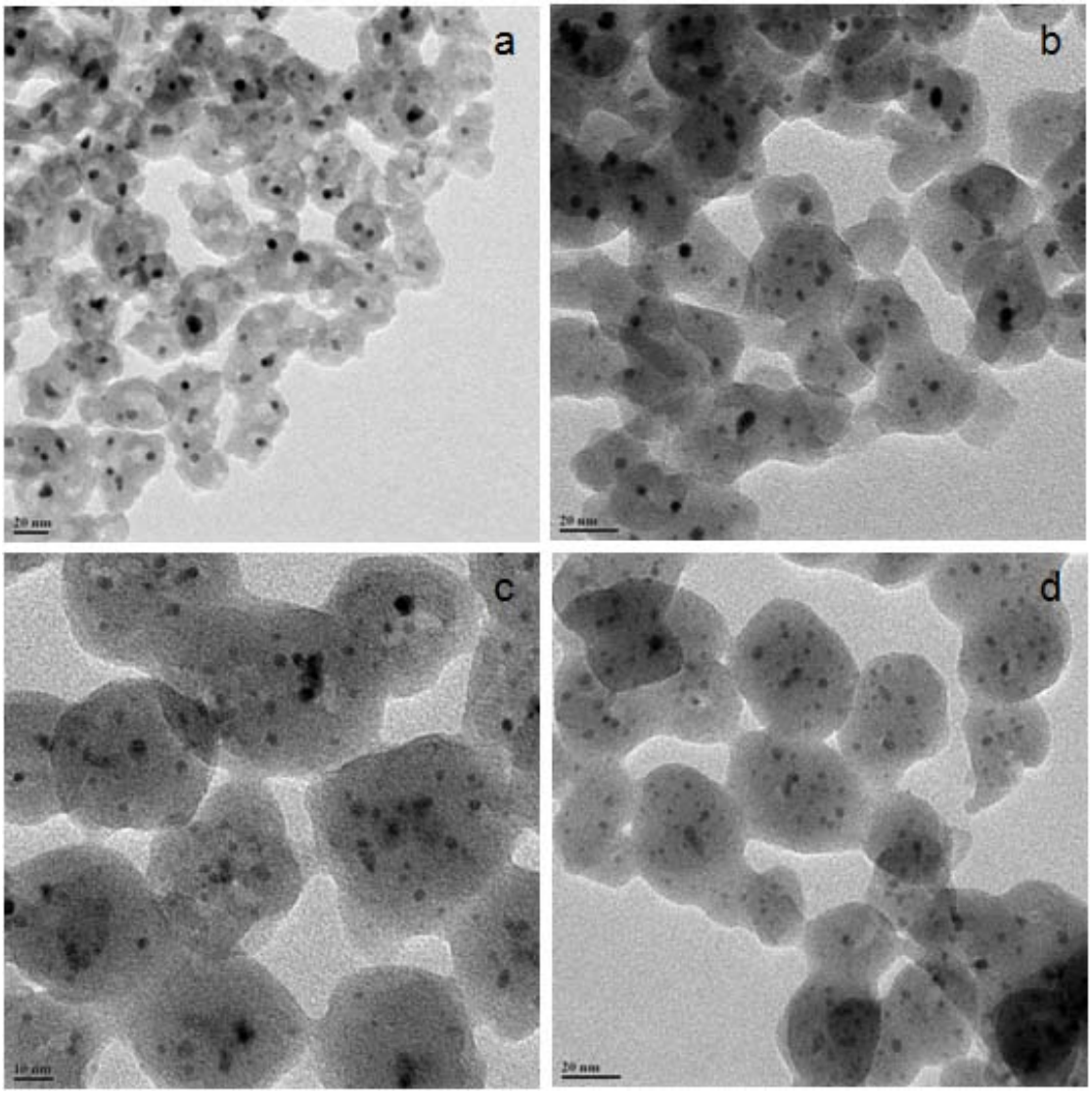

Fig. 4.21. TEM images of Au3Pd@SiO_2, b) AuPd@SiO_2, c) AuPd10@SiO_2 and Pd@SiO_2 after CO oxidation study, Scale Bars = 20 nm.

4.7. SUMMARY

In summary, highly monodisperse Au-Pd alloy nanoparticles could be encapsulated within porous silica matrix by a simple hydrolysis method which employs water dispersible ultra-small clusters of Au and Pd as precursors. The pristine Au and Pd clusters are synthesized by a modified Brust method using a novel long chain alkyl ligand with thiol group at one end and propyl ammonium group at the other end. The synergism of hydrophobicity and hydrophilicity ensures encapsulation of individual clusters with silica and these organics act more or less like templates and

helps in creating pores in the silica matrix when they are removed by high temperature calcination. Intimate mixing of the nanoclusters prior to encapsulation due to same ligand characteristics and the confined space available for growth during calcination at 550 °C assures monophasic alloy formation. Elemental analysis, structural characterization by Rietveld refinement of powder XRD profiles and XPS point to the formation of monophasic alloys. In the three concentration ratios attempted, viz., Au:Pd = 3:1, 1:1 and 1:10, alloy phases equivalent to $Au_{86}Pd_{14}$, $Au_{66}Pd_{34}$ and $Au_{10}Pd_{90}$ are present in 100, 94.5 and 7.7 %. The unalloyed Pd is observed to be present as PdO phase. It is noteworthy here that the alloy phases are formed without the reduction step followed in most of the reported cases. Also compared to other reported supported Au-Pd alloys, alloy composition and particle size could be much better controlled. Particle size seems to have a correlation with the Au amount with alloy phase having higher Au concentration, $Au3Pd@SiO_2$ forming bigger particles (4.2 nm) when compared to $AuPd@SiO_2$ (3.3 nm). Thermal stability of these materials also was found be very high; average particle sizes maintained at 4.5 nm at 750 °C. These catalysts were also found to be very active in CO oxidation with light-off temperatures decreasing drastically for AuPd composition. The thermal stability in conjunction with increased activity of CO oxidation renders these catalysts potential for automotive catalysts where relays into high temperature regimes are usually detrimental due to consequent deactivation.

4.8. REFERENCES

1. F. Tao, M. E. Grass, Y. Zhang, D. R. Butcher, F. Aksoy, S. Aloni, V. Altoe, S. Alayoglu, J. R. Renzas, C-K. Tsung, Z. Zhu, Z. Liu, M. Salmeron and G. A. Somorjai, *J. Am. Chem. Soc.*, 2010, **132**, 8697.
2. F. Gao and D. W. Goodman, *Chem. Soc. Rev.*, 2012, **41**, 8009.
3. J. Wu, P. Li, Y-T, Pan, S. Warren, X. Yin and H. Yang, *Chem. Soc. Rev*., 2012, **41**, 8066.
4. X. Peng, Q. Pan and G. L. Rempel, *Chem. Soc. Rev.*, 2008, **37**, 1619.
5. J. K. Edwards, B. E. Solsona, P. Landon, A. F. Carley, A. Herzing, C. J. Kiely and G. J. Hutchings, *J. J. Catal.*, 2005, **69**, 236.
6. B. E. Solsona, J. K. Edwards, P. Landon, A. F. Carley, A. Herzing, C. J. Kiely and

G. J. Hutchings, *Chem. Mater.*, 2006, **18**, 2689.

7. J. K. Edwards, A. F. Carley, A. A. Herzing, C. J. Kiely and G. J. Hutchings, *Faraday Discuss*., 2008, **138**, 225.
8. J. K. Edwards, E. Ntainjua, A. F. Carley, A. A. Herzing, C. J. Kiely and G. J. Hutchings, *Angew. Chem., Int. Ed.*, 2009, **48**, 8512.
9. F. Gao, Y. L. Wang and D. W. Goodman, *J. Am. Chem. Soc.*, 2009. **131**, 5734.
10. F. Gao, Y. L. Wang and D. W. Goodman, *J. Phys. Chem.* C, 2009, **113**, 14993.
11. J. Xu, T. White, P. Li, C. H. He, J. G. Yu, W. K. Yuan and Y. F. Han, *J. Am.Chem. Soc.*, 2010, **132**, 10398.
12. Y. F. Han, J. H. Wang, D. Kumar, Z. Yan and D. W. Goodman, *J. Catal.* 2005, **232**, 467
13. F. R. Fan, D. Y. Liu, Y. F. Wu, S. Duan, Z. X. Xie, Z. Y. Jiang and Z. Q. Tian, *J.Am. Chem. Soc.*,2008, **130**, 6494.
14. P. D. Beer, D. Ozkaya, J. Cookson and C. J. Serpell, *Nat. Chem.*, 2011, **130**, 478.
15. A. M. Henning, J. Watt, P. J. Miedziak, S. Cheong, M. Santonastaso, M. Song, Y. Takeda, A. I. Kirkland, S. H. Taylor and R. D. Tilley, *Angew. Chem. Int. Ed.* 2012, **51**, 1.
16. N. Dimitratos, J. A. Lopez-Sanchez, D. Morgan, A. F. Carley, R. Tiruvalam, C. J. Kiely, D. Bethell and G. J. Hutchings, *Phys. Chem. Chem. Phys*., 2009, **11**, 5142.
17. H. Wang, S. Zhenhua, Y. Yang and D. Su, *Nanoscale*, 2013, **5**, 139.
18. R. W. J. Scott, O. M. Wilson, S-K. Oh, E. A. Kenik and R. M. *J. Am. Chem. Soc*., 2004, **126**, 15583.
19. M. G. Weir, M. R. Knecht, A. I. Frenkel and R. M. Crooks, *Langmuir*, 2010, **26**, 1137.
20. M. G. Weir, M. R. Knecht, A. I. Frenkel and R. M. Crooks, *Langmuir*, 2010, **26**, 1137.
21. A. M. Venezia, V. I. Parola, G. Deganello, B. Pawelec and J. L. G. Fierro, *J.Catal.* 2003, **215**, 317.
22. S. Nishimura, Y. Yakita, M. Katayama, K. Higashimine and K. Ebitani, *Catal. Sci. Technol.*, 2013, **3**, 351.
23. Y. Liu, L. Wang, G. Wang, C. Deng, B. Wu and Y. Gao, *J. Phys. Chem. C*, 2010,

114, 21417.

24. B. H. Toby, *Appl. Crystallogr.*, 2001, **34**, 210.
25. M-L. Wu, D-H. Chen and T-C. Huang, *Langmuir,* 2001, **17**, 3877.
26. R. J. Farrauto, J. K. Lampert, M. C. Hobson and E. M. Waterman, *Appl. Catal. B*, 1995, **6**, 263.
27. P. J. Berlowitz, C. H. F. Peden and D. W. Goodman, *J. Phys. Chem.*, 1998, **92**, 5213
28. T. Engel, and G. Ertl, *Ad*V.*Catal.*, 1979, **28**, 1
29. F. Gao, S. M. McClure, Y. Cai, K. K. Gath, Y. Wang, M. S. Chen, Q. L. Guo and D. W. Goodma, Surf. Sci. 2009, **603**, 65.
30. F. Gao, Y. Wang, Y. Cai and D. W. Goodman, *J. Phys. Chem. C*, 2009, **113**, 174.

CHAPTER 5

SYNTHESIS AND CHARACTERIZATION OF THIOL STABILIZED Ag AND Pt NANOCLUSTERS AND NANOPARTICLES AND THEIR SILICA ENCAPSULATION

5.1. INTRODUCTION

Other than Au and Pd nanoparticle system, research on supported Pt and Ag nanoparticles is also of great importance due to their applications in the field of catalysis for a variety of industrial processes. Pt based catalysts are well known for oxidation of CO and hydrocarbons in automotive catalytic converters, petrochemical cracking, oxidation of NH_3 in nitric acid synthesis, hydrosilylation of alkenes and aryl alkynes, hydrogenation of benzene and cyclohexene, and direct decomposition and oxidation of alcohols [1-10]. A detailed discussion of Pt nanoparticles in catalysis is already given in Chapter 1 (section 1.4). Similarly, supported silver catalysts have long been extensively used for industrial epoxidation of ethylene [11,12]. Ag based catalysts are also potential candidates for the selective hydrogenation of a range of chloronitrobenzenes to their corresponding chloroanilines, which are of great advantage as industrially viable and cheap alternatives for the production of chloroanilines [13].

In this scenario we have further used our *N*,*N*,*N*-Tripropyl(11-mercaptoundecyl)ammonium chloride ligand to prepare highly stable and water dispersible Ag nanoarchitectures ranging from nanoclutsers to nanoparticles. We have employed varying thiol:Ag ratios to prepare Ag nanoparticles of different sizes. As in the case of Au and Pd, here also particle size increases with decreasing thiol amount. We have used similar protocol for the synthesis of Pt nanoparticles; however, we are not successful in synthesising a range of particle sizes as in other cases. It is observed that with higher amounts of thiol, Pt nanoclusters could be stabilized but lower amount of thiol could not stabilize Pt nanoparticles. A strategy similar to that of Au and Pd nanoparticles described in Chapter 2 (section 2B.1) and 3 (section 3.1) respectively has been employed for the synthesis of porous silica encapsulated Ag and Pt nanoparticles. Due to low Tamman temperature of Ag metal, silica encapsulated Ag nanoparticles are agglomerated during calcination at high temperature. To control the sintering of Ag nanoparticle, Ag nanoclusers are mixed with Pd nanoclusters and a strategy similar to AuPd@SiO_2, described in Chapter 4 has been utilized for the preparation of porous silica encapsulated alloyed AgPd nanoparticles.

5.2. SYNTHESIS

5.2.1. Synthesis of N,N,N-Tripropyl(11-mercaptoundecyl)ammonium chloride stabilized Ag nanoclusters and nanoparticles

The strategy employed for synthesizing water dispersible Ag nanoparticles (Ag NPs) involves surface protection by a bifunctional thiol, *N,N,N*-Tripropyl(11-mercaptoundecyl)ammonium chloride, similar to that of Au and Pd nanoparticles described in Chapter 2 (2A.2.2) and Chapter 3 (section 3.2.1) respectively. We followed reduction of $AgNO_3$ salt precursor with $NaBH_4$ by varying only the concentration of thiol so that Ag:thiol ratio is progressively changed. For constant molar concentrations of Ag precursor and reducing agent ie. $NaBH_4$, thiol concentration was varied as 0.4, 0.05, 0.02 and 0.01 mmol, corresponding to thiol:Ag ratios of 4.8, 0.6, 0.24 and 0.12 respectively. A stock solution of $AgNO_3$ in water (2.8 mL, 30 mm) was mixed with Millipore water (30 mL). Appropriate amount of stock solution of thiol in methanol (0.4 M) was added to this solution. The mixture was stirred for 2 h. $NaBH_4$ solution (450 µL, 1.58 M) in methanol was added and stirring was continued for 45 min. All the steps were performed at RT. Aqueous solution of Ag nanoparticles were purified by dialysis through a cellulose membrane (Aldrich, pore size 12 kDa). When the thiol ligand was added to $AgNO_3$ solution, the colorless solution became yellow and on addition of $NaBH_4$, the colour of the solution again changed from yellow to brown. Ag nanoparticles corresponding to thiol:Ag ratio of 4.8, 0.6, 0.24 and 0.12 will be mentioned hereafter as AgNP1, AgNP2, AgNP3 and AgNP4 respectively.

5.2.2. Synthesis of N,N,N-Tripropyl(11-mercaptoundecyl) ammonium chloride stabilized Pt nanoclusters

A stock solution of H_2PtCl_6 in water (2.8 mL, 30 mm) was mixed with water (30 mL). Thiol (0.148 g, 0.4 mmol) in methanol (0.5 mL) was added to this solution. The mixture was stirred for 2 h. $NaBH_4$ solution (450 µL, 1.58m) in methanol was added and stirring was continued for 45 min. All the steps were performed at RT. An aqueous solution of Pt nanoclusters was purified by dialysis through a cellulose membrane (Aldrich, pore size 12 kDa). On the addition of thiol ligand to Pt metal

precursor solution, a yellow gel like material formed but after dialysis gel material transformed to clear yellow solution.

5.2.3. Synthesis of porous silica encapsulated Ag nanoparticles (Ag@p-SiO_2)

The Ag nanocluster (AgNP1) solution (10 mL) was mixed with a 1:4 water/ethanol mixture (200 mL). 0.1 M NaOH solution (0.9 mL) and tetraethyl orthosilicate (300 mL, Aldrich, 98%) were added to this mixture and stirred at RT for 3 d. Silica-encapsulated platinum nanoclusters were separated from the reaction medium by centrifugation at 14000 rpm and redispersion in water several times.

The above as-synthesized material was calcined to remove the thiol ligand by heating with a rate of 0.8 °C/min from room temperature to 350 °C. First the temperature was increased up to 350 °C under nitrogen and then it was kept constant for 12 h under air for removing the organic ligand.

5.2.4. Synthesis of porous silica encapsulated alloyed Ag-Pd nanoparticles (Ag-Pd@p-SiO_2)

1 mL mixtures of Ag (AgNP1) and Pd nanoclusters (PdNP1) in 1:1 ratio were sonicated for 1 h. The sonicated nanocluster solution (1 mL) was mixed with a 1:4 water/ethanol mixture (20 mL). 0.1 M NaOH solution (90 µL) and tetraethyl orthosilicate (30 µL, Aldrich, 98%) were added to this mixture and stirred at RT for 3 d. Silica-encapsulated silver-palladium nanoclusters were separated from the reaction medium by centrifugation at 14000 rpm and redispersion in water several times.

The above as-synthesized materials were calcined to remove the thiol ligand and for the intimate mixing of nanclusters to form alloy nanoparticles by heating with a rate of 0.8 °C/min from room temperature to 550 °C. First the temperature was increased up to 550 °C under nitrogen and then it was kept constant for 12 h under air for removing the organic ligand.

5.2.5. Syntheis of porous silica encapsulated Pt nanoparticles (Pt@p-SiO_2)

The Pt nanocluster (PtNP1) solution (10 mL) was mixed with a 1:4 water/ethanol mixture (200 mL). 0.1 M NaOH solution (0.9 mL) and tetraethyl orthosilicate (300 mL, Aldrich, 98%) were added to this mixture and stirred at RT for 3 d. Silica-encapsulated platinum nanoclusters were separated from the reaction medium by centrifugation at 14000 rpm and redispersion in water several times.

The above as-synthesized material was calcined to remove the thiol ligand by heating with a rate of 0.8 °C/min from room temperature to 550 °C. First the temperature was increased up to 350 °C under nitrogen and then it was kept constant for 12 h under air for removing the organic ligand.

5.3. INSTRUMENTS FOR CHARACTERIZATION

High resolution transmission electron microscopy (HRTEM) and UV-Vis spectroscopy are employed for the characterization of Ag, Pt nanoparticles and their silica encapsulated material also. Instrumental details of HRTEM and UV-Vis spectroscopy are already been described in Chapter 2 (section 2A.3).

5.4. CHARACTERIZATION

5.4.1. Characterization of *N,N,N*-Tripropyl(11-mercaptoundecyl)ammonium chloride ligand protected Ag nanoclusters and nanoparticles

5.4.1.1. High Resolution Transmission Electron Microscopy

HRTEM analysis has revealed the shape and size of Ag nanoclusters and nanoparticles. Unfortunately, the nanoclusters were highly unstable under electron beam and agglomerated during imaging; hence HRTEM could not give real particle size for AgNP1. HRTEM images show average particle size of ~ 3.5 nm for AgNP1 [Fig. 5.1] and 4-7 nm [Fig. 5.2], 5-10 nm [Fig. 5.3] and 5-15 nm [Fig. 5.4] for AgNP2, AgNP3 and AgNP4 respectively. This shows a progressive increase in particle size as thiol concentration in the reaction mixture decreases. HRTEM analysis has also revealed that all Ag nanoparticles are spherical in nature.

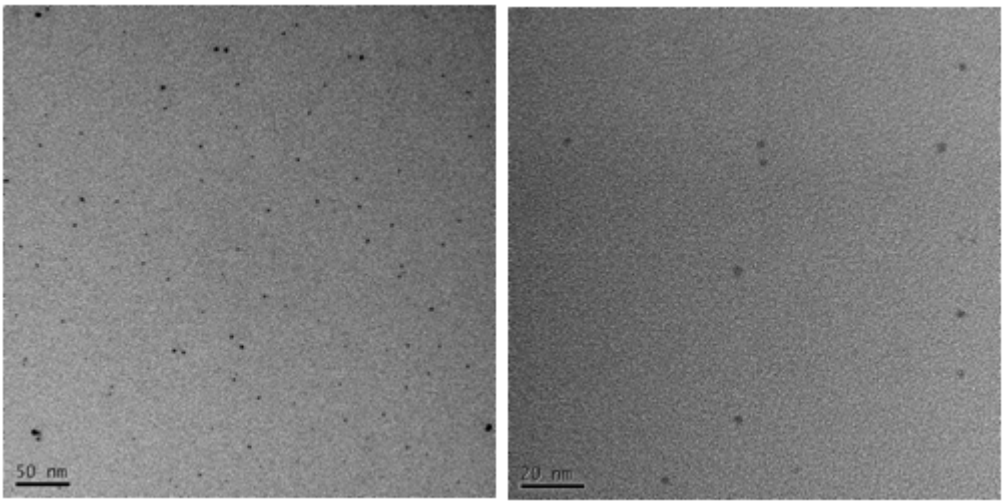

Fig. 5.1. HRTEM images of AgNP1

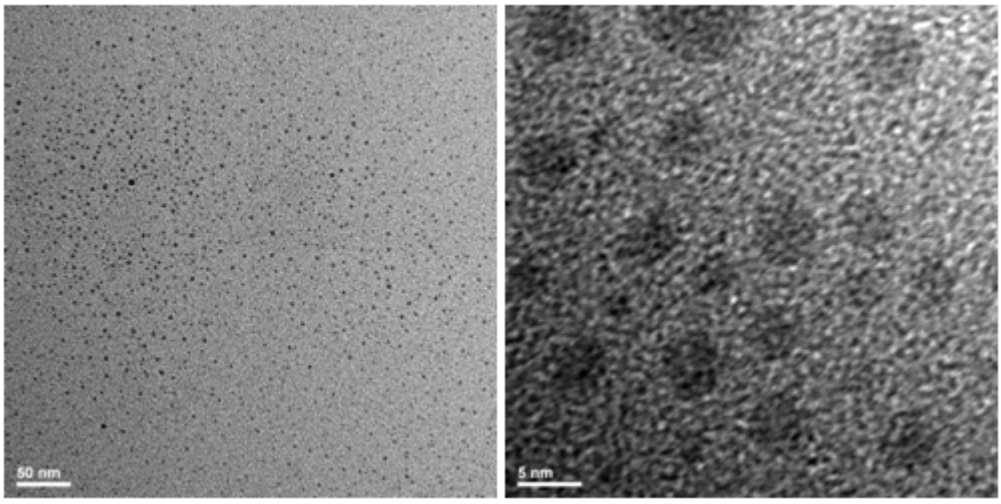

Fig. 5.2. HRTEM images of AgNP2

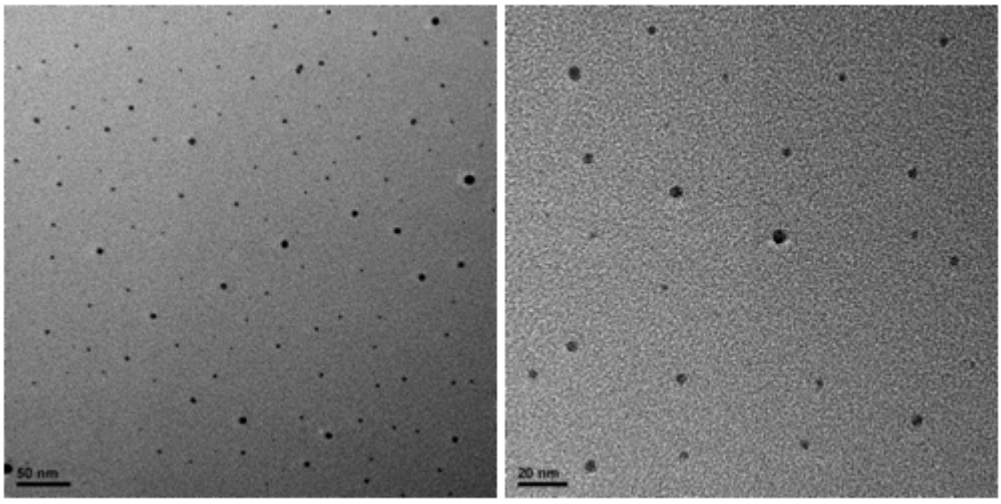

Fig. 5.3. HRTEM images of AgNP3

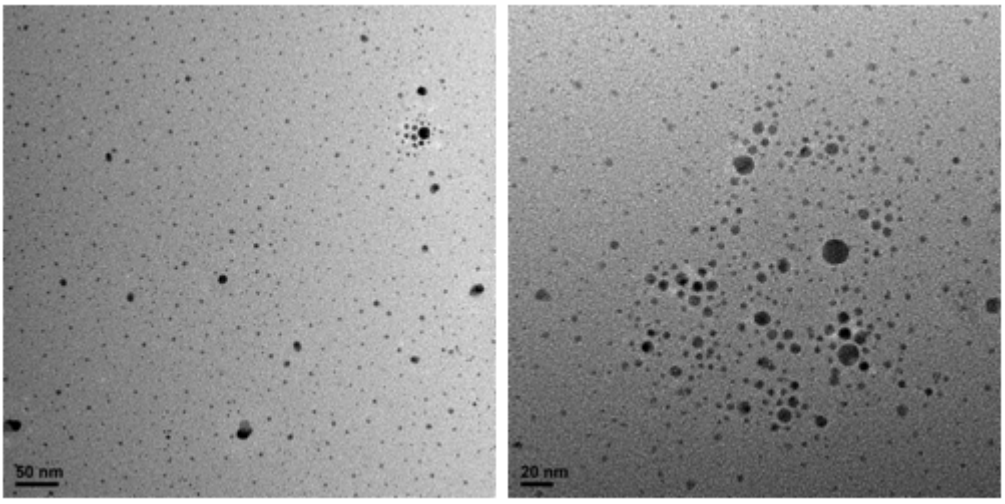

Fig. 5.4. HRTEM images of AgNP4.

5.4.1.2. UV-Vis Spectroscopy

Fig. 5.5 represents the UV-vis spectra of AgNP1-4. Spectrum of AgNP1 shows an exponential decay curve and does not exhibit characteristic surface plasmon resonance band of metallic silver. This indicates that the size is within the quantum confinement regime and ultra-small in nature. Spectra of AgNP2-4 show characteristic SPR absorption band and the intensity increases with increasing particle size. This also indicates an increase in particle size as thiol concentration decreases. However, AgNP1 did not show any characteristic emission peak probably due to polydispersity, albeit in ultra small size regime.

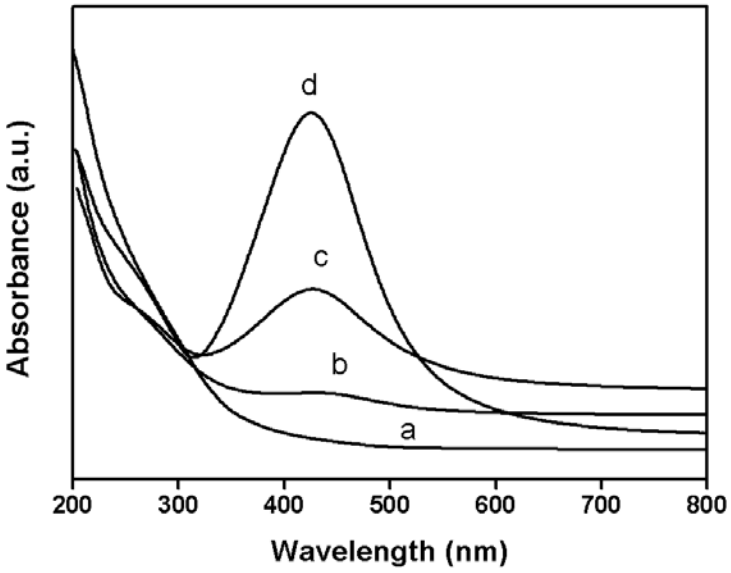

Fig. 5.5. UV-vis spectra of (a) AgNP1, (b) AgNP2, (c) AgNP3 and (d) AgNP4.

5.4.2. Characterization of thiol ligand protected Pt nanoclusters

5.4.2.1. High Resolution Transmission Electron Microscopy

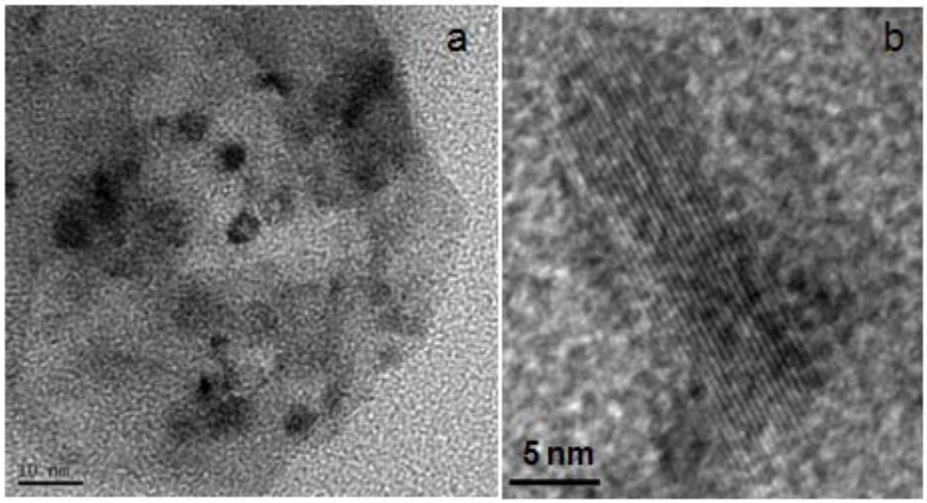

Fig. 5.6. a) HRTEM image of Pt nanoclusters and b) lattice plane of nanorods.

HRTEM analysis shows that the case of Pt is very different from those of other noble metals studied. Spongy gel like material which is highly agglomerated could be seen with some portions darker than the surroundings [Fig. 5.6a]. It is safe to assume that these portions represent some form of Pt metallic species. The size of these portions

are found to be ~ 5 nm. On closer observation these seem to be agglomerations of smaller particles of size ~ < 1 nm. In some places, nanorods of dimension 35 nm x 5 nm could be observed [Fig. 5.6b].

It is known that $[PtCl_6]^{2-}$ forms ion pairs with cationic quarternary ammonium surfactants like CTAB [14,15]. It is possible that such an ion pair material with a gel like consistency is formed at high thiol concentrations which is not stabilized at lower thiol concentrations. In an earlier study in our group, such ion pair spongy material was found to diffuse slowly and agglomerate to give anisotropic nanoparticles like nanorods, rugby ball shaped particles etc [16]. The above observation is reminiscent of such a material.

5.4.2.2. UV-Vis Spectroscopy

UV-vis spectra shows the characteristic exponential decay curve for small size Pt nanoparticles [Fig. 5.7]. This also indicates the formation of ion pairs or ultra small Pt nanoclusters, but definitely rules out bigger Pt nanoparticles.

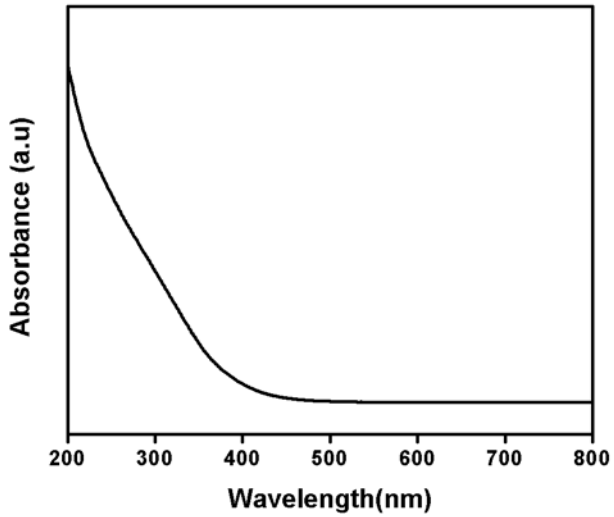

Fig. 5.7. UV-vis spectra of Pt nanoclusters.

5.4.3. Characterization of porous silica encapsulated Ag nanoparticles (Ag@p-SiO_2), alloyed Ag-Pd nanoparticles (Ag-Pd@p-SiO_2) and Pt nanoparticles (Pt@p-SiO_2)

High Resolution Transmission Electron Microscopy

HRTEM analysis of calcined Ag@p-SiO_2 shows that severe agglomeration occurs during thermal treatment. Even though, some particles are encapsulated completely inside the silica [Fig. 5.8a] shell, many big particles could be seen outside of the silica spheres [Fig. 5.8b]. Obviously, due to low melting point of Ag metal, Ag nanoparticles face severe agglomeration problem which could not be addressed fully by encapsulation.

HRTEM images [Fig. 5.9] of alloyed Ag-Pd@p-SiO_2 (synthesized by mixing of Ag:Pd=1:1) shows that all particles are completey encapsualted inside silica shell, no particles could be found outside the silica sphere even after high temperature calcination. This evidences that Pd metal helps to control the growth of Ag nanoparticle by formation of metallic alloy and mimimize the agglomeration problem.

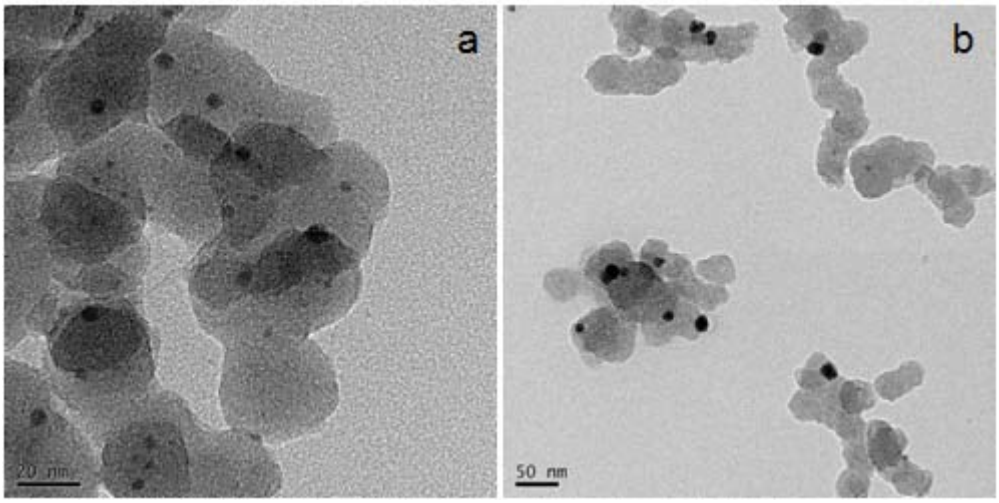

Fig. 5.8. HRTEM images of Ag@p-SiO_2, a) all Ag particles are inside silica sphere and b) agglomerated Ag nanoparticles came out from silica.

Fig. 5.10 represents the HRTEM images of Pt@p-SiO_2. Interestingly, all Pt nanoparticles are fully encapsulated inside silica shell and no agglomeration occurred.

Apparently, the spongy material with ionic Pt species has facilitated successful encapsulation. Average particle size also is highly controlled ≤ 5 nm.

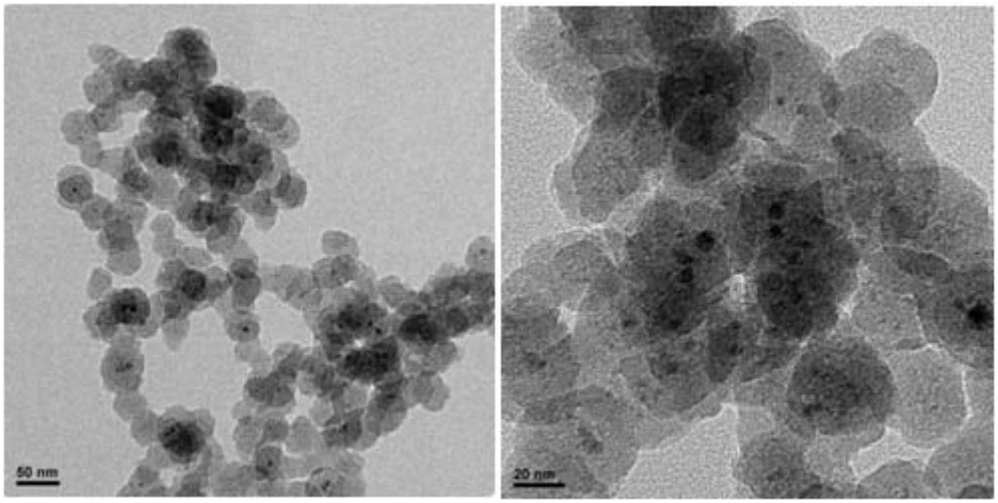

Fig. 5.9. HRTEM images of alloyed Ag-Pd@p-SiO_2.

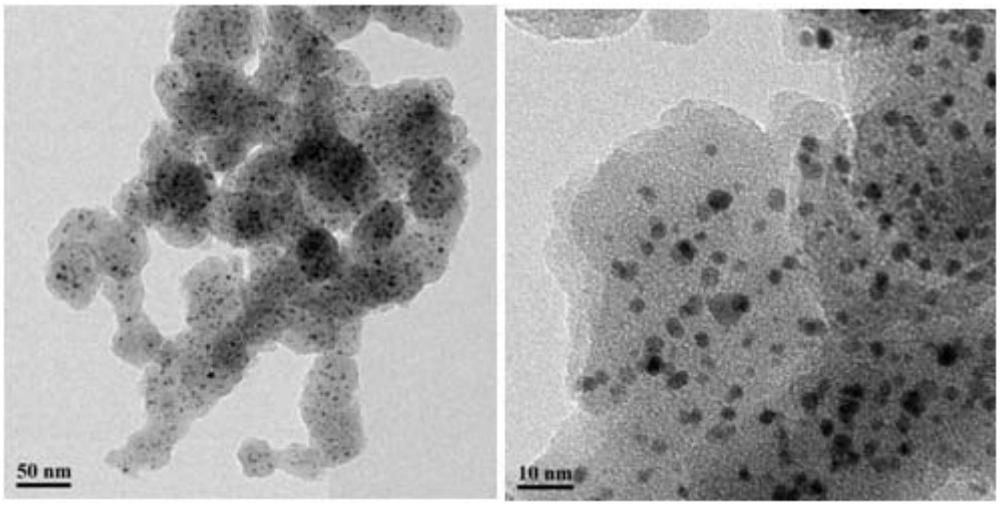

Fig. 5.10. HRTEM images of Pt@p-SiO_2.

5.5. SUMMARY

Preliminary studies have been performed for the synthesis of Ag and Pt nanoclusters and nanoparticles and their silica encapsulation. Thiol ligand, *N,N,N*-Tripropyl(11-mercaptoundecyl)ammonium chloride is capable of synthesizing Ag nanoparticles of ultra-small to bigger size. However, Pt nanostructures could be synthesized only at high thiol concentrations and failed to give any fruitful results with lower

concentrations. At higher concentrations, spongy gel like ion pairs between $[PtCl_6]^{2-}$ and quarternary ammonium group may have formed, which stabilized the Pt species. The strategy similar to Au and Pd has been employed for the synthesis of porous silica encapsulated nanoparticles. Ag and Pt nanoclusters are utilized as precursors for this synthesis. Ag agglomeration at high temperatures could be controlled only by alloying with Pd. Pt particles could be successfully encapsulated and particle size controlled at high temperatures. Further work is necessary to fully characterize the nanoarchitectures formed and understand the effect of the ligand on Pt species. This will lead to better ways of utilizing the ion pairs as precursors for silica encapsulation and stabilizing against agglomeration, as preliminary studies have shown. Work presented in this chapter paves the way for future directions in this area of research.

5.6. REFERENCES

1. D. A. King and D. P. Woodruff, *The Chemical Physics of Solid Surfaces and Heterogeneous Catalysis;* Elsevier: Amsterdam, 1982; Vol. 4.
2. H. J. Freund, *Surf. Sci.*, 2002, **500**, 271.
3. A. K. Santra and D. W. Goodman, *Electrochim. Acta*, 2002, **47**, 3595.
4. W. J. Arblaster, *Platinum Metals Rev.*, 2005, **49**, 141.
5. N. Seriani, Z. Jin, W. Pompe and L. Colombi Ciacchi, *Phys. Rev.* B, 2007, **76**, 155421.
6. J. R. Croy, S. Mostafa, J. Liu, Y. H. Sohn, H. Heinrich, B. Roldan Cuenya, *Catal. Lett.*, 2007, **119**, 209.
7. J. R. Croy, S. Mostafa, J. Liu, Y. H. Sohn and B. Roldan Cuenya, *Catal. Lett.*, 2007, **118**, 1.
8. J. R. Croy, S. Mostafa, L. Hickman, H. Heinrich and B. Roldan Cuenya, *Appl. Catal., A*, 2008, **350**, 207.
9. J. R. Croy, S. Mostafa, H. Heinrich and B. Roldan Cuenya, *Catal. Lett.*, 2009, **131**, 21.
10. S. Mostafa, J. R. Croy, H. Heinrich and B. Roldan Cuenya, *Appl. Catal., A*, 2009, **366,** 353.
11. D. J. Guo and H. L. Li, *Carbon*, 2005, **43**, 1259.
12. J. Q. Lu, J. J. Bravo-Suarez, A. Takahashi, M. Haruta and S. T. Oyama, *J.*

Catal., 2005, **232**, 85.

13. Y. Chen, C. Wang, H. Liu, J. Qiu and X. Bao, *Chem. Commun.* 2005, 5298.
14. I. P. Beletskaya, A. N. Kashin, A. E. Litvinov, V. S. Tyurin, P. M. Valetsky and G. van Koten, *Organometallics,* 2006, **25**, 154.
15. L. M. Bronstein, D. M. Chernyshov, G. I. Timofeeva, L. V. Dubrovina, P. M. Valetsky, E. S. Obolonkova and A. R. Khokhov, *Langmuir*, 2000, **16**, 3626.
16. A. K. Prashar, R. P. Hodgkins, J. N. Chandran, P. R. Rajamohanan and R. N. Devi, *Chem. Mater.*, 2010, **22**, 1633.

CHAPTER 6

SUMMARY AND CONCLUSIONS

6.1. SUMMARY

Chapter 1 presents a general introduction to the role of noble metal nanoclusters and nanoparticles in versatile applications including catalysis and bioimaging. It gives details about current status of synthesis procedure of noble metal nanoparticles and their application in catalysis and bioimaging. It has described that particle size of metal nanoparticles plays an important role for exhibiting photo physical property like fluorescence and also for catalytic activity. Though supported metal nanocatalysts are highly active for various types of reactions, one of the major problems associated with them is deactivation due to agglomeration process. This can be solved by encapsulating metal nanoparticles in porous silica shell to get both activity and stability. Various examples of silica encapsulated and porous silica encapsulated metal nanoparticles have been described in this chapter.

Chapter 2A describes the synthesis of a novel *N*,*N*,*N*-Tripropyl(11-mercaptoundecyl)ammonium chloride ligand which is capable of synthesizing stable water dispersible Au ultra-small clusters and nanoparticles. Particle size could be controlled by the thiol concentration in the synthesis medium. Ultra-small Au clusters show good fluorescence intensity at NIR region. This photophysical property has been used for the detection of *E.coli* bacteria cell. A novel inorganic fluorescent probe based on Au nanoclusters has been developed which is capable of selectively binding to receptor sites involved in quorum sensing. This probe targets the binding sites for QS molecules within bacterial cells and not the concentration of signal molecules produced which is the current practice. This property makes these systems independent of cell density and can be used before the bacteria attain a virulent quorate state. This is the first time such inorganic fluorescent probes are used for bacterial detection before quorate state and the excellent specificity for binding sites renders this system indeed ideal for targeted biosensors.

Chapter 2B describes the development of a stable and novel catalyst based on Au nanoparticles encapsulated in porous silica sphere and its utilization for H_2O_2 and glucose detection. Thiolate protected ultra-small Au clusters are used as precursors for the preparation of porous silica encapsulated Au nanoparticle catalysts. The catalyst is found to be a peroxidase mimic nanomaterial following Michaelis-Menten kinetics for

enzyme catalyzed reactions. The activity is found to be the highest at a pH of 4.5 and increase exponentially with temperature. Incubation stability is also found to be reasonably high in the range of pH 2.5-10 and temperature till 90 °C. Kinetic parameters reveal that the affinity of the catalyst to H_2O_2 is very high compared to other reported systems leading to a minimal concentration for maximum activity. So this Au@p-SiO_2 is a good alternative of natural peroxidase enzyme based on its activity and stability. Combined effect of porosity inside the silica layer and control of particle size of active Au nanoparticles has rendered this material ideal for catalysis. Also, the silica layer protecting the active Au particles is advantageous for the stability of the catalyst.

Chapter 3 describes that highly stable and water dispersible Pd nanoparticles ranging from nanoclutsers to nanoparticles are prepared by using a *N*,*N*,*N*-Tripropyl(11-mercaptoundecyl)ammonium chloride ligand. Fine tuning of particle size was achieved by systematically varying the thiol concentration in the reaction mixture. Various characterization techniques were used to ascertain the formation of Pd thiolate nanoparticles and evolution of the nanoparticle structure was followed. As expected, size of the particle decreases with increase in thiol concentration during synthesis. Also with increase in thiol concentration, the particle characteristics move towards Pd-thiolate complexes whereas with decrease in thiol concentration the particle characteristics incline more towards metallic nature. Sulphur is considered as poison for the catalyst and hence limits the application of thiolate capped palladium nanoparticles as catalysts. But in case of thiol ligand used here, the palladium nanoparticles with less concentrations of thiol are shown to be effective catalysts. Further silica encapsulation of the ultra-small Pd clusters is successful in a simple condensation process. Calcination and subsequent removal of organics led to the formation of nanocatalyst with arrays of ~ 3 nm Pd particles individually encapsulated within porous silica spheres. These nanocatalysts have exhibited excellent catalytic activity as well as thermal stability. Even at 750 °C near Tamman temperature of Pd, sintering is highly controlled and particle size remained intact at ~ 3 nm. Such nanocatalysts with efficient catalytic activity as well as stability against deactivation can be envisaged to be highly useful in many industrially important reactions including high temperature processes.

Chapter 4 describes a very simple strategy employed for the synthesis of fully alloyed AuPd nanoparticles encapsulated in porous silica shell. For bimetallic system, a mixture of Au and Pd nanoclusters are used as precursors instead of single nanocluster precursors for silica encapsulation as in case of simple Au or Pd. Prior to hydrolysis, a random mixing of Au and Pd nanoclusters can be expected since interparticle interactions will be similar due to same outer surface functionality, viz., propyl ammonium group. Presence of intimate mixtures of the clusters within the silica encapsulation ensures the formation of fully alloyed nanoparticles at high temperatures, at the same time controlling further growth and sintering. Elemental analysis, structural characterization by Rietveld refinement of powder XRD profiles and XPS point to the formation of monophasic alloys. In the three concentration ratios attempted, viz., Au:Pd = 3:1, 1:1 and 1:10, alloy phases equivalent to $Au_{86}Pd_{14}$, $Au_{66}Pd_{34}$ and $Au_{10}Pd_{90}$ are present in 100, 94.5 and 7.7 %. The unalloyed Pd is observed to be present as PdO phase. It is noteworthy here that the alloy phases are formed without the reduction step followed in most of the reported cases. Also compared to other reported supported Au-Pd alloys, alloy composition and particle size could be much better controlled. Particle size seems to have a correlation with the Au amount with alloy phase having higher Au concentration, Au3Pd@SiO_2 forming bigger particles (4.2 nm) when compared to AuPd@SiO_2 (3.3 nm). Thermal stability of these materials also is found be very high; average particle sizes maintained at 4.5 nm at 750 °C. These catalysts are also found to be very active in CO oxidation with light-off temperatures decreasing drastically for AuPd composition. The thermal stability in conjunction with increased activity of CO oxidation renders these catalysts potential for automotive catalysts where relays into high temperature regimes are usually detrimental due to consequent deactivation.

Chapter 5 describes preliminary study for the synthesis of Ag and Pt nanoclusters and nanoparticles and their silica encapsulation. Thiol ligand, *N*,*N*,*N*-tripropyl (11-mercaptoundecyl) ammonium chloride is capable of synthesizing Ag nanoparticles of ultra-small to bigger size. However, Pt nanostructures could be synthesized only at high thiol concentrations and failed to give any fruitful results with lower concentrations. At higher concentrations, spongy gel like ion pairs between $[PtCl_6]^{2-}$ and quaternary ammonium group may have formed, which stabilized the Pt species.

The strategy similar to Au and Pd has been employed for the synthesis of porous silica encapsulated nanoparticles. Ag and Pd nanoclusters are utilized as precursors for this synthesis. Ag agglomeration at high temperatures could be controlled only by alloying with Pd. Pt particles could be successfully encapsulated and particle size controlled at high temperatures. Further work is necessary to fully characterize the nanoarchitectures formed and understand the effect of the ligand on Pt species. This will lead to better ways of utilizing the ion pairs as precursors for silica encapsulation and stabilizing against agglomeration, as preliminary studies have shown. Work presented in this chapter paves the way for future directions in this area of research.

6.2. CONCLUSIONS

- Ultra-small Au clusters have high potential as fluorescent probes in imaging biological systems.
- Water dispersibility, NIR emission and high quantum yield are desirable properties for such applications which could be engineered successfully in this work.
- Ultra-small clusters of Au, Pd, Ag and Pt can be used as precursors for synthesis of sinter resistant catalysts by encapsulating in porous silica.
- Synergism of hydrophilicity of the ammonium group and hydrophobicity of the propyl group has facilitated encapsulation of individual clusters instead of a core shell structure of multiple clusters inside a silica shell.
- The peculiar structure in which individual clusters are encapsulated within silica has helped in controlling the agglomeration to a large extent on heating to high temperatures.
- Abundance of organic ligands around the individual particles has acted as template and led to porosity in the silica matrix after calcination.
- The developed method is universal and general as well as simple which can be further developed for other nanoclusters and their encapsulation.
- The functionality of the fluorescent nanoclusters can also be further exploited for developing fluorescent probes for various biological systems.

List of Publications and Patents

1. Ultrasmall Gold Cluster Arrays Encapsulated in Silica Nanospheres: Applications in Fluorescence Imaging and Catalysis.

   Anupam Samanta, Basab B. Dhar and R. Nandini Devi, *J. Phys. Chem. C*, 2012, **116**, 1748-1754.

2. Novel porous silica encapsulated Au nanoreactors as peroxidase mimic for one-pot glucose detection.

   Anupam Samanta, Basab B. Dhar and R. Nandini Devi, *New J. Chem.*, 2012, **36**, 2625-2629.

3. Pd Ultra-Small Clusters as Precursors for Silica-Encapsulated Pd Nanoreactors: Highly Sinter Resistant Catalysts.

   Anupam Samanta and R. Nandini Devi, *ChemCatChem*, 2013, **5**, 1911-1916.

4. Selective imaging of quorum sensing receptors in bacteria using fluorescent Au nanocluster probes surface functionalized with signal molecules.

   Ruchira Mukherj, **Anupam Samanta**, Rajith Illathvalappil, Somak Chowdhury, Asmita Prabhune and R. Nandini Devi, *ACS Appl. Mater. Interfaces*, 2013, **5**, 13076–13081

5. Confined space synthesis of fully alloyed and sinter resistant AuPd nanoparticles encapsulated in porous silica.

   Anupam Samanta, Thattarathody Rajesh and R. Nandini Devi. *J. Mater. Chem. A*, 2014, **2**, 4398-4405.

6. Stable oxide encapsulated metal clusters and nanoparticles.

   R. Nandini Devi and **Anupam Samanta**, Patent Application no: PCT/IN 2012/000260.

Contributions to National/International Symposia/Conferences

1. Synthesis and Characterization of Silicalite/SBA-15 Composites

Atul Kumar Prashar, **Anupam Samanta** and Nandini Devi

"Catalysis for Sustainable Energy and Chemicals 19th National Symposium On Catalysis"

18-21 January 2009, National Chemical Laboratory (NCL), Pune, India.

(Poster Presentation)

2. Synthesis and Characterization of ZSM-5/SBA-15 Composites

Anupam Samanta, Atul Kumar and R. Nandini Devi

"International Conference on Materials for the Millennium"

11-13 January 2010, at Cochin Institute of Applied Science and Technology,
Kochi-22, Kerala, India ***(Poster Presentation)***

3. Aggregation resistant water dispersible Au nanoparticles

Anupam Samanta and R. Nandini Devi

"Catalysis for Energy Conversion and Conservation of Environment 20th National Symposium"

19-22 December 2010, Indian institute of Technology (IIT), Madras ***(Poster Presentation)***

4. Ultra Small Gold Cluster Arrays encapsulated in Silica Nanospheres: Applications in Fluorescence Imaging and showing Peroxidase activity.

Anupam Samanta and R. Nandini Devi

" GOLD 2012, the 6th International Conferences on Gold Science, Technology and it's Applications"

5- 8 September 2012, Keio Plaza Hotel Tokyo, Japan ***(Poster Presentation)***

APPENDIX 1

1.1.Transmission Electron Microscopy

Transmission electron microscopy (TEM) is typically used for high resolution imaging of thin sections of solid samples for nanostructural and compositional analysis. The technique involves: (i) irradiation of a very thin sample by a high energy electron beam, which is diffracted by the lattice of a crystalline or semi crystalline material and propagated along different directions, (ii) imaging and angular distribution analysis of the forward-scattered electron (unlike SEM where backscattered electrons are detected) and (iii) energy analysis of the emitted X-rays. A beam of accelerated electrons can interact with an object in a conventional transmission electron microscope in one of two ways. Usually elastic scattering takes place, whereby the electrons change their path in the specimen without a loss of energy. Inelastic scattering can also occur, resulting in a loss of energy due to an interaction of the impinging electrons with the orbital electrons surrounding the nucleus of each atom in the object. Those electrons, which are not or hardly scattered, contribute positively to the image. However, considerably deflected electrons are prevented from doing so by apertures in the optical path. As a result, differences in light intensity (contrast) are created in the final image, which relate to areas in the object with different scattering potentials. As the atomic number increases, their scattering efficiency will also increase. Hence, heavy metals can form images with good contrast. The imaging system consists of an objective lens and one or more projector lenses. The chief lens in transmission microscopes is the objective. It determines the degree of resolution in the image. It forms the initial enlarged image of the illuminated portion of the specimen in a plane that is suitable for further enlargement by the projector lens. The projector lens, as it implies, serves to project the final magnified image on the screen or photographic emulsion. The great depth of focus provides the high magnification of the sample. The topographic information obtained by TEM in the vicinity of atomic resolution can be utilized for structural characterization and identification of various phases of mesoporous materials, viz., hexagonal, cubic or lamellar. TEM also provides real space image on the atomic distribution in the bulk and surface of a nanocrystal.

1.2. Scanning Electron Microscopy

Scanning electron microscopy (SEM) is one of the most widely used techniques for characterization of nanomaterials and nanostructures. The resolution of the SEM approaches a few nanometres, and the instruments can operate atmagnifications that are easily adjusted from ~10 to over 300,000. This technique provides not only topographical information like optical microscopes do, but also information of chemical composition near the surface. A scanning electron microscope can generate an electron beam scanning back and forth over a solid sample. The interaction between the beam and the sample produces different types of signals providing detailed information about the surface structure and morphology of the sample. When an electron from the beam encounters a nucleus in the sample, the resultant columbic attraction leads to a deflection in the electron's path, known as Rutherford elastic scattering. A fraction of these electrons will be completely backscattered, remerging from the incident surface of the sample. Since the scattering angle depends on the atomic number of the nucleus, the primary electrons arriving at a given detector position can be used to produce images containing topological and compositional information. The high-energy incident electrons can also interact with the loosely bound conduction band electrons in the sample. However, the amount of energy given to these secondary electrons as a result of the interactions is small, and so they have a very limited range in the sample. Hence, only those secondary electrons that are produced within a very short distance from the surface are able to escape from the sample. As a result, high-resolution topographical images can be obtained in this detection mode.

1.3. UV-Visible Spectroscopy

It deals with the study of electronic transitions between orbitals or bands of atoms, ions or molecules in gaseous, liquid and solid state. In the case of transition metal ions or atoms, any change in their coordination sphere may affect their optical properties and therefore can be characterized by UV-Vis. The metallic nanoparticles are known to exhibit different characteristic colours. Mie was the first to explain the origin of this colour theoretically in 1908 by solving Maxwell’s equation for the absorption and scattering of electromagnetic radiation by small nanoparticles. This absorption of electromagnetic radiation by metallic nanoparticles originates from the coherent

oscillation of the valence band electrons induced by an interaction with the electromagnetic field. These resonances are known as surface plasmons, which occur only in case of nanoparticles and not in case of bulk metallic particles. Hence, UV-Visible spectroscopy can be utilized to study the unique optical properties of the hybrid mesoporous materials containing occluded metallic nanoparticles, exploiting the size- and shape dependent surface plasmon resonance.

1.4. Fourier Transform Infrared Spectroscopy

Fourier transforms infrared (FTIR) spectroscopy deals with the vibration of chemical bonds in a molecule at various frequencies depending on the elements and types of bonds. After absorbing electromagnetic radiation the frequency of vibration of a bond increases leading to transition between ground state and several excited states. These absorption frequencies represent excitations of vibrations of the chemical bonds and thus are specific to the type of bond and the group of atoms involved in the vibration. The energy corresponding to these frequencies correspond to the infrared region (4000–400 cm^{-1}) of the electromagnetic spectrum. The term Fourier transform (FT) refers to a recent development in the manner in which the data are collected and converted from an interference pattern to an infrared absorption spectrum that is like a molecular "fingerprint".

1.5. Nuclear Magnetic Resonance Spectroscopy

Nuclear magnetic resonance (NMR) spectroscopy is one of the most powerful tools to investigate structure and dynamics of a molecular system in liquid phase. Atomic nuclei consisting of odd number of protons and/or neutrons possessing a nuclear spin $I \neq 0$ and consequently a magnetic moment $\mu = \gamma\hbar I$ (γ = gyromagnetic ratio), when placed in a magnetic field of strength B_0, Zeeman interaction results in quantized orientations of the nuclear magnetic moments. The nucleus can adopt $2I + 1$ Eigen states with energies $E(m) = -m\gamma\hbar B_0$, where m = (I, I–1,…., –I). Transitions between neighbouring energy states ($\Delta m = \pm 1$) can be induced by electromagnetic radiation (energy $E = h\nu$) of frequency $\nu 0 = \gamma B0/2\pi$. The chemical shift interaction arises from secondary local magnetic fields induced by the interaction of the electrons surrounding the nucleus. The induced local field opposes B_0 and hence shields the

nucleus under observation. The shielding is spatially anisotropic due to the nonspherical electron distribution around the nucleus.

1.6. Adsorption Measurements

Gas adsorption measurements are widely used for determining the surface area and pore size of porous solid materials. Nitrogen is commonly used as the adsorbate at liquid nitrogen temperature. Type I isotherms are given by microporous solids having relatively small external surfaces (e.g. activated carbons, molecular sieve zeolites and certain porous oxides), the limiting uptake being governed by the accessible micropore volume rather than by the internal surface area. The reversible Type II isotherm is the normal form of isotherm obtained with a non-porous or macroporous adsorbent. The Type II isotherm represents unrestricted monolayer-multilayer adsorption. Point B, the beginning of the almost linear middle section of the isotherm, is often taken to indicate the stage at which monolayer coverage is complete and multilayer adsorption about to begin. The reversible Type III isotherm is convex to the pip° axis over its entire range and therefore does not exhibit a Point B . Isotherms of this type are not common, but there are a number of systems (e.g. nitrogen on polyethylene) which give isotherms with gradual curvature and an indistinct Point B. In such cases, the adsorbate-adsorbate interactions play an important role. Characteristic features of the Type IV isotherm are its hysteresis loop, which is associated with capillary condensation taking place in mesopores, and the limiting uptake over a range of high p/p°. The initial part of the Type IV isotherm is attributed to monolayer-multilayer adsorption since it follows the same path as the corresponding part of a Type II isotherm obtained with the given adsorptive on the same surface area of the adsorbent in a non-porous form. Type IV isotherms are given by many mesoporous industrial adsorbents. The Type V isotherm is uncommon; it is related to the Type III isotherm in that the adsorbent-adsorbate interaction is weak, but is obtained with certain porous adsorbents. The Type VI isotherm, in which the sharpness of the steps depends on the system and the temperature, represents stepwise multilayer adsorption on a uniform non-porous surface. The step-height now represents the monolayer capacity for each adsorbed layer and, in the simplest case, remains nearly constant for two or three adsorbed layers. Amongst the best examples of Type VI isotherms are those obtained with argon or krypton on graphitised carbon

blacks at liquid nitrogen temperature. Types of physisorption isotherms are give in Fig. 1.1.

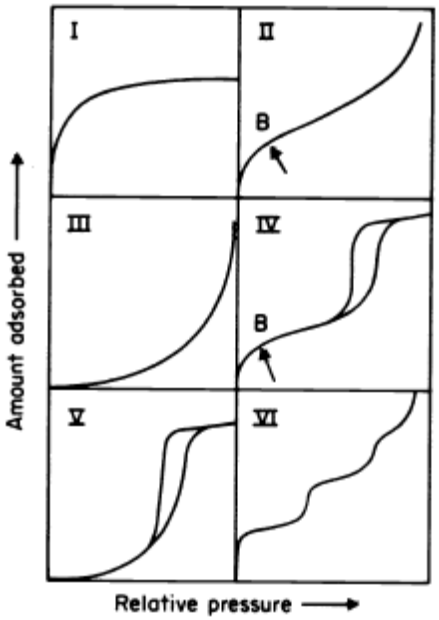

Fig. 1.1. Types of physisorption isotherms.

1.7. Powder X-Ray Diffraction

It is well recognised that XRD, based on wide-angle elastic scattering of Xrays, has been the single most important tool to determine the structure of the materials characterized by the long range ordering. The XRD patterns are obtained by the measurements of the angles at which the X-ray beam is diffracted by the sample. Bragg's equation relates the distance between two *hkl* planes *(d)* and angle of diffraction (2θ) as: $n\lambda = 2d\sin\theta$, where λ = wavelength of X-rays, n= an integer known as the order of reflection (*h, k,* and *l* represent Miller indices of respective planes). From the diffraction patterns, the uniqueness of mesoporous structures, phase purity, degree of crystallinity and unit cell parameters of the semi crystalline hybrid materials can be determined. The identification of phase is based on a comparison of a set of reflections of the sample with that of pure reference phases distributed by International Center for Diffraction Data (ICDD). Unit cell parameter of a cubic lattice can be determined by the following equation:

$$a_0 = d_{hkl}\sqrt{(h^2 + k^2 + l^2)},$$

where d=distance between two consecutive parallel planes having Miller indices *h, k,* and *l*. XRD broadening analysis has been widely used to characterize supported metal crystallites in the nanoscale. The average size of nanoparticles can be estimated using Debye-Scherrer equation: $D = k\lambda / \beta \cos\theta$, where D=thickness of the nanocrystal, k is a constant, λ= wavelength of X-rays, β = width at half maxima of reflection at Bragg's angle 2θ.

1.8. Fluorescence Spectroscopy

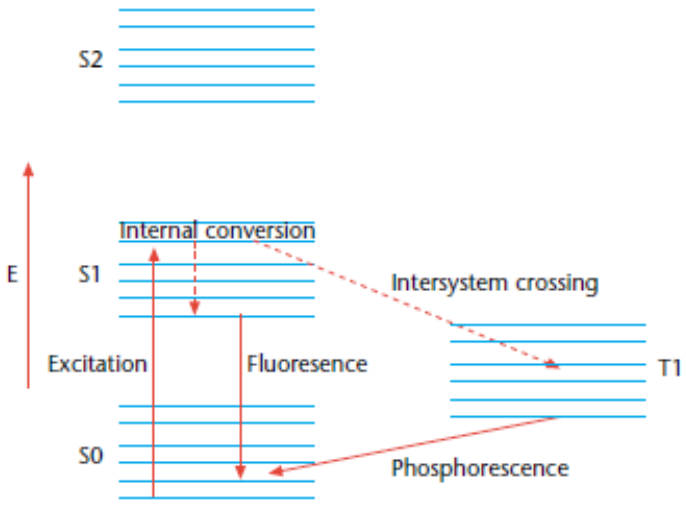

Fig. 1.2. The Jablonski diagram of fluorophore excitation, radiative decay and nonradiative decay pathways. E denotes the energy scale; S_0 is the ground singlet electronic state; S1 and S2 are the successively higher energy excited singlet electronic states. T1 is the lowest energy triplet state.

Fluorescence and phosphorescence are photon emission processes that occur during molecular relaxation from electronic excited states. These photonic processes involve transitions between electronic and vibrational states of polyatomic fluorescent molecules (fluorophores). The Jablonski diagram (Fig. 1.2) offers a convenient representation of the excited state structure and the relevant transitions. Electronic states are typically separated by energies on the order of 10 000 cm^{-1}. Each electronic

state is split into multiple sublevels representing the vibrational modes of the molecule. The energies of the vibrational levels are separated by about 100 cm^{-1}. Photons with energies in the ultraviolet to the blue-green region of the spectrum are needed to trigger an electronic transition. Further, since the energy gap between the excited and ground electronic states are significantly larger than the thermal energy, thermodynamics predicts that molecule predominately reside in the electronic ground state.

1.9. Confocal Microscopy

Confocal microscopy is an imaging technique used to increase micrograph contrast and/or to reconstruct three-dimensional images by using a spatial pinhole to eliminate out-of-focus light or flare in specimens that are thicker than the focal plane. This technique has been gaining popularity in the scientific and industrial communities. Typical applications include life sciences and semiconductor inspection. The principle of confocal imaging was patented by Marvin Minsky in 1961. In a conventional (i.e., widefield) fluorescence microscope, the entire specimen is flooded in light from a light source. Due to the conservation of light intensity transportation, all parts of specimen throughout the optical path will be excited and the fluorescence detected by a photodetector or a camera. In contrast, a confocal microscope uses point illumination and a pinhole in an optically conjugate plane in front of the detector to eliminate out-of-focus information. Only the light within the focal plane can be detected, so the image quality is much better than that of wide-field images. As only one point is illuminated at a time in confocal microscopy, 2D or 3D imaging requires scanning over a regular raster (i.e. a rectangular pattern of parallel canning lines) in the specimen. The thickness of the focal plane is defined mostly by the square of the numerical aperture of the objective lens, and also by the optical properties of the specimen and the ambient index of refraction.

1.10. Thermogravimetric Analysis

Thermogravimetric analysis (TGA) is an analytical technique used to determine a material’s thermal stability and its fraction of volatile components by monitoring the weight change that occurs as a specimen is heated. The measurement is normally carried out in air or in an inert atmosphere, such as Helium or Argon, and the weight

is recorded as a function of increasing temperature. Sometimes, the measurement is performed in a lean oxygen atmosphere (1 to 5% O_2 in N2 or He) to slow down oxidation. In addition to weight changes, some instruments also record the temperature difference between the specimen and one or more reference pans (differential thermal analysis, or DTA) or the heat flow into the specimen pan compared to that of the reference pan (differential scanning calorimetry, or DSC). The latter can be used to monitor the energy released or absorbed via chemical reactions during the heating process. In the particular case of carbon nanotubes, the weight change in an air atmosphere is typically a superposition of the weight loss due to oxidation of carbon into gaseous carbon dioxide and the weight gain due to oxidation of residual metal catalyst into solid oxides.

1.11. Zeta Potential Analysis

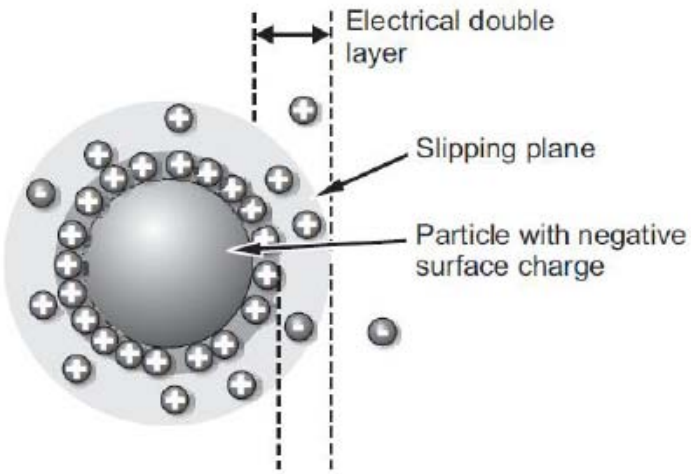

Fig. 1.3. Electric double layer surrounding nanoparticle.

Zeta Potential analysis is a technique for determining the surface charge of nanoparticles in solution (colloids). Nanoparticles have a surface charge that attracts a thin layer of ions of opposite charge to the nanoparticle surface. This double layer of ions travels with the nanoparticle as it diffuses throughout the solution (Fig. 1.3) The electric potential at the boundary of the double layer is known as the Zeta potential of the particles and has values that typically range from +100 mV to -100 mV. The magnitude of the zeta potential is predictive of the colloidal stability. Nanoparticles with Zeta Potential values greater than +25 mV or less than -25 mV typically have high degrees of stability. Dispersions with a low zeta potential value will eventually

aggregate due to Van Der Waal inter-particle attractions. Zeta Potential is an important tool for understanding the state of the nanoparticle surface and predicting the long term stability of the nanoparticle. At nanoComposix we routinely use Zeta Potential analysis to determine if a surface modification to the nanoparticle has been successful or if a processing step has modified the nanoparticle surface. However, the measurement data can be easily mis-interpreted and it is important to understand the strengths and limitations of Zeta potential measurements when interpreting results.

1.12. CHNS Analysis

CHNS elemental analysers provide a means for the rapid determination of carbon, hydrogen, nitrogen and sulphur in organic matrices and other types of materials. They are capable of handling a wide variety of sample types, including solids, liquids, volatile and viscous samples, in the fields of pharmaceuticals, polymers, chemicals, environment, food and energy. The analysers are often constructed in modular form such that they can be set up in a number of different configurations to determine, for example, CHN, CHNS, CNS or N depending on the application. This adaptability allows not only flexibility of operation but also the use of a wide range of sample weights from a fraction of a milligram to several grams (macro-systems). In its simplest form, simultaneous CHNS analysis requires high temperature combustion in an oxygen-rich environment and is based on the classical Pregl-Dumas method. This combustion can be carried out under both static conditions i.e. introduction of a set volume of oxygen or dynamic conditions i.e. a constant flow of oxygen for a set period of time. Often, catalysts are also added to the combustion tube in order to aid conversion.

1.13. Inductively Coupled Plasma-Atomic Emission Spectrometry (ICP-AES)

Inductively Coupled Plasma-Atomic Emission Spectrometry (ICP-AES) is one of the most common techniques for elemental analysis. Its high specificity, multi-element capability and good detection limits result in the use of the technique in a large variety of applications. All kinds of dissolved samples can be analyzed, varying from solutions containing high salt concentrations to diluted acids. A plasma source is used to dissociate the sample into its constituent atoms or ions, exciting them to a higher energy level. They return to their ground state by emitting photons of a characteristic

wavelength depending on the element present. This light is recorded by an optical spectrometer. When calibrated against standards the technique provides a quantitative analysis of the original sample.

APPENDIX 2

2.1. Quantum yield calculation of ultra-small Au clusters

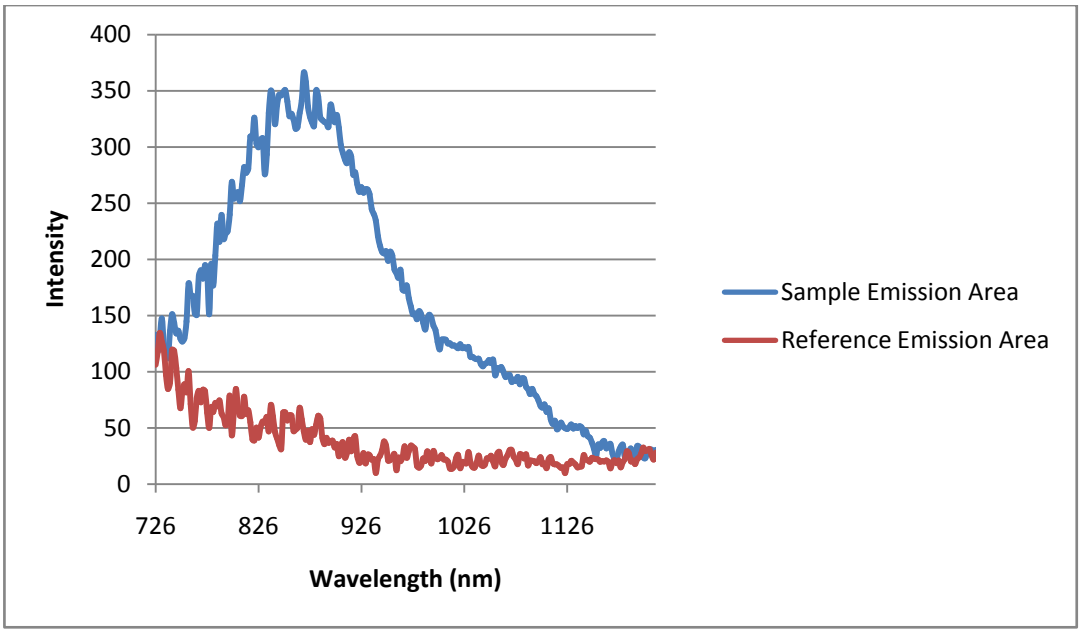

2.2. Quantum yield calculation of Au-thiol@oleic acid@C6-AHL

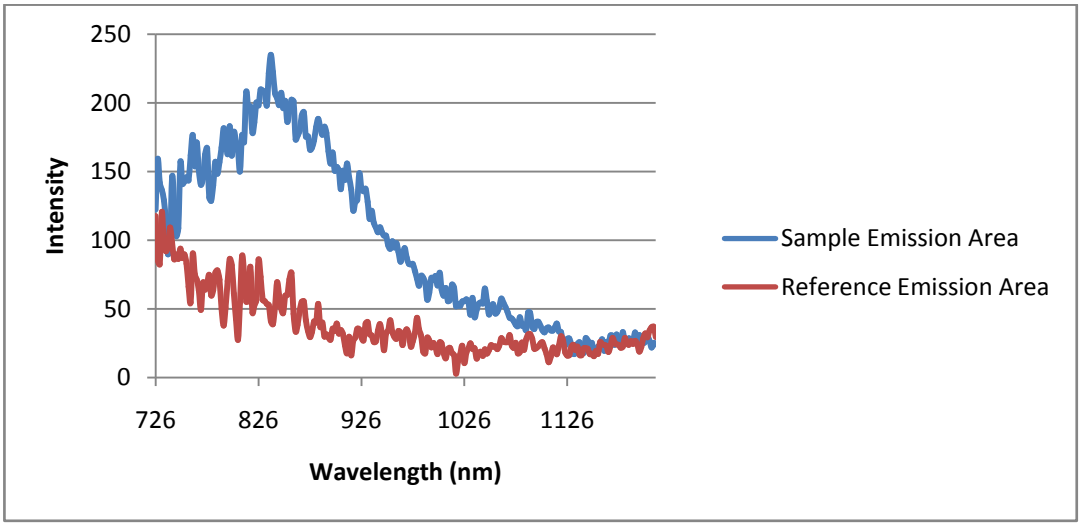

APPENDIX 3

Calculation of Pd:Thiol ratio based on TGA

Sample taken for TGA = 3.0086 mg

Thiol Ligand = 1.6773 mg

Molecular weight of thiol = 366 g

Mole of thiol = $1.6773X10^{-3}/366$

$= 4.5X10^{-6}$

Residue PdO = 3.0086-1.6773

= 1.3313 mg

Residue Pd = 1.1561 mg

Molecular weight of Pd = 106.41 g

Mole of Pd = $1.1561X10^{-3}/106.41$

$= 10.86X10^{-6}$

Pd:Thiol = $10.86X10^{-6}$: $4.5X10^{-6}$

= 2.41:1

APPENDIX 4

4.1. Rietveld refinement

a)

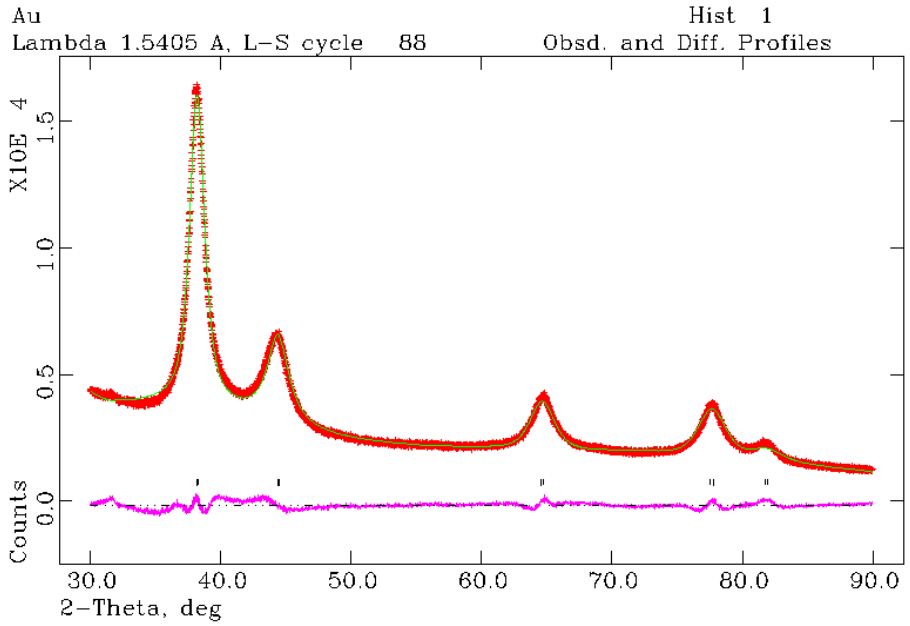

b)

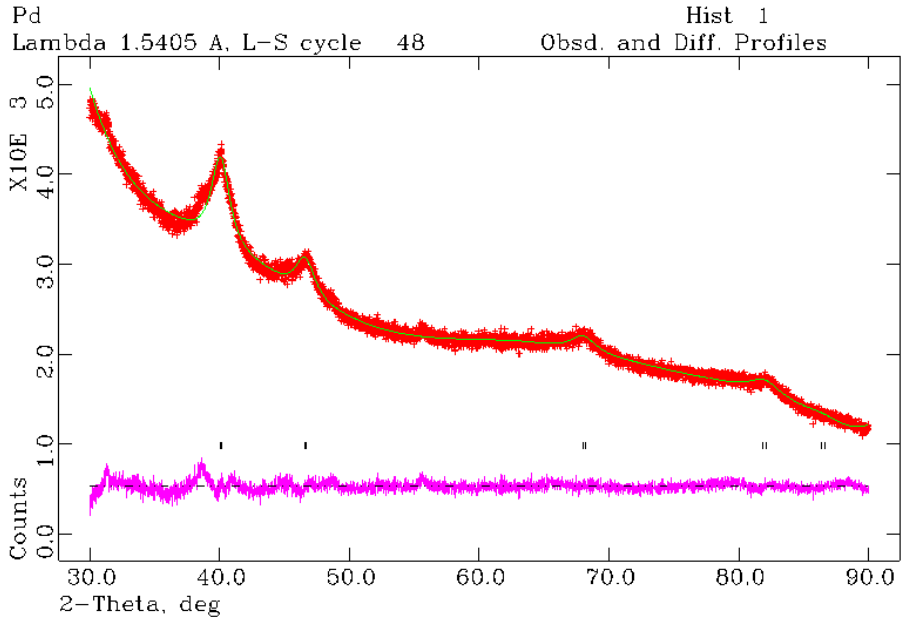

c)

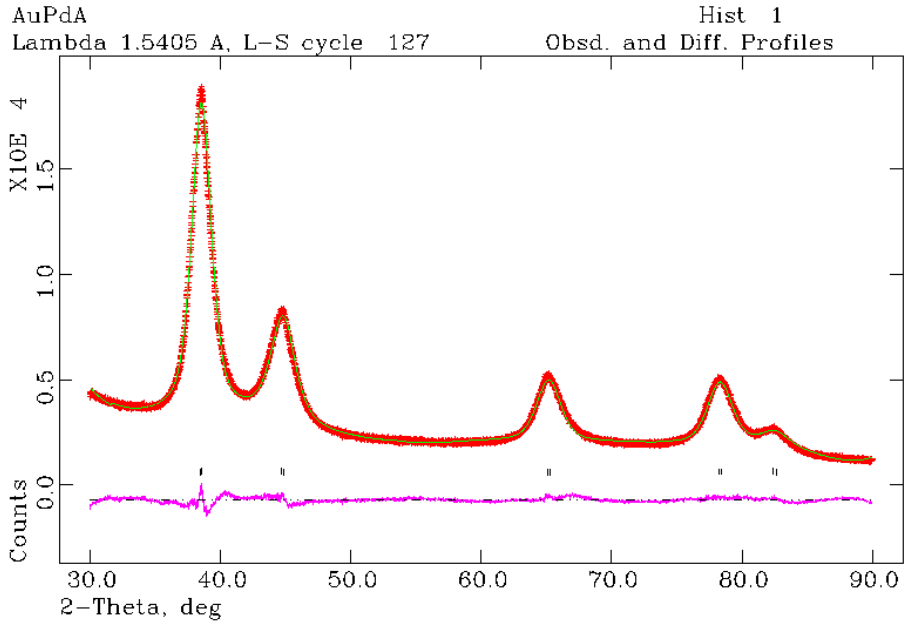
AuPdA
Hist 1
Lambda 1.5405 A, L-S cycle 127
Obsd. and Diff. Profiles
X10E 4
1.5
1.0
0.5
0.0
Counts
30.0
40.0
50.0
60.0
70.0
80.0
90.0
2-Theta, deg

d)

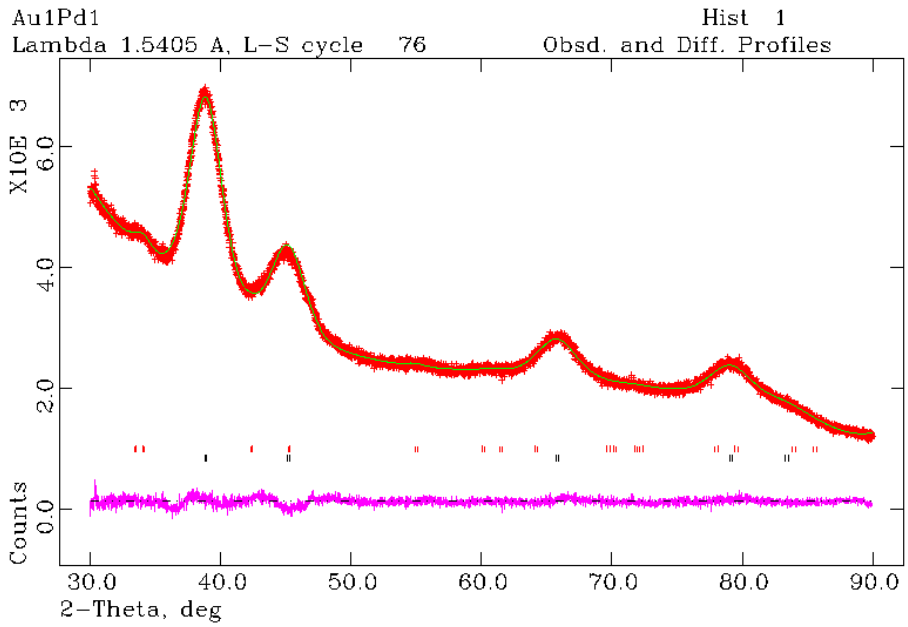
Au1Pd1
Hist 1
Lambda 1.5405 A, L-S cycle 76
Obsd. and Diff. Profiles
X10E 3
6.0
4.0
2.0
0.0
Counts
30.0
40.0
50.0
60.0
70.0
80.0
90.0
2-Theta, deg

e)

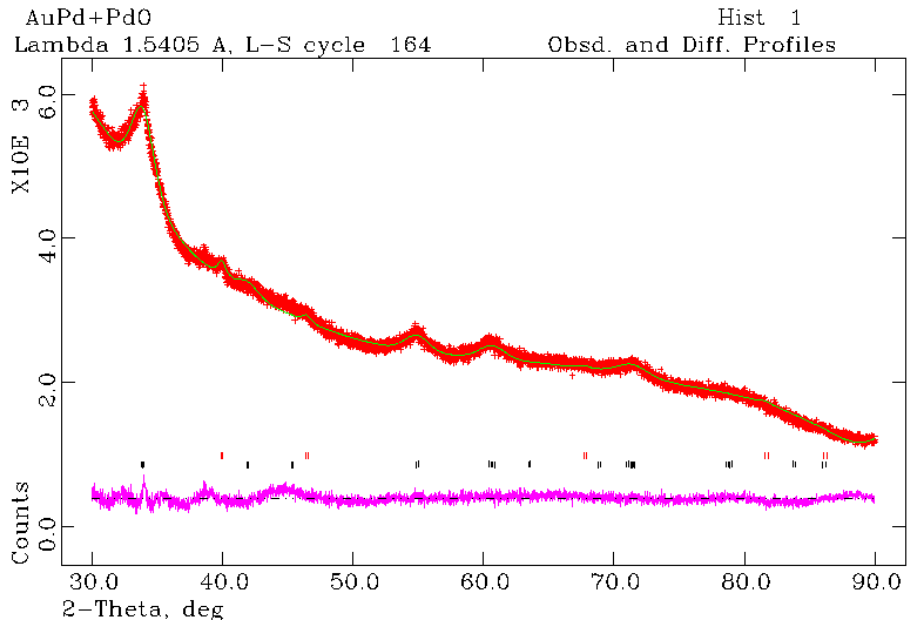

Fig. 4.1. Rietveld refinement of a) $Au@SiO_2$, b) $Pd@SiO_2$, (reduced) C) $Au3Pd@SiO_2$, d) $AuPd@SiO_2$, and e) $AuPd10@SiO_2$.

4.2. Calculation of AuPd alloy composition

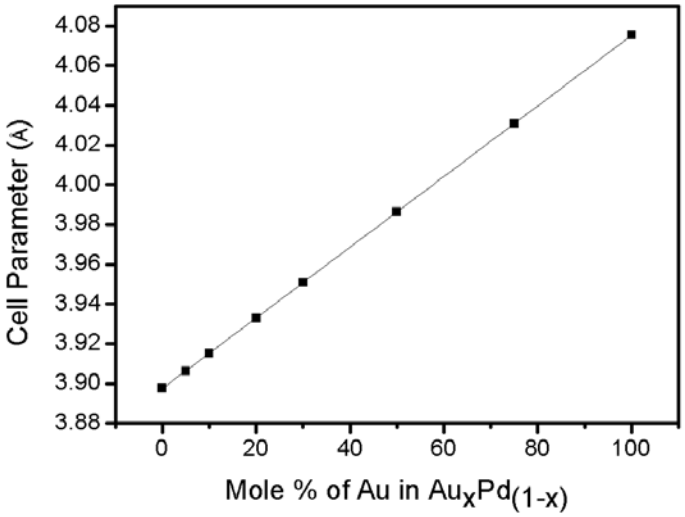

Fig. 4.2. Linear variation of lattice constants with composition

Vegard's law has been used extensively in mineralogy, metallurgy and materials science for the past six decades. According to the law, unit cell parameters should vary linearly with composition for a continuous substitutional solid solution in which

atoms or ions that substitute for each other are randomly distributed. Fig. 4.2 demonstrates Vegard's law of the linear dependence of the lattice parameter on concentration. Taking the cell parameters of pure $Au@SiO_2$ and $Pd@SiO_2$ as the end members of the bimetallic system, their linear relation to composition is reached by the equation y=0.00178x+3.8982, y and x are cell parameter and mole fraction of Au respectively.

For $Au3Pd@SiO_2$

y = 0.00178x+3.8982

x = y-3.8982/0.00178

= 4.0499-3.8982/0.00178 = 86

then Au = 86 and Pd = 100-86 = 14

then composition is $Au_{86}Pd_{14}$.

For $AuPd@SiO_2$

x = y-3.8982/0.00178

= 4.0149-3.8982/0.00178 = 66

the Au = 66 and Pd = 100-66 = 34

then composition is $Au_{66}Pd_{34}$

For $AuPd10@SiO_2$

x = y-3.8982/0.00178

= 3.9156-3.8982/0.00178 = 10

then Au = 10 and Pd = 100-10 = 90

then composition is $Au_{10}Pd_{90}$.

4.3. Details of calculations of CO (mole) conversion per Pd (mole) per second by the four catalysts

Calculation of CO amount passing through reactor per second

The flow rate of the reaction gas mixture is 25 mL min^{-1} (1:5:15.7, $CO:O_2:N_2$).

Amount of CO in 25 mL gas mixture is =1.15 mL.

Temperature of the gas is = 28 $^{\circ}$C= 301K.

Volume of CO at STP = 1.15X273/301 = 1.043 mL.

At STP volume of 1 mole CO is $22.4X10^3$ mL

Then at STP 1.043 mL of CO = $0.046X10^{-3}$ mole CO.

Then amount of CO gas passing through reactor per minute is $0.046X10^{-3}$ mole.

Then amount of CO gas passing through reactor per second $7.76X10^{-7}$ mole.

Then 100 % CO conversion = $7.76X10^{-7}$ mole CO conversion per second.

Catalyst $Au3Pd@SiO_2$

Amount of catalyst taken for CO oxidation = 17 mg

Loading of Pd based on ICP-AES = 1.1 %

Amount of Pd in 17 mg catalyst = $1.757X10^{-6}$ mole

Temperature ($^{\circ}C$)	CO conversion (%)	CO(mole) conversion s^{-1}	CO(mole) conversion s^{-1} Pd $(mole)^{-1}$
100	0	0	0
180	4	$31.04X10^{-9}$	$1.76X10^{-2}$
190	7	$54.32X10^{-9}$	$3.08X10^{-2}$
200	100	$7.76X10^{-7}$	0.44

Catalyst $AuPd@SiO_2$

Amount of catalyst taken for CO oxidation = 17 mg

Loading of Pd based on ICP-AES = 1.6 %

Amount of Pd in 17 mg catalyst = $2.55X10^{-6}$ mole

Temperature ($^{\circ}C$)	CO conversion (%)	CO(mole) conversion s^{-1}	CO(mole) conversion s^{-1} Pd $(mole)^{-1}$
100	0	0	0
120	9	$69.84X10^{-9}$	$2.74X10^{-2}$
135	50	$3.88X10^{-7}$	$15.2X10^{-2}$
140	100	$7.76X10^{-7}$	0.30

Catalyst AuPd10@SiO_2

Amount of catalyst taken for CO oxidation = 17 mg

Loading of Pd based on ICP-AES = 2.48 %

Amount of Pd in 17 mg catalyst = $3.956X10^{-6}$ mole

Temperature (^{o}C)	CO conversion (%)	CO(mole) conversion s^{-1}	CO(mole) conversion s^{-1} Pd (mole)$^{-1}$
100	0	0	0
150	5	$38.8X10^{-9}$	$9.80X10^{-3}$
160	19	$147.44X10^{-9}$	$37.26X10^{-3}$
170	100	$7.76X10^{-7}$	0.19

Catalyst Pd@SiO_2

Amount of catalyst taken for CO oxidation = 17 mg

Loading of Pd based on ICP-AES = 2.62 %

Amount of Pd in 17 mg catalyst = $4.18X10^{-6}$ mole

Temperature (^{o}C)	CO conversion (%)	CO(mole) conversion s^{-1}	CO(mole) conversion s^{-1} Pd (mole)$^{-1}$
100	0	0	0
150	4	$31.04X10^{-9}$	$7.42X10^{-3}$
160	12	$93.12X10^{-9}$	$22.27X10^{-3}$
170	100	$7.76X10^{-7}$	0.185